Computational Studies of Graphene on Nanostructured Ionic Substrates

Wu, Ying

Award date:
2016

Awarding institution:
University of Bath

Computational Studies of Graphene on Nanostructured Ionic Substrates

submitted by

Ying Wu

for the degree of Doctor of Philosophy

of the

University of Bath

Department of Physics

January 2016

Abstract

This work studies graphene on nanostructured ionic substrates using density functional theory (DFT) and the density functional tight binding (DFTB). Flat ionic substrates can provide graphene with a mechanical support without compromising its electronic properties, while the nanostructures can modify the electron behaviour in graphene sheets and potentially create devices such as on-sheet junctions.

Previous to the calculations, we extend the self-consistent charge DFTB method (SCC-DFTB) to a self-consistent charge and dipole DFTB scheme (SCCD-DFTB), which allows atomic dipoles to be considered self-consistently. This new scheme is implemented and its parametrisation discussed. Assessment is made based upon calculations of some electronic properties of Carbon-based systems including fullerenes, nanotubes and graphenes.

Studies of graphene on ionic substrates confirm that flat ionic substrates do not influence the electronic structure of graphene in the vicinity of Dirac points. In the case of nanostructured surfaces, it is identified that steps or pits with divalent impurity and cation vacancy pair with possible relaxations are the key to introducing sizeable electrostatic potential variations on graphene layers that can cause changes of the electronic structures of graphene at the low energy range recently observed in experiments.

Acknowledgement

First of all, I would like to thank my supervisors Dr. Simon Crampin and Dr. Adelina Ilie for their enthusiastic guidance and support. Among all their help, to think scientifically, creatively and independently is the most precious thing I have ever learnt.

I would also like to express my appreciation and thanks to Dr. Ryan Curtis, Dr. Asieh Kazemi, Dr. James Grant, Dr. Gavin Jones, Mr. Zichen Liu and all the colleagues in our office for the useful discussions and warm support.

I would also like to thank my grandparents, parents, uncle and my dear friends Hanqing Shen and Mengxi Ren for their day to day emotional support.

Finally, I am very grateful that University of Bath gave me a fully funded opportunity to study my PhD, alongside with all the facilities and support provided by the University, Department of Physics and Centre for Graphene Science.

Contents

Chapter 1

Introduction

Graphene, by definition [1], is a flat monolayer of carbon atoms tightly packed into a two-dimensional (2D) honeycomb lattice. Graphene is a basic building block for graphitic materials of all other dimensionalities. It can be wrapped up into 0D fullerenes, rolled into 1D nanotubes or stacked into 3D graphite.

In 2004, Novoselov *et al.* [2] obtained monolayer graphene through mechanical exfoliation. This was the very first time that a 2D material had been made in the real world, and resulted in the award of the *Nobel Prize in Physics 2010* to Andre Geim and Konstantin Novoselov for "groundbreaking experiments regarding the two-dimensional material graphene" [3]. Their work [2] also reported a carrier mobility at room temperature for graphene of up to 10000 $cm^2\ V^{-1}\ s^{-1}$, which is nearly 10 times the typical carrier mobility (1400 $cm^2\ V^{-1}\ s^{-1}$ for electrons, 480 $cm^2\ V^{-1}\ s^{-1}$ for holes) in traditional silicon-based devices [4].

The term *graphene* was not invented recently. In 1947, Wallace [5] used a tight binding method to calculate the band structure of graphite, reporting a in-plane/between-plane conductivity ratio of 100. This finding suggested that single layer graphite would have extraordinary electronic properties if it could be obtained. Later, in 1984, Semenoff [6] suggested that, theoretically, an independent graphite layer has effectively massless charge carriers. Two years later, in 1986, Boehm *et al.* [7] firstly mentioned the term "graphene". Although significant efforts were put into investigating graphene, over an extended period of time, both theorists and experimentalists believed that suspended graphene could not exist in principle, due to the thermal fluctuations [8–10], until graphene was eventually obtained in 2004. In 2007, Meyer *et al.* [11] identified a nanoscale corrugation in the third dimension of graphene, which explained the stability of the graphene sheet.

Since 2004, graphene related study has developed rapidly, to the extend that some graphene-based industrial products have been released recently, such as a Samsung flexible graphene-based OLED released in 2011 [12], an IBM 10 GHz broadband radio-frequency mixer in 2010 [13], and the NOKIA graphene-based camera sensor [14] in 2012.

Previous work has revealed graphene has attractive properties for applications in mechanical, thermal, optical, electronic, magnetic, chemical and biological realms.

With a breaking strength of 42 N m^{-1} and Young's Modulus of $E = 1$ TPa [15], graphene is one of the strongest materials known. On the other hand, graphene shows high pliability, can be stretched by 20 % [16] and it can be folded easily. Furthermore, although graphene is a one-atom-thick material, it is highly impermeable [17]. Also, graphene has by mass a very large surface area ($400 \sim 700$ m^2 g^{-1} [18]). With these excellent mechanical properties, graphene is an ideal candidate for nanoelectromechanical systems (NMES) [19, 20], water and gas storage devices [21, 22], gas or single molecule sensors [21], ultracapacitor [18], flexible screen [12], ultra strong recyclable paper [23] and for use in sports equipment such as badminton rackets and bicycle frames.

Regarding thermal properties, according to Balandin *et al.* [24] the thermal conductivity of single layer graphene at room temperature is $\sim$ 5000 W/mK, the thermal conduction being phonon-dominated. Carbon nanotubes, which are widely studied for heat conduction in electronic devices, have thermal conductivities of $\sim$ 3500 W/mK (single wall) [25], much less than that of graphene. In addition, graphene has an isotropic ballistic thermal conductance [26]. Therefore, graphene may outperform carbon nanotubes in heat spread and conduction [24]. Because of its excellent thermal transport properties, Wang *et al.* [27] and Li *et al.* [28] have proposed using phonons in graphene as a heat current to create so-called phonon-transistors, and further applications such as a thermal logic gate [29] and thermal memory [30] have followed.

Graphene also has good optical properties with potential applications. The light absorption rate of pure graphene is (2.3 ± 0.2) %, making it nearly transparent [31]. This transparency, along with the flexibility and high carrier mobility makes graphene a promising candidate to take over from indium tin oxide for transparent conducting electrodes, which are required for applications such as folding touchscreens, organic LEDs [12] and photovoltaic cells. In addition, graphene can be decorated and the absorption rate changed dramatically to 100 %. Thongrattanasiri *et al.* [32] have demonstrated 100 % light absorption by graphene, that has been periodically patterned with nanodisks. This controllable light absorption property

enables potential applications of optoelectronics. Under a biased voltage or applied magnetic field, graphene and graphene-based materials (bilayer graphene, graphene nanoribbons, graphene oxide, et al) show a tunable bandgap (0 ~ 0.25 eV [21]) or tunable optical response frequency (significantly enhanced THz response [33]), which can be used in electrochromic devices and as optical modulators. Furthermore, above a threshold input optical intensity the absorption of light can become saturated [34], which has wide application in ultrafast photonics [35].

In chemistry and biology related areas, graphene also has applications. As mentioned above, graphene has a large surface area, mono atom thickness and can be modified easily. For example, molecules, different functional groups, antibody, DNA and living cells can all be absorbed on graphene. This makes graphene suitable for gas and single molecule detection [21], sea water desalination [36], microbial detection and diagnosis, DNA/RNA testing, sequencing and modification and even DNA transistors [37]. Hu *et al.* [38] have shown that graphene and graphene-based materials have a selectivity towards bacteria and human cells, which means on those surfaces human cells can live but bacterial cannot, therefore making graphene a perfect material for hygiene products or packaging.

Among all of these properties and applications, the most tantalizing field is still electronic related devices. Not only because of the incredibly high carrier mobility and the needs to further scale down and speed up in the integrated circuits industry, but also because many other applications are designed to be integrated into the electronic devices framework, such as NMES, sensors or detectors of various purpose, heat spreaders, ultracapacitors, ultrabatteries, electrochromic devices, optical modulators, disease detection and diagnosis system, DNA transistors and so on.

The first graphene-based electronic device is the Field-Effect-Transistor (FET). In 2004, Novoselov *et al.* [2] reported an on-off ratio of about 30 at room temperature. In 2007, Lemme *et al.* [39] demonstrated the first top-gate FET, although the on-off ratio was very low (less than 2). The next year, Echtermeyer *et al.* [40] used a reversible chemical decoration method to significantly improve the on-off ratio (larger than 10^6) in a graphene FET. The first logic gates appeared in 2009, and Sordan *et al.* [41] managed to create four basic types of logic gates using graphene. In the same year, Wang *et al.* [42] reported the first graphene chip, a frequency multiplier. In 2010, Lin *et al.* [13] released a 10 GHz broadband radio-frequency mixer. In 2012, Torrisi *et al.* [43] have demonstrated an ink-jet printer that can be used for graphene device fabrication.

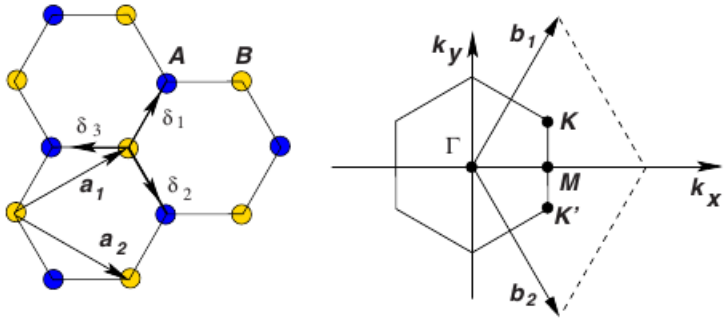

Figure 1.1: Monolayer graphene lattice (left) and its first Brillouin zone (right) adapted from Castro Neto *et al.* [44]. Blue and yellow atoms indicate site A and site B. $\mathbf{a}_1$ ($\mathbf{b}_1$) and $\mathbf{a}_2$ ($\mathbf{b}_2$) are the real (reciprocal) space lattice vectors. Γ, M, K and K' indicate the high symmetry points of the first Brillouin zone. $\boldsymbol{\delta}_1$, $\boldsymbol{\delta}_2$ and $\boldsymbol{\delta}_3$ are the three nearest neighbour vectors for site B atom.

1.1 Electronic properties of monolayer and bilayer graphene

Having briefly introduced the outstanding potential of graphene for electronic applications, we now discuss the electronic properties of graphene using tight-binding model. We begin by reviewing the physical structure of graphene.

As shown in the left panel of Fig. 1.1, monolayer graphene has a two dimensional hexagonal crystal structure with a Carbon-Carbon bond length of $a_{cc} = 1.42$ Å [45]. The honeycomb structure does not form a Bravais lattice because the blue atoms (site A) and yellow atoms (site B) are not equivalent. As shown in Fig. 1.1, real space primitive lattice vectors are

$$\mathbf{a}_1 = \frac{a}{2}\left(\sqrt{3}, 1\right), \qquad \mathbf{a}_2 = \frac{a}{2}\left(\sqrt{3}, -1\right), \tag{1.1}$$

where $a = |\mathbf{a}_1| = |\mathbf{a}_2|$ is the lattice constant, and we have $a = \sqrt{3}a_{cc} = 2.46$ Å. The corresponding primitive reciprocal lattice vectors $\mathbf{b}_1$ and $\mathbf{b}_2$ are given by

$$\mathbf{b}_1 = \frac{2\pi}{a}\left(\frac{1}{\sqrt{3}}, 1\right), \qquad \mathbf{b}_2 = \frac{2\pi}{a}\left(\frac{1}{\sqrt{3}}, -1\right). \tag{1.2}$$

The first Brillouin zone, defined as the smallest polyhedron centred at the origin and enclosed by perpendicular bisectors of the reciprocal lattice vectors [46], is shown in the right panel of Fig. 1.1, and the center, corners and other special points with high symmetry of the first Brillouin zone are labelled. The two non-equivalent corners K and K' are located in reciprocal space at

$$\boldsymbol{K} = \frac{2\pi}{3a}\left(\sqrt{3}, 1\right), \qquad \boldsymbol{K}' = \frac{2\pi}{3a}\left(\sqrt{3}, -1\right). \tag{1.3}$$

Carbon has 4 covalent electrons: $2s$, $2p_x$, $2p_y$ and $2p_z$. In graphene, $2s$, $2p_x$ and $2p_y$ form three sp^2 hybridized orbitals lying in-plane and oriented at 120° to each other. Interacting with sp^2 orbitals on adjacent other atoms, they form the σ band. The $2p_z$ orbital is perpendicular to the plane. Interacting with p_z orbitals on adjacent atoms, they form the π band. To see the structure of the π band, we briefly introduce the tight-binding model. Because graphene is a periodic system, the wave function $\Psi_{\mathbf{k}}(\mathbf{r})$ is expressed as a linear combination of Bloch functions $\Phi^{\mu}_{\mathbf{k}}(\mathbf{r})$ with coefficients $C^{\mu}_{\mathbf{k}}$ (see Section 2.2.1 for more detail of Bloch's theorem [47])

$$\Psi_{\mathbf{k}}(\mathbf{r}) = \sum_{\mu} C^{\mu}_{\mathbf{k}} \Phi^{\mu}_{\mathbf{k}}(\mathbf{r}), \tag{1.4}$$

where $\mathbf{k}$ is the wave vector and μ is the orbital, indicating both the orbital and the site A or B in the unit cell. The Bloch function $\Phi^{\mu}_{\mathbf{k}}(\mathbf{r})$ is a linear combination of atomic orbitals $\varphi_{\mu}(\mathbf{r}-\mathbf{R}_{\mu})$ in different unit cells

$$\Phi^{\mu}_{\mathbf{k}}(\mathbf{r}) = \frac{1}{\sqrt{N}} \sum_{i=1}^{N} e^{i\mathbf{k}\cdot\mathbf{R}_{\mu}} \varphi_{\mu}(\mathbf{r}-\mathbf{R}_{\mu}), \tag{1.5}$$

where $\mathbf{R}_{\mu}$ is the nuclei position the orbital μ is centred on, and i indicates the unit cells.

$\Psi_{\mathbf{k}}(\mathbf{r})$ satisfies the Schrödinger equation

$$\hat{H}\,|\Psi_{\mathbf{k}}\rangle = \epsilon_{\mathbf{k}}\,|\Psi_{\mathbf{k}}\rangle\,, \tag{1.6}$$

where $\epsilon_{\mathbf{k}}$ is the eigenvalue. Multiplying both sides with $\langle\Phi^{\mu}_{\mathbf{k}}|$ and applying Eq. 1.4

$$\begin{aligned} \langle\Phi^{\mu}_{\mathbf{k}}|\,\hat{H}\,|\Psi_{\mathbf{k}}\rangle &= \epsilon_{\mathbf{k}}\,\langle\Phi^{\mu}_{\mathbf{k}}|\Psi_{\mathbf{k}}\rangle \\ \sum_{\nu} C^{\nu}_{\mathbf{k}}\,\langle\Phi^{\mu}_{\mathbf{k}}|\hat{H}|\Phi^{\nu}_{\mathbf{k}}\rangle &= \sum_{\nu} C^{\nu}_{\mathbf{k}}\epsilon_{\mathbf{k}}\,\langle\Phi^{\mu}_{\mathbf{k}}|\Phi^{\nu}_{\mathbf{k}}\rangle\,. \end{aligned} \tag{1.7}$$

If we define the Hamiltonian matrix element $H_{\mu\nu}(\mathbf{k})$ and overlap matrix element $S_{\mu\nu}(\mathbf{k})$ as

$$H_{\mu\nu}(\mathbf{k}) = \langle\Phi^{\mu}_{\mathbf{k}}|\hat{H}|\Phi^{\nu}_{\mathbf{k}}\rangle \tag{1.8}$$

and

$$S_{\mu\nu}(\mathbf{k}) = \langle\Phi^{\mu}_{\mathbf{k}}|\Phi^{\nu}_{\mathbf{k}}\rangle\,, \tag{1.9}$$

Eq. 1.7 becomes

$$\sum_{\nu} \left(H_{\mu\nu}(\mathbf{k}) - \epsilon_{\mathbf{k}} S_{\mu\nu}(\mathbf{k}) \right) C_{\mathbf{k}}^{\nu} = 0. \tag{1.10}$$

Eq. 1.10 is the secular equation equivalent to the Schrödinger equation that needs to be solved (a different approach can be found in Section 3.1.6).

Now we apply this tight-binding model to monolayer graphene only considering the π band, which means only the $2p_z$ orbitals are included. There is only one $2p_z$ orbital per atom, and we denote the $2p_z$ orbital on site A (B) in unit cell i (j) orbital $\{A, i\}$ ($\{B, j\}$).

The diagonal Hamiltonian matrix element $H_{AA}(\mathbf{k})$ is

$$H_{AA}(\mathbf{k}) = \frac{1}{N} \sum_{i=1}^{N} \sum_{j=1}^{N} e^{i\mathbf{k}\cdot(\mathbf{R}_{A,j} - \mathbf{R}_{A,i})} \langle \varphi_{A,i}(\mathbf{r} - \mathbf{R}_{A,i}) | \hat{H} | \varphi_{A,j}(\mathbf{r} - \mathbf{R}_{A,j}) \rangle . \tag{1.11}$$

Assuming the contribution from $i = j$ is dominant [48]

$$H_{AA}(\mathbf{k}) \approx \frac{1}{N} \sum_{i=1}^{N} \langle \varphi_{A,i}(\mathbf{r} - \mathbf{R}_{A,i}) | \hat{H} | \varphi_{A,i}(\mathbf{r} - \mathbf{R}_{A,i}) \rangle . \tag{1.12}$$

If we introduce

$$\epsilon_A = \langle \varphi_{A,i}(\mathbf{r} - \mathbf{R}_{A,i}) | \hat{H} | \varphi_{A,i}(\mathbf{r} - \mathbf{R}_{A,i}) \rangle , \tag{1.13}$$

then

$$H_{AA}(\mathbf{k}) = \frac{1}{N} \sum_{i=1}^{N} \epsilon_A = \epsilon_A. \tag{1.14}$$

Because of the symmetry of sublattice A and B, $H_{BB}(\mathbf{k}) = \epsilon_B = H_{AA}(\mathbf{k}) = \epsilon_A$. Similarly, for the overlap matrix element, because of the orthonormality of the same orbital on the same atom, $S_{AA}(\mathbf{k}) = S_{BB}(\mathbf{k}) = 1$.

The off-diagonal Hamiltonian matrix element $H_{AB}(\mathbf{k})$ is

$$H_{AB}(\mathbf{k}) = \frac{1}{N} \sum_{i=1}^{N} \sum_{j=1}^{N} e^{i\mathbf{k}\cdot(\mathbf{R}_{B,j} - \mathbf{R}_{A,i})} \langle \varphi_{A,i}(\mathbf{r} - \mathbf{R}_{A,i}) | \hat{H} | \varphi_{B,j}(\mathbf{r} - \mathbf{R}_{B,j}) \rangle . \tag{1.15}$$

We only consider interactions between orbitals are the nearest neighbours. If we consider the B atom, three nearest A atoms are shown in Fig. 1.1 with the vectors $\boldsymbol{\delta}_i = \mathbf{R}_{A,i} - \mathbf{R}_{B,j}$

$$\boldsymbol{\delta}_1 = \left(\frac{a}{2\sqrt{3}}, \frac{a}{2}\right), \qquad \boldsymbol{\delta}_2 = \left(\frac{a}{2\sqrt{3}}, -\frac{a}{2}\right), \qquad \boldsymbol{\delta}_3 = \left(-\frac{a}{\sqrt{3}}, 0\right). \tag{1.16}$$

The Eq. 1.15 becomes

$$H_{AB}(\mathbf{k}) \approx \frac{1}{N}\sum_{i=1}^{3}\sum_{j=1}^{N} e^{-i\mathbf{k}\cdot\boldsymbol{\delta}_i} \left\langle \varphi_{A,i}(\mathbf{r} - \left(\mathbf{R}_{B,j} + \boldsymbol{\delta}_i\right) | \hat{H} | \varphi_{B,j}(\mathbf{r} - \mathbf{R}_{B,j}) \right\rangle . \tag{1.17}$$

Because of symmetry, $\langle \varphi_{A,i}(\mathbf{r} - \left(\mathbf{R}_{B,j} + \boldsymbol{\delta}_i\right) | \hat{H} | \varphi_{B,j}(\mathbf{r} - \mathbf{R}_{B,j}) \rangle$ is the same with $i = 1,2,3$, which we denote using

$$\gamma_0 = -\left\langle \varphi_{A,i}(\mathbf{r} - \left(\mathbf{R}_{B,j} + \boldsymbol{\delta}_i\right) | \hat{H} | \varphi_{B,j}(\mathbf{r} - \mathbf{R}_{B,j}) \right\rangle . \tag{1.18}$$

Eq. 1.17 becomes

$$H_{AB}(\mathbf{k}) = -\frac{1}{N}\sum_{i=1}^{3}\sum_{j=1}^{N} e^{-i\mathbf{k}\cdot\boldsymbol{\delta}_i}\gamma_0 = -\gamma_0 f(\mathbf{k}), \tag{1.19}$$

where

$$\begin{aligned} f(\mathbf{k}) &= \sum_{i=1}^{3} e^{-i\mathbf{k}\cdot\boldsymbol{\delta}_i} \\ &= e^{-i(k_x\frac{a}{2\sqrt{3}} + k_y\frac{a}{2})} + e^{-i(k_x\frac{a}{2\sqrt{3}} - k_y\frac{a}{2})} + e^{i(k_x\frac{a}{\sqrt{3}})} \\ &= 2\cos(\frac{a}{2}k_y)e^{-i(\frac{a}{2\sqrt{3}}k_x)} + e^{i(\frac{a}{\sqrt{3}}k_x)}. \end{aligned} \tag{1.20}$$

Similarly, for the off-diagonal overlap matrix, one gets

$$\begin{aligned} S_{AB}(\mathbf{k}) &= \frac{1}{N}\sum_{i=1}^{N}\sum_{j=1}^{N} e^{i\mathbf{k}\cdot(\mathbf{R}_{B,j} - \mathbf{R}_{A,i})} \left\langle \varphi_{A,i}(\mathbf{r} - \mathbf{R}_{A,i}) | \varphi_{B,j}(\mathbf{r} - \mathbf{R}_{B,j}) \right\rangle \\ &\approx \frac{1}{N}\sum_{i=1}^{3}\sum_{j=1}^{N} e^{-i\mathbf{k}\cdot\boldsymbol{\delta}_i} \left\langle \varphi_{A,i}(\mathbf{r} - \left(\mathbf{R}_{B,j} + \boldsymbol{\delta}_i\right) | \varphi_{B,j}(\mathbf{r} - \mathbf{R}_{B,j}) \right\rangle \\ &= S_0 f(\mathbf{k}), \end{aligned} \tag{1.21}$$

where

$$S_0 = -\left\langle \varphi_{A,i}(\mathbf{r} - \left(\mathbf{R}_{B,j} + \boldsymbol{\delta}_i\right) | \varphi_{B,j}(\mathbf{r} - \mathbf{R}_{B,j}) \right\rangle . \tag{1.22}$$

Because the Hamiltonian is Hermitian, it follows that $H_{BA}(\mathbf{k}) = H^*_{AB}(\mathbf{k})$ and $S_{BA}(\mathbf{k}) = S^*_{AB}(\mathbf{k})$.

With the Hamiltonian and overlap matrix elements so obtained,

$$\hat{H} = \begin{pmatrix} \epsilon_A & -\gamma_0 f(\mathbf{k}) \\ -\gamma_0 f^*(\mathbf{k}) & \epsilon_B \end{pmatrix}, \qquad S = \begin{pmatrix} 1 & S_0 f(\mathbf{k}) \\ S_0 f^*(\mathbf{k}) & 1 \end{pmatrix}, \tag{1.23}$$

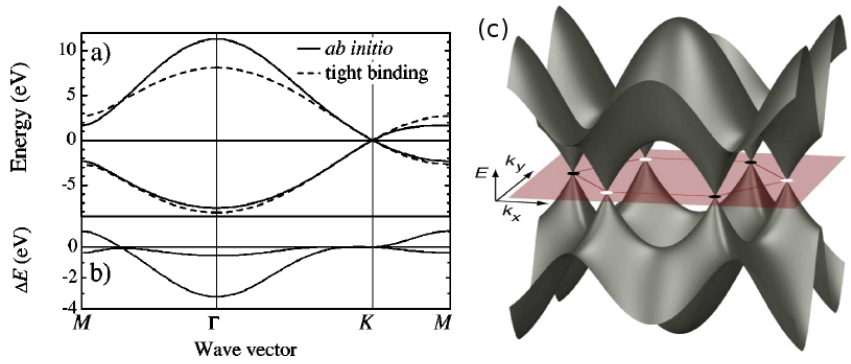

Figure 1.2: Band structure of monolayer graphene. a,b) Comparison of the result obtained from tight binding and from first principles calculation [49]. c) Result from nearest neighbour tight binding model [50], energy range differs from the range showing in a,b).

and we can solve Eq. 1.10. The resulting eigenvalues are [26]

$$E_{\pm}(\mathbf{k}) = \frac{\epsilon_A \pm \gamma_0 |f(\mathbf{k})|}{1 \mp S_0 |f(\mathbf{k})|}. \tag{1.24}$$

For intrinsic graphene it then follows $\epsilon_F = 0$. The tight-binding model cannot determine the values of γ_0 and S_0, which are either taken from first principle calculations, such as values $\gamma_0 = 3.033$eV, $S_0 = 0.129$ obtained by Painter and Ellis [45], or from fitting to experimental results. Fig. 1.2c) shows an example of the monolayer graphene band structure calculated from the method discussed above. The bands touch at the corners of the Brillouin zone at energy $E = 0$, showing that graphene is a gapless semiconductor. Fig. 1.2a,b) shows a comparison of the band structure obtained by the tight-binding approach and from first principle methods (see later). The bands near the K points agreed with each other very well. The dispersions in the vicinity of the K and K' points, also known as the low-energy range, will be discussed in detail.

At the six corners of the first Brillouin zone, $f(\mathbf{k})$ vanishes. For example, for the two non-equivalent $\mathbf{k}$ points given in Eq. 1.3, one has

$$f(\boldsymbol{K}) = f(\boldsymbol{K}') = e^{-i\frac{2\pi}{3}} + e^{0} + e^{i\frac{2\pi}{3}} = 0. \tag{1.25}$$

Let us define a momentum related to the K point: $\mathbf{p} = \mathbf{k} - \boldsymbol{K}$ [1], where $p = |\mathbf{p}| \ll 1/a$. Expanding the Hamiltonian around the K point one obtain the leading order

[1] the atomic unit is used here, $\hbar = 1$.

$$\hat{H}(\mathbf{p}) = v_F \begin{pmatrix} 0 & p_x - ip_y \\ p_x + ip_y & 0 \end{pmatrix}, \tag{1.26}$$

where

$$v_F = \frac{\sqrt{3}a\gamma_0}{2} \tag{1.27}$$

is the Fermi velocity, with magnitude $\sim 1 \times 10^6$ m/s [5].

Now we substitute p_x with $-i\frac{\partial}{\partial x}$ and p_y with $-i\frac{\partial}{\partial y}$, Eq. 1.26 becomes

$$\hat{H}(\mathbf{p}) = v_F \hat{\boldsymbol{\sigma}} \cdot \mathbf{p}, \tag{1.28}$$

where $\hat{\boldsymbol{\sigma}} = (\sigma_x, \sigma_y)$, write σ_x and σ_y as the 2D Pauli matrices

$$\sigma_x = \begin{pmatrix} 0 & 1 \\ 1 & 0 \end{pmatrix}, \qquad \sigma_y = \begin{pmatrix} 0 & -i \\ i & 0 \end{pmatrix}. \tag{1.29}$$

A similar result can be found expanding around the K' point,

$$\hat{H}(\mathbf{p}) = v_F \hat{\boldsymbol{\sigma}}' \cdot \mathbf{p}, \tag{1.30}$$

where $\hat{\boldsymbol{\sigma}}' = (-\sigma_x, \sigma_y)$ and $\mathbf{p} = \mathbf{k} - \boldsymbol{K}'$.

Note that Eqs. 1.28 and 1.30 have the form of the Dirac equation describing a massless spin 1/2 particle with velocity v_F (instead of the speed of light c).

Solving for the eigenvalues and eigenstates of Eq. 1.28 given

$$E_\pm(\mathbf{k}) = \pm v_F p, \tag{1.31}$$

and

$$\Psi_\pm(\mathbf{k}) = \frac{1}{\sqrt{2}} \begin{pmatrix} e^{-\theta_\mathbf{k}/2} \\ \pm e^{\theta_\mathbf{k}/2} \end{pmatrix}, \qquad \theta_\mathbf{k} = \arctan\left(\frac{p_x}{p_y}\right). \tag{1.32}$$

The subscripts + or − denotes the conduction or valence band, respectively. From Eq. 1.31 we can see that, at low energy, the band structure near the corners of the Brillouin zone has two bands with linear dispersion that cross at zero energy. These corners are also known as the Dirac points. The effective Dirac Hamiltonian of Eq. 1.28 or Eq. 1.30 is the origin of a whole range of interesting physical phenomenon, such as massless Dirac quasiparticles,

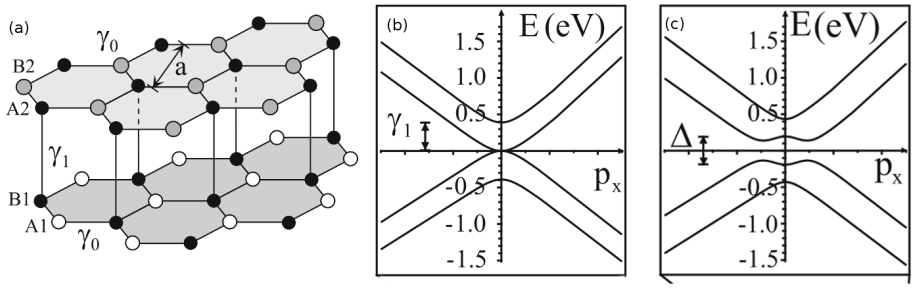

Figure 1.3: a) Geometry of AB-stacked bilayer graphene [48]. b) Band structure of bilayer graphene, $\Delta = 0$ and c) $\Delta = \gamma_1$ [48].

chiral tunnelling, integer quantum Hall effect and so on.

Now we consider AB-stacked bilayer graphene. Fig. 1.3a) shows the geometry of AB-stacked bilayer graphene, where site B1 and A2 have Carbon atoms above or underneath, and sites A1 and B2 do not. We can apply the tight binding model in the nearest neighbour approximation, and assuming that for interlayer hopping, only hopping between B1 and A2 is relevant. Similar to the definition of γ_0 and S_0, we introduce

$$\gamma_1 = -\langle \varphi_{A2,i}(\mathbf{r}-\mathbf{R}_{A2,i})|\hat{H}|\varphi_{B1,j}(\mathbf{r}-\mathbf{R}_{B1,j})\rangle\,, \tag{1.33}$$

and

$$S_1 = -\langle \varphi_{A2,i}(\mathbf{r}-\mathbf{R}_{A2,i})|\varphi_{B1,j}(\mathbf{r}-\mathbf{R}_{B1,j})\rangle\,. \tag{1.34}$$

Therefore, the Hamiltonian matrix element $H_{A2,B1}(\mathbf{k}) = \gamma_1$. McCann [48] has argued that for the energy range $|E| \ll \gamma_1$, S_1 can be ignored. The Hamiltonian and overlap matrices are (assuming the order A1, B1, A2, B2 for rows and columns)

$$\hat{H} = \begin{pmatrix} \epsilon_{A1} & -\gamma_0 f(\mathbf{k}) & 0 & 0 \\ -\gamma_0 f^*(\mathbf{k}) & \epsilon_{B1} & \gamma_1 & 0 \\ 0 & \gamma_1 & \epsilon_{A2} & -\gamma_0 f(\mathbf{k}) \\ 0 & 0 & -\gamma_0 f^*(\mathbf{k}) & \epsilon_{B2} \end{pmatrix}, \tag{1.35}$$

$$S = \begin{pmatrix} 1 & S_0 f(\mathbf{k}) & 0 & 0 \\ S_0 f^*(\mathbf{k}) & 1 & 0 & 0 \\ 0 & 0 & 1 & S_0 f(\mathbf{k}) \\ 0 & 0 & S_0 f^*(\mathbf{k}) & 1 \end{pmatrix}. \tag{1.36}$$

Unlike the monolayer case, diagonal entries in the Hamiltonian can be different for the dif-

ferent layers, e.g. duo to the presence of an electric field across the bilayer. If we introduce $\epsilon_{A1} = \epsilon_{B1} = -\frac{1}{2}\Delta$ and $\epsilon_{A2} = \epsilon_{B2} = \frac{1}{2}\Delta$, the Hamiltonian matrix becomes

$$\hat{H} = \begin{pmatrix} -\frac{1}{2}\Delta & -\gamma_0 f(\mathbf{k}) & 0 & 0 \\ -\gamma_0 f^*(\mathbf{k}) & -\frac{1}{2}\Delta & \gamma_1 & 0 \\ 0 & \gamma_1 & \frac{1}{2}\Delta & -\gamma_0 f(\mathbf{k}) \\ 0 & 0 & -\gamma_0 f^*(\mathbf{k}) & \frac{1}{2}\Delta \end{pmatrix}. \tag{1.37}$$

To evaluate the dispersion at low energy range (around the Dirac points), following McCann [48] we set $S_0 = 0$ which results in

$$E_{\pm}^2(\mathbf{p}) = \frac{\Delta^2}{4} + v_F^2 p^2 + \frac{\gamma_1^2}{2} \pm \sqrt{1 + \frac{4v_F^2 p^2}{\gamma_1^2} + \frac{4\Delta^2 v_F^2 p^2}{\gamma_1^4}}. \tag{1.38}$$

The band structure with $\Delta = 0$ is plotted in Fig. 1.3b), calculated with the value $\gamma_0 = 3.033$eV, $\gamma_1 = 0.39$eV [45], and that for $\Delta = \gamma_1$ is shown in Fig. 1.3c). In the $\Delta = 0$ case, the bands originating from sites A2 and B1 split away by γ_1 from zero energy, due to the interlayer coupling, and the linear dispersion has been replaced by a parabolic one. For the $\Delta = \gamma_1$ case, the band gap opens up and forms a "Mexican hat" shape in general. The band separation at the Dirac points are exactly Δ, but the band gap is depending on the of value Δ, indicating bilayer graphene possesses a tunable band gap.

1.2 Graphene on various substrates

As discussed in the previous Section, free standing monolayer and bilayer graphene have exciting electronic properties, however, the study of graphene on substrates is essential. Firstly, free standing graphene in most cases is not mechanically stable, but requires a substrate to support the graphene while operating. Secondly, substrates can be important functioning components of actual devices. Thirdly, many methods of obtaining large scale graphene involve growth on substrates. Finally and most importantly, the modification of free standing graphene is limited, whereas substrates can impose interesting and controllable modifications to the electrons in graphene. Therefore, in this Section, we will review graphene on the widely studied substrates: Silicon-based (Si, SiC and SiO_2), transition metal (Ni, Cu, Co, Ir, Pt and Ru), and other atomically flat insulators (BN, mica, CaF_2 and Al_2O_3).

The first graphene was obtained by micromechanical exfoliation of graphite with tape [2], but using this method, a technique to identify the mono or several layered flake among a majority of thicker flakes is required. Novoselov *et al.* [51] found that when 2D materi-

als are put onto a Si wafer with a certain thickness of SiO_2, they become visible in optical microscopy. Later in 2006, Gupta *et al.* [52] and Ferrari *et al.* [53] reported clear signal differences between mono-, bi- and few-layer graphene on top of a SiO_2/Si substrate in Raman microscopy. Furthermore, transferred graphene to SiO_2/Si substrate showed the conservation of the metallic band structure and high carrier mobility to some extent [51, 54].

With micromechanically exfoliated graphene it is difficult to achieve wafer size. To solve this, epitaxial growth from SiC is believed to be a good approach [55]. When annealing in high temperature, excess carbon atoms come out from bulk SiC and form a graphene sheet with careful control. Using this method, large homogeneous graphene sheets can be obtained under certain atmospheric conditions (e.g. argon) and pressures (e.g. 1 bar) [56]. It has been shown that graphene on SiC exhibits some properties of suspended graphene, such as the quantum Hall effect [57].

For Si-based substrates, there is an obvious advantage: the standard microelectronics fabrication methods can be used, so that graphene devices on Si-based substrates are compatible with the silicon chips existing today. This is important for the immediate use of graphene.

On the other hand, both SiO_2/Si and SiC substrates have their own disadvantages. For SiO_2/Si substrate, the surface roughness is very high (more than 1 nm [58]) and graphene flakes with high mobility only exist between two hills. Fig 1.4a,b) show the 3D and 2D STM image of monolayer graphene on a SiO_2 surface. The lateral corrugation is around 1 nm and the distance between the hills is about 15 nm. Graphene on SiC suffers from a relatively low carrier mobility (1200 V^{-1} s^{-1} [59]) and band gap opening [60]. Fig 1.4c) shows the result obtained from first principle calculation, illustrating the band gap opening in the case of single layer graphene on SiC (0001) substrate.

Another way to achieve macroscopic scaled graphene is chemical vapor deposition (CVD) on transition metals. Reina *et al.* [62] have reported ambient pressure CVD on polycrystalline Ni films which achieved area of graphene layer ($1 \sim 12$ layers) of around cm^2. By etching away the Ni substrate, graphene can be then transferred to any substrate, such as SiO_2, insulators or polymer. At low temperature, transferred graphene from Ni to SiO_2 showed an electron mobility of 3700 V^{-1} s^{-1} [63]. Similar results have been found for Co [64], Pt [65, 66], Ir [67] and Ru [68], but in some cases needed high doses of hydrocarbon gas as the atmosphere and under low pressure. On Ru surfaces, the interaction between graphene and ruthenium has been found to be considerably stronger than the interlayer interaction

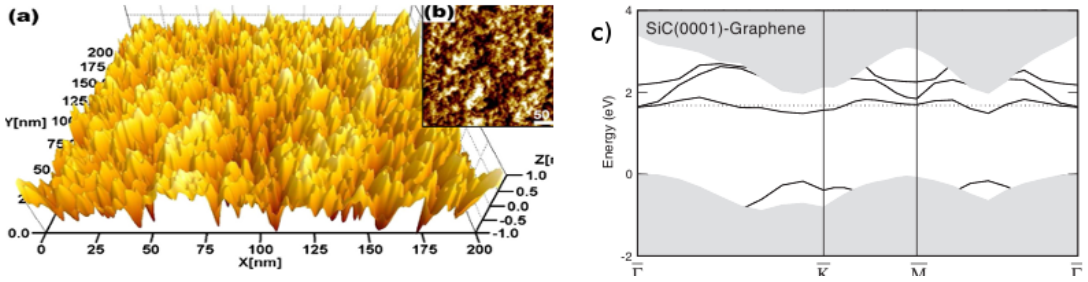

Figure 1.4: a) and b) STM topology of graphene on SiO_2 [58]. c) Band structure of single layer graphene on SiC (0001) [60].

in graphite, and this may result in a relatively large area of monolayer graphene ($\sim 30\times30$ Å^2) without any multilayer [68]. Souzu and Tsukada [69] reported that graphene/Ni(111) system showed a band gap opening about 1.0 eV, and this opening was believed due to the coupling of graphene π/π^* bands to metal states near the K point. Grüneis and Vyalikh [70] modified the band gap of graphene/Ni(111) system using gradual intercalation of potassium metal. Different density of potassium resulted in different strength of hybridization between the graphene and the nickel. Khomyakov *et al.* [61] performed a systematic set of first principle calculations of the interactions between graphene and transition metal surfaces. The band structures are shown in Fig. 1.5. They have found that there is strong interaction between graphene and Co, Ni, and Pd (111) surfaces, and the Ti(001) surface perturbs the electronic structure significantly. In contrast, only weak absorption is found on Al, Cu, Ag, Au, and Pt (111) surfaces, which preserve the conical points. However, Marchini *et al.* [68] argued that the use of a (1 × 1) unit cell is not sufficient if taking Moiré pattern and formation kinetics into consideration. Also, Amft *et al.* [71] pointed out that Khomyakov *et al.* [61] failed to take van der Waals corrections into account, which are essential for accurately describing the graphene metal surface separation.

For metal substrates, under proper environment, relatively large area of single layer graphene can be obtained and then patterned and transferred to other substrates [63–66, 68]. The band gap can be modified by inserting other atoms [61, 69], but further understanding of the growth mechanisms and interactions between graphene and substrates are still needed.

Recently, another set of substrates has become of increasing interest, namely atomically flat substrates. One reason is the growing need to retain the graphene quality when it is put on supporting substrates. Although graphene transferred on SiO_2 can have quasi-free-standing graphene features to some extent, the highly disordered SiO_2 surface geometry

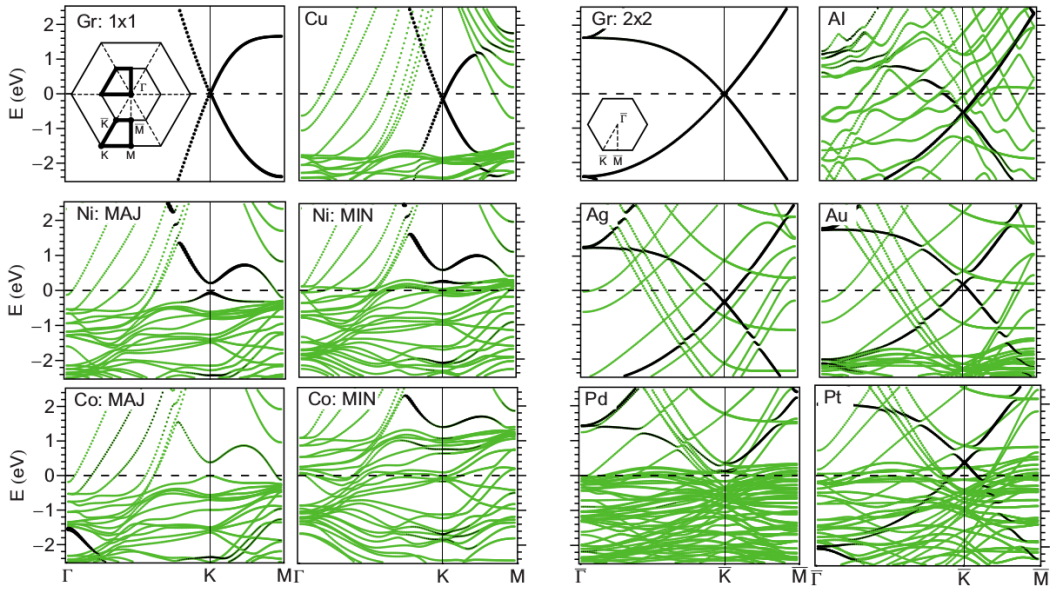

Figure 1.5: Band structures of graphene on Au, Pt, Cu, Ag, Al, Pd, Ni and Co (111) surfaces. The Fermi level is at zero energy, MIN/MAJ indicate the majority/minority spin bands in the spin polarised substrates. Black lines are graphene bands, green lines are the metal bands [61].

still largely affects the graphene. Some metal substrates such as Ni, Cu and Ru (111) can serve as smooth surfaces enabling homogeneous monolayer graphene to be achieved, but in these systems, the interaction between the metal and graphene change the energy dispersion qualitatively.

Th hexagonal boron nitride (h-BN) as a substrate has been investigated widely, due to its similar lattice constant to that of graphene, and its large band gap [72, 73]. Dean *et al.* [72] reported an exfoliated graphene on h-BN with a carrier mobility almost an order of magnitude better than that obtained on SiO_2. Giovannetti *et al.* [73] and Yelgel and Srivastava [74] have reported that the band gap of graphene/BN is $\sim$ 50 meV using first principle calculations. Some first principle calculations suggest that graphene/Cu has a smaller band gap ($\sim$ 10 meV [73]), the first principle method is perhaps unsuitable for the transition metal systems. Lui *et al.* [75] have demonstrated monolayer graphene deposited on mica surfaces and Akcöltekin *et al.* [76] have demonstrated the successful transfer of graphene to various atomically flat crystalline substrates, including $SrTiO_3$, Al_2O_3, TiO_2 and CaF_2.

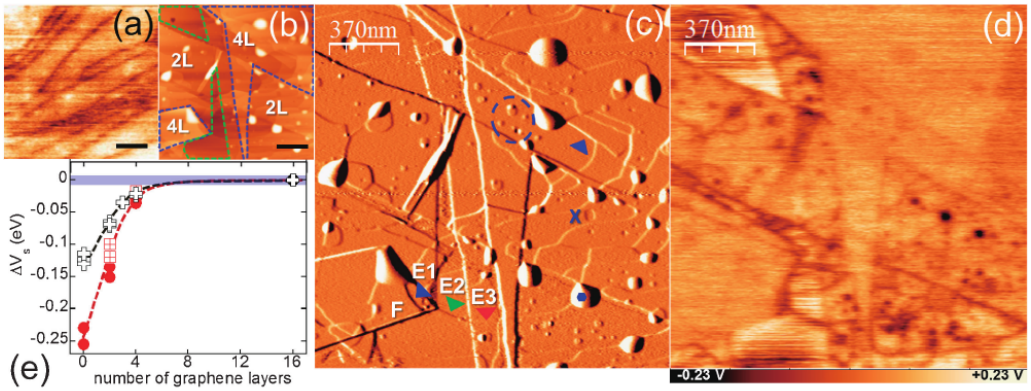

Figure 1.6: a) Kelvin probe force microscopy of a bare KBr surface. b) Topography, with boundaries of few layer graphene domains and substrate highlighted: KBr (green), four-layer graphene (blue) and bi-layer between them. c) Amplitude image of the few layer graphene. Step edges (triangle), pits (cross), protrusions (encircled), and organic contaminations (hexagon) are all indicated. d) Surface potential image corresponding to c). e) Surface potential ΔV_s originating from edges (crosses), and pits/protrusions (circles/squares) of 40 nm diameter [77].

1.3 Motivation for the work of this thesis

In this thesis, we consider graphene on atomically flat and nanostructured ionic substrates. In the case of flat substrates, we can expect graphene properties to be well preserved due to a weak interaction between graphene and the surface. Secondly, it is envisaged that the nanostructured ionic surfaces can provide atomic-scale electrostatic potentials, which will be good candidates to modify the electron behaviour in graphene. Therefore, different regions on the substrate could potentially provide different potentials and be exploited to create on-sheet junctions. This ability to pattern the graphene will be of highly interest both in terms of applications and from a fundamental point of view.

As motivation to this work, we note the experimental studies [77] in which graphene has been deposited on nano-structured KBr and NaCl surfaces. Fig. 1.6 shows few layer graphene flakes on a nanostructured KBr surface investigated by Kelvin probe microscopy. Fig. 1.6a) is the Kelvin probe force microscopy of a bare KBr surface. Fig. 1.6b) shows the topography of few layer graphene on top of KBr, the green lined region is KBr substrate, blue lined region is the four layer graphene and other area is bilayer graphene. Fig. 1.6c) shows the presence of several different types of the nanostructures on the surfaces. Triangles indicate the edges, cross the pits, encircled the protrusions and hexagon the organic contaminations. Fig. 1.6d) shows the surface potential of Fig. 1.6c), with a clear potential variation

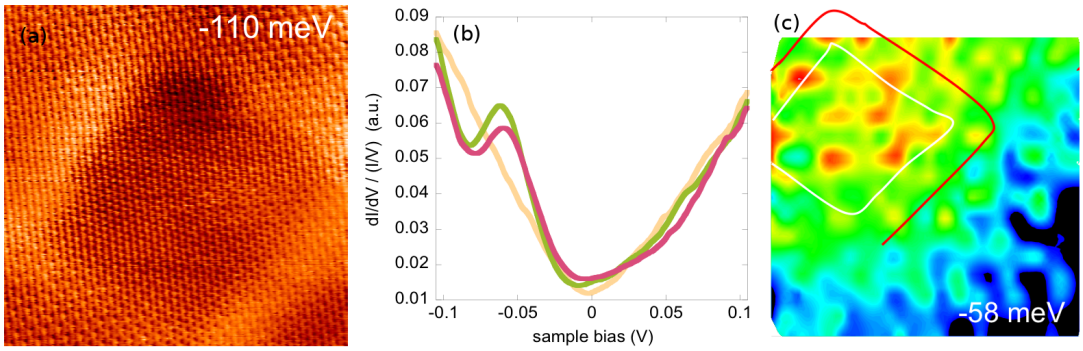

Figure 1.7: STM images of graphene on NaCl with pits . a) STM image taken at a bias of −110 meV [78]. b) dI/dV with respect to the bias V measured with the STM tip positioned at selected locations. c) dI/dV maps at −58 meV. White and red lines indicate the possible pits edges (Courtesy by Dr. Adelina Ilie).

found near the edges, pits and protrusions. More quantitative details are displayed in Fig. 1.6e), from which it can be seen that the edges, pits and protrusions correspond to potential variations of 0.15 eV, 0.25 eV and 0.10 eV, respectively. Controllable nanostructures such as steps and kinks on the ionic surfaces are therefore seen to create sizeable and local electrostatic perturbations in the eV range of the graphene surface potential. Exploiting these potential could enable the constitution of devices such as electron guides with the knowledge of previous findings [79].

Fig. 1.7 shows experimental results from a study of bilayer graphene above a pit at the NaCl(001) surface. Fig. 1.7a) shows s STM image taken at a bias of −110 meV, which shows the presence of a rectangular pit of size 8×8 nm. Enhanced contrast is visible in the top corner. Fig. 1.7b) shows dI/dV with respect to the bias V measured with the STM tip positioned at selected locations, green and red curves are from the locations above the pit, and yellow curve is from the location far away from the pit. A peak around −58 meV can be seen at two of the locations which are above the pit. Fig. 1.7c) shows the appearance of a dI/dV map at the bias voltage −58 meV, which indicates that the electronic features at −58 meV in favoured in the areas above the pit on the NaCl surfaces.

Both these experimental works present experimental evidence that nanostructures on ionic surfaces can induce sizeable electrostatic potentials in depositing graphene layers, and further modify the electronic behaviour in the graphene. In this work, we use theoretical computational methods to study both the electrostatic potential and electronic structures of graphene on nanostructured ionic substrates, with a view to gaining insight with theses systems.

The rest of this thesis is structured as follow: Chapter 2 is a brief introduction to density functional theory (DFT), which is a computational method we use in the studies. Chapter 3 introduces the self-consistent-charge density functional tight binding (SCC-DFTB) method, and discusses the extension of the scheme to include dipole contribution; Chapter 4 describes the implementation of this self-consistent charge and dipole density functional tight binding method (SCCD-DFTB), its validation, and discusses the parameterisation. Chapter 5 then presents the results of studies of graphene on nanostructured ionic substrates obtained from DFT, SCC-DFTB and SCCD-DFTB methods. Chapter 6 concludes the findings of this work, and gives an outlook for further work.

Chapter 2

Density Functional Theory

This Chapter begins by briefly presenting the theoretical framework of density functional theory. Some popular implementations are then introduced.

2.1 Theoretical framework

2.1.1 Many-body Hamiltonian and Born-Oppenheimer approximation

The starting point for the theoretical framework of non-relativistic density functional theory is the many-body Hamiltonian $\hat{H}_{tot}$ describing a system contains both atomic nuclei I and electrons i [80]:

$$\begin{aligned}\hat{H}_{tot} = &-\sum_i \frac{\hbar^2}{2m_e}\nabla^2_{\mathbf{r}_i} + \frac{1}{2}\sum_i\sum_{j\neq i}\frac{e^2}{|\mathbf{r}_i-\mathbf{r}_j|} - \sum_i\sum_I \frac{Z_I e^2}{|\mathbf{R}_I-\mathbf{r}_i|} \\ &-\sum_I \frac{\hbar^2}{2M_I}\nabla^2_{\mathbf{R}_I} + \frac{1}{2}\sum_I\sum_{J\neq I}\frac{Z_I Z_J e^2}{|\mathbf{R}_I-\mathbf{R}_J|},\end{aligned} \tag{2.1}$$

where m_e (M_I) is the mass, $\mathbf{r}_i$ ($\mathbf{R}_I$) is the position, and e ($-Z_I e$) is the charge of electron i (nucleus I). The first term on the right hand side is the kinetic energy of the electrons, the second term is the electrostatic Coulomb repulsion of the electrons, the third term is the attractive electron-ion Coulomb interaction, the fourth term is the kinetic energy of the ions and the fifth term is the repulsive ion-ion interaction. We can write the first three terms as $\hat{H}_e$ which contains electron contributions, and the remainder as $\hat{H}_n$, which contains exclusively ion contributions.

Because a system can be completely described by its wave function $\Psi_{tot}(\{\mathbf{R}_I\},\{\mathbf{r}_i\};t)$ (the spin information of the electrons is assumed included in the $\{\mathbf{r}_i\}$), by solving the Schrödinger equation

$$\hat{H}_{tot}\Psi_{tot}(\{\mathbf{R}_I\},\{\mathbf{r}_i\};t) = i\hbar\frac{\partial}{\partial t}\Psi_{tot}(\{\mathbf{R}_I\},\{\mathbf{r}_i\};t), \tag{2.2}$$

we can access the full information. If we assume a stationary state, the wave function can be separated as

$$\Psi_{tot}(\{\mathbf{R}_I\},\{\mathbf{r}_i\};t) = \tilde{\Psi}_{tot}(\{\mathbf{R}_I\},\{\mathbf{r}_i\})T(t), \tag{2.3}$$

which leads to the time-independent Schrödinger equation

$$\hat{H}_{tot}\tilde{\Psi}_{tot}(\{\mathbf{R}_I\},\{\mathbf{r}_i\}) = E_{tot}\tilde{\Psi}_{tot}(\{\mathbf{R}_I\},\{\mathbf{r}_i\}), \tag{2.4}$$

$$\Psi_{tot}(\{\mathbf{R}_I\},\{\mathbf{r}_i\};t) = \tilde{\Psi}_{tot}(\{\mathbf{R}_I\},\{\mathbf{r}_i\})\exp(-iE_{tot}/\hbar), \tag{2.5}$$

where the separation constant E_{tot} has a physical meaning as the energy eigenvalue.

Although we only need to solve Eq. 2.4 to find the wave function and from it the properties of the system, the wave function $\tilde{\Psi}_{tot}(\{\mathbf{R}_I\},\{\mathbf{r}_i\})$ is a function of $3(N_i+N_e)$ variables, where N_i (N_e) is the total number of ions (electrons). Even for small system such as few unit cells of simple cubic crystals, it is nearly impossible to solve it exactly, let alone a macroscopic sample of a material has $> 10^{21}$ atoms. Therefore, some plausible approximations are desirable.

The first step is to decouple the motion of ions and the electrons. Since the mass of one electron is about 1/1836 that of one proton, the ions have much lower velocities than the electrons. This motivates the Born-Oppenheimer approximation [81], which assumes that the electrons respond instantaneously to the movement of the ions. In finding the electronic states, the ions can therefore be treated as static, with the wave function $\tilde{\Psi}_{tot}(\{\mathbf{R}_I\},\{\mathbf{r}_i\})$ separated as an electronic wave function $\Psi_{e,\{\mathbf{R}_I\}}(\{\mathbf{r}_i\})$ and ionic wave function $\Phi(\{\mathbf{R}_I\})$:

$$\tilde{\Psi}_{tot}(\{\mathbf{R}_I\},\{\mathbf{r}_i\}) = \Psi_{e,\{\mathbf{R}_I\}}(\{\mathbf{r}_i\})\Phi(\{\mathbf{R}_I\}). \tag{2.6}$$

Note that the electron wave function depends parametrically on the ionic coordinates. Then the time-independent Schrödinger equation for electrons in a frozen nuclei system is

$$\hat{H}_e\Psi_{e,\{\mathbf{R}_I\}}(\{\mathbf{r}_i\}) = E_{e,\{\mathbf{R}_I\}}\Psi_{e,\{\mathbf{R}_I\}}(\{\mathbf{r}_i\}), \tag{2.7}$$

where $E_{e,\{\mathbf{R}_I\}}$ is the energy eigenvalue of the electrons, which depends on the specific arrangement of the nuclei $\{\mathbf{R}_I\}$. From now on, because the nuclei are frozen at positions $\{\mathbf{R}_I\}$,

we will omit reference to their positions in writing the electronic part of the wave function and the eigenvalues, and drop the subscript e on them and the Hamiltonian. Also we will use the Hartree atomic units [1] from now on, so that Eq. 2.7 becomes

$$\hat{H}\Psi(\{\mathbf{r}_i\}) = E\Psi(\{\mathbf{r}_i\}), \tag{2.8}$$

where

$$\begin{aligned}\hat{H} &= \hat{T} + \hat{V}_{int} + \hat{V}_{ext} \\ &= -\sum_i \frac{1}{2}\nabla^2_{\mathbf{r}_i} + \frac{1}{2}\sum_i \sum_{j\neq i} \frac{1}{|\mathbf{r}_i - \mathbf{r}_j|} - \sum_i \sum_I \frac{Z_I}{|\mathbf{R}_I - \mathbf{r}_i|}.\end{aligned} \tag{2.9}$$

$\hat{T}$ is the kinetic energy term, $\hat{V}_{int}$ is the electron-electron interaction, and $\hat{V}_{ext}$ is the nuclear potential acting on the electrons, which can be specifically defined as $\hat{V}_{ext} = \sum_i V_{ext}(\mathbf{r}_i)$. Note that the electronic energy eigenvalue is labelled as E from now on, and the total energy E_{tot}, assuming stationary ions, is sum of electronic energy E and the ion-ion interaction energy E_{II}: $E_{tot} = E + E_{II}$, where E_{II} is a constant for specific ionic positions, given by

$$E_{II} = \frac{1}{2}\sum_I \sum_{J\neq I} \frac{Z_I Z_J e^2}{|\mathbf{R}_I - \mathbf{R}_J|}. \tag{2.10}$$

Although Eq. 2.8 is a significant simplification to Eq. 2.4, because the electron wave function is still a function of $3N$ independent variables it remains impractical to solve it exactly for systems other than the smallest. Density functional theory is based upon the reasoning that instead of the wave function, the ground state properties of the system can be completely described by the electron density $n(\mathbf{r})$.

2.1.2 Variational principle and ground state

Before we present the famous Hohenberg-Kohn theorems, we state some underlying concepts: the electron density operator, the ground state and the variational principle.

For a Hermitian operator $\hat{O}$, the expectation value of the operator in state Ψ is defined as [82]

$$\langle \hat{O} \rangle = \frac{\langle \Psi | \hat{O} | \Psi \rangle}{\langle \Psi | \Psi \rangle}. \tag{2.11}$$

[1] $\hbar = 1$, $m_e = 1$, $4\pi\epsilon_0 = 1$, $e = -1$

The electron density $n(\mathbf{r})$ is the expectation value of density operator $\hat{n}(\mathbf{r}) = \sum_{i=1}^{N} \delta(\mathbf{r} - \mathbf{r}_i)$, where N is the total number of electrons,

$$n(\mathbf{r}) = \frac{\langle \Psi | \hat{n}(\mathbf{r}) | \Psi \rangle}{\langle \Psi | \Psi \rangle} = N \frac{\int \prod_{i=2}^{N} d\mathbf{r}_i |\Psi(\mathbf{r}, \mathbf{r}_2, \mathbf{r}_3, ..., \mathbf{r}_N)|^2}{\int \prod_{i=1}^{N} d\mathbf{r}_i |\Psi(\mathbf{r}_1, \mathbf{r}_2, \mathbf{r}_3, ..., \mathbf{r}_N)|^2}. \tag{2.12}$$

Similarly the energy E is the expectation value of the Hamiltonian operator $\hat{H}$, and can be decomposed as

$$\begin{aligned} E =& \frac{\langle \Psi | \hat{H} | \Psi \rangle}{\langle \Psi | \Psi \rangle} = \langle \hat{T} \rangle + \langle \hat{V}_{int} \rangle + \langle \hat{V}_{ext} \rangle = T + E_{int} + E_{ext} \\ =& F + \int d\mathbf{r} V_{ext}(\mathbf{r}) n(\mathbf{r}), \end{aligned} \tag{2.13}$$

where $\hat{F} = \hat{T} + \hat{V}_{int}$. Clearly the energy E is a functional of the wave function Ψ, or $E \equiv E[\Psi]$.

A general state $|\Psi\rangle$ can be written as a linear combination of eigenstates [82],

$$|\Psi\rangle = \sum_{n=0}^{\infty} C_n |\Psi_n\rangle, \tag{2.14}$$

where $|\Psi_0\rangle$ is the ground state and the other $|\Psi_n\rangle$ are excited states, for convenience assumed non-degenerate. These eigenstates satisfy

$$\hat{H} |\Psi_n\rangle = E_n |\Psi_n\rangle, \tag{2.15}$$

and can be chosen to be orthonormal

$$\langle \Psi_n | \Psi_m \rangle = \delta_{nm}. \tag{2.16}$$

Then E_n is the expectation value of the Hamiltonian in the state Ψ_n : $E_n = \langle \Psi_n | \hat{H} | \Psi_n \rangle$, and all excited state energies are greater than the ground state energy: $E_n \geq E_0$.

Thus the energy of the system in state $|\Psi\rangle$ is

$$
\begin{aligned}
E[\Psi] &= \frac{\left(\sum_{n=0}^{\infty} C_n^* \langle \Psi_n |\right) |\hat{H}| \left(\sum_{n=0}^{\infty} C_n |\Psi_n\rangle\right)}{\left(\sum_{n=0}^{\infty} C_n^* \langle \Psi_n |\right) \left(\sum_{n=0}^{\infty} C_n |\Psi_n\rangle\right)} \\
&= \frac{|C_0|^2 E_0 + \sum_{n=1}^{\infty} |C_n|^2 E_n}{|C_0|^2 + \sum_{n=1}^{\infty} |C_n|^2} \\
&= E_0 + \frac{\sum_{n=1}^{\infty} |C_n|^2 (E_n - E_0)}{|C_0|^2 + \sum_{n=1}^{\infty} |C_n|^2} \\
&\geq E_0,
\end{aligned}
\tag{2.17}
$$

where the equality only holds when $|\Psi\rangle = |\Psi_0\rangle$ and $C_n = \delta_{n0}$.

It follows that for all possible $|\Psi\rangle$, the ground state $|\Psi_0\rangle$ gives the lowest value of $E[\Psi]$. Therefore, a method for determining the ground state energy E_0 and eigenstates $|\Psi_0\rangle$ is to fully parametrically vary $|\Psi\rangle$, and to minimize $E[\Psi]$ with respect to these parameters.

2.1.3 The Hohenberg-Kohn theorems

As previously mentioned, the key idea behind DFT is to describe the ground state properties of a system based upon knowledge of the ground state electron density rather than the wave function. The density is a function of only 3 independent variables (x, y and z) and so much more manageable. The Hohenberg and Kohn [83] theorems ensures that the ground state electron density $n(\mathbf{r})$ uniquely determines the Hamiltonian, and thus all ground states properties, and demonstrates the method by which the ground state electron density can be obtained.

Theorem I. The external potential $V_{ext}(\mathbf{r})$ is a unique functional, except for a constant, of the ground state electron density $n(\mathbf{r})$.

To prove this statement, let us suppose that, in contradictory to the theorem, there are two different external potentials, $V_{ext}(\mathbf{r})$ with ground state $|\Psi\rangle$ and $V'_{ext}(\mathbf{r})$ with ground state $|\Psi'\rangle$, that lead to the same ground state density $n(\mathbf{r})$. The corresponding Hamiltonians for $V_{ext}(\mathbf{r})$ and $V'_{ext}(\mathbf{r})$ are $\hat{H}$ and $\hat{H}'$, respectively. Because the ground state energy E_0 (E'_0) is the lowest expectation value of $\hat{H}$ ($\hat{H}'$) in any state, and is obtained from state $|\Psi\rangle$ ($|\Psi'\rangle$), it follows that

$$
\begin{aligned}
E_0 = \langle \Psi | \hat{H} | \Psi \rangle &< \langle \Psi' | \hat{H} | \Psi' \rangle = \langle \Psi' | \hat{H}' | \Psi' \rangle + \langle \Psi' | \hat{H} - \hat{H}' | \Psi' \rangle \\
&= E'_0 + \int d\mathbf{r} \left[V_{ext}(\mathbf{r}) - V'_{ext}(\mathbf{r}) \right] n(\mathbf{r}).
\end{aligned}
\tag{2.18}
$$

We have used here the fact that the kinetic energy ($\hat{T}$) and electron-electron operator ($\hat{V}_{int}$)

are the same for $\hat{H}$ and $\hat{H}'$, which differ only in the external potential. Similarly,

$$\begin{aligned} E_0' &= \langle \Psi' | \hat{H}' | \Psi' \rangle < \langle \Psi | \hat{H}' | \Psi \rangle = \langle \Psi | \hat{H} | \Psi \rangle + \langle \Psi | \hat{H}' - \hat{H} | \Psi \rangle \\ &= E_0 - \int d\mathbf{r} \left[V_{ext}(\mathbf{r}) - V_{ext}'(\mathbf{r}) \right] n(\mathbf{r}). \end{aligned} \tag{2.19}$$

Adding Eq. 2.18 and Eq. 2.19 gives

$$E_0 + E_0' < E_0 + E_0', \tag{2.20}$$

an obvious falsity. Hence our initial assumption must have been incorrect, and hence *Hohenberg-Kohn Theorem I* is proven.

Theorem II. A universal functional for the energy $E[n]$ can be defined, valid for any external potential $V_{ext}(\mathbf{r})$. The density $n(\mathbf{r})$ that minimises the total energy is the exact ground state density.

From *Theorem I*, $n(\mathbf{r})$ uniquely determines the external potential $V_{ext}(\mathbf{r})$, and the external potential $V_{ext}(\mathbf{r})$ uniquely determines the Hamiltonian. Since by solving $\hat{H}|\Psi\rangle = E_0|\Psi\rangle$ we can determine the $|\Psi\rangle$, which means the ground state wave function is a unique function of the density $n(\mathbf{r}) : \Psi \equiv \Psi[n]$. This ensures that any ground state observable is a functional of electron density. Therefore the expectation value of $\hat{F}$ and $\hat{H}$ are both functionals of $n(\mathbf{r})$:

$$\langle \Psi[n] | \hat{F} | \Psi[n] \rangle = \langle \Psi[n] | \hat{T} + \hat{V}_{int} | \Psi[n] \rangle \equiv F[n], \tag{2.21}$$

and

$$E = \langle \Psi[n] | \hat{H} | \Psi[n] \rangle \equiv E[n]. \tag{2.22}$$

Substituting Eq. 2.21 into Eq. 2.22 gives

$$\begin{aligned} E[n] &= \langle \Psi[n] | \hat{F} + \hat{V}_{ext} | \Psi[n] \rangle \\ &= F[n] + \int d\mathbf{r} V_{ext}(\mathbf{r}) n(\mathbf{r}). \end{aligned} \tag{2.23}$$

Clearly, $F[n]$ is a universal functional of $n(\mathbf{r})$, which doesn't depend on the external potential $V_{ext}(\mathbf{r})$.

Now consider an electron density $n'(\mathbf{r})$ different from ground state density $n(\mathbf{r})$, which corresponds to a normalized state $|\Psi'[n']\rangle$. Since only the ground state $|\Psi[n]\rangle$ which corresponds to $\hat{H}$ gives the lowest energy, using Eq. 2.23

$$
\begin{aligned}
E[n'] &= \langle \Psi'[n']|\hat{H}|\Psi'[n']\rangle = \langle \Psi'[n']|\hat{F}|\Psi'[n']\rangle + \int d\mathbf{r} V_{ext}(\mathbf{r}) n'(\mathbf{r}) \\
&= F[n'] + \int d\mathbf{r} V_{ext}(\mathbf{r}) n'(\mathbf{r}) \\
&> \langle \Psi[n]|\hat{H}|\Psi[n]\rangle = F[n] + \int d\mathbf{r} V_{ext}(\mathbf{r}) n(\mathbf{r}) \\
&= E[n],
\end{aligned}
\tag{2.24}
$$

which means that the ground state density gives the lowest energy. Therefore *Hohenberg-Kohn Theorem II* is proven.

As mentioned in the previous section, minimizing E with respect to the parameters which influence $|\Psi\rangle$ is a method to determine the ground state energy and its wave function. Since the *Hohenberg-Kohn Theorems* ensure that the ground state wave function uniquely depends upon the electron density, if we ensure charge neutrality by introducing a Lagrangian multiplier μ, the variational condition is

$$
\frac{\delta}{\delta n(\mathbf{r})}\left[E[n] - \mu\left(\int d\mathbf{r} n(\mathbf{r}) - N\right)\right] = 0, \tag{2.25}
$$

which with the relation $E[n] = F[n] + V_{ext}(\mathbf{r})$, becomes the Euler-Lagrange equation

$$
\mu = \frac{\delta E[n]}{\delta n(\mathbf{r})} = \frac{\delta F[n]}{\delta n(\mathbf{r})} + V_{ext}(\mathbf{r}). \tag{2.26}
$$

2.1.4 The Kohn-Sham equations

Although the Hohenberg-Kohn theorems form the theoretical foundation of DFT, they do not provide an explicit form for the energy functional $E[n]$ from which the ground state density (and subsequent properties) can be obtained. Kohn and Sham [84] presented a scheme that makes DFT practically possible.

Previous to Kohn and Sham [84], Thomas [85] and Fermi [86] were the first people to define an explicit form of the density functional. Due to the difficulty in defining the exact functional for systems with more than one electron, they employed the independent electron approximation. This allows the wave function of a system to be written as an determinant of single-particle states $\psi_i(\mathbf{r}_i)$ consistent with the Pauli Exclusion principle [82]

$$
\Psi(\mathbf{r}_1, \mathbf{r}_2, ..., \mathbf{r}_N) = \frac{1}{\sqrt{N!}}\begin{vmatrix} \psi_1(\mathbf{r}_1) & ... & \psi_N(\mathbf{r}_1) \\ ... & & ... \\ \psi_1(\mathbf{r}_N) & ... & \psi_N(\mathbf{r}_N) \end{vmatrix}. \tag{2.27}
$$

With this approximation, a system of independent electrons is treated as a system of non-interacting electrons in a homogeneous gas which has the same density as the local density of the real system at any given point. The Thomas-Fermi energy functional is

$$E_{TF}[n] = T_{TF}[n] + E_H[n] + \int d\mathbf{r} V_{ext}(\mathbf{r}) n(\mathbf{r}), \tag{2.28}$$

where the Thomas-Fermi kinetic energy is

$$T_{TF}[n] = \frac{3}{10}\left(3\pi^2\right)^{(2/3)} \int d\mathbf{r} n(\mathbf{r})^{(5/3)} \tag{2.29}$$

and

$$E_H[n] = \frac{1}{2}\int d\mathbf{r} \int d\mathbf{r}' \frac{n(\mathbf{r})n(\mathbf{r}')}{|\mathbf{r}-\mathbf{r}'|} \tag{2.30}$$

is the classical electron-electron interaction energy, also called the Hartree energy.

Thomas-Fermi method has been used to calculated the electronic structures of isolated atoms and some small molecules [87], however (e.g. Sheldon [88] and Teller [89]) this and similar methods cannot correctly describe properties such as the molecular binding energy. So although it remains an often-used semi-empirical method, more sophisticated schemes have been developed to accurately describe electronic properties.

The Kohn-Sham method adopts the idea of replacing the real interacting system with a fictitious non-interacting one, but the approach is in principle exact so that it doesn't lose the physics. Kohn-Sham constituted a system with non-interacting electrons which has the the same ground state density as the real system. And under this construction, instead of the real external potential $V_{ext}(\mathbf{r})$, each electron experiences an artificial effective potential $V_{\text{eff}}[n](\mathbf{r})$. Each electron is described by a wave function $\psi_i(\mathbf{r})$ that satisfies the time-independent Schrödinger equation

$$\left[-\frac{1}{2}\nabla^2 + V_{\text{eff}}[n](\mathbf{r})\right]\psi_i(\mathbf{r}) = \epsilon_i \psi_i(\mathbf{r}), \tag{2.31}$$

and the single electron wave functions $\psi_i(\mathbf{r})$ satisfy orthonormality: $\langle\psi_i|\psi_j\rangle = \delta_{ij}$. If we know the effective potential $V_{\text{eff}}[n](\mathbf{r})$, we can solve these equations and then obtain the ground state density

$$n(\mathbf{r}) = \sum_i f_i |\psi_i(\mathbf{r})|^2, \tag{2.32}$$

where f_i is the occupation number of state i, which is a step function at $T = 0K$, and can be

replaced by Fermi distribution function when $T > 0K$. We assume $n(\mathbf{r})$ given by Eq. 2.32 is the same as the ground state density of the interacting electron system, as a result of appropriate choice of $V_{\text{eff}}[n](\mathbf{r})$, which we now derive.

For each single electron, the universal functional $F_i[n]$ is just its kinetic energy term $F_i[n] = T_{s,i}[n]$, because there is no electron-electron interaction for independent electrons. $T_{s,i}[n]$ is given by

$$T_{s,i}[n] = -\frac{1}{2}\langle\psi_i|\nabla^2|\psi_i\rangle\,, \tag{2.33}$$

and the total kinetic energy of the system $T_s[n]$ is the sum of the kinetic energy of each independent electron

$$T_s[n] = \sum_i f_i T_{s,i}[n] = -\frac{1}{2}\sum_i f_i \langle\psi_i|\nabla^2|\psi_i\rangle\,. \tag{2.34}$$

If we apply the Euler-Lagrange equation Eq. 2.26 on each electron

$$\mu_i = \frac{\delta T_{s,i}[n]}{\delta n(\mathbf{r})} + V_{\text{eff}}[n](\mathbf{r}_i), \tag{2.35}$$

and sum over all electrons, will get the Euler-Lagrange equation for the whole system

$$\begin{aligned}\mu = \sum_i \mu_i &= \sum_i \left(\frac{\delta T_{s,i}[n]}{\delta n(\mathbf{r})} + V_{\text{eff}}[n](\mathbf{r}_i)\right) \\ &= \frac{\delta T_s[n]}{\delta n(\mathbf{r})} + V_{\text{eff}}[n](\mathbf{r}).\end{aligned} \tag{2.36}$$

On the other hand, if we apply the Euler-Lagrange equation directly on the many-body system, assumed to have the same ground state density $n(\mathbf{r})$,

$$\mu = \frac{\delta F[n]}{\delta n(\mathbf{r})} + V_{ext}(\mathbf{r}). \tag{2.37}$$

Now we rearrange the universal functional $F[n]$:

$$\begin{aligned}F[n] &= T[n] + E_{int}[n] \\ &= T_s[n] + E_H[n] + E_{xc}[n],\end{aligned} \tag{2.38}$$

where the exchange-correlation energy $E_{xc}[n]$ is defined as the difference

$$E_{xc}[n] = T[n] - T_s[n] + E_{int}[n] - E_H[n]. \tag{2.39}$$

Now Eq. 2.36 becomes

$$\begin{aligned}\mu &= \frac{\delta}{\delta n(\mathbf{r})}\left(T_s[n] + E_H[n] + E_{xc}[n]\right) + V_{ext}(\mathbf{r}) \\ &= \frac{\delta T_s[n]}{\delta n(\mathbf{r})} + \left(\frac{\delta E_H[n]}{\delta n(\mathbf{r})} + \frac{\delta E_{xc}[n]}{\delta n(\mathbf{r})} + V_{ext}(\mathbf{r})\right) \\ &= \frac{\delta T_s[n]}{\delta n(\mathbf{r})} + \left[V_H[n](\mathbf{r}) + V_{xc}[n](\mathbf{r}) + V_{ext}(\mathbf{r})\right],\end{aligned} \tag{2.40}$$

where the Hartree potential $V_H[n](\mathbf{r})$ is defined as

$$V_H[n](\mathbf{r}) = \frac{\delta E_H[n]}{\delta n(\mathbf{r})} = \int d\mathbf{r}\frac{n(\mathbf{r}')}{|\mathbf{r}-\mathbf{r}'|}, \tag{2.41}$$

and the exchange-correlation potential $V_{xc}[n](\mathbf{r})$ is defined as

$$V_{xc}[n](\mathbf{r}) = \frac{\delta E_{xc}[n]}{\delta n(\mathbf{r})}. \tag{2.42}$$

Comparing Eq. 2.36 and Eq. 2.40 gives the effective potential $V_{\text{eff}}[n](\mathbf{r})$ experienced by the non-interacting electrons,

$$V_{\text{eff}}[n](\mathbf{r}) = V_H[n](\mathbf{r}) + V_{xc}[n](\mathbf{r}) + V_{ext}(\mathbf{r}). \tag{2.43}$$

Finally we can solve the single electron Schrödinger equations. With the obtained $V_{\text{eff}}[n](\mathbf{r})$, these equations are also called the Kohn-Sham equations

$$\begin{aligned}\left(-\frac{1}{2}\nabla^2 + V_{\text{eff}}[n](\mathbf{r})\right)\psi_i(\mathbf{r}) &= \epsilon_i\psi_i(\mathbf{r}) \\ V_{\text{eff}}[n](\mathbf{r}) &= V_H[n](\mathbf{r}) + V_{xc}[n](\mathbf{r}) + V_{ext}(\mathbf{r}).\end{aligned} \tag{2.44}$$

If we write the Kohn-Sham Hamiltonian $\hat{H}_{KS}$ as

$$\begin{aligned}\hat{H}_{KS} &= -\frac{1}{2}\nabla^2 + \hat{V}_{\text{eff}} \\ &= -\frac{1}{2}\nabla^2 + V_H[n](\mathbf{r}) + V_{xc}[n](\mathbf{r}) + V_{ext}(\mathbf{r}),\end{aligned} \tag{2.45}$$

the total energy can be written as

$$\begin{aligned}E_{tot} &= E[n] + E_{II} \\ &= \sum_i f_i \langle\psi_i|\hat{H}_{KS}|\psi_i\rangle - E_H[n] + E_{xc}[n] - \int d\mathbf{r}V_{xc}(\mathbf{r})[n]n(\mathbf{r}) + E_{II}.\end{aligned} \tag{2.46}$$

We can see that there is no approximation in Kohn-Sham ansatz, but that everything unknown and hard to define has been placed into the exchange-correlation energy $E_{xc}[n]$. However we should note that the single electron wave function $\psi_i(\mathbf{r})$ as well as the effective potential $V_{\text{eff}}[n](\mathbf{r})$ are both artificial, and have no direct physical meanings.

2.1.5 Exchange-correlation functionals

Until now everything is exact. However, in order to determine the exchange-correlation energy $E_{xc}[n]$, approximation is needed. In the same paper, Kohn and Sham [84] proposed a simple approximation called the Local-Density-Approximation (LDA). The LDA treats the exchange-correlation energy of each infinitesimal volume as that of a homogeneous electron gas system with the same density,

$$E_{xc}[n] = \int d\mathbf{r} n(\mathbf{r}) \epsilon_{xc}(n(\mathbf{r})), \tag{2.47}$$

where $\epsilon_{xc}(n(\mathbf{r}))$ is the exchange-correlation energy per electron in a homogeneous electron gas system with the density $n = n(\mathbf{r})$. Then the exchange-correlation potential is

$$V_{xc}(\mathbf{r}) = \frac{\delta E_{xc}[n]}{\delta n} = \epsilon_{xc}(n(\mathbf{r})) + n(\mathbf{r}) \frac{\delta \epsilon_{xc}(n(\mathbf{r}))}{\delta n}. \tag{2.48}$$

Practically, $\epsilon_{xc}(n(\mathbf{r}))$ is split into an exchange term $\epsilon_x(n(\mathbf{r}))$ and a correlation term $\epsilon_c(n(\mathbf{r}))$. The exchange term determined analytically by Dirac [90] is

$$\epsilon_x(n(\mathbf{r})) = -\frac{3}{4}\left(\frac{3}{\pi}\right)^{\frac{1}{3}} n(\mathbf{r})^{\frac{1}{3}}, \tag{2.49}$$

and the correlation term has been calculated numerically but essentially exactly using Quantum Monte Carlo methods by Ceperley and Alder [91], and subsequently parametrised by many works for use in calculations, such as Cole and Perdew [92], Perdew and Zunger [93] and Vosko *et al.* [94]. Although simple, the LDA has proven to be accurate when predicting physically properties such as total energy, lattice constant/bond length, bonding energy and electronic properties for various system. For example, Towler *et al.* [95] have compared experimental and DFT-LDA predictions. The lattice parameters for Si, NaCl and Al show differences less than 2.2%, bond lengths of CO, H_2O and CH_4 differences of less than 1.9% and the atomic energies of C, O and Ne differences less than 1.0%. Langreth and Perdew [96] pointed out that for non-uniform systems such as metallic surfaces, although the exchange and correlation term are both poor, when they summed, the errors cancel and give total energy better than 10%.

Although LDA has proven useful in many successful applications, it lacks the ability to accurately describe the spatial varying inhomogeneous density. The Generalized Gradient Approximation (GGA) improves upon the LDA by expressing the exchange-correlation energy not just as a function of the density $n(\mathbf{r})$ but also the gradient of the density $\nabla n(\mathbf{r})$,

$$E_{xc}^{\mathrm{GGA}}[n] = \int d\mathbf{r} n(\mathbf{r}) \epsilon_{xc}^{\mathrm{GGA}}(n(\mathbf{r}), \nabla n(\mathbf{r})). \tag{2.50}$$

There are many different GGAs that have been developed and which have proven to give an improved performance. Widely used ones are PBE [97] and PW91 [98]. Comparing with experimental data, Ruzsinszky *et al.* [99] reported the lattice constant mean average difference of 18 solids using DFT calculation with the PBE functional was 0.04 Å, while that using the LDA was 0.26 Å; Ross [100] reported the bond length (atomization energy) mean average difference of 6 molecules containing C, H, O and S was 0.66% (3.58%) using PBE, and 0.74% (15.15%) using LDA.

With the particular choice of E_{xc}, the Kohn-Sham equations Eq. 2.44 can be solved, the electron density obtained and other ground state properties of the system determined.

2.2 Computational implementations

In practice, there are many different ways to solve the Kohn-Sham equations implementing DFT, such as expanding the single-electron wave function $\psi_i(\mathbf{r})$ using different basis sets. The two most widely used computational implementations are the pseudopotential plane wave method, and methods based on linear combinations of atomic orbitals (LCAO).

2.2.1 Pseudopotential plane wave method

The choice of the plane waves as basis functions is motivated by the fact that plane waves are the eigenfunctions of the homogeneous electron gas. We begin by introducing the periodic boundary condition.

According to Bloch [47], the eigenstates of single-electron Hamiltonian, such as the Kohn-Sham Hamiltonian, with a periodic potential can be written as

$$\psi_{\mathbf{k}}(\mathbf{r}+\mathbf{R}) = \psi_{\mathbf{k}}(\mathbf{r})e^{i\mathbf{k}\cdot\mathbf{R}}, \tag{2.51}$$

where $\mathbf{R} = n\mathbf{a}_1 + m\mathbf{a}_2 + l\mathbf{a}_3$, an integer linear combination of primitive lattice vectors. The wave vector $\mathbf{k}$ can be restricted to the one reciprocal unit cell (Brillouin zone). Eq. 2.51 implies

$$\psi^j_{\mathbf{k}}(\mathbf{r}) = \mu^j_{\mathbf{k}}(\mathbf{r})e^{i\mathbf{k}\cdot\mathbf{r}}, \tag{2.52}$$

where $\mu^j_{\mathbf{k}}(\mathbf{r})$ is a periodic function satisfying $\mu^j_{\mathbf{k}}(\mathbf{r}+\mathbf{R}) = \mu^j_{\mathbf{k}}(\mathbf{r})$. The index j has been introduced to distinguish different solutions with the same wave vector $\mathbf{k}$. Expanding $\mu^j_{\mathbf{k}}(\mathbf{r})$ as a Fourier series, one has

$$\mu(\mathbf{r}) = \frac{1}{\sqrt{\Omega}} \sum_{\mathbf{G}} c_{\mathbf{G}} e^{i\mathbf{G}\cdot\mathbf{r}}, \tag{2.53}$$

where $\mathbf{G}$ is a reciprocal lattice vector $c_{\mathbf{G}}$ the plane-wave expansion coefficient and Ω is the unit cell volume. Therefore, Eq. 2.52 becomes

$$\psi^{j}_{\mathbf{k}}(\mathbf{r}) = \frac{1}{\sqrt{\Omega}} \sum_{\mathbf{G}} c_{\mathbf{G}} e^{i(\mathbf{k}+\mathbf{G})\cdot\mathbf{r}}. \tag{2.54}$$

In general, an infinite number of plane waves is required for exact expansion, but in practice, the series is truncated by only retaining terms corresponding to the reciprocal lattice vectors with plane wave energy within some cutoff energy E_{cut}

$$\frac{1}{2}|\mathbf{k}+\mathbf{G}|^2 \leqslant E_{\text{cut}}. \tag{2.55}$$

There are many advantages in using plane waves as basis functions: they are orthonormal, they do not depend on the atomic positions so that they remain unchanged when atoms are displaced, and the convergence can be easily monitored by increasing the cutoff energy. However, thousands of plane waves per atom are needed to properly describe the system since in reality atomic-like states tightly bound to atoms are a long way for plane wave. In order to make the plane wave method practical, the pseudopotential approximation is made.

States tightly bound to the nucleus, core states, play very little role in determining the properties of condensed matter, which are primarily due to interactions between valence electrons. The wave functions of valence electrons oscillate rapidly due to the requirement of orthogonality to the tightly bond core states, and this oscillation requires a large number of plane waves for an accurate description. The pseudopotential approximation constructs a fictitious ionic potential, the pseudopotential, which is weak enough to not bind core states, but which does nevertheless accurately describe the valence state in the important outer region of the atom. Because the requirement of orthogonality to the core states has been removed, leaving the results valence wave functions are much smoother, permitting an efficient plane wave expansion.

There are several ways to construct pseudopotentials, such as norm-conserving [101] and ultrasoft [102] pseudopotentials, shown in Fig. 2.1, but they share some procedures. For a specific atom, first of all, a certain radius R_c is chosen which inversely influences the transferability, and a full all-electron DFT calculation is performed to obtain the all-electron wave function, such as that indicated by the dashed line in Fig. 2.1a. Next, the all electron wave

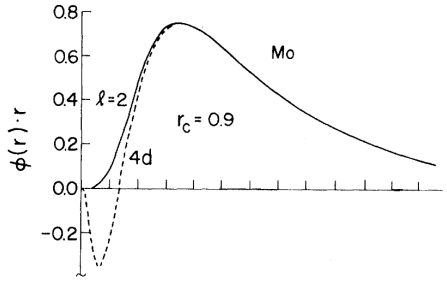

(a) Norm-conserving pseudo wave function (solid line) and all-electron wave function (dashed line) for Mo by Hamann *et al.* [101].

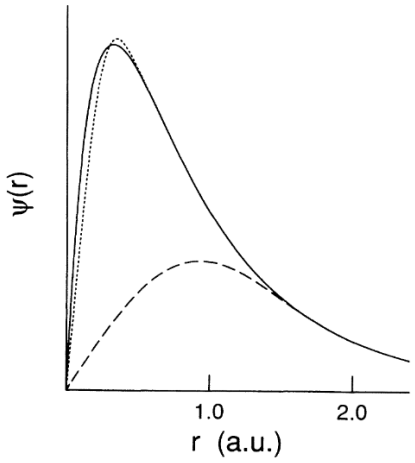

(b) 2p oxygen wave function comparing all-electron (solid line), norm-conserving by Hamann *et al.* [101] (dotted line) and Ultrasoft by Vanderbilt [102] (dashed line).

Figure 2.1: Wave functions corresponding to norm-conserving and ultrasoft pseudopotentials.

function within R_c is replaced by an artificial nodeless wave function while outside R_c it remains unchanged, such as the solid line in Fig. 2.1a. This constructed wave function is called the pseudo wave function. Finally, the pseudopotential is found that generates the pseudo wave function where used in the Kohn-Sham Schrödinger equation. A norm-conserving pseudopotential satisfies the condition that the integrated charge inside the radius R_c agrees with that of the all-electron wave function, while this requirement is relaxed for the ultrasoft pseudopotential. For a practical point of view, norm-conserving pseudopotentials result in longer computational time compared to ultrasoft pseudopotentials, but exhibits better transferability.

2.2.2 Linear combination of atomic orbitals method

Unlike the pseudopotential plane wave method, the LCAO method expands the wave function as a superposition of the atomic orbitals $\varphi_\mu(\mathbf{r}-\mathbf{R})$

$$\psi^j(\mathbf{r}) = \sum_{\mu,\mathbf{R}} c_{\mu,\mathbf{R}} \varphi_\mu(\mathbf{r}-\mathbf{R}), \tag{2.56}$$

where $\mathbf{R}$ is the coordinate of the nucleus on which φ_μ is centred, and μ labels the atomic orbitals (e.g. $1s$, $2p$, ...). An exact expansion requires an infinite number of atomic orbitals. However, in practice, a finite number are chosen and parametrized to yield best result for

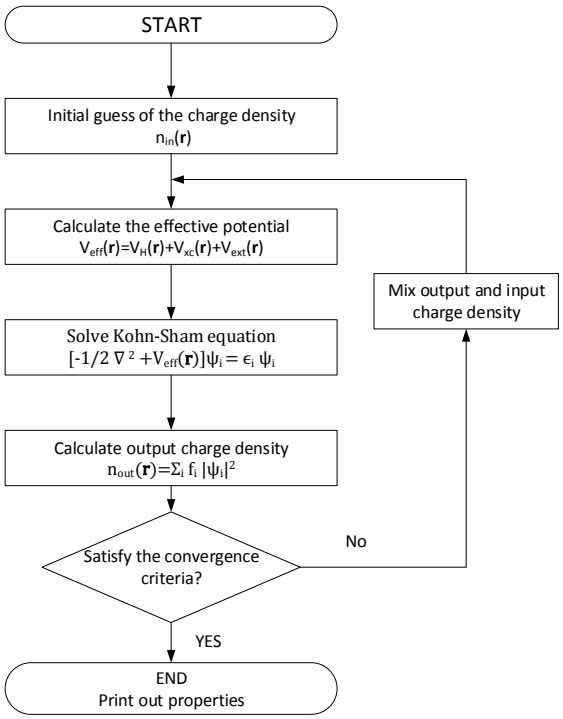

Figure 2.2: Schematic diagram of self-consistent iterations.

different systems, such as STO-3G [103], 6-311G [104], cc-pVTZ [105] and so on. Different analytical form can be used to describe the atomic orbitals φ_μ, among which the Gaussian-type orbitals (GTO) and Slater-type orbitals (STO) are the mostly used ones. These have the general forms

$$\begin{aligned}\varphi_\mu^{\mathrm{GTO}}(\mathbf{r}) &= Y_{lm}(\theta,\phi)\,r^l\,e^{-\tau r^2},\\ \varphi_\mu^{\mathrm{STO}}(\mathbf{r}) &= Y_{lm}(\theta,\phi)\,r^{n-1}\,e^{-\sigma r},\end{aligned} \tag{2.57}$$

where n, l and m are the principal, azimuthal and magnetic quantum numbers. More details about atomic orbitals will be given in the next Chapter, when the density functional tight binding method is described.

2.2.3 Self-consistently solution of the Kohn-Sham equations

In modern implementations of DFT, the Kohn-Sham equations Eq. 2.44 are typically solved computationally via the self-consistent scheme shown in Fig. 2.2. An initial guess of the charge density $n_{\mathrm{in}}(\mathbf{r})$ is made often as a superposition of atomic orbitals, and the effective

potential $V_{\text{eff}}[n](\mathbf{r})$ is constructed. Next, the Kohn-Sham equations Eq. 2.44 are solved, and the output density $n_{\text{out}}(\mathbf{r})$ is generated from the solutions using Eq. 2.32. If this density $n(\mathbf{r})$ agrees with the input density to within some tolerance, then the output density will be considered as the final solution. Otherwise the output density $n_{\text{out}}(\mathbf{r})$ is combined with the input density $n_{\text{in}}(\mathbf{r})$, via some scheme (simple linear mixing, or more sophisticated such as Broyden [106, 107]), and the mixture becomes a new input density and the process repeats until convergence is achieved. The choice of convergence tolerance depends upon the properties of interests and may involve convergence checks on other properties such as the total energy of the system.

2.2.4 Limitations of DFT

Although DFT has proven to be trustworthy to calculate the mechanical, electrical, optical, etc. properties of various class of materials, it has its limitations. First of all, because the Hohenberg-Kohn theorems are only valid for ground states, DFT is limited to the ground states properties (extensions to excited states do exist, such as TDDFT [108]). Secondly, the effective potential experienced by the electron depending upon the density which include the electron itself, this is an artificial self-interaction. Self-interaction largely affects strongly-correlated systems, with more localized electrons, and several self-interaction corrections have been developed to improve standard DFT. Both theses issues are due to the theoretical foundation of DFT. In addition, the exchange-correlation functionals cause further limitations. First of all, there is the well-known "band-gap problem", due to the lack of discontinuity in the exchange-correlation potentials. For a real system, the chemical potential for a system is discontinuous with respect to electron numbers, and failure to correctly describe this means standard DFT gives poor prediction for band gaps in semiconductors and insulators. Secondly, because the most widely used exchange-correlation family LDA and GGA are both localized potentials, these are limited when describing long-range interactions such as the van der Waals interactions. To minimize this particular limitation, some semi-empirical corrections have been introduced [109–112], and are implemented in most modern DFT packages.

Despite these limitations, if used appropriately, DFT is an accurate but for large systems an expensive calculation method. In order to study larger systems, a much faster semi-empirical method based upon the DFT framework, the density functional tight binding method, has been developed and will be introduced in the next Chapter.

Chapter 3

Density Functional Tight Binding

3.1 Self-consistent charge DFTB

In this Chapter, we will summarize the theoretical background of self-consistent-charge-DFTB (SCC-DFTB), and extend the standard SCC-DFTB with dipole approximation.

3.1.1 Total energy

From DFT theory and the Kohn-Sham ansatz [84], the total energy can be written as a functional of the electron number density $n(\mathbf{r})$:

$$\begin{aligned} E[n] &= \sum_k f_k \langle \Psi_k | \hat{H} | \Psi_k \rangle - E_H[n] + E_{xc}[n] - \int V_{xc}[n](\mathbf{r}) n(\mathbf{r}) d\mathbf{r} + E_{II} \\ \hat{H} &= \hat{T}_s + \hat{V}_{ext} + \hat{V}_H[n] + \hat{V}_{xc}[n], \end{aligned} \tag{3.1}$$

where $\hat{H}$ is the Kohn-Sham Hamiltonian, f_k is the Fermi-Dirac occupation function of the state k, and Ψ_k is the corresponding single-particle wave function. $E_H[n]$ is the electron-electron Coulomb energy (also known as the Hartree energy), E_{II} is the nuclear-nuclear Coulomb energy and $E_{xc}[n]$ is the exchange-correlation energy. $\hat{T}_s$ is the non-interacting electron kinetic energy operator, $\hat{V}_{ext}$ describes the nuclear potential acting on the electrons, $\hat{V}_H[n]$ is the Hartree potential and $\hat{V}_{xc}[n]$ is the exchange-correlation potential. Adopting atomic units, these energies and potentials are given by

$$\begin{aligned} E_H[n] &= \frac{1}{2} \int d\mathbf{r} \int d\mathbf{r}' \frac{n(\mathbf{r}) n(\mathbf{r}')}{|\mathbf{r} - \mathbf{r}'|} \\ V_H[n](\mathbf{r}) &= \int d\mathbf{r}' \frac{n(\mathbf{r}')}{|\mathbf{r} - \mathbf{r}'|} \\ V_{xc}[n](\mathbf{r}) &= \frac{\delta E_{xc}[n]}{\delta n(\mathbf{r})}. \end{aligned} \tag{3.2}$$

In the SCC-DFTB scheme [113], the charge density $n(\mathbf{r})$ is written as a superposition of a reference density $n_0(\mathbf{r})$ and a small charge fluctuation $\delta n(\mathbf{r})$. The total energy becomes

$$\begin{aligned} E[n_0+\delta n] = &\sum_k f_k \langle\Psi_k| \left(-\frac{\nabla^2}{2} + \hat{V}_{ext} + \int d\mathbf{r}' \frac{n_0(\mathbf{r}')+\delta n(\mathbf{r}')}{|\mathbf{r}-\mathbf{r}'|} + V_{xc}[n_0+\delta n]\right) |\Psi_k\rangle \\ &- E_H[n_0+\delta n] + E_{xc}[n_0+\delta n] - \int d\mathbf{r} V_{xc}[n_0+\delta n](n_0(\mathbf{r})+\delta n(\mathbf{r})) + E_{II}. \end{aligned} \tag{3.3}$$

The Hamiltonian term on the first line can be written as $\hat{H} = \hat{H}_0 + \left(\hat{H} - \hat{H}_0\right)$, or

$$\begin{aligned} \hat{H} = &\left(-\frac{\nabla^2}{2} + \hat{V}_{ext} + \int d\mathbf{r}' \frac{n_0(\mathbf{r}')}{|\mathbf{r}-\mathbf{r}'|} + V_{xc}[n_0]\right) \\ &+ \left(\int d\mathbf{r}' \frac{\delta n(\mathbf{r}')}{|\mathbf{r}-\mathbf{r}'|} + V_{xc}[n_0+\delta n] - V_{xc}[n_0]\right), \end{aligned} \tag{3.4}$$

so that Eq. 3.3 becomes

$$\begin{aligned} E[n_0+\delta n] = &\sum_k f_k \langle\Psi_k| \hat{H}_0 |\Psi_k\rangle + \int d\mathbf{r} \int d\mathbf{r}' \frac{\delta n(\mathbf{r}')(n_0(\mathbf{r})+\delta n(\mathbf{r}))}{|\mathbf{r}-\mathbf{r}'|} \\ &+ \int d\mathbf{r} V_{xc}[n_0+\delta n](n_0(\mathbf{r})+\delta n(\mathbf{r})) - \int d\mathbf{r} V_{xc}[n_0](n_0(\mathbf{r})+\delta n(\mathbf{r})) \\ &- \frac{1}{2}\int d\mathbf{r} \int d\mathbf{r}' \frac{(n_0(\mathbf{r}')+\delta n(\mathbf{r}'))(n_0(\mathbf{r})+\delta n(\mathbf{r}))}{|\mathbf{r}-\mathbf{r}'|} \\ &- \int d\mathbf{r} V_{xc}[n_0+\delta n](n_0(\mathbf{r})+\delta n(\mathbf{r})) + E_{xc}[n_0+\delta n] + E_{II} \\ = &\sum_k f_k \langle\Psi_k| \hat{H}_0 |\Psi_k\rangle - \int d\mathbf{r} V_{xc}[n_0](n_0(\mathbf{r})+\delta n(\mathbf{r})) \\ &+ \frac{1}{2}\int d\mathbf{r} \int d\mathbf{r}' \frac{1}{|\mathbf{r}-\mathbf{r}'|}(\delta n(\mathbf{r}')\delta n(\mathbf{r}) - n_0(\mathbf{r})n_0(\mathbf{r}') + n_0(\mathbf{r})\delta n(\mathbf{r}') - n_0(\mathbf{r}')\delta n(\mathbf{r})) \\ &+ E_{xc}[n_0+\delta n] + E_{II}. \end{aligned} \tag{3.5}$$

Since

$$\int d\mathbf{r} \int d\mathbf{r}' \frac{n_0(\mathbf{r})\delta n(\mathbf{r}')}{|\mathbf{r}-\mathbf{r}'|} = \int d\mathbf{r} \int d\mathbf{r}' \frac{n_0(\mathbf{r}')\delta n(\mathbf{r})}{|\mathbf{r}-\mathbf{r}'|}, \tag{3.6}$$

this becomes

$$\begin{aligned} E[n_0+\delta n] = &\sum_k f_k \langle\Psi_k| \hat{H}_0 |\Psi_k\rangle - \int d\mathbf{r} V_{xc}[n_0](n_0(\mathbf{r})+\delta n(\mathbf{r})) \\ &+ \frac{1}{2}\int d\mathbf{r} \int d\mathbf{r}' \frac{1}{|\mathbf{r}-\mathbf{r}'|}(\delta n(\mathbf{r}')\delta n(\mathbf{r}) - n_0(\mathbf{r})n_0(\mathbf{r}')) \\ &+ E_{xc}[n_0+\delta n] + E_{II} \end{aligned} \tag{3.7}$$

Expanding $E_{xc}[n_0+\delta n]$ as a Taylor series

$$\begin{aligned} E_{xc}[n_0+\delta n] = E_{xc}[n_0] &+ \int d\mathbf{r} \frac{\delta E_{xc}[n]}{\delta n(\mathbf{r})}\bigg|_{n_0(\mathbf{r})} \delta n(\mathbf{r}) \\ &+ \frac{1}{2}\int d\mathbf{r}\int d\mathbf{r}' \frac{\delta^2 E_{xc}[n]}{\delta n(\mathbf{r})\delta n(\mathbf{r}')}\bigg|_{n_0(\mathbf{r}),n_0(\mathbf{r}')} \delta n(\mathbf{r})\delta n(\mathbf{r}') + ... \end{aligned} \tag{3.8}$$

and inserting into Eq. 3.7, gives for the energy to second order in $\delta n(\mathbf{r})$

$$\begin{aligned} E[n] \approx &\sum_k f_k \langle \Psi_k | \hat{H}_0 | \Psi_k \rangle \\ &+ \frac{1}{2}\int d\mathbf{r}\int d\mathbf{r}' \left(\frac{1}{|\mathbf{r}-\mathbf{r}'|} + \frac{\delta^2 E_{xc}[n]}{\delta n(\mathbf{r})\delta n(\mathbf{r}')}\bigg|_{n_0(\mathbf{r}),n_0(\mathbf{r}')} \right) \delta n(\mathbf{r}')\delta n(\mathbf{r}) \\ &- \int d\mathbf{r} V_{xc}[n_0] n_0(\mathbf{r}) - \frac{1}{2}\int d\mathbf{r}\int d\mathbf{r}' \frac{n_0(\mathbf{r}) n_0(\mathbf{r}')}{|\mathbf{r}-\mathbf{r}'|} + E_{xc}[n_0] + E_{II}. \end{aligned} \tag{3.9}$$

The total energy can be grouped into band structure energy E_{BS} (first line), second order energy E_{2nd} (second line) and the repulsive energy E_{rep}(third line).

3.1.2 Repulsive energy

The repulsive energy in Eq. 3.9

$$E_{\mathrm{rep}} = E_{xc}[n_0] - \int d\mathbf{r} V_{xc}[n_0] n_0(\mathbf{r}) - \frac{1}{2}\int d\mathbf{r}\int d\mathbf{r}' \frac{n_0(\mathbf{r}) n_0(\mathbf{r}')}{|\mathbf{r}-\mathbf{r}'|} + E_{II} \tag{3.10}$$

contains not only the ion-ion interaction, but also the more complicated exchange-correlation terms. In order to preserve accuracy and the calculation speed, the repulsive energy E_{rep} is expressed as a sum of pair potentials $V_{\mathrm{rep}}^{i,j}$ whose form is obtained by fitting to full DFT calculations [114][113] [115]

$$E_{\mathrm{rep}} = \sum_{i,j>i} V_{\mathrm{rep}}^{i,j} = E_{\mathrm{DFT}} - E_{\mathrm{el}} \tag{3.11}$$

where E_{el} is the DFTB total energy without repulsive term, and $V_{\mathrm{rep}}^{i,j}$ is approximated as a function of the distance between atoms i and j,

$$V_{\mathrm{rep}}^{i,j}(R) = E_{\mathrm{DFT}}^{i,j}(R) - E_{\mathrm{el}}^{i,j}(R). \tag{3.12}$$

There are many parameters and parametrization methods available for various atom pairs, for example, Koskinen and Mäkinen [115] have presented a parametrization procedure for the Carbon-Hydrogen pair. In order to improve transferability, systems contain different

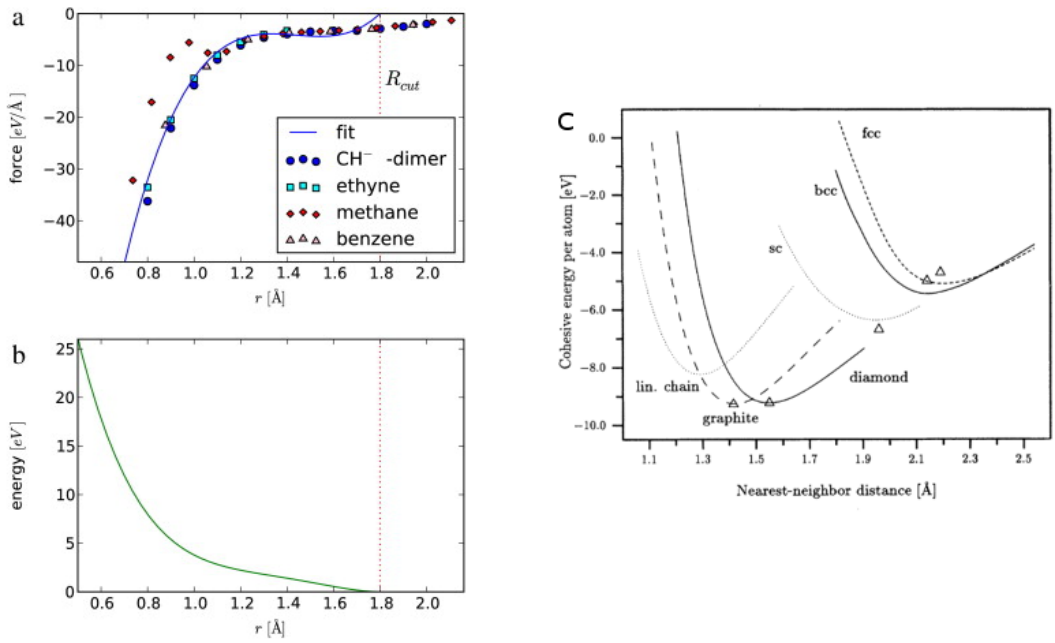

Figure 3.1: Repulsive energy parametrization. a) Fitting the derivative of repulsive potential, using different systems [115]; b) the energy vs seperation of a); c) cohesive energies per carbon atom for different lattice types versus neighbor distance. Triangles give the reference from DFT calculations [114].

bonds such as C-H dimer, ethyne, methane and benzene were chosen. Calculations using DFT and DFTB without repulsive energies were carried out, and the repulsive term fitted using the derivative of the energy instead of the energy itself, in order to improve the smoothness of the curve, as shown in Fig. 3.1a and Fig. 3.1b. In order to have good transferability, the fitted result should be close to as many data points as possible, rather than displaying very good agreement with one set of data but very poor with another set. A reasonable cut-off radius is chosen beyond which no interaction is assumed.

The fitted repulsive energy for Carbon-Carbon used in the present work is that parametrized by Porezag *et al.* [114]. The systems chosen to be fitted are bulk graphite and diamond, and fit performed on the difference between the DFT energy and the DFTB band structure energy: $E^{i,j}_{\mathrm{DFT}}(R) - E^{i,j}_{\mathrm{BS}}(R)$. Fig. 3.1c shows the good performance of this parametrization for determining the lattice parameter of Carbon in different crystal structures.

3.1.3 Band structure energy

The band structure energy in Eq. 3.7 contains no contribution from charge fluctuations, with the Hamiltonian $\hat{H}_0$ determined by the reference charge density $n_0(\mathbf{r})$. In the DFTB scheme, the reference charge density is constructed as a summation of atomic charge densities. Correspondingly, the single-particle wave functions are expanded as linear combination of atomic orbitals $\varphi_\mu(\mathbf{r})$,

$$\Psi_k(\mathbf{r}) = \sum_\mu c_\mu^k \varphi_\mu(\mathbf{r}), \quad \mu = \{\alpha, i\} \tag{3.13}$$

where $\varphi_\mu(\mathbf{r}) = \varphi_\alpha(\mathbf{r} - \mathbf{R}_i)$ and μ indexes orbital α on atom i. Then the band structure energy is

$$\begin{aligned} E_{\mathrm{BS}} &= \sum_k f_k \langle \Psi_k | \hat{H}_0 | \Psi_k \rangle \\ &= \sum_k f_k \sum_\mu \sum_\nu c_\mu^{k*} c_\nu^k \langle \varphi_\mu | \hat{H}_0 | \varphi_\nu \rangle \\ &= \sum_k f_k \sum_\mu \sum_\nu c_\mu^{k*} c_\nu^k H_{\mu\nu}^0, \quad \mu = \{\alpha, i\}, \nu = \{\beta, j\}. \end{aligned} \tag{3.14}$$

In order to determine the band structure energy, the Hamiltonian matrix elements $H_{\mu\nu}^0$ and wave function c_μ^k are needed.

Atomic orbitals

The atomic orbitals $\varphi_\mu(\mathbf{r})$ are atom-centred pseudoatomic wave functions, which are determined by self-consistently solving modified Kohn-Sham equations for an isolated confined atom using DFT [84]:

$$\left[\hat{T}_s + V_i^{\mathrm{eff}}[n](\mathbf{r}) \right] \varphi_\mu(\mathbf{r}) = \epsilon_\mu^{\mathrm{eff}} \varphi_\mu(\mathbf{r}), \quad \forall \mu \tag{3.15}$$

where the effective potential $V_i^{\mathrm{eff}}[n](\mathbf{r})$ is given as

$$V_i^{\mathrm{eff}}[n](\mathbf{r}) = V_{ext,i}(\mathbf{r}) + V_H[n](\mathbf{r}) + V_{xc}^{LDA}[n](\mathbf{r}) + \left(\frac{r_i}{r_0} \right)^N, \tag{3.16}$$

where $r_i = |\mathbf{r}_i| = |\mathbf{r} - \mathbf{R}_i|$ and $V_{ext,i}(\mathbf{r})$ is the electrostatic potential from the ion i. Any exchange-correlation functions such as PZ [93] and PBE [97] can be used in $V_{xc}^{LDA}[n]$. As Koskinen and Mäkinen [115] suggested, more recent exchange-correlation functions than LDA can be used, but they do not improve the accuracy [115]. The confining potential $(r/r_0)^N$ was first introduced by Eschrig and Bergert [116] to improve the performance of band structure calculations using the LCAO method. It prevents the wavefuction from extending too far away from the atom center. As described in Ref. [116], N and r_0 are chosen

to give optimum results. Results reported in Refs. [116] and [114] suggested that twice the covalent radius is always a good choice for r_0, and that $N = 2$ is good for all types of atoms.

Different representations can be employed for the atomic orbital $\varphi_\mu(\mathbf{r})$, such as Slater-type orbitals and Gaussian-type orbitals. Using Slater-type orbitals, the atomic orbitals have the form

$$\varphi_\mu(\mathbf{r}) = \sum_{n,\tau,\ell_\mu,m_\mu} a_{n\tau} r_i^{\ell_\mu+n} \exp(-\tau r_i) Y_{\ell_\mu m_\mu}(\hat{\mathbf{r}}_i) \tag{3.17}$$

where ℓ and m are the azimuthal and magnetic quantum numbers. As suggested in Ref. [114], many tests show that five different values of τ and $n = 0,1,2,3$ enable a sufficiently accurate basis set for elements up to the third row. The coefficients $a_{n\tau}$ are self-consistently obtained by solving Eq. 3.15.

Hamiltonian matrix elements

Following Ref.[114], the Hamiltonian matrix elements $H^0_{\mu\nu}$ are evaluated using the two-centre approximation

$$H^0_{\mu\nu} = \begin{cases} \epsilon^{\text{atom}}_\mu & \mu = \nu \\ \langle\varphi_\mu|\,\hat{T}_s + V_i + V_j\,|\varphi_\nu\rangle & i \neq j \\ 0 & i = j, \mu \neq \nu. \end{cases} \tag{3.18}$$

V_i is the effective free atom potential of atom i given by the expression in Eq. 3.16 but without the confining potential. The diagonal term $\epsilon^{\text{atom}}_\mu$ is the energy eigenvalue obtained by solving Eq. 3.15 where $V_i^{\text{eff}}(\mathbf{r})$ again omits the confining potential.

3.1.4 Second order energy

The second order energy in Eq. 3.7 is

$$E_{2\text{nd}} = \frac{1}{2}\int d\mathbf{r}\int d\mathbf{r}'\left(\frac{1}{|\mathbf{r}-\mathbf{r}'|} + \left.\frac{\delta^2 E_{xc}[n]}{\delta n(\mathbf{r})\delta n(\mathbf{r}')}\right|_{n_0(\mathbf{r}),n_0(\mathbf{r}')}\right)\delta n(\mathbf{r}')\delta n(\mathbf{r}). \tag{3.19}$$

If the LDA is used for the exchange-correlation contributions

$$\frac{\delta^2 E_{xc}[n]}{\delta n(\mathbf{r})\delta n(\mathbf{r}')} \propto \delta(\mathbf{r}-\mathbf{r}'), \tag{3.20}$$

so that when $\mathbf{r} \neq \mathbf{r}'$ the exchange-correlation contributions vanish. When integrated over all space, the contribution from $\mathbf{r} = \mathbf{r}'$ is very small, so we ignore the on-site term of the exchange-correlation contributions. Then the second order energy $E_{2\text{nd}}$ is just the electro-

static interaction from the charge fluctuation.

In a similar manner to the reference charge density $n_0(\mathbf{r})$ being expressed as a superposition of atomic densities centred on each atom, the fluctuation $\delta n(\mathbf{r})$ can also be partitioned into atom-centred contributions

$$\delta n(\mathbf{r}) = \sum_i \delta n_i(\mathbf{r}_i). \tag{3.21}$$

Ideally, the atomic fluctuation $\delta n_i(\mathbf{r}_i)$ would be calculated using the actual density distribution in every self-consistent step of the electronic structure calculation, but to perform this consumes too much time, which is against the spirit of DFTB. Therefore the following approximation is made.

The atomic fluctuation $\delta n_i(\mathbf{r})$ is expressed as a superposition of multipole densities $\rho_i(\mathbf{r})[\Delta Q_\ell]$[1]

$$\delta n_i(\mathbf{r}) = \sum_\ell \rho_i(\mathbf{r})[\Delta Q_\ell], \tag{3.22}$$

where ℓ is the number denoting the rank of the Cartesian multipole, such as Q_0 being the charge and $\mathbf{Q}_1$ being the dipole. The multipole densities themselves $\rho_i(\mathbf{r})[\Delta Q_\ell]$ are expressed in terms of a standard normalised isotropic density $\rho_i^{\text{iso}}(r)$ scaled by the multipole moment ΔQ_ℓ. The dipole densities can be constructed from $\rho_i^{\text{iso}}(r)$ in an analogous manner to how a standard dipole can be constructed from opposing point charges.

The standard SCC-DFTB uses the monopole approximation to deal with $E_{2\text{nd}}$, in which the expansion of the density fluctuation only includes the charge difference

$$\delta n_i(\mathbf{r}) \approx \rho_i(\mathbf{r})[\Delta q_i] = \Delta q_i \rho_i^{\text{iso}}(r). \tag{3.23}$$

Then $E_{2\text{nd}}$ becomes

$$\begin{aligned} E_{2\text{nd}} &= \frac{1}{2}\sum_{i=1}^{N}\sum_{j=1}^{N}\int\int \frac{\delta n_i(\mathbf{r}_i)\delta n_j(\mathbf{r}'_j)}{|\mathbf{r}-\mathbf{r}'|}d\mathbf{r}d\mathbf{r}' \\ &= \frac{1}{2}\sum_{i=1}^{N}\sum_{j=1}^{N}\Delta q_i\left(\int\int \frac{\rho_i^{\text{iso}}(r_i)\rho_j^{\text{iso}}(r'_j)}{|\mathbf{r}-\mathbf{r}'|}d\mathbf{r}d\mathbf{r}'\right)\Delta q_j \\ &= \frac{1}{2}\sum_{i=1}^{N}\sum_{j=1}^{N}\Delta q_i \hat{\Gamma}^{00}_{ij}\Delta q_j \end{aligned} \tag{3.24}$$

[1] The square brackets here denotes that the density $\rho_i(\mathbf{r})[\Delta Q_\ell]$ depends upon the multipole difference ΔQ_ℓ, not that it is a functional of ΔQ_ℓ as implied by similar notation used for quantities in section 3.1.

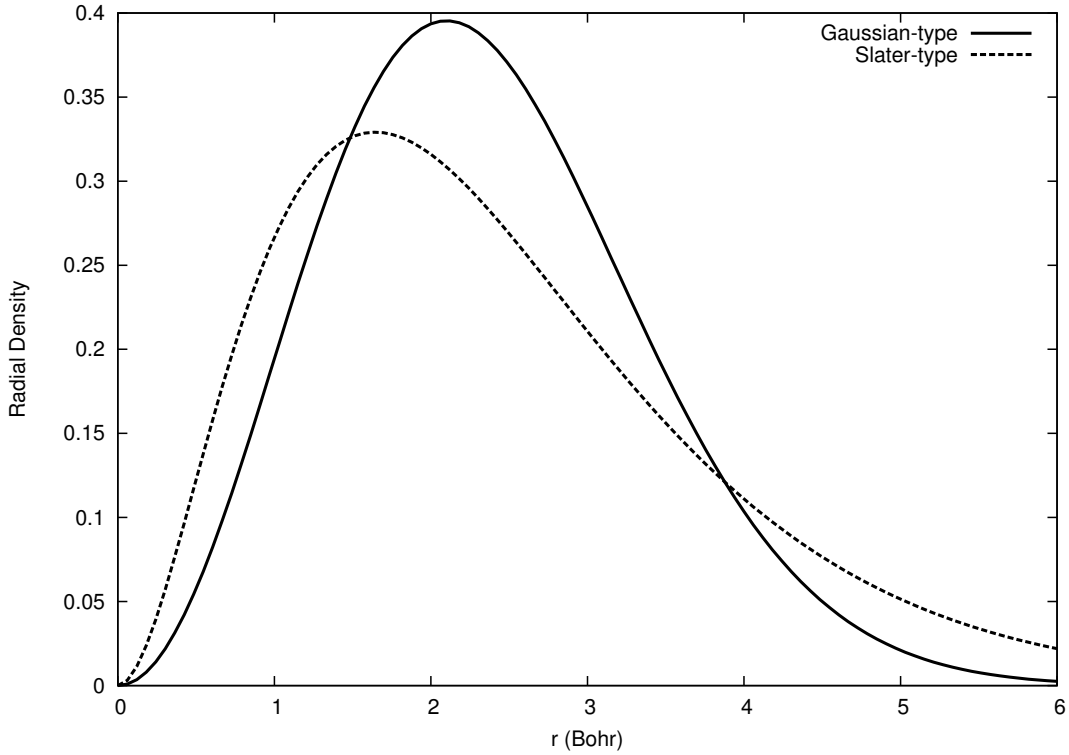

Figure 3.2: Gaussian-type (solid line) and Slater-type (dash line) charge distributions.

where $\hat{\Gamma}^{00}_{ij}$ is defined as

$$\hat{\Gamma}^{00}_{ij} = \int\int \frac{\rho^{\text{iso}}_i(r_i)\rho^{\text{iso}}_j(r'_j)}{|\mathbf{r}-\mathbf{r}'|} d\mathbf{r}d\mathbf{r}'. \tag{3.25}$$

Evaluating $\hat{\Gamma}^{00}_{ij}$

To evaluate $\hat{\Gamma}^{00}_{ij}$, analytical forms such as Slater-type orbital (STO) distributions and Gaussian-type orbital (GTO) distributions are adopted for $\rho^{\text{iso}}(r)$

$$\rho^{\text{iso}}_{i,\text{GTO}}(r) = \left(\frac{\sigma_i}{\pi}\right)^{\frac{3}{2}} e^{-\sigma_i r^2}, \tag{3.26}$$

$$\rho^{\text{iso}}_{i,\text{STO}}(r) = \frac{\tau_i^3}{8\pi} e^{-\tau_i r}. \tag{3.27}$$

One parameter, either σ_i or τ_i, is required for each atom. Fig. 3.2 illustrates the general shape of these two distributions, showing $4\pi r^2\rho(r)$, with σ and τ values appropriate for Carbon. The result of using each of these distributions in evaluating Eq. 3.25 is (see Appendix A)

$$\hat{\Gamma}^{00}_{ij,\mathrm{GTO}} = \begin{cases} \frac{1}{R_{ij}} \operatorname{erf}\left(\sqrt{\frac{\sigma_i\sigma_j}{\sigma_i+\sigma_j}} R_{ij}\right) & i \neq j \\ \sqrt{\frac{2\sigma_i}{\pi}} & i = j, \end{cases}$$

$$\hat{\Gamma}^{00}_{ij,\mathrm{STO}} = \begin{cases} \frac{1}{R_{ij}} - e^{-\tau_i R_{ij}} \left(\frac{\tau_j^4 \tau_i}{2(\tau_i^2-\tau_j^2)^2} - \frac{\tau_j^6 - 3\tau_j^4\tau_i^2}{(\tau_i^2-\tau_j^2)^3 R_{ij}} \right) & \\ -e^{-\tau_j R_{ij}} \left(\frac{\tau_i^4 \tau_j}{2(\tau_j^2-\tau_i^2)^2} - \frac{\tau_i^6 - 3\tau_i^4\tau_j^2}{(\tau_j^2-\tau_i^2)^3 R_{ij}} \right) & i \neq j, \tau_i \neq \tau_j \\ \frac{1}{R_{ij}} - e^{-\tau_i R_{ij}} \left(\frac{1}{R_{ij}} + \frac{11}{16}\tau_i + \frac{3}{16}\tau_i^2 R_{ij} + \frac{1}{48}\tau_i^3 R_{ij}^2 \right) & i \neq j, \tau_i = \tau_j \\ \frac{5}{16}\tau_i & i = j, \end{cases} \tag{3.28}$$

where $R_{ij} = |\mathbf{R}_i - \mathbf{R}_j|$.

To use these expressions, we need values for the parameters τ_i or σ_i. Note that the on-site value $\hat{\Gamma}^{00}_{ii}$ is directly related to σ_i (τ_i), meaning τ_i and σ_i can be obtained from $\hat{\Gamma}^{00}_{ii}$. Elsner [117] suggested that the on-site $\hat{\Gamma}^{00}_{ii}$ can be approximated by the difference of ionization energy I_i and electron affinity A_i of the atom, or the Hubbard U

$$U_i \approx I_i - A_i. \tag{3.29}$$

If we expand the energy of atom i as a function of charge difference Δq_i

$$E(\Delta q_i) = E_0 + \left(\frac{\partial E}{\partial q_i}\right)\Delta q_i + \frac{1}{2}\left(\frac{\partial^2 E}{\partial q_i^2}\right)\Delta q_i^2 + \ldots \tag{3.30}$$

and comparing the second order term with Eq. 3.24, we identify

$$\hat{\Gamma}^{00}_{ii} = \frac{\partial^2 E}{\partial q_i^2}. \tag{3.31}$$

Ionization energy is defined as the energy needed to remove an electron from a system with N electrons: $I = E(N-1) - E(N)$. Electron affinity is defined as the energy needed to add an electron: $A = E(N) - E(N+1)$. The difference between ionization energy and electron affinity is the energy difference of a system with one electron more and the same system with one electron less: $I - A = [E(N+1) - E(N)] - [E(N) - E(N-1)]$, so that $\partial^2 E/\partial q_i^2$ can be approximated as $I_i - A_i$. Therefore

$$\hat{\Gamma}^{00}_{ii,\mathrm{GTO}} = \sqrt{\frac{2\sigma_i}{\pi}} = U_i \quad \Rightarrow \quad \sigma_i = \frac{\pi}{2}U_i^2. \tag{3.32}$$

$$\hat{\Gamma}^{00}_{ii,\mathrm{STO}} = \frac{5}{16}\tau_i = U_i \quad \Rightarrow \quad \tau_i = \frac{16}{5}U_i, \tag{3.33}$$

Obtaining the charge differences Δq_i

To identify the charge difference on each atom, we first determine the total charge Q. This is obtained from the wave functions $\Psi_k(\mathbf{r})$ as

$$Q = e\sum_k f_k \int |\Psi_k(\mathbf{r})|^2 d\mathbf{r}, \tag{3.34}$$

where e is the charge of an electron. As described in Eq. 3.13, the wave function is expanded using atomic orbitals, so the charge is

$$\begin{aligned} Q =& e\sum_k f_k \sum_\mu \sum_\nu \int c_\mu^{k*} \varphi_\mu^*(\mathbf{r}) c_\nu^k \varphi_\nu(\mathbf{r}) d\mathbf{r} \\ =& e\sum_k f_k \sum_\mu \sum_\nu c_\mu^{k*} c_\nu^k S_{\mu\nu}, \quad \mu = \{\alpha, i\}, \nu = \{\beta, j\} \end{aligned} \tag{3.35}$$

where the overlap matrix is introduced as

$$S_{\mu\nu} = \int \varphi_\mu^*(\mathbf{r}) \varphi_\nu(\mathbf{r}) d\mathbf{r}. \tag{3.36}$$

In order to calculate the charge on each atom, different partitioning schemes can be used. Mulliken population analysis [118] is one of the most widely used and is that employed in the present work. Consider a diatomic molecule with two atoms i and j and atomic wave functions $\psi_i(\mathbf{r})$ and $\psi_j(\mathbf{r})$. The charge of the molecule is

$$\begin{aligned} q &= e\int |\left(\psi_i(\mathbf{r}) + \psi_j(\mathbf{r})\right)|^2 d\mathbf{r} \\ &= e\int \left(|\psi_i(\mathbf{r})|^2 + \psi_i(\mathbf{r})^* \psi_j(\mathbf{r}) + \psi_j(\mathbf{r})^* \psi_i(\mathbf{r}) + |\psi_j(\mathbf{r})|^2\right) d\mathbf{r} \\ &= e\left(\langle\psi_i|\psi_i\rangle + \langle\psi_i|\psi_j\rangle + \langle\psi_j|\psi_i\rangle + \langle\psi_j|\psi_j\rangle\right) \end{aligned} \tag{3.37}$$

According to Mulliken [118], the charge on each atom is composed from the on-site contribution $\langle\psi_i|\psi_i\rangle$ ($\langle\psi_j|\psi_j\rangle$) plus half of the overlap contribution $\langle\psi_i|\psi_j\rangle + \langle\psi_j|\psi_i\rangle$, which is

$$q_i = e\left[\langle\psi_i|\psi_i\rangle + \frac{1}{2}\left(\langle\psi_i|\psi_j\rangle + \langle\psi_j|\psi_i\rangle\right)\right]. \tag{3.38}$$

If we expand the atomic wave functions as

$$\psi_i(\mathbf{r}) = \sum_k f_k \sum_\alpha c_\mu^k \varphi_\mu(\mathbf{r}), \quad \psi_j(\mathbf{r}) = \sum_k f_k \sum_\beta c_\nu^k \varphi_\nu(\mathbf{r}), \quad \mu = \{\alpha, i\}, \nu = \{\beta, j\}, \tag{3.39}$$

then Eq. 3.38 becomes

$$
\begin{aligned}
q_i &= e\sum_k f_k \left[\sum_\alpha c_\mu^{k*} c_\mu^k \langle \varphi_\mu | \varphi_\mu \rangle + \frac{1}{2} \left(\sum_\alpha c_\mu^{k*} \sum_\beta c_\nu^k \langle \varphi_\mu | \varphi_\nu \rangle + \sum_\beta c_\nu^{k*} \sum_\alpha c_\mu^k \langle \varphi_\nu | \varphi_\mu \rangle \right) \right] \\
&= e\sum_k f_k \left[\sum_\alpha c_\mu^{k*} c_\mu^k S_{\mu\mu} + \frac{1}{2} \sum_\alpha \sum_\beta \left(c_\mu^{k*} c_\nu^k S_{\mu\nu} + c_\nu^{k*} c_\mu^k S_{\mu\nu}^* \right) \right], \quad \mu = \{\alpha, i\}, \nu = \{\beta, j\}.
\end{aligned}
\tag{3.40}
$$

This is the charge q_i for an atom in a diatomic molecule. For a general system, the expression for the charge associated with each atom contains a sum over all other atoms,

$$
\begin{aligned}
q_i &= e\sum_k f_k \left[\sum_\alpha c_\mu^{k*} c_\mu^k S_{\mu\mu} + \frac{1}{2} \sum_{j \neq i} \sum_\alpha \sum_\beta \left(c_\mu^{k*} c_\nu^k S_{\mu\nu} + c_\nu^{k*} c_\mu^k S_{\mu\nu}^* \right) \right] \\
&= e\frac{1}{2} \sum_k f_k \sum_\alpha \sum_\nu \left(c_\mu^{k*} c_\nu^k S_{\mu\nu} + c_\nu^{k*} c_\mu^k S_{\mu\nu}^* \right), \quad \mu = \{\alpha, i\}, \nu = \{\beta, j\}.
\end{aligned}
\tag{3.41}
$$

Finally, the charge difference Δq_i is calculated as $\Delta q_i = q_i - q_i^0$, where q_i^0 is the valence charge of the reference atom.

3.1.5 Tabulating the overlap matrix

In order to calculate q_i, we need to calculate overlap matrix elements $S_{\mu\nu}$. For practical applications, $S_{\mu\nu}$ is tabulated for a range of atomic separations and stored as an input file to be used during calculations. The atomic orbital $\varphi_\mu(\mathbf{r})$ has the form

$$
\varphi_\mu(\mathbf{r}) = R_\mu(r_i) Y_\alpha(\hat{\mathbf{r}}_i) \quad \mu = \{\alpha, i\}
\tag{3.42}
$$

where R_μ is a radial function and Y_α a spherical harmonic. Real harmonics given in Table 3.1 are used. In Eq. 3.42, the spherical harmonics can also be written as $Y_\alpha(\theta_i, \phi_i)$, where θ_i and ϕ_i are the polar and azimuthal angle of $\hat{\mathbf{r}}_i$. The radial function R_μ is found by DFT calculation described in section 3.1.3.

When two orbitals μ and ν are centred on the same atom (on-site), because of the orthonormality of the spherical harmonics

$$
S_{\mu\nu} = \int \varphi_\mu^*(\mathbf{r}) \varphi_\nu(\mathbf{r}) d\mathbf{r} = \delta_{\mu\nu}.
\tag{3.43}
$$

When μ and ν are on different atoms (off-site), $S_{\mu\nu}$ becomes

$$
\begin{aligned}
S_{\mu\nu} &= \int \varphi_\mu^*(\mathbf{r}) \varphi_\nu(\mathbf{r}) d\mathbf{r} \\
&= \int R_\mu(r) Y_\alpha(\theta, \phi) R_\nu(\tilde{r}) Y_\beta(\tilde{\theta}, \tilde{\phi}) d\mathbf{r}
\end{aligned}
\tag{3.44}
$$

Orbital	$Y(\theta,\phi)$
s	$\frac{1}{\sqrt{4\pi}}$
p_x	$\sqrt{\frac{3}{4\pi}}\sin\theta\cos\phi$
p_y	$\sqrt{\frac{3}{4\pi}}\sin\theta\sin\phi$
p_z	$\sqrt{\frac{3}{4\pi}}\cos\theta$
$d_{3z^2-r^2}$	$\sqrt{\frac{5}{16\pi}}(3\cos^2\theta-1)$
$d_{x^2-y^2}$	$\sqrt{\frac{15}{16\pi}}\sin^2\theta\cos 2\phi$
d_{xy}	$\sqrt{\frac{15}{16\pi}}\sin^2\theta\sin 2\phi$
d_{yz}	$\sqrt{\frac{15}{16\pi}}\sin 2\theta\sin\phi$
d_{zx}	$\sqrt{\frac{15}{16\pi}}\sin 2\theta\cos\phi$

Table 3.1: Real spherical harmonics up to and including d orbitals.

where the origin of $\mathbf{r}$ has been chosen to be on atom i, and $\tilde{\mathbf{r}} = \mathbf{r} - \mathbf{R}_{ji}$, with $(\tilde{\theta},\tilde{\phi})$ the angles corresponding to $\tilde{\mathbf{r}}$. Following Slater and Koster [119], Eq. 3.44 can be further manipulated as

$$\begin{aligned} S_{\mu\nu} &= \int_0^\infty dr \int_0^\pi d\theta \int_0^{2\pi} d\phi \quad R_\mu(r) R_\nu(\tilde{r}) Y_\alpha(\theta,\phi) Y_\beta(\tilde{\theta},\tilde{\phi}) r^2 \sin\theta \\ &= \int_0^\infty dr \int_0^\pi d\theta \quad R_\mu(r) R_\nu(\tilde{r}) \Phi_{\alpha\beta}(\theta,\tilde{\theta}) r^2 \sin\theta \end{aligned} \tag{3.45}$$

where

$$\Phi_{\alpha\beta}(\theta,\tilde{\theta}) = \int_0^{2\pi} d\phi\, Y_\alpha(\theta,\phi) Y_\beta(\tilde{\theta},\tilde{\phi}). \tag{3.46}$$

$\Phi_{\alpha\beta}(\theta,\tilde{\theta})$ can be calculated analytically by introducing the Slater-Koster transformation coefficients [119] $T^\tau_{\alpha\beta}$.

The spherical harmonics satisfy [120]

$$Y_{\ell m}(\theta_2,\phi_2) = \sum_{m'} D^\ell_{mm'}(a,b,c) Y_{\ell m'}(\theta_1,\phi_1) \tag{3.47}$$

where $D^\ell_{mm'}(a,b,c)$ is the Wigner D-matrix [121] and (a,b,c) are the Euler angles between two coordinate systems, in which angle (θ_1,ϕ_1) measured in the first coordinate system is (θ_2,ϕ_2) measured in the second.

To evaluate Eq. 3.45, the global coordinate system has been translated so that atom i lies at

τ	$\Theta_\tau(\theta_1,\theta_2)$
$ss\sigma$	$\frac{1}{2}$
$sp\sigma$	$\frac{\sqrt{3}}{2}\cos\theta_2$
$sd\sigma$	$\frac{\sqrt{5}}{4}(3\cos^2\theta_2-1)$
$pp\sigma$	$\frac{3}{2}\cos\theta_1\cos\theta_2$
$pp\pi$	$\frac{3}{4}\sin\theta_1\sin\theta_2$
$ps\sigma$	$\frac{\sqrt{15}}{4}\cos\theta_1(3\cos^2\theta_2-1)$
$pd\pi$	$\frac{\sqrt{45}}{4}\sin\theta_1\sin\theta_2\cos\theta_2$

Table 3.2: Azimuthal integrals.

the origin and atom j at $\mathbf{R}_j-\mathbf{R}_i=\mathbf{R}_{ji}$. If we now rotate the coordinate system so that atom j is on the z-axis at $R_{ij}\hat{\mathbf{z}}$, then $\mathbf{r}\rightarrow\mathbf{r}'$, and spherical harmonics of α (β) will turn from $Y_\alpha(\hat{\mathbf{r}})$ ($Y_\beta(\widehat{\mathbf{r}-\mathbf{R}_{ji}})$) into linear combinations of $Y_{\alpha'}(\hat{\mathbf{r}'})$ ($Y_{\beta'}(\widehat{\mathbf{r}'-\mathrm{R_{ji}}\hat{\mathbf{z}}})$)

$$\begin{aligned} Y_\alpha(\theta,\phi) &= \sum_{\alpha'} t_\alpha^{\alpha'}\, Y_{\alpha'}(\theta_1,\phi_1) \\ Y_\beta(\tilde{\theta},\tilde{\phi}) &= \sum_{\beta'} t_\beta^{\beta'}\, Y_{\beta'}(\theta_2,\phi_1), \end{aligned} \tag{3.48}$$

where the coefficients $t_\alpha^{\alpha'}$ and $t_\beta^{\beta'}$ are calculated according to Eq. 3.47, and θ_1,θ_2,ϕ_1 are angles measured from the new coordinate system. Because atom j is located at $R_{ji}\hat{\mathbf{z}}$, $\mathbf{r}'$ and $\mathbf{r}'-R_{ji}\hat{\mathbf{z}}$ have the same azimuthal angle. Each pair of orbitals (α',β') overlap and form bond such as σ, π or δ bonds, indexed by τ. Introducing $T_\tau^{\alpha\beta}=t_\alpha^{\alpha'}\,t_\beta^{\beta'}$, Eq. 3.46 becomes

$$\Phi_{\alpha\beta}(\theta,\tilde{\theta})=\sum_\tau T_\tau^{\alpha\beta}\Theta_\tau(\theta_1,\theta_2) \tag{3.49}$$

where

$$\Theta_\tau(\theta_1,\theta_2)=\int_0^{2\pi} d\phi_1\, Y_{\alpha'}(\theta_1,\phi_1)\,Y_{\beta'}(\theta_2,\phi_1). \tag{3.50}$$

The non-vanishing $\Theta_\tau(\theta_1,\theta_2)$ are calculated analytically and listed in table 3.2. The transformation coefficients $T_\tau^{\alpha\beta}$ are tabulated [119] in Table 3.3 when x,y,z are the direction cosines of $\mathbf{R}_{ji}$ which is $\hat{\mathbf{R}}_{ji}=(x,y,z)$.

Because of the isotropic symmetry, radial functions $R_\mu(r)$ and $R_\nu(\tilde{r})$ will stay the same when rotating the coordinate system. Combining the radial and angular part, Eq. 3.45 becomes

$$S_{\mu\nu}=\sum_\tau T_\tau^{\alpha\beta}S_{\mu\nu}^\tau \tag{3.51}$$

α	β	$T_\sigma^{\alpha\beta}$	$T_\pi^{\alpha\beta}$
s	s	1	
s	p_x	x	
s	p_y	y	
s	p_z	z	
s	d_{xy}	$\sqrt{3}xy$	
s	d_{yz}	$\sqrt{3}yz$	
s	d_{zx}	$\sqrt{3}zx$	
s	$d_{x^2-y^2}$	$\frac{\sqrt{3}}{2}(x^2-y^2)$	
s	$d_{3z^2-r^2}$	$\frac{3}{2}z^2-\frac{1}{2}$	
p_x	p_x	x^2	$1-x^2$
p_x	p_y	xy	$-xy$
p_x	p_z	xz	$-xz$
p_x	d_{xy}	$\sqrt{3}x^2y$	$y(1-2x^2)$
p_x	d_{yz}	$\sqrt{3}xyz$	$-2xyz$
p_x	d_{zx}	$\sqrt{3}x^2z$	$z(1-2x^2)$
p_x	$d_{x^2-y^2}$	$\frac{\sqrt{3}}{2}x(x^2-y^2)$	$x(1-x^2+y^2)$
p_x	$d_{3z^2-r^2}$	$\frac{1}{2}x(3z^2-1)$	$-\sqrt{3}xz^2$
p_y	p_y	y^2	$1-y^2$
p_y	p_z	yz	$-yz$
p_y	d_{xy}	$\sqrt{3}xy^2$	$x(1-2y^2)$
p_y	d_{yz}	$\sqrt{3}y^2z$	$z(1-2y^2)$
p_y	d_{zx}	$\sqrt{3}xyz$	$-2xyz$
p_y	$d_{x^2-y^2}$	$\frac{\sqrt{3}}{2}y(x^2-y^2)$	$-y(1+x^2-y^2)$
p_y	$d_{3z^2-r^2}$	$\frac{1}{2}y(3z^2-1)$	$-\sqrt{3}yz^2$
p_z	p_z	z^2	$1-z^2$
p_z	d_{xy}	$\sqrt{3}xyz$	$-2xyz$
p_z	d_{yz}	$\sqrt{3}yz^2$	$y(1-2z^2)$
p_z	d_{zx}	$\sqrt{3}xz^2$	$x(1-2z^2)$
p_z	$d_{x^2-y^2}$	$\frac{\sqrt{3}}{2}z(x^2-y^2)$	$-z(x^2-y^2)$
p_z	$d_{3z^2-r^2}$	$\frac{1}{2}z(3z^2-1)$	$\sqrt{3}z(x^2+y^2)$

Table 3.3: Transformation coefficient $T_\tau^{\alpha\beta}$.

where

$$S_{\mu\nu}^{\tau} = \int_0^{\infty} dr \int_0^{\pi} d\theta_1 R_\mu(r) R_\nu(\tilde{r}) \Theta_\tau(\theta_1,\theta_2) r^2 \sin\theta_1 \tag{3.52}$$

where $S_{\mu\nu}^{\tau}$ is called the Slater-Koster integral for atomic orbital pair $\mu\nu$ and bond τ. It is evaluated numerically, with a cutoff distance used when integrating the radial part (for technical details see Appendix B).

3.1.6 Obtaining the eigenvector coefficients c_μ^k

The ground state energy should be the lowest possible energy, recall the variational principle of the total energy with the restriction of charge neutrality

$$\delta\left[E_{tot}-\epsilon\left(\int n(\mathbf{r})d\mathbf{r}-N\right)\right]=0, \tag{3.53}$$

where N is the total number of electrons, ϵ is the Lagrange multiplier, and $\int n(\mathbf{r})d\mathbf{r}$ is given as

$$\begin{aligned}\int n(\mathbf{r})d\mathbf{r}&=\sum_k f_k\langle\Psi_k|\Psi_k\rangle\\&=\sum_k f_k\sum_{\mu\nu}c_\mu^{k*}c_\nu^k S_{\mu\nu}.\end{aligned} \tag{3.54}$$

Because Eq.3.53 can be differentiated with respect to any variables entering the wave function, in order to obtain the eigenvector coefficients c_μ^k, we differentiate Eq.3.53 with respect to wave function coefficient $c_\mu^{k'*}$. For different k', the Lagrange multiplier will be different

$$\frac{\partial}{\partial c_\mu^{k'*}}\left[E_{tot}-\epsilon_{k'}\left(\int n(\mathbf{r})d\mathbf{r}-N\right)\right]=0. \tag{3.55}$$

Because the total energy has three components, this leads to

$$\begin{aligned}\frac{\partial}{\partial c_\mu^{k'*}}\left[E_{\mathrm{BS}}+E_{\mathrm{2nd}}+E_{\mathrm{rep}}-\epsilon_{k'}\left(\sum_k f_k\sum_{\mu\nu}c_\mu^{k*}c_\nu^k S_{\mu\nu}-N\right)\right]&=0\\ \frac{\partial}{\partial c_\mu^{k'*}}\left(E_{\mathrm{BS}}+E_{\mathrm{2nd}}+E_{\mathrm{rep}}\right)&=\epsilon_{k'}\frac{\partial}{\partial c_\mu^{k'*}}\sum_k f_k\sum_{\mu\nu}c_\mu^{k*}c_\nu^k S_{\mu\nu}\\ \frac{\partial}{\partial c_\mu^{k'*}}\sum_k f_k\sum_{\mu\nu}c_\mu^{k*}c_\nu^k H^0_{\mu\nu}+\frac{\partial E_{\mathrm{2nd}}}{\partial c_\mu^{k'*}}&=\epsilon_{k'}\frac{\partial}{\partial c_\mu^{k'*}}\sum_k f_k\sum_{\mu\nu}c_\mu^{k*}c_\nu^k S_{\mu\nu}\\ f_k\sum_\nu c_\nu^k H^0_{\mu\nu}+\frac{\partial E_{\mathrm{2nd}}}{\partial c_\mu^{k'*}}&=\epsilon_k f_k\sum_\nu c_\nu^k S_{\mu\nu},\end{aligned} \tag{3.56}$$

where $\hat{H}_0$ is the non-SCC Hamiltonian and $H^0_{\mu\nu}$ is obtained from Eq. 3.18. $\partial E_{\mathrm{2nd}}/\partial c_\mu^{k'*}$ is calculated as follows

$$\frac{\partial E_{\mathrm{2nd}}}{\partial c_\mu^{k'*}}=\frac{1}{2}\sum_{i=1}^N\sum_{j=1}^N\frac{\partial\Delta q_i}{\partial c_\mu^{k'*}}\hat{\Gamma}^{00}_{ij}\Delta q_j+\frac{1}{2}\sum_{i=1}^N\sum_{j=1}^N\Delta q_i\hat{\Gamma}^{00}_{ij}\frac{\partial\Delta q_j}{\partial c_\mu^{k'*}}, \tag{3.57}$$

because $\hat{\Gamma}^{00}_{ij}$ satisfies the symmetry

$$\hat{\Gamma}^{00}_{ij}=\hat{\Gamma}^{00}_{ji}, \tag{3.58}$$

so that

$$\frac{\partial E_{2\mathrm{nd}}}{\partial c_\mu^{k'*}} = \sum_{i=1}^{N}\sum_{j=1}^{N} \frac{\partial\left(q_i - q_i^0\right)}{\partial c_\mu^{k'*}} \hat{\Gamma}_{ij}^{00} \Delta q_j = \sum_{i=1}^{N}\sum_{j=1}^{N} \frac{\partial q_i}{\partial c_\mu^{k'*}} \hat{\Gamma}_{ij}^{00} \Delta q_j. \tag{3.59}$$

If we use the Mulliken population scheme described in section 3.1.4 , the charge q_i is

$$q_i = e\sum_k f_k \frac{1}{2} \sum_\alpha \sum_b (c_a^{k*} c_b^k S_{ab} + c_b^{k*} c_a^k S_{ab}^*), \quad a = \{\alpha, i\}, b = \{\beta, h\} \tag{3.60}$$

and the partial derivative with respect to $c_\mu^{k'*}$ is

$$\begin{aligned}
\frac{\partial q_i}{\partial c_\mu^{k'*}} =& e f_k \frac{1}{2} \sum_\alpha \sum_b \delta_{\mu a} c_b^k S_{ab} \\
&+ e f_k \frac{1}{2} \sum_\alpha \sum_b \delta_{\mu b} c_a^k S_{ab}^*, \quad a = \{\alpha, i\}, b = \{\beta, h\}, \mu = \{\sigma, l\} \\
=& e f_k \frac{1}{2} \left(\delta_{il} \sum_b c_b^k S_{\mu b} + \sum_\alpha c_a^k S_{a\mu}^* \right), \quad a = \{\alpha, i\}, b = \{\beta, h\}, \mu = \{\sigma, l\}.
\end{aligned} \tag{3.61}$$

Inserting Eq. 3.61 into Eq. 3.59

$$\begin{aligned}
\frac{\partial E_{2\mathrm{nd}}}{\partial c_\mu^{k'*}} =& e f_k \frac{1}{2} \sum_{i=1}^{N}\sum_{j=1}^{N} \left(\delta_{il} \sum_b c_b^k S_{\mu b} + \sum_\alpha c_a^k S_{a\mu}^* \right) \hat{\Gamma}_{ij}^{00} \Delta q_j, \quad a = \{\alpha, i\}, b = \{\beta, h\}, \mu = \{\sigma, l\} \\
=& e f_k \frac{1}{2} \sum_{j=1}^{N} \sum_b c_b^k S_{\mu b} \hat{\Gamma}_{ij}^{00} \Delta q_j \\
&+ e f_k \frac{1}{2} \sum_{j=1}^{N} \sum_a c_a^k S_{a\mu}^* \hat{\Gamma}_{ij}^{00} \Delta q_j, \quad b = \{\beta, h\}, \mu = \{\sigma, i\}.
\end{aligned} \tag{3.62}$$

Because now the second line is summed over all orbitals, thus the restriction of orbital a on atom i is removed. We can see that the first line is also summed over all orbitals, therefore we can write a and b both as $\nu = \{\beta, h\}$

$$\begin{aligned}
\frac{\partial E_{2\mathrm{nd}}}{\partial c_\mu^{k'*}} =& e f_k \frac{1}{2} \sum_{j=1}^{N} \sum_\nu c_\nu^k S_{\mu\nu} \hat{\Gamma}_{ij}^{00} \Delta q_j \\
&+ e f_k \frac{1}{2} \sum_{j=1}^{N} \sum_\nu c_\nu^k S_{\nu\mu}^* \hat{\Gamma}_{hj}^{00} \Delta q_j, \quad \nu = \{\beta, h\}, \mu = \{\sigma, i\} \\
=& e f_k \frac{1}{2} \sum_{j=1}^{N} \sum_\nu c_\nu^k \left(S_{\mu\nu} \hat{\Gamma}_{ij}^{00} + S_{\nu\mu}^* \hat{\Gamma}_{hj}^{00} \right) \Delta q_j, \quad \nu = \{\beta, h\}, \mu = \{\sigma, i\},
\end{aligned} \tag{3.63}$$

swapping h and j

$$\frac{\partial E_{2\mathrm{nd}}}{\partial c_\mu^{k'*}} = e f_k \frac{1}{2} \sum_{h=1}^{N} \sum_{\nu} c_\nu^k \left(S_{\mu\nu} \hat{\Gamma}_{ih}^{00} + S_{\nu\mu}^* \hat{\Gamma}_{jh}^{00} \right) \Delta q_h, \quad \mu = \{\sigma, i\}, \nu = \{\beta, j\}. \tag{3.64}$$

Inserting Eq. 3.64 into Eq. 3.56

$$f_k \sum_{\nu} c_\nu^k H_{\mu\nu}^0 + e f_k \frac{1}{2} \sum_{h=1}^{N} \sum_{\nu} c_\nu^k \left(S_{\mu\nu} \hat{\Gamma}_{ih}^{00} + S_{\nu\mu}^* \hat{\Gamma}_{jh}^{00} \right) \Delta q_h = \epsilon_k f_k \sum_{\nu} c_\nu^k S_{\mu\nu}, \quad \mu = \{\sigma, i\}, \nu = \{\beta, j\} \tag{3.65}$$

rearranging the terms, Kohn-Sham like equations are obtained

$$\sum_{\nu} \left(H_{\mu\nu}^0 + H_{\mu\nu}^1 - \epsilon_k S_{\mu\nu} \right) c_\nu^k = 0, \tag{3.66}$$

where the Hamiltonian elements shift $H_{\mu\nu}^1$ is introduced and here defined as

$$H_{\mu\nu}^1 = e \frac{1}{2} \sum_{h=1}^{N} \left(S_{\mu\nu} \hat{\Gamma}_{ih}^{00} + S_{\nu\mu}^* \hat{\Gamma}_{jh}^{00} \right) \Delta q_h, \quad \mu = \{\sigma, i\}, \nu = \{\beta, j\}. \tag{3.67}$$

3.2 Dipole approximation

3.2.1 Second order energy

As described in section 3.1.4, the atomic charge density fluctuation $\delta n_i(\mathbf{r})$ used in evaluating the second order energy $E_{2\mathrm{nd}}$ has been approximated as a normalised spherical distribution $\rho_i^{\mathrm{iso}}(r)$ multiply by charge difference Δq_i. This monopole approximation has fundamentally improved the accuracy of the DFTB allowing for the incorporation of charge transfer effects. However, for highly polarised system extending the approximation to dipole term is desirable.

In this case the atomic charge density fluctuation $\delta n_i(\mathbf{r})$ can be expressed as a superposition of a density $\rho_i(\mathbf{r})[\Delta q_i]$ associated with charge difference Δq_i, and a density $\rho_i(\mathbf{r})[\Delta \mathbf{p}_i]$ associated with dipole difference $\Delta \mathbf{p}_i$

$$\delta n_i(\mathbf{r}) = \rho_i(\mathbf{r})[\Delta q_i] + \tilde{\rho}_i(\mathbf{r})[\Delta \mathbf{p}_i]. \tag{3.68}$$

Then the second order energy is

$$
\begin{aligned}
E_{\text{2nd}} =& \frac{1}{2}\sum_{i=1}^{N}\sum_{j=1}^{N}\int\int \frac{\delta n_i(\mathbf{r}_i)\delta n_j(\mathbf{r}'_j)}{|\mathbf{r}-\mathbf{r}'|}d\mathbf{r}d\mathbf{r}' \\
=& \frac{1}{2}\sum_{i=1}^{N}\sum_{j=1}^{N}\int\int \frac{\left(\rho(\mathbf{r}_i)[\Delta q_i]+\tilde{\rho}(\mathbf{r}_i)[\Delta\mathbf{p}_i]\right)\left(\rho(\mathbf{r}'_j)[\Delta q_j]+\tilde{\rho}(\mathbf{r}'_j)[\Delta\mathbf{p}_j]\right)}{|\mathbf{r}-\mathbf{r}'|}d\mathbf{r}d\mathbf{r}' \\
=& \frac{1}{2}\sum_{i=1}^{N}\sum_{j=1}^{N}\int\int \frac{\rho(\mathbf{r}_i)[\Delta q_i]\rho(\mathbf{r}'_j)[\Delta q_j]}{|\mathbf{r}-\mathbf{r}'|}d\mathbf{r}d\mathbf{r}' + \sum_{i=1}^{N}\sum_{j=1}^{N}\int\int \frac{\tilde{\rho}(\mathbf{r}_i)[\Delta\mathbf{p}_i]\rho(\mathbf{r}'_j)[\Delta q_j]}{|\mathbf{r}-\mathbf{r}'|}d\mathbf{r}d\mathbf{r}' \\
&+ \frac{1}{2}\sum_{i=1}^{N}\sum_{j=1}^{N}\int\int \frac{\tilde{\rho}(\mathbf{r}_i)[\Delta\mathbf{p}_i]\tilde{\rho}(\mathbf{r}'_j)[\Delta\mathbf{p}_j]}{|\mathbf{r}-\mathbf{r}'|}d\mathbf{r}d\mathbf{r}'.
\end{aligned}
\tag{3.69}
$$

The charge part has been previously considered in Eq. 3.23. For the terms containing the influence of the dipole part of the density, we can consider this as resulting from two opposite signed charge densities displaced from atom center $\mathbf{R}_i$ by $\pm d$ ($\lim_{d\to 0}$) in the direction of dipole $\Delta\mathbf{p}_i$. These charge densities are taken to have distribution $\tilde{\rho}_i^{\text{iso}}(r)$, and magnitude $|\Delta\mathbf{p}_i|/d$:

$$
\begin{aligned}
\tilde{\rho}_i(\mathbf{r})[\Delta\mathbf{p}_i] &= \lim_{d\to 0}\frac{|\Delta\mathbf{p}_i|}{d}\left[\tilde{\rho}_i^{\text{iso}}\left(\left|\mathbf{r}-\left(\mathbf{R}_i+\frac{1}{2}d\hat{\mathbf{u}}\right)\right|\right)-\tilde{\rho}_i^{\text{iso}}\left(\left|\mathbf{r}-\left(\mathbf{R}_i-\frac{1}{2}d\hat{\mathbf{u}}\right)\right|\right)\right] \\
&= |\Delta\mathbf{p}_i|\hat{\mathbf{u}}\cdot\nabla_{\mathbf{R}_i}\tilde{\rho}_i^{\text{iso}}(r_i) \\
&= \Delta\mathbf{p}_i\cdot\nabla_{\mathbf{R}_i}\tilde{\rho}_i^{\text{iso}}(r_i)
\end{aligned}
\tag{3.70}
$$

where $\hat{\mathbf{u}}$ is the unit vector in the direction of $\Delta\mathbf{p}_i$, and $\nabla_{\mathbf{R}_i}$ denotes that ∇ operates which respect to the atomic center $\mathbf{R}_i$. Note that $\tilde{\rho}_i^{\text{iso}}(r)$ used to describe the dipole fluctuation density is not necessarily the same as $\rho_i^{\text{iso}}(r)$ which describe the charge fluctuation density. This will lead to one more free parameter.

We then have for Eq. 3.69

$$
\begin{aligned}
E_{\text{2nd}} =& \frac{1}{2}\sum_{i=1}^{N}\sum_{j=1}^{N}\Delta q_i\left(\int\int\frac{\rho_i^{\text{iso}}(r_i)\rho_j^{\text{iso}}(r'_j)}{|\mathbf{r}-\mathbf{r}'|}d\mathbf{r}d\mathbf{r}'\right)\Delta q_j \\
&+\sum_{i=1}^{N}\sum_{j=1}^{N}\left(\int\int\frac{\Delta\mathbf{p}_i\cdot\nabla_{\mathbf{R}_i}\tilde{\rho}_i^{\text{iso}}(r_i)\rho_j^{\text{iso}}(r'_j)}{|\mathbf{r}-\mathbf{r}'|}d\mathbf{r}d\mathbf{r}'\right)\Delta q_j \\
&+\frac{1}{2}\sum_{i=1}^{N}\sum_{j=1}^{N}\int\int\frac{\Delta\mathbf{p}_i\cdot\nabla_{\mathbf{R}_i}\tilde{\rho}_i^{\text{iso}}(r_i)\Delta\mathbf{p}_j\cdot\nabla_{\mathbf{R}_j}\tilde{\rho}_j^{\text{iso}}(r'_j)}{|\mathbf{r}-\mathbf{r}'|}d\mathbf{r}d\mathbf{r}' \\
=&\frac{1}{2}\sum_{i=1}^{N}\sum_{j=1}^{N}\Delta q_i\hat{\Gamma}_{ij}^{00}\Delta q_j \\
&+\sum_{i=1}^{N}\sum_{j=1}^{N}\Delta\mathbf{p}_i\cdot\left(\nabla_{\mathbf{R}_i}\int\int\frac{\tilde{\rho}_i^{\text{iso}}(r_i)\rho_j^{\text{iso}}(r'_j)}{|\mathbf{r}-\mathbf{r}'|}d\mathbf{r}d\mathbf{r}'\right)\Delta q_j \\
&+\frac{1}{2}\sum_{i=1}^{N}\sum_{j=1}^{N}\Delta\mathbf{p}_i\cdot\left(\nabla_{\mathbf{R}_j}\otimes\nabla_{\mathbf{R}_i}\int\int\frac{\tilde{\rho}_i^{\text{iso}}(r_i)\tilde{\rho}_j^{\text{iso}}(r'_j)}{|\mathbf{r}-\mathbf{r}'|}d\mathbf{r}d\mathbf{r}'\right)\Delta\mathbf{p}_j.
\end{aligned}
\tag{3.71}
$$

Similar to $\hat{\Gamma}_{ij}^{00}$ (scalar), we introduce $\hat{\Gamma}_{ij}^{10}$ (vector) and $\hat{\Gamma}_{ij}^{11}$ (tensor) as

$$
\hat{\Gamma}_{ij}^{10} = \nabla_{\mathbf{R}_i}\int\int\frac{\tilde{\rho}_i^{\text{iso}}(r_i)\rho_j^{\text{iso}}(r'_j)}{|\mathbf{r}-\mathbf{r}'|}d\mathbf{r}d\mathbf{r}', \tag{3.72}
$$

$$
\hat{\Gamma}_{ij}^{11} = \nabla_{\mathbf{R}_j}\otimes\nabla_{\mathbf{R}_i}\int\int\frac{\tilde{\rho}_i^{\text{iso}}(r_i)\tilde{\rho}_j^{\text{iso}}(r'_j)}{|\mathbf{r}-\mathbf{r}'|}d\mathbf{r}d\mathbf{r}'. \tag{3.73}
$$

Then the second order energy E_{2nd} with dipole extension can be expressed as

$$
E_{\text{2nd}} = \frac{1}{2}\sum_{i=1}^{N}\sum_{j=1}^{N}\Delta q_i\hat{\Gamma}_{ij}^{00}\Delta q_j + \sum_{i=1}^{N}\sum_{j=1}^{N}\Delta\mathbf{p}_i\cdot\hat{\Gamma}_{ij}^{10}\Delta q_j + \frac{1}{2}\sum_{i=1}^{N}\sum_{j=1}^{N}\Delta\mathbf{p}_i\cdot\hat{\Gamma}_{ij}^{11}\Delta\mathbf{p}_j, \tag{3.74}
$$

representing charge-charge, charge-dipole and dipole-dipole contributions.

Expressions for $\hat{\Gamma}_{ij}^{10}$ and $\hat{\Gamma}_{ij}^{11}$ can be obtained similarly to $\hat{\Gamma}_{ij}^{00}$ (see Appendix A). The precise form depends upon the choice of isotropic distributions $\rho^{\text{iso}}(r)$ and $\tilde{\rho}^{\text{iso}}(r)$, either Gaussian-type or Slater-type (see Eq. 3.26 and Eq. 3.27). As mentioned above, the parameter σ or τ used for $\tilde{\rho}^{\text{iso}}(r)$ need not be the same as that for $\rho^{\text{iso}}(r)$, but can be treated as a further free parameter. Expressions for $\hat{\Gamma}_{ij}^{10}$ and $\hat{\Gamma}_{ij}^{11}$ are given in Appendix A.

In order to use the E_{2nd} gives in Eq. 3.74, in calculations, we need to calculate dipole difference $\Delta\mathbf{p}_i$ on atoms. We consider their evaluation in the next section.

3.2.2 Dipole moment

As described in the previous section, $\Delta q_i = q_i - q_i^0$ in Eq. 3.69 is estimated using Mulliken population analysis. The dipole difference $\Delta \mathbf{p}_i$ can also be obtained by a similar scheme.

The total electric dipole moment of the system observed from an arbitrary origin is

$$\mathbf{p} = e \int \mathbf{r} n(\mathbf{r}) d\mathbf{r} \tag{3.75}$$

where $\mathbf{r}$ is the position vector, $n(\mathbf{r})$ is the electron number density of the system and the integration is performed over the whole space.

Regarding the direction of the dipole defined here, if only two point charges with opposite sign are considered, $q_+ = +q$ located at $\mathbf{r}_+$ and $q_- = -q$ located at $\mathbf{r}_-$

$$\begin{aligned} \mathbf{p} &= \mathbf{r}_+ q_+ + \mathbf{r}_- q_- \\ &= q(\mathbf{r}_+ - \mathbf{r}_-) \end{aligned} \tag{3.76}$$

is consistent with the dipole defined as $\mathbf{p} = q\mathbf{d}$, which is the same as in Eq. 3.70.

Similar as Eq. 3.35, the total dipole of the system is evaluated as

$$\begin{aligned} \mathbf{p} &= e \sum_k f_k \int \mathbf{r} \sum_\mu c_\mu^{k*} \varphi_\mu^*(\mathbf{r}) \sum_\nu c_\nu^k \varphi_\nu(\mathbf{r}) d\mathbf{r} \\ &= e \sum_k f_k \sum_\mu \sum_\nu c_\mu^{k*} c_\nu^k \int (\mathbf{r}_i + \mathbf{R}_i) \varphi_\mu^*(\mathbf{r}) \varphi_\nu(\mathbf{r}) d\mathbf{r} \\ &= e \sum_k f_k \sum_\mu \sum_\nu c_\mu^{k*} c_\nu^k \left[\mathbf{R}_i \int \varphi_\mu^*(\mathbf{r}) \varphi_\nu(\mathbf{r}) d\mathbf{r} + \int \mathbf{r}_i \varphi_\mu^*(\mathbf{r}) \varphi_\nu(\mathbf{r}) d\mathbf{r} \right], \quad \mu = \{\alpha, i\}, \quad \nu = \{\beta, j\}. \end{aligned} \tag{3.77}$$

By analogy to the overlap matrix elements $S_{\mu\nu}$, we introduce dipole matrix elements $\mathbf{P}_{\mu\nu}$ as

$$\mathbf{P}_{\mu\nu} = \int \mathbf{r}_i \varphi_\mu^*(\mathbf{r}) \varphi_\nu(\mathbf{r}) d\mathbf{r}. \tag{3.78}$$

where $\mathbf{r}_i = \mathbf{r} - \mathbf{R}_i$ and the integrand is over all space. Then Eq. 3.77 becomes

$$\mathbf{p} = e \sum_k f_k \sum_\mu \sum_\nu c_\mu^{k*} c_\nu^k \mathbf{R}_i S_{\mu\nu} + e \sum_k f_k \sum_\mu \sum_\nu c_\mu^{k*} c_\nu^k \mathbf{P}_{\mu\nu}. \tag{3.79}$$

The total dipole moment of the system is seen to be made up of two contributions, the first the macroscopic part $\mathbf{p}_{ext}$ due to charges distributed on atoms, throughout the system, and the second the atomic part $\mathbf{p}_{int}$ due to the atomic dipole distribution.

Similar to the way Mulliken charges are defined in Eq. 3.38, the Mulliken dipoles on each atom are taken to be

$$\begin{aligned}
\mathbf{p}^i_{ext} &= e\frac{1}{2}\sum_k f_k \sum_\alpha \sum_\nu \left(c^{k*}_\mu c^k_\nu S_{\mu\nu} + c^{k*}_\nu c^k_\mu S^*_{\mu\nu} \right) = \mathbf{R}_i q_i, \quad \mu = \{\alpha, i\} \quad \nu = \{\beta, j\} \\
\mathbf{p}^i_{int} &= e\frac{1}{2}\sum_k f_k \sum_\alpha \sum_\nu \left(c^{k*}_\mu c^k_\nu \mathbf{P}_{\mu\nu} + c^{k*}_\nu c^k_\mu \mathbf{P}^*_{\mu\nu} \right), \quad \mu = \{\alpha, i\} \quad \nu = \{\beta, j\}.
\end{aligned} \tag{3.80}$$

$\mathbf{p}^i_{int}$ is the atomic contribution, and because the initial reference dipole of the free atom is zero, $\mathbf{p}^i_{int}$ is the dipole difference on each atom to be used in Eq. 3.74.

3.2.3 Calculating $\mathbf{P}_{\mu\nu}$

Constructing artificial orbitals.

In order to find $\mathbf{P}_{\mu\nu}$ in Eq. 3.78, it is convenient to construct artificial orbitals $\chi^\xi_\mu(\mathbf{r})$ which are defined as

$$\chi^\xi_\mu(\mathbf{r}) = \hat{\mathbf{e}}_\xi \cdot \left(\mathbf{r}_i \varphi_\mu(\mathbf{r}) \right) \qquad \xi = x, y, z \tag{3.81}$$

so that

$$\mathbf{r}_i \varphi_\mu(\mathbf{r}) = \sum_\xi \hat{\mathbf{e}}_\xi \chi^\xi_\mu(\mathbf{r}). \tag{3.82}$$

Since we can write $\mathbf{r} = \sum_\xi \hat{\mathbf{e}}_\xi r \sqrt{\frac{4\pi}{3}} Y_\xi(\theta, \phi)$, then

$$\begin{aligned}
\mathbf{r}_i \varphi_\mu(\mathbf{r}) &= \sum_\xi \hat{\mathbf{e}}_\xi \left(r_i \sqrt{\frac{4\pi}{3}} Y_\xi(\theta_i, \phi_i) \right) \left(R_\mu(r_i) Y_\alpha(\theta_i, \phi_i) \right) \\
&= \sum_\xi \hat{\mathbf{e}}_\xi \left(r_i R_\mu(r_i) \right) \sum_\omega C^\omega_{\alpha,\xi} Y_\omega(\theta_i, \phi_i),
\end{aligned} \tag{3.83}$$

allowing the identification of

$$\chi^\xi_\mu(\mathbf{r}) = r_i R_\mu(r_i) \sum_\omega C^\omega_{\alpha,\xi} Y_\omega(\theta_i, \phi_i). \tag{3.84}$$

where the coefficients $C^\omega_{\alpha,\xi}$ are given by

$$C^\omega_{\alpha,\xi} = \sqrt{\frac{4\pi}{3}} \int Y_\omega(\theta, \phi) Y_\alpha(\theta, \phi) Y_\xi(\theta, \phi) \sin\theta \, d\theta \, d\phi \tag{3.85}$$

For sp systems, $\alpha \in \{s, p_x, p_y, p_z\}$ and $\xi \in \{x, y, z\}$. Using Table 3.1 and Eq. 3.85, non-vanishing coefficients $C^\omega_{\alpha,\xi}$ can be obtained and are given in table 3.4.

α \ ξ	x	y	z
s	$C^{x}_{s,x}=\frac{1}{\sqrt{3}}$	$C^{y}_{s,y}=\frac{1}{\sqrt{3}}$	$C^{z}_{s,z}=\frac{1}{\sqrt{3}}$
p_x	$C^{s}_{x,x}=\frac{1}{\sqrt{3}}$, $C^{x^2-y^2}_{x,x}=\frac{1}{\sqrt{5}}$ $C^{3z^2-r^2}_{x,x}=-\frac{1}{\sqrt{15}}$	$C^{xy}_{x,y}=\frac{1}{\sqrt{5}}$	$C^{zx}_{x,z}=\frac{1}{\sqrt{5}}$
p_y	$C^{xy}_{y,x}=\frac{1}{\sqrt{5}}$	$C^{s}_{y,y}=\frac{1}{\sqrt{3}}$, $C^{x^2-y^2}_{y,y}=-\frac{1}{\sqrt{5}}$ $C^{3z^2-r^2}_{y,y}=-\frac{1}{\sqrt{15}}$	$C^{yz}_{y,z}=\frac{1}{\sqrt{5}}$
p_z	$C^{zx}_{z,x}=\frac{1}{\sqrt{5}}$	$C^{yz}_{z,y}=\frac{1}{\sqrt{5}}$	$C^{s}_{z,z}=\frac{1}{\sqrt{3}}$, $C^{3z^2-r^2}_{z,z}=\frac{2}{\sqrt{15}}$

Table 3.4: Non-vanishing coefficients $C^{\omega}_{\alpha,\xi}$.

When both μ and ν are orbitals on atom i, replacing $\mathbf{r}_i\varphi_\mu(\mathbf{r})$ with $\sum_\xi \hat{\mathbf{e}}_\xi \chi^\xi_\mu(\mathbf{r})$ gives

$$\begin{aligned}\hat{\mathbf{e}}_\xi\cdot\mathbf{P}_{\mu\nu} &= \int \chi^{\xi *}_\mu(\mathbf{r})\varphi_\nu(\mathbf{r})d\mathbf{r}\\ &= \int \Big(r_i R_\mu(r_i)\sum_\omega C^\omega_{\alpha,\xi}Y_\omega(\theta_i,\phi_i)\Big)\Big(R_\nu(r_i)Y_\beta(\theta_i,\phi_i)\Big)d\mathbf{r}_i \\ &= C^\beta_{\alpha,\xi}\int_0^\infty r^3 R_\mu(r)R_\nu(r)dr, \quad \mu=\{\alpha,i\} \quad \nu=\{\beta,j\},\end{aligned} \tag{3.86}$$

due to the orthonormality of the spherical harmonics. When orbital μ is on atom i, and orbital ν is on different atom j, then we have

$$\begin{aligned}\hat{\mathbf{e}}_\xi\cdot\mathbf{P}_{\mu\nu} &= \int \chi^{\xi *}_\mu(\mathbf{r})\varphi_\nu(\mathbf{r})d\mathbf{r}\\ &= \int \sum_\omega \Big(rR_\mu(r)\Big)\Big(C^\omega_{\alpha,\xi}Y_\omega(\theta,\phi)\Big)\Big(R_\nu(\tilde{r})Y_\beta(\tilde{\theta},\tilde{\phi})\Big)d\mathbf{r}\\ &= \sum_\omega C^\omega_{\alpha,\xi}\int_0^\infty dr\int_0^\pi d\theta\int_0^{2\pi} d\phi R_\mu(r)R_\nu(\tilde{r})r^3\sin\theta Y_\omega(\theta,\phi)Y_\beta(\tilde{\theta},\tilde{\phi})\end{aligned} \tag{3.87}$$

when $\tilde{\mathbf{r}}=\mathbf{r}-\mathbf{R}_{ji}$, using Eq. 3.46 and Eq. 3.49, this becomes

$$\hat{\mathbf{e}}_\xi\cdot\mathbf{P}_{\mu\nu} = \sum_\omega C^\omega_{\alpha,\xi}\sum_\tau T^{\omega\beta}_\tau P^\tau_{\mu\nu} \tag{3.88}$$

where

$$P^\tau_{\mu\nu} = \int_0^\infty dr\int_0^\pi d\theta_1 R_\mu(r)R_\nu(\tilde{r})r^3\sin\theta_1\Theta_\tau(\theta_1,\theta_2). \tag{3.89}$$

Note that because τ is the bond between ω and β, but the radial part contains wave function α and β, more integrals are needed for $P^\tau_{\mu\nu}$ than $S^\tau_{\mu\nu}$.

Similar to $S_{\mu\nu}$, for each pair of atoms $\mathbf{P}_{\mu\nu}$ is evaluated numerically.

3.2.4 Solving the Kohn-Sham equation

We write the $E_{2\mathrm{nd}}$ in Eq. 3.74 as three components

$$\begin{aligned} E_{2\mathrm{nd}}^{\mathrm{qq}} &= \frac{1}{2}\sum_{i=1}^{N}\sum_{j=1}^{N}\Delta q_i \hat{\Gamma}_{ij}^{00}\Delta q_j \\ E_{2\mathrm{nd}}^{\mathrm{pq}} &= \sum_{i=1}^{N}\sum_{j=1}^{N}\Delta \mathbf{p}_i \cdot \hat{\Gamma}_{ij}^{10}\Delta q_j \\ E_{2\mathrm{nd}}^{\mathrm{pp}} &= \frac{1}{2}\sum_{i=1}^{N}\sum_{j=1}^{N}\Delta \mathbf{p}_i \cdot \hat{\Gamma}_{ij}^{11}\Delta \mathbf{p}_j. \end{aligned} \tag{3.90}$$

For $E_{2\mathrm{nd}}^{\mathrm{pq}}$, similar to Eq. 3.61, the partial derivative of dipole is

$$\frac{\partial \mathbf{p}_i}{\partial c_\mu^{k'*}} = e f_k \frac{1}{2}\left(\delta_{il}\sum_b c_b^k \mathbf{P}_{\mu b} + \sum_\alpha c_a^k \mathbf{P}_{a\mu}^*\right), \quad a=\{\alpha,i\}, b=\{\beta,h\}, \mu=\{\sigma,l\}. \tag{3.91}$$

$E_{2\mathrm{nd}}^{\mathrm{pq}}/\partial c_\mu^{k'*}$ has two components

$$\frac{\partial E_{2\mathrm{nd}}^{\mathrm{pq}}}{\partial c_\mu^{k'*}} = \sum_{i=1}^{N}\sum_{j=1}^{N}\frac{\partial \mathbf{p}_i}{\partial c_\mu^{k'*}}\cdot\hat{\Gamma}_{ij}^{10}\Delta q_j + \sum_{i=1}^{N}\sum_{j=1}^{N}\Delta \mathbf{p}_i \cdot \hat{\Gamma}_{ij}^{10}\frac{\partial q_j}{\partial c_\mu^{k'*}}. \tag{3.92}$$

If we name the first term as F_{10} and the second term F_{01}, using the same methods as in Eq. 3.64, inserting Eq. 3.61 and Eq. 3.91

$$\begin{aligned} F_{10} &= e f_k \frac{1}{2}\sum_{i=1}^{N}\sum_{j=1}^{N}\left(\delta_{il}\sum_b c_b^k \mathbf{P}_{\mu b} + \sum_\alpha c_a^k \mathbf{P}_{a\mu}^*\right)\cdot\hat{\Gamma}_{ij}^{10}\Delta q_j, \quad a=\{\alpha,i\}, b=\{\beta,h\}, \mu=\{\sigma,l\} \\ &= e f_k \frac{1}{2}\sum_{j=1}^{N}\sum_\nu c_\nu^k\left(\mathbf{P}_{\mu\nu}\cdot\hat{\Gamma}_{ij}^{10} + \mathbf{P}_{\nu\mu}^*\cdot\hat{\Gamma}_{hj}^{10}\right)\Delta q_j, \quad \nu=\{\beta,h\}, \mu=\{\sigma,i\} \\ &= e f_k \frac{1}{2}\sum_{h=1}^{N}\sum_\nu c_\nu^k\left(\mathbf{P}_{\mu\nu}\cdot\hat{\Gamma}_{ih}^{10} + \mathbf{P}_{\nu\mu}^*\cdot\hat{\Gamma}_{jh}^{10}\right)\Delta q_h, \quad \mu=\{\sigma,i\}, \nu=\{\beta,j\}, \end{aligned} \tag{3.93}$$

and

$$\begin{aligned} F_{01} &= e f_k \frac{1}{2}\sum_{j=1}^{N}\sum_{i=1}^{N}\Delta \mathbf{p}_j\cdot\hat{\Gamma}_{ji}^{10}\left(\delta_{il}\sum_b c_b^k S_{\mu b} + \sum_\alpha c_a^k S_{a\mu}^*\right), \quad a=\{\alpha,i\}, b=\{\beta,h\}, \mu=\{\sigma,l\} \\ &= e f_k \frac{1}{2}\sum_{j=1}^{N}\sum_\nu c_\nu^k \Delta \mathbf{p}_j\cdot\left(\hat{\Gamma}_{ji}^{10}S_{\mu\nu} + \hat{\Gamma}_{jh}^{10}S_{\nu\mu}^*\right), \quad \nu=\{\beta,h\}, \mu=\{\sigma,i\} \\ &= e f_k \frac{1}{2}\sum_{h=1}^{N}\sum_\nu c_\nu^k \Delta \mathbf{p}_h\cdot\left(\hat{\Gamma}_{hi}^{10}S_{\mu\nu} + \hat{\Gamma}_{hj}^{10}S_{\nu\mu}^*\right), \quad \mu=\{\sigma,i\}, \nu=\{\beta,j\}. \end{aligned} \tag{3.94}$$

So

$$\begin{aligned}\frac{\partial E^{\mathrm{pq}}_{2\mathrm{nd}}}{\partial c^{k'*}_{\mu}} =& e f_k \frac{1}{2}\sum_{h=1}^{N}\sum_{\nu} c^{k}_{\nu}\,[\,\left(\mathbf{P}_{\mu\nu}\cdot\hat{\Gamma}^{10}_{ih}+\mathbf{P}^{*}_{\nu\mu}\cdot\hat{\Gamma}^{10}_{jh}\right)\Delta q_h \\ &+\Delta\mathbf{p}_h\cdot\left(\hat{\Gamma}^{10}_{hi}S_{\mu\nu}+\hat{\Gamma}^{10}_{hj}S^{*}_{\nu\mu}\right)\,],\quad \mu=\{\sigma,i\},\nu=\{\beta,j\}.\end{aligned} \tag{3.95}$$

For $E^{\mathrm{pp}}_{2\mathrm{nd}}$ with the symmetry $\hat{\Gamma}^{11}_{ij}=\hat{\Gamma}^{11}_{ji}$

$$\begin{aligned}\frac{\partial E^{\mathrm{pp}}_{2\mathrm{nd}}}{\partial c^{k'*}_{\mu}} &= \frac{1}{2}\sum_{i=1}^{N}\sum_{j=1}^{N}\frac{\partial\mathbf{p}_i}{\partial c^{k'*}_{\mu}}\cdot\hat{\Gamma}^{11}_{ij}\Delta\mathbf{p}_j+\frac{1}{2}\sum_{i=1}^{N}\sum_{j=1}^{N}\Delta\mathbf{p}_i\cdot\hat{\Gamma}^{11}_{ij}\frac{\partial\mathbf{p}_j}{\partial c^{k'*}_{\mu}} \\ &= \sum_{i=1}^{N}\sum_{j=1}^{N}\frac{\partial\mathbf{p}_i}{\partial c^{k'*}_{\mu}}\cdot\hat{\Gamma}^{11}_{ij}\Delta\mathbf{p}_j, \\ &= e\sum_{k}f_k\frac{1}{2}\sum_{h=1}^{N}\sum_{\nu}c^{k}_{\nu}(\mathbf{P}_{\mu\nu}\cdot\hat{\Gamma}^{11}_{ih}+\mathbf{P}^{*}_{\nu\mu}\cdot\hat{\Gamma}^{11}_{jh})\Delta\mathbf{p}_h,\quad \mu=\{\sigma,i\},\nu=\{\beta,j\}.\end{aligned} \tag{3.96}$$

Combing Eq. 3.64, Eq. 3.95 and Eq. 3.96

$$\begin{aligned}\frac{\partial E_{2\mathrm{nd}}}{\partial c^{k'*}_{\mu}} =& e f_k \frac{1}{2}\sum_{h=1}^{N}\sum_{\nu} c^{k}_{\nu}\,[\,(S_{\mu\nu}\hat{\Gamma}^{00}_{ih}+S^{*}_{\nu\mu}\hat{\Gamma}^{00}_{jh})\Delta q_h \\ &+(\mathbf{P}_{\mu\nu}\cdot\hat{\Gamma}^{10}_{ih}+\mathbf{P}^{*}_{\nu\mu}\cdot\hat{\Gamma}^{10}_{jh})\Delta q_h+\Delta\mathbf{p}_h\cdot(\hat{\Gamma}^{10}_{hi}S_{\mu\nu}+\hat{\Gamma}^{10}_{hj}S^{*}_{\nu\mu}) \\ &+(\mathbf{P}_{\mu\nu}\cdot\hat{\Gamma}^{11}_{ih}+\mathbf{P}^{*}_{\nu\mu}\cdot\hat{\Gamma}^{11}_{jh})\Delta\mathbf{p}_h\,],\quad \mu=\{\sigma,i\},\nu=\{\beta,j\}.\end{aligned} \tag{3.97}$$

So the Hamiltonian shift including dipole fluctuation is

$$\begin{aligned}H^{1}_{\mu\nu} =& e\frac{1}{2}\sum_{h=1}^{N}\,[\,(S_{\mu\nu}\hat{\Gamma}^{00}_{ih}+S^{*}_{\nu\mu}\hat{\Gamma}^{00}_{jh})\Delta q_h \\ &+(\mathbf{P}_{\mu\nu}\cdot\hat{\Gamma}^{10}_{ih}+\mathbf{P}^{*}_{\nu\mu}\cdot\hat{\Gamma}^{10}_{jh})\Delta q_h+\Delta\mathbf{p}_h\cdot(\hat{\Gamma}^{10}_{hi}S_{\mu\nu}+\hat{\Gamma}^{10}_{hj}S^{*}_{\nu\mu}) \\ &+(\mathbf{P}_{\mu\nu}\cdot\hat{\Gamma}^{11}_{ih}+\mathbf{P}^{*}_{\nu\mu}\cdot\hat{\Gamma}^{11}_{jh})\Delta\mathbf{p}_h\,],\quad \mu=\{\sigma,i\},\nu=\{\beta,j\}.\end{aligned} \tag{3.98}$$

3.2.5 External field

When an external field is present, the energy due to interaction with the external field is an additional contribution added into the second order energy as

$$E_{2\mathrm{nd}} = E^{\mathrm{qq}}_{2\mathrm{nd}}+E^{\mathrm{pq}}_{2\mathrm{nd}}+E^{\mathrm{pp}}_{2\mathrm{nd}}+\sum_{i=1}^{N}\Delta q_i V^{ext}_i-\sum_{i=1}^{N}\Delta\mathbf{p}_i\cdot\mathbf{E}^{ext}_i. \tag{3.99}$$

where $\mathbf{E}^{ext}_i$ is the external field at the location of atom i, and V^{ext}_i is the corresponding external potential.

This then results in an additional contribution $H^{ext}_{\mu\nu}$ to be added to the Hamiltonian shift in

Eq. 3.98. Since in addition to the Hamiltonian

$$\begin{aligned}&\frac{1}{\partial c_\mu^{k'*}}\left[\sum_{i=1}^{N}\Delta q_i V_i^{ext}-\sum_{i=1}^{N}\Delta \mathbf{p}_i \mathbf{E}_i^{ext}\right]\\&=ef_k\frac{1}{2}\sum_\nu c_\nu^k\left[(S_{\mu\nu}V_i^{ext}+S_{\nu\mu}^*V_j^{ext})-(\mathbf{P}_{\mu\nu}\cdot\mathbf{E}_i^{ext}+\mathbf{P}_{\nu\mu}^*\cdot\mathbf{E}_j^{ext})\right],\quad \mu=\{\alpha,i\},\nu=\{\beta,j\}.\end{aligned}\tag{3.100}$$

we have

$$H_{\mu\nu}^{ext}=e\frac{1}{2}\left[(S_{\mu\nu}V_i^{ext}+S_{\nu\mu}^*V_j^{ext})-(\mathbf{P}_{\mu\nu}\cdot\mathbf{E}_i^{ext}+\mathbf{P}_{\nu\mu}^*\cdot\mathbf{E}_j^{ext})\right],\quad \mu=\{\alpha,i\},\nu=\{\beta,j\}.\tag{3.101}$$

Thus the total Hamiltonian matrix is

$$H_{\mu\nu}=H_{\mu\nu}^0+H_{\mu\nu}^1+H_{\mu\nu}^{ext}.\tag{3.102}$$

Note that on can easily demonstrate that $H_{\mu\nu}=H_{\nu\mu}^*$, so that the Hamiltonian's hermitian nature is preserved.

In this Chapter, we have extended the standard SCC-DFTB to a scheme allowing dipole fluctuation, by modifying the second order energy, evaluating the atomic dipole moment, constructing dipole matrix element $\mathbf{P}_{\mu\nu}$ and updating the Hamiltonian. From now on, our extended SCC-DFTB scheme will be called SCCD-DFTB, where D indicates the dipole contribution.

Chapter 4

Applications of Density Functional Tight Binding with Dipole Extension

In this Chapter, a brief summary of the implementation of SCCD-DFTB is given. In support of this implementation, we apply it to some Carbon-based systems, and compare the results with those obtained by other means. This includes the determination of the parameters which are used in further calculations.

4.1 Implementation

Our implementation is based on the existing SCC-DFTB code "DFTB+" [117, 122]. From the 2nd order energy (Eq. 3.74) and the Hamiltonian shift (Eq. 3.98) when including the dipole extension (reproduced here)

$$
\begin{aligned}
E_{\text{2nd}} =& \frac{1}{2}\sum_{i=1}^{N}\sum_{j=1}^{N}\Delta q_i \hat{\Gamma}^{00}_{ij}\Delta q_j + \sum_{i=1}^{N}\sum_{j=1}^{N}\Delta \mathbf{p}_i \cdot \hat{\Gamma}^{10}_{ij}\Delta q_j + \frac{1}{2}\sum_{i=1}^{N}\sum_{j=1}^{N}\Delta \mathbf{p}_i \cdot \hat{\Gamma}^{11}_{ij}\Delta \mathbf{p}_j, \\
H^1_{\mu\nu} =& e\frac{1}{2}\sum_{h=1}^{N}[\ (S_{\mu\nu}\hat{\Gamma}^{00}_{ih} + S^*_{\nu\mu}\hat{\Gamma}^{00}_{jh})\Delta q_h \\
&+ (\mathbf{P}_{\mu\nu}\cdot\hat{\Gamma}^{10}_{ih} + \mathbf{P}^*_{\nu\mu}\cdot\hat{\Gamma}^{10}_{jh})\Delta q_h + \Delta\mathbf{p}_h\cdot(\hat{\Gamma}^{10}_{hi}S_{\mu\nu} + \hat{\Gamma}^{10}_{hj}S^*_{\nu\mu}) \\
&+ (\mathbf{P}_{\mu\nu}\cdot\hat{\Gamma}^{11}_{ih} + \mathbf{P}^*_{\nu\mu}\cdot\hat{\Gamma}^{11}_{jh})\Delta\mathbf{p}_h\ ], \quad \mu = \{\sigma, i\}, \nu = \{\beta, j\},
\end{aligned}
\tag{4.1}
$$

we can see that the atomic dipole difference $\Delta\mathbf{p}$ (defined in Eq. 3.77 using a similar approach as is used for the Mulliken charges), the charge-dipole interaction operator $\hat{\Gamma}^{10}_{ij}$ and dipole-dipole interaction operator $\hat{\Gamma}^{11}_{ij}$ (defined in Eq. 3.72 and Eq. 3.73, details in Appendix A), and the dipole matrix $\mathbf{P}_{\mu\nu}$ (defined in Section 3.2.3, technical details in Appendix B) are the new quantities introduced at this enhanced level of the theory, with the 2nd order energy E_{2nd} and the Hamiltonian shift $H^1_{\mu\nu}$ quantities that are modified accordingly.

We adopt the Mulliken scheme when considering the atomic dipole difference $\Delta\mathbf{p}$, but this is not unique and any other reasonable population scheme could be implemented. However, it should be noted that the precise form of the Hamiltonian shift $H^1_{\mu\nu}$ depends on the definition of $\Delta\mathbf{p}$, and that Eq. 3.98 is only valid with the Mulliken definition.

For $\hat{\Gamma}^{10}_{ij}$ and $\hat{\Gamma}^{11}_{ij}$, both Gaussian-type and Slater-type distributions have been considered. However, the original "DFTB+" code uses only the Slater-type distributions for the charge-charge interaction operator $\hat{\Gamma}^{00}_{ij}$, and other physical properties that can be calculated also depend upon $\hat{\Gamma}^{00}_{ij}$. Since exploring the difference of Gaussian-type and Slater-type distributions has not been a priority, it has been decided at this stage not to implement the Gaussian-type $\hat{\Gamma}^{00}_{ij}$ and to change other properties which depend upon it.

Because the systems of our primary interest are Carbon-based, the dipole matrix $\mathbf{P}_{\mu\nu}$ has been parameterised and generated for the Carbon-Carbon atom pair. By following the procedure described in Section 3.2.3 and in Appendix B, $\mathbf{P}_{\mu\nu}$ for other atom pairs can also be generated.

When an external field is present, additional terms enter into the expressions for the total energy and the Hamiltonian shift. According to Eq. 3.99 and Eq. 3.101 (reproduced here)

$$\begin{aligned} E_{\mathrm{2nd}} &= E^{\mathrm{qq}}_{\mathrm{2nd}} + E^{\mathrm{pq}}_{\mathrm{2nd}} + E^{\mathrm{pp}}_{\mathrm{2nd}} + \sum_{i=1}^{N} \Delta q_i V_i^{ext} - \sum_{i=1}^{N} \Delta\mathbf{p}_i \cdot \mathbf{E}_i^{ext}, \\ H^{ext}_{\mu\nu} &= e\frac{1}{2}\left[(S_{\mu\nu}V_i^{ext} + S^*_{\nu\mu}V_j^{ext}) - (\mathbf{P}_{\mu\nu}\cdot\mathbf{E}_i^{ext} + \mathbf{P}^*_{\nu\mu}\cdot\mathbf{E}_j^{ext})\right], \quad \mu = \{\alpha, i\}, \nu = \{\beta, j\}. \end{aligned} \tag{4.2}$$

The interaction of the external electric field with each atom involves the dipole extension, which is new to the SCCD-DFTB formulation.

Basically, we adopt the structure of "DFTB+" code, which is written using Fortran in a modern manner: subroutines realizing related purpose are grouped into modules, and the main program contains the modules and calls the subroutines. For our implementation, we added subroutines and modified the modules and main programs, and we also wrote a separate program to generate the Slater-Koster integrals for dipole matrix $\mathbf{P}_{\mu\nu}$. First of all, the Slater-Koster integrals for dipole matrix $\mathbf{P}_{\mu\nu}$ have been generated, and the input module has been modified to read in those Slater-Koster integrals, and a subroutine has been added to transform the input Slater-Koster integrals into dipole matrix $\mathbf{P}_{\mu\nu}$. Secondly, subroutines similar to those which calculate $\hat{\Gamma}^{00}_{ij}$, Mulliken charge difference Δq_i and external potential

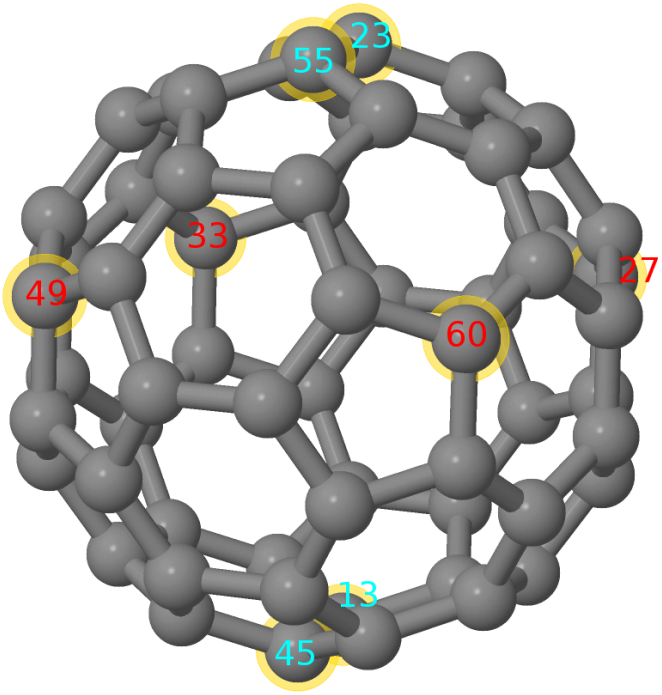

Figure 4.1: Geometry of C60 molecule. Two sets of atoms are highlighted and labelled with red or cyan numbers.

V_i^{ext} have been added to obtain $\hat{\Gamma}_{ij}^{10}/\hat{\Gamma}_{ij}^{11}$, Mulliken dipole difference $\Delta\mathbf{p}_i$ and external field $\mathbf{E}_i^{ext}$, respectively. Finally, additional terms of total energy and Hamiltonian shift have been added to the subroutines that calculate them, and the main program has been modified accordingly.

4.2 Validation

Initially a series of calculations were performed to validate the implementation.

Firstly, we confirmed that the implementation of the new SCCD-DFTB scheme was correct regarding the symmetry of the self-consistently included dipoles. This was done by calculating the electronic properties of a number of different Carbon clusters and molecules placed in uniformed external field in random directions. The C60 molecule serves as an example here. Convergence was assumed (see Chapter 2 for the discussion regarding self-consistency in DFT calculations) when the difference in charges and dipoles fall below 1.0×10^{-8} e and 1.0×10^{-8} eÅ, respectively, and when the energy was converged to 1.0×10^{-5} eV. These convergence criteria are used for all the calculations reported in this Chapter. Fig. 4.2

				no field			with field
Atom number	x (Å)	y (Å)	z (Å)	$\mathbf{p}_x$ (eÅ)	$\mathbf{p}_y$ (eÅ)	$\mathbf{p}_z$ (eÅ)	$\mathbf{p}'_z$ (eÅ)
27	2.584	2.292	0.721	0.007	0.036	-0.013	-0.011
33	-2.584	2.292	0.721	-0.007	0.036	-0.013	-0.011
49	-2.584	-2.292	0.721	-0.007	-0.036	-0.013	-0.011
60	2.584	-2.292	0.721	0.007	-0.036	-0.013	-0.011
13	0.000	0.694	-3.461	0.000	0.032	-0.020	-0.016
23	0.000	0.694	3.461	0.000	0.032	0.020	0.024
45	0.000	-0.694	-3.461	0.000	-0.032	-0.020	-0.016
55	0.000	-0.694	3.461	0.000	-0.032	0.020	0.024

Table 4.1: Atomic dipoles on selected atoms of a C60 molecule in different conditions.

shows the geometry of the C60 molecule with specific atoms labelled. The C60 molecule is made of 20 hexagons and 12 pentagons, with each Carbon atom belonging to 2 hexagons and 1 pentagon. The bond lengths are $r_{6-6} \sim 1.40$ Å (the bonds belong only to hexagons) and $r_{5-5} \sim 1.46$ Å (bonds in pentagon) [123]. Because of this geometry, the C60 molecule has ten 3-fold axes and six 5-fold axes. In these calculations the geometry is fixed and the bond lengths used are $r_{6-6} = 1.39$ Å and $r_{5-5} = 1.47$ Å. We consider the properties of two sets of atoms, a first set, atoms 27, 33, 49 and 60, lie in a plane parallel to the xy plane when the molecule is in the chosen orientation. A second set, atoms 13, 23, 45 and 55, lie in a plane parallel to the yz plane. The Cartesian positions and the self-consistently calculated atomic dipoles of each of these atoms are listed in Table. 4.1. In the absence of an applied field, both sets of atoms possess dipoles that exhibit the correct symmetry. For the same geometry, we consider the C60 molecule placed in an external electric field directed along $\hat{\mathbf{z}}$ with a magnitude of 1.0×10^9 V/m (1.94×10^{-3} ea_0). The resulting atomic dipoles in the z direction are tabulated in Table. 4.1. Only the z components are shown here because the x and y components are the same as in the absence of the external field. Comparing the 7th and 8th column of Table. 4.1, it can be seen that each Carbon atom of the first set had been induced a dipole of 0.002 eÅ in the z direction by the filed, while the atoms of the second set the field induced dipole is 0.004 eÅ. The direction of these dipoles is consistent with the direction of the applied external field (see Section 3.2.2 for the detail of dipole direction).

Second, we tested the ability to calculate the electronic structures of extended systems by comparing the band structures of Carbon-based systems obtained from both the standard SCC-DFTB method and SCCD-DFTB approach. Monolayer and bilayer graphene are shown here as examples. Initially the geometry of monolayer and bilayer graphene was fully relaxed using SCC-DFTB with the force fell below 1.0×10^{-4} eV/Å. Then for this fixed geome-

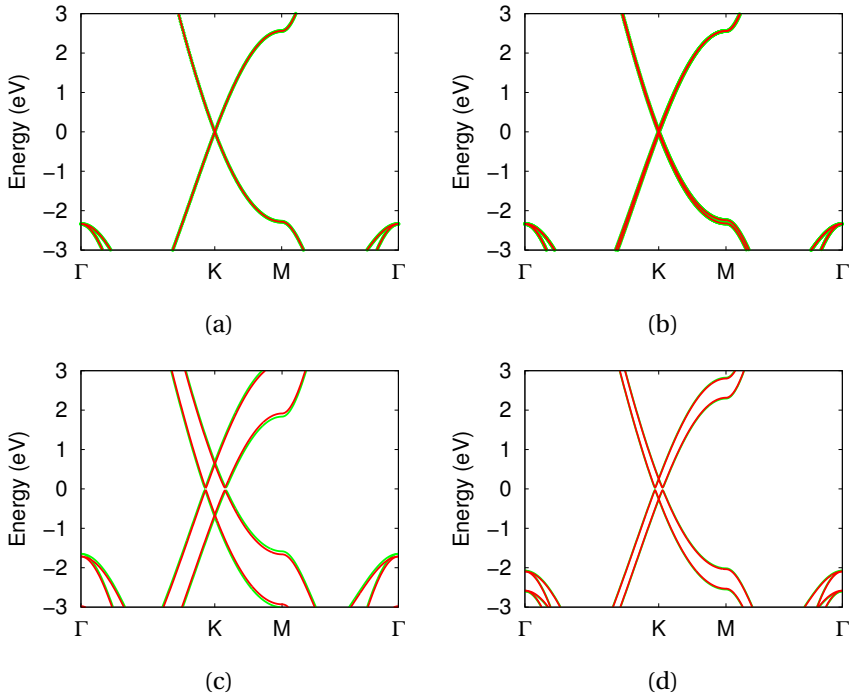

Figure 4.2: Comparison of band structures of mono/bilayer graphene calculated along high symmetry directions in the 2 dimensional Brillouin zone. a) Monolayer, without field; b) Bilayer, without field; c) Bilayer, with uniform field; d) Bilayer, with point charges. The green line is the result obtained using SCCD-DFTB; the red line is that of standard SCC-DFTB.

try, the electronic structure was calculated using both SCC- and SCCD-DFTB, with a k point sampling of $72 \times 72 \times 1$ (see Chapter 2 and Section 5.2.1 for the detail about k point sampling and convergence check). The structure corresponds to C-C bond length of 1.42 Å and the bilayer interlayer separation of 3.55 Å. Because of the symmetry of monolayer graphene, we should expect the band structures obtained from the SCCD-DFTB the same with the standard SCC-DFTB. Fig. 4.2a shows that the results agreed with this expectation. For bilayer graphene, the band structures obtained from SCC- and SCCD-DFTB differ smaller than 1×10^{-5} eV, as shown in Fig. 4.2b, which is corresponding to the magnitude of 1×10^{-5} eÅ for the calculated atomic dipole using SCCD-DFTB. Note that the predicting bilayer graphene interlayer spacing of 3.55 Å from SCC-DFTB is lager than the experimental result 3.35 Å [124]. We also calculated the atomic dipoles with the interlayer spacing fixing to 3.35 Å, the magnitude of the atomic dipoles are 5×10^{-5} eÅ.

Because SCCD-DFTB scheme includes the interaction between the atomic dipoles and the external field, therefore, validating the ability to properly describe the electronic structure under the external field is essential. Now we apply an external field normal to the bilayer

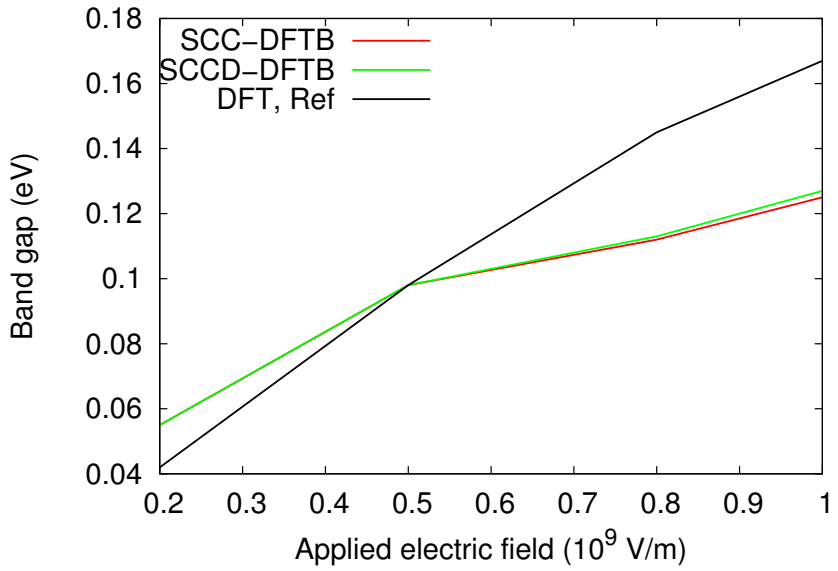

Figure 4.3: The band gap as a function of the strength of the applied field. The green line is the result from SCCD-DFTB, the red line from SCC-DFTB, and the black line is adapted from Yu *et al.* [125].

graphene. With Fig. 4.2c showing the case when the field strength is 1.0×10^9 V/m (1.94×10^{-3} ea_0). For comparison, Fig. 4.2d consider the normal field generated by two point charges: $+e$ $(0.0, 0.0, -3.4)$, $-e$ $(0.0, 0.0, -6.72)$ repeated periodically with the unit cell, where the lower layer of graphene lies on the $z = 0$ plane. (The reason we consider this test system with point charges is related to the ionic system of interest which will be discussed in the next Chapter.) Both cases show the opening of the band gap. The band structure obtained using SCCD-DFTB is slightly different than the result of SCC-DFTB.

In order to gain quantitatively understanding of the difference between the band structure obtained from the SCC-DFTB and that from SCCD-DFTB, we exam the band gap opening with different field strength, for the reason that the tunable band gap in bilayer graphene is well studied [125–133] . We compare the SCC-/SCCD-DFTB result with a recent DFT-LDA calculation from the literature Yu *et al.* [125]. In order to compare with the literature , the interlayer separation is fixed to 3.35 Å. Fig. 4.3 shows the band gap as a function of the strength of the applied field. At the region the strength is less than 0.5×10^9 V/m (9.60×10^{-4} ea_0, the SCC- and SCCD-DFTB band gap differ less than 10^{-4} eV and they are larger than that obtained using DFT; in the region from 0.5×10^9 V/m to 10^9 V/m (1.536×10^{-3} ea_0), the SCC- and SCCD-DFTB band gaps are lower then that of DFT, and SCCD-DFTB predicts the band gap 2.5% closer to the DFT result than SCC-DFTB at the strength of 10^9

C60 (Å^3)	C70 (Å^3)	C84 (Å^3)
58.0 SCC-DFTB	77.7 SCC-DFTB	93.2 SCC-DFTB
63.9 SCCD-DFTB	84.6 SCCD-DFTB	100.7 SCCD-DFTB
83.0 exp EELS[134]	103.5 exp EELS[134]	
76.5±8 exp molecular		
beam deflection [135]	102±14 exp gas phase [136]	
75.1 MCSCF [137]	89.8 MCSCF [137]	109.4 MCSCF [137]
75.1 charge-dipole [138]	91.5 charge-dipole [138]	115.9 charge-dipole [138]
86.1 DFT-LDA [139]	104.8 DFT-LDA [139]	
82.9 DFT-PBE [140]	102.8 DFT-PBE [140]	
CNT(6,6) (Å^2)	CNT(9,0) (Å^2)	CNT(15,0) (Å^2)
10.7 SCC-DFTB	8.0 SCC-DFTB	23.1 SCC-DFTB
11.4 SCCD-DFTB	8.7 SCCD-DFTB	24.9 SCCD-DFTB
11.0 MCSCF [137]	11.0 MCSCF [137]	20.1 MCSCF [137]
11.3 charge-dipole [138]	8.9 charge-dipole [138]	21.5 charge-dipole [138]

Table 4.2: Polarizabilities of selected systems obtained from different methods. The values of SCC- and SCCD-DFTB are from this work, exp indicates the experimental results.

V/m. This comparison shows with a smaller strength of the external field, the electronic structure SCCD-DFTB describes are very close to that of SCC-DFTB, while at larger strength, the results from SCCD-DFTB are closer to the results from DFT.

4.3 Parametrisation

If we recall the definition of the distribution function used in describing the charge and dipole fluctuation, Eq. 3.27, (reproduced here)

$$\rho^{\text{iso}}(r) = \frac{\tau^3}{8\pi} e^{-\tau r}, \tag{4.3}$$

the parameter τ used for charge and dipole distributions need not be the same. The tests presented in the previous section have been done with the dipole parameter the same as the charge parameter. We consider here the benefit of varying τ for the dipole distribution while keeping the τ for the charge fixed.

In this investigation, we study different buckyballs (C60, C70 and C84) and Carbon nanotubes (CNT) (CNT(6,6), CNT(9,0) and CNT(15,0)), which are chosen due to the availability of experimental data and previous computational studies. Monolayer graphene is also considered with results compare to LCAO-DFT results.

Table. 4.2 gives the polarizabilities of selected buckyballs and CNTs calculated from SCC-DFTB and SCCD-DFTB using the same τ value for both charge and dipole distribution functions along with experimental and theoretical results from references [135–141]. The geometries of buckyballs and CNTs used in these calculations are those used in Ref. [138]. All systems are treated as non-periodic clusters; more than 400 atoms are used for the CNTs to ensure that the edge effect is negligible. The quantity tabulated is the mean polarizability for buckyballs or lateral polarizability per unit length for CNTs. The polarizability α is acquired using the relation $\mathbf{P} = \alpha\mathbf{E}$, where $\mathbf{E}$ is the applying electric field and the $\mathbf{P}$ is the resulting static dipole. Note that the dipole $\mathbf{P}$ here is the total dipole of the system, which is a combination of the atomic dipole on each atom and the dipole due to the distribution of the charges (see Section 3.2.2). With this default parameterisation, the results obtained using SCCD-DFTB show a ~ 9% enhancement of the polariabilities of all systems.

In order to put the present results in context, we briefly summarize the literature concerning the polarizabilities of the buckyballs and CNTs. The experimental results in Table. 4.2 were obtained using different methods, and the theoretical results were acquired from not only different level of theory, but different geometries as well. For C60, a value of 83.0 $Å^3$ was obtained by Sohmen *et al.* [134] using an electro energy-loss spectroscopy (EELS) measurement. The result obtained by Antoine *et al.* [135] using a molecule beam deflection is 76.5±8 $Å^3$, quoting an uncertainty of ~ 10%. Zope [140] used DFT with PBE functional and LCAO basis to calculated the polarizability of a fully relaxed molecule, and obtained 82.9 $Å^3$. van Faassen *et al.* [139] also optimized the geometry, this time was DFT with LDA functional and a TZP+ LCAO basis, obtaining 86.1 $Å^3$. For C70, Compagnon *et al.* [136] reported a value of 102±14 $Å^3$ using the gas phase measurements. And the same papers reporting C60 results reported a polarizability of 103.5 $Å^3$ (EELS) [134] , 102.8 $Å^3$ (DFT-LDA) [140] and 104.8 $Å^3$ (DFT-PBE) [139]. From these values, it can be seen that modern DFT calculations and EELS measurement are in a good agreement, so that polarizability of 84.0 $Å^3$ for C60 and 103.7 $Å^3$ for C70 are reasonable values for these systems.

All systems have the results from Ref. [137] and Ref. [138], where Ref. [137] used a multi-configurational self-consistent-field (MCSCF) level of theory, which is a less sophisticated method than DFT, lacking the exchange-correlation contribution. And the results of Ref. [138] were fitted with Ref. [137] and experimental results. The concluded values from DFT and EELS of C60 and C70 are 10.6% and 13.4% higher than the MCSCF results in Ref. [137]. If we assume the MCSCF systematically underestimate the polarizability with a ratio of 12.0% (mean value for C60 and C70 cases) for all buckyballs and CNTs, the estimated values for C84 and CNTs will be: 131.3 $Å^3$ for C84, 13.2 $Å^2$ for CNT(6,6), 10.7$Å^2$ for CNT(9,0) and 24.1

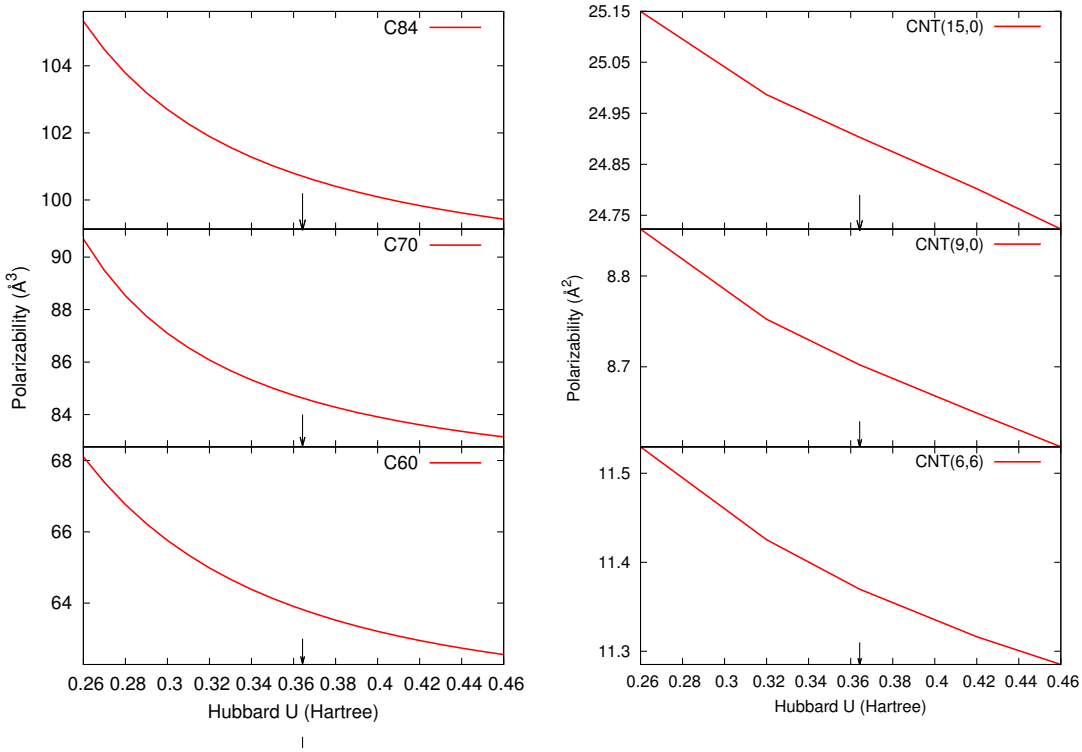

Figure 4.4: Calculated polarizability of various buckyballs and CNTs using SCCD-DFTB with different Hubbard U for dipole. The arrows indicate the Hubbard U for charge.

Å^2 for CNT(15,0).

This analysis shows that including the dipole fluctuation in the DFTB approach systematically improves calculated polarizabilities for 9% even with the same distribution parameter τ for charge. However, there is still some disagreement, so we consider varying τ for dipole. Recall that parameter τ for charge is parameterised using its relation to Hubbard U in Eq. 3.33

$$\tau = \frac{16}{5}U, \tag{4.4}$$

with the Hubbard U value approximated using Eq. 3.29 for the Carbon atom being 0.364302 Hartree. This is the value used for charge distribution function. From now on, we will refer to Hubbard U instead of τ for convenience.

Now we calculate the polarizabilities for each system varying the Hubbard U value for dipole while fix that for charge. The smaller the τ or Hubbard U value is, the broader the distribution function is. When the Hubbard U value is too small (smaller than 0.26 Hartree), we

	SCC-DFTB	SCCD-DFTB U = 0.26 Hartree	Estimated value from DFT and EELS
C60 ($Å^3$)	58.0 (-31%)	68.1 (-19%)	84.0
C70 ($Å^3$)	77.7 (-25%)	90.6 (-13%)	103.7
C84 ($Å^3$)	93.2 (-30%)	105.3 (-20%)	131.3
CNT(6,6) ($Å^2$)	10.7 (-19%)	11.5 (-13%)	13.2
CNT(9,0) ($Å^2$)	8.0 (-25%)	8.9 (-17%)	10.7
CNT(15,0) ($Å^2$)	23.1 (-4%)	25.2 (+5%)	24.1

Table 4.3: Comparison of polarizabilities of selected systems calculated from SCC-DFTB, SCCD-DFTB with U = 0.26 Hartree and estimated from DFT and EELS. The values in the bracket are the percentage differ from the value in column 4.

observe a band gap closing for buckyballs, where these buckyballs are all semiconductors, which indicate that those Hubbard U values are not physical. So we deicide the range of parameterisation is within ± 30%, which is approximately from 0.26 to 0.46 Hartree.

Fig. 4.4 shows the results. All systems show similar trends: smaller Hubbard U with results in larger polarizability. And two sets: buckyballs (left panel in Fig. 4.4) and CNTs (right panel in Fig. 4.4) also show the same trend within the set.

Comparing the results in Fig. 4.4, except CNT(15,0), the polarizability with the Hubbard U value of 0.26 Hartree are all among the range from 80% to 87% of the estimated values, listed in Table. 4.3. The result of CNT(15,0) indicates that either the assumption that MC-SCF underestimate 12 % is not valid for CNT(15,0), or the MCSCF and the SCCD-DFTB result do not have a linear dependency. For buckyballs and CNTs without CNT(15,0), the SCCD-DFTB with the Hubbard U value of 0.26 Hartree improves the polarizabilities acquired from SCC-DFTB by a mean value of 16.6%, and predicts on average 86.3 % that of estimated value from DFT and EELS.

On the other hand, we calculate the perpendicular polarizability per unit cell of monolayer graphene using both DFT-LCAO and SCCD-DFTB. Because of the symmetry of monolayer graphene, the perpendicular polarizability is 0 when using SCC-DFTB due to the lack of atomic dipole description. The DFT-LCAO calculations were performed using the code "CRYSTAL" [142] with the available basis sets for Carbon [143–145]. A k point sampling of $24 \times 24 \times 1$ is used. The polarizability was calculated using LDA [84] or PBE [146] functional, and the results are listed in Table. 4.4. The results obtained from LDA and PBE shows little difference, and the polarizability increased with the number of basis.

basis set	LDA	PBE
minimal	0.47	0.47
6-21G* [143]	0.51	0.52
6-31d1G [144]	0.59	0.60
TZVP [145]	0.63	0.63

Table 4.4: Perpendicular polarizability per unit cell ($Å^3$) of monolayer graphene using DFT-LCAO with different basis set.

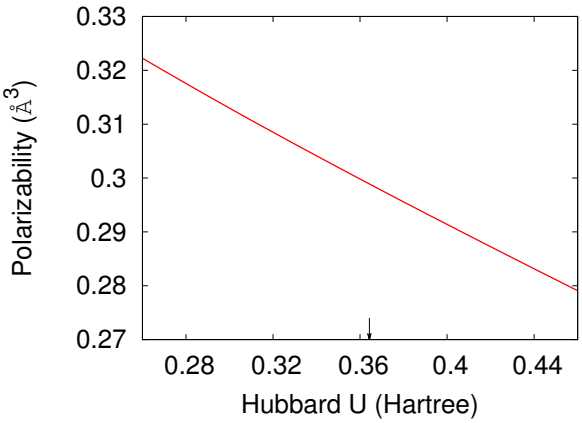

Figure 4.5: Calculated perpendicular polarizability per unit cell of monolayer graphene using SCCD-DFTB with different Hubbard U for dipole. The arrows indicate the Hubbard U for charge.

Fig. 4.5 shows the calculated polarizability using SCCD-DFTB with different Hubbard U for dipole. It shows the similar trend as those of buckyballs and CNTs. The basis set used in DFTB is the minimal basis set, so we compare the result with that of DFT-LCAO with minimal basis set. The result of SCCD-DFTB with Hubbard U for dipole of 0.26 Hartree is 0.32 $Å^3$, which is ~ 70% of that value 0.47 $Å^3$ obtained from DFTB-LCAO with minimal basis set. The percentage is lower than that of the buckyballs or CNTs (86.3%), but shows the systematic trend.

For our systems of interest, in the physical range, 0.26 Hartree is the value that gives the polarizabilities of buckyballs, CNTs and graphene closest to the results from experiments and DFT calculations, therefore we decide that 0.26 Hartree will be used in the further calculations.

In this Chapter, we have briefly introduced the implementation of SCCD-DFTB scheme,

demonstrated the validity of that scheme of calculating electronic properties, and decided a reasonable parameter which will be used in the next Chapter.

Chapter 5

Graphene on nanostructured ionic surfaces

In this Chapter, we will use both DFT and semi-empirical methods to investigate the electronic effects on mono/bilayer graphene due to the nanostructures on ionic substrates. The DFT calculations will serve as benchmarks and will help determine the parameters used for the semi-empirical calculations, and we will use the semi-empirical methods to explore more thoroughly the possibilities.

5.1 Systems of interest

As mentioned in Chapter 1, experimental results indicate the presence of a sizeable electrostatic potential in multilayer graphene on nanostructured KBr and NaCl surfaces. In this section, we will briefly introduce some types of nanostructures present on ionic surfaces.

Evidence for the presence of nanostructures on ionic surfaces can be found from the images recorded by scanning probe microscopy (SPM) with atomic resolution. In 1998, Bammerlin *et al.* [147] reported for the first time true atomic resolution images of various pure and doped (doped with 2% $MgCl_2$) alkali halide surfaces using dynamic force microscopy (DFM) [151]. Samples were prepared by cleaving in ultrahigh vacuum (UHV) (10^{-10} mbar) along {001} planes and annealing up to 150 Celsius for half an hour. As shown in Fig. 5.1a, the resulting surface shows the presence of atomic vacancies (indicated by arrows in Fig. 5.1a-a) and steps (Fig. 5.1a-c). In 1999, Bennewitz *et al.* [148, 152] reported atomic steps and kinks due to (001) NaCl islands grown on Cu(111) surface, shown in Fig. 5.1b. Two main steps were observed along <100> directions, which analysis suggested had a thickness of no more than 2 atom-layers; small steps in <110> directions and kinks were also identified. it

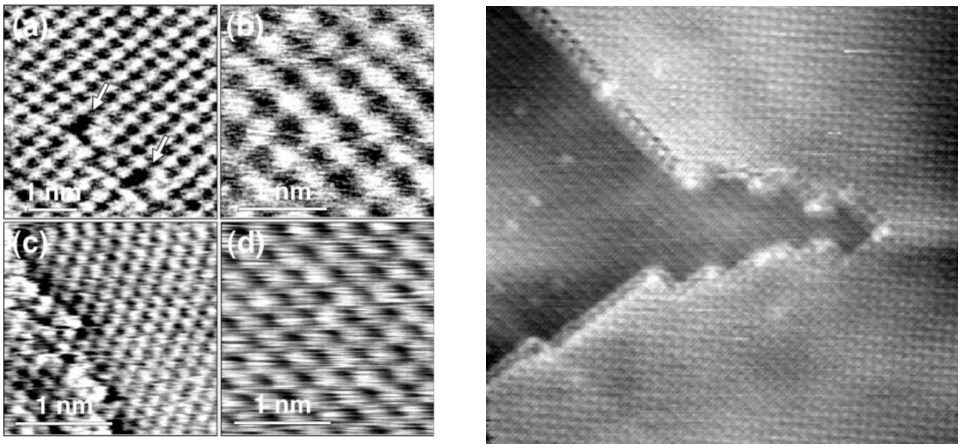

(a) (b)

Figure 5.1: Scanning probe microscopy images of nanostructures on ionic surfaces. a) Dynamic force microscopy images of a-a) NaCl(001); a-b) NaF(001); a-c)LiF(001); a-d) RbBr(001) [147]. b) Dynamic force microscopy topography of NaCl islands on Cu(111) [148].

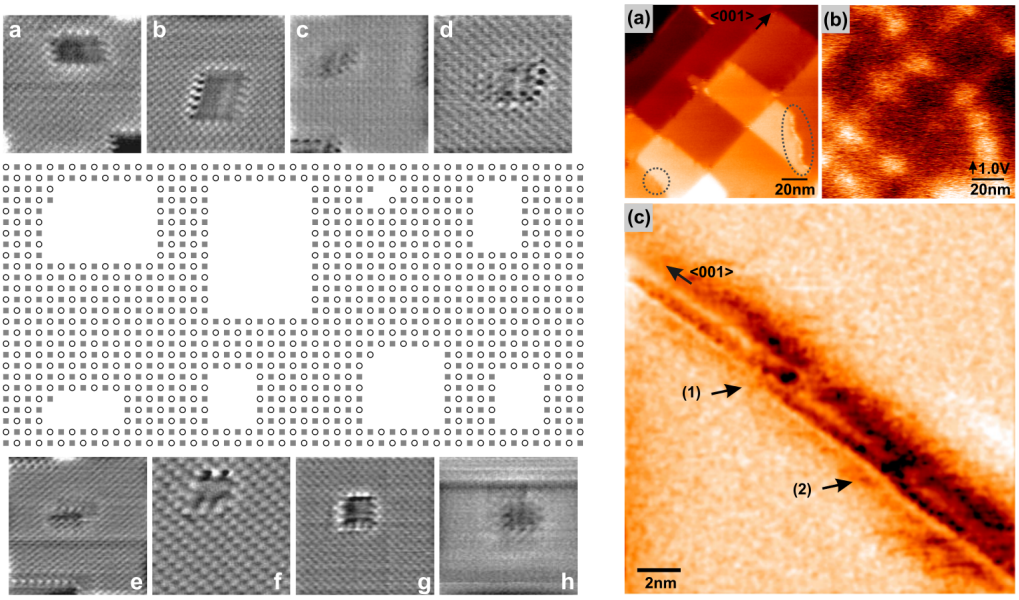

(a) (b)

Figure 5.2: Scanning probe microscopy images of nanostructures on ionic surfaces. a) Dynamic force microscopy images of pits on KBr(001) and their configurations [149]. Kelvin probe force microscopy b-a) topography; b-b) potential image; b-c) Constant height image recorded in KCl surface region marked by the dotted circle in b-a)[150].

was suggested that the increase in contrast observed over the step edges and kink sites was due to displacements in the positions of ions at the edges, with Na moving 0.24 Å outwards

and Cl 0.09 Å inwards. Subsequently, Such *et al.* [153] and Bennewitz *et al.* [149] reported the formation of atomic pits on KBr(001) surfaces with electron irradiation. Bennewitz *et al.* [149] cleaved their samples in air, transferred to vacuum and annealed at 430 K for 0.5 hours, before irradiating with 1 keV electrons for 5 s at 430 K. Fig. 5.2a shows the high resolution DFM images recorded of 8 pits generated this way and their atomic configurations. They reported that most pits observed had no more than one kink site, and the kinks were all at the corners of the pits. Pit edges were aligned along <100>, and all pits were formed by an even number of missing KBr molecules which restored the stoichiometry. Pits as small as only two molecules were found to be stable. In 2006, Barth and Henry [150, 154] studied steps on UHV cleaved alkali halides using Kelvin probe force microscopy (KPFM) and DFM with atomic resolution. The crystals were cleaved in UHV and annealed at 150-200 Celsius for two hours. Fig. 5.2b shows the topography and potential map which they obtained on KCl(001) surfaces. Fig. 5.2b-a) shows steps that lie along <100> (non-polar steps) and also other directions (polar steps) are both present. More non-polar steps than polar steps were seen, while the polar steps exhibited more contrast. Fig. 5.2b-c) highlights the kinks that change the non-polar step directions and formed the polar steps. It was verified that the bright contrast was due to the presence of charged defects, specifically divalent impurities and cation vacancies, present on the first two layers of the surface, by imaging sample of NaCl intentionally doped with 0.1% $MgCl_2$.

Followed this interpretation that the contrast was from charged surface defects such as divalent impurities, Barth and Henry [155, 156] along with Foster *et al.* [157] systematically studied ionic surfaces which were intentionally doped with divalent impurities. This resulted surface divided into different regions, with parts exhibits a structure called the Suzuki structure [158], and other the regular surface structure. The presence of the Suzuki structure gave further variants of nanostructures. Fig. 5.3a shows the atomic configuration of the Suzuki structure. As shown in Fig. 5.3a-b and Fig. 5.3a-d, four corner Na^+ ions are alternately exchanged with two divalent impurity ions such as Mg^{2+} and two Na^+ vacancies. The Suzuki structure for different ionic solid exhibit different displacement of the positions of cation and anion atoms on the first two surface layers. On average the cation and anion atoms move by 0.2 Å in opposite directions. Fig. 5.3b shows DFM (Fig. 5.3b-a) and KPFM (Fig. 5.3b-b) images recorded on NaCl : Mg^{2+}. Fig. 5.3b-c and Fig. 5.3b-d are DFM and KPFM images of the dotted area in Fig. 5.3b-a, and Fig. 5.3c is an atomic resolution image of dotted area indicated in Fig. 5.3b-c. Although the structures in Fig. 5.3b-c have the appearance of the pits, 5.3c-a suggests that they are of almost uniform height, so that the feature in Fig. 5.3b-c is the boundary between the Suzuki structure and regular region. Fig. 5.4 shows an example of atomic height polar steps along <110> with the Suzuki structure.

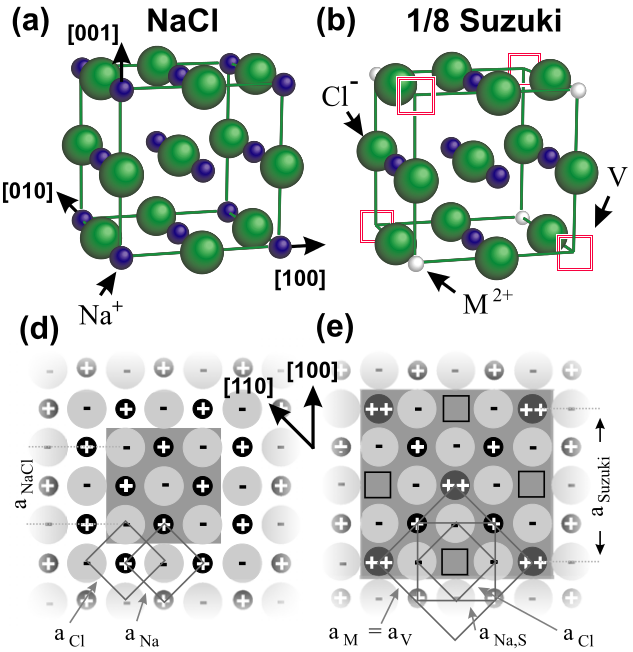

(a)

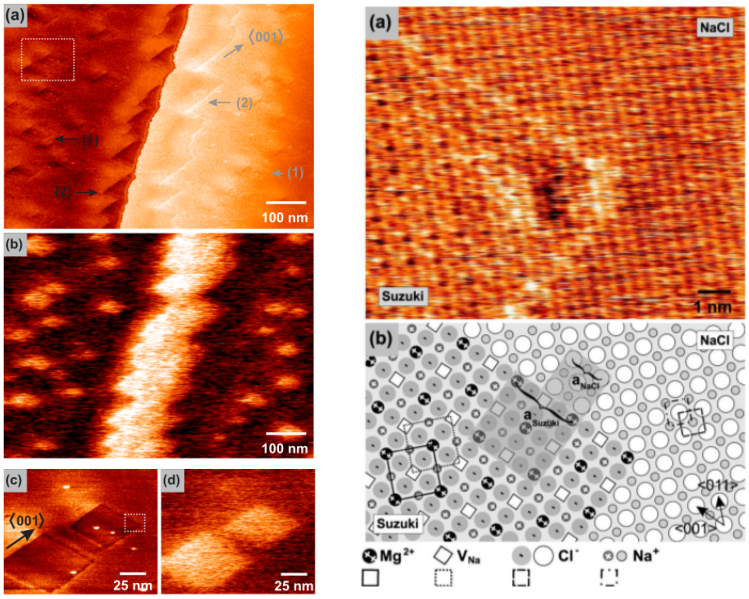

(b) (c)

Figure 5.3: Suzuki structures on ionic surfaces. a) The atomic structure of Suzuki structures [155]. b) Dynamic force microscopy and Kelvin probe force microscopy images of NaCl : Mg^{2+} [156]. c) Atomic resolution of b) [156].

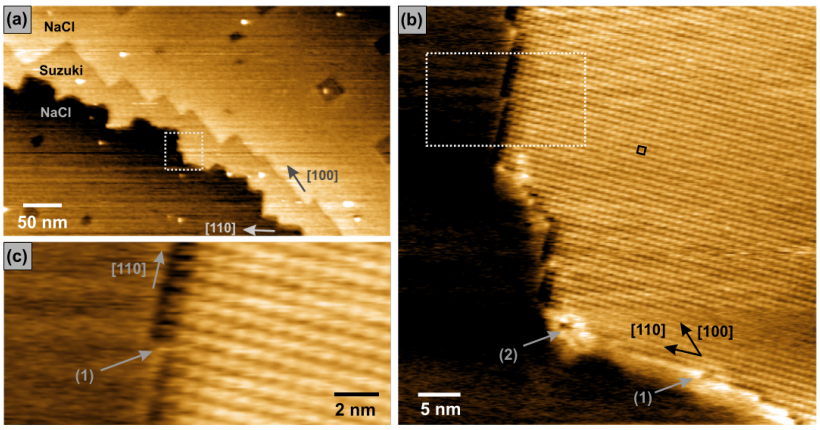

Figure 5.4: Suzuki structures on ionic surfaces. Example of <110> steps on NaCl [155].

Fig. 5.4-a is the topography and Fig. 5.4-b a constant height image taken from the dotted area indicated in Fig. 5.4-a, with Fig. 5.4-c a magnified image of the dotted area in Fig. 5.4-b. Barth and Henry [155] pointed out that the polar steps along <110> occurred not from the cleavage, but from annealing and slowly cooling down the sample. This finding suggested that, surprisingly, the polar steps were energetically favoured, implying that the divalent impurities and cation vacancies had important roles to play in the formation of the polar structures.

Evidence of nanostructures on ionic surfaces can also be found indirectly from experiments that use the nanostructures to absorb molecules. Fig. 5.5a shows non-contact atomic force microscopy (NC-AFM) images of truxene molecules adsorbed on a KBr(001) surface with monolayer steps. The truxene molecule has a length of 21 Å, and Fig. 5.5a-c shows the KBr steps are covered continuously by truxene. Such *et al.* [159] concluded that the separation of the kink sites on the step edges must be 6 K-Br separations. Because the outermost and innermost ion observed in the image in Fig. 5.5a-c are seen to have the same sign, this suggests that the KBr monolayer step lies along [620], with the configuration indicated in Fig. 5.5a-d. Fig. 5.5b shows NC-AFM images of molecules absorbed on the KBr(001) surface. In the right hand panel of Fig. 5.5b, most of the molecules have been removed by manipulation with the AFM tip, leaving only one molecule. This reveals the geometry of KBr step edge: several kink sites forming a polar step.

Nanostructures on ionic surfaces have also been investigated in DFT calculations. Li *et al.* [161] have examined the geometric, energetic and electronic properties of bulk NaCl, the NaCl(001) surface, and steps along <100> and <110> on NaCl(001). According to their find-

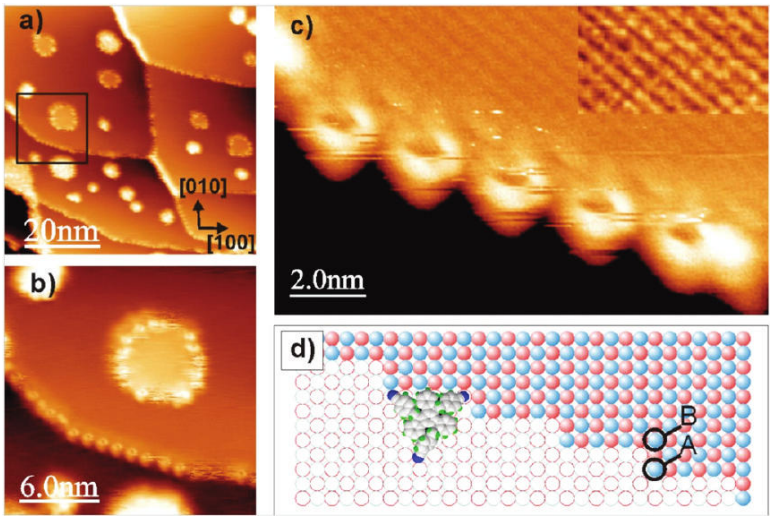

(a)

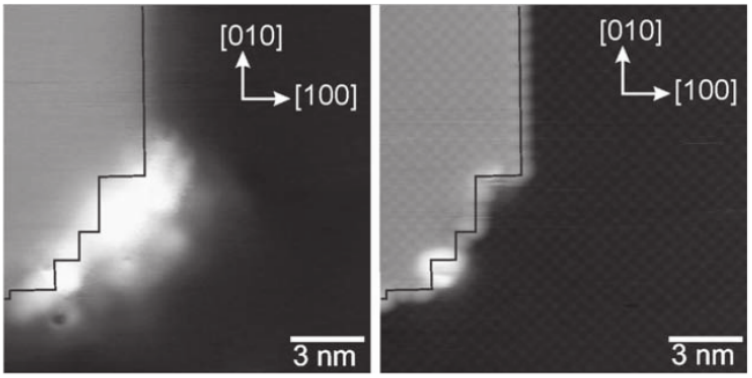

(b)

Figure 5.5: Molecules absorbed on ionic surfaces. a) Non-contact AFM images of truxene molecules adsorbed on KBr(001) surface[159]. b) Non-contact-AFM images of KBr(001) terrace decorated with molecules [160].

ing, steps along <100> are significantly more stable than steps along <110>, and the formation energy of steps along <100> is as small as 40 ~ 60 meV and comparable with step formation energies of noble metals.

In summary, ionic solids cleaved in air or UHV followed by annealing at elevated temperatures for hours result in surface with structures such as pits and steps of atomic depth, which can also be created by electron beam irradiation; increased contrast over the step edge or kinks are observed from atomic resolution DFM images [147–149, 153, 154], with the relaxation of edge atoms [148] and charge defects [150] believed to result in brighter contrast. Both non-polar and polar steps have been observed and polar steps are believed to play an

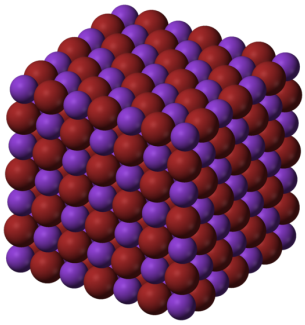

Figure 5.6: A representation of the atomic arrangement of KBr. Different colours represent different elements.

important role in the absorption of molecules and for other functional uses [159, 160]. DFT calculations indicates NaCl steps along <100> are favoured [161], and the presence of divalent impurities and cation vacancies are believed to be the origin of the formation of the polar steps [150]. By intentionally doping with divalent impurities, the Suzuki structures can be formed, and are increasing the number of polar features on surfaces [155–157].

According to this review of the literature and also with the experimental results described in Chapter 1, our focus will be on steps and pits on the KBr(001) surface. Both non-polar and polar steps will be considered. Polar steps formed only from KBr and formed with divalent impurities will be explored. For pits, we will investigate the pits with no kinks, one kink and two kinks. As with the step edges, the kink sites will be treated as just KBr atoms or with divalent impurities with cation vacancies. Relaxation of edge/kink site atoms will be considered, and both mono and bilayer graphene will be overlay onto these nanostructures.

5.2 DFT calculations

In order to understand the more complex systems, we first consider the bulk properties of KBr and mono/bilayer graphene, then the KBr slabs and steps, and finally graphene on nanostructured KBr.

5.2.1 Bulk properties

Bulk KBr

Lattice parameters and the band structure have been calculated to demonstrate the structural and electronic properties of bulk KBr.

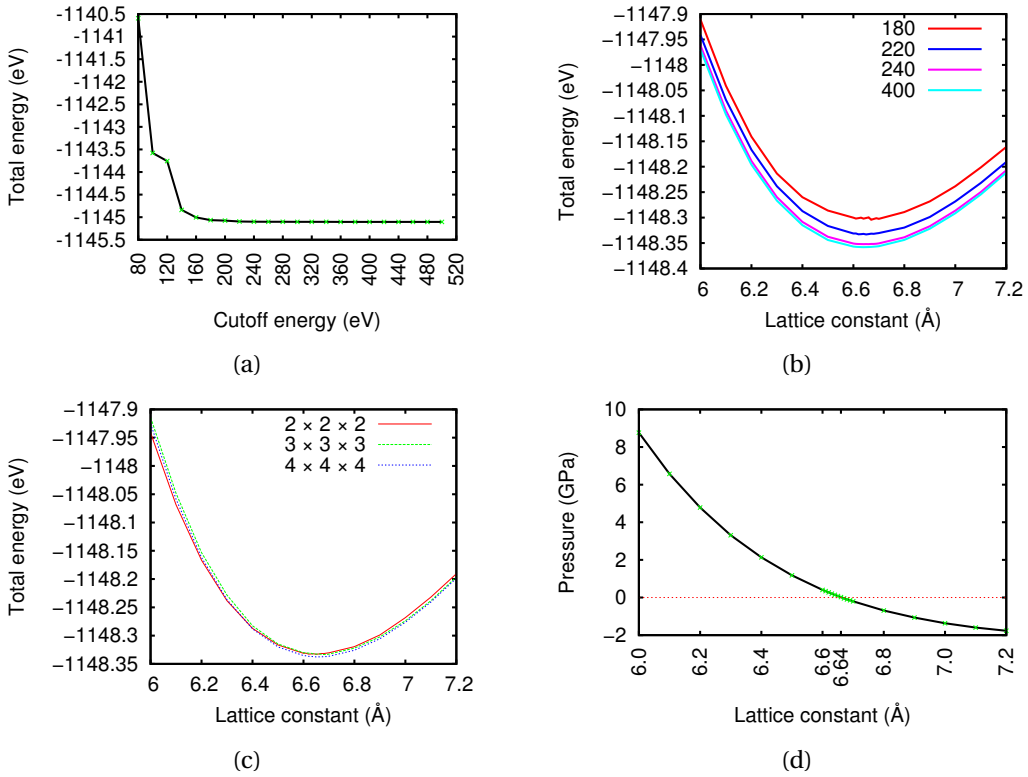

Figure 5.7: Convegence test. a) Cutoff energy versus total energy. b) Lattice constant with different cutoff energies. c) Lattice constant with different k point sampling. d) Total pressure with different lattice constant.

KBr is a salt of sodium chloride type with the structure shown in Fig 5.6. K and Br form interpenetrating face-centred cubic structures. To calculate the lattice constant and band structure, a pseudopotential plane wave method package CASTEP [162] has been used. As mentioned in Chapter 2, the pseudopotential plane-wave method is well developed and the CASTEP package [162] is a widely used implementation. The exchange-correlation functional we choose here is GGA-PBE [97, 146], which is expected to be more accurate than LDA in non-covalent systems. The convergence criteria have been chosen as 0.01 eV/ Å for forces during geometry optimization and 10^{-6} eV/atom for energy. If not mentioned, these two parameters remain the same in this Section. As mentioned in Chapter 2, cutoff energy is a parameter that controls accuracy. In addition, ideally an infinite number of k points is needed to sample the Brillouin zone, but in practice a finite number of k points is used. The Monkhorst-Pack [163] k point sampling scheme is the most widely used, corresponding to a uniform grid in reciprocal space in each direction. Therefore, to monitor the convergence of the total energy and lattice constant, both cutoff energy and k point sampling have been

method	lattice constant (Å)	comment
Experiment [164]	6.60 ± 0.28	X-ray diffraction
HF [165]	6.939	
DFT [166]	6.58	LDA, LCAO
DFT [167]	6.59	LDA, LAPW
DFT [168]	6.60	LDA, LAPW
DFT [169]	6.51	GGA, LCAO
DFT [170]	6.60	LDA, PPW

Table 5.1: KBr lattice obtained by experiments and theoretical calculations. The third column indicates the details of the method.

varied. Firstly, a Monkhorst-Pack [163] k points of $2 \times 2 \times 2$ is used and the cutoff energy varied from 80 eV to 500 eV, separated by 20 eV. Fig. 5.7a shows the relationship between the cutoff energy with total energy, and it is clear that below 160 eV is not acceptable and above 300 eV is sufficient, indicating 300 eV is sufficient for energy calculations. Fig. 5.7b shows the relationship between the cutoff energy with the lattice constant. The cutoff energy of 240 eV converges the lattice parameter to 0.01 Å, indicating 240 eV is sufficient for structural calculations. Then the cutoff energy of 240 eV is used and the k point sampling varied from $2 \times 2 \times 2$ to $4 \times 4 \times 4$. Fig. 5.7c shows that $2 \times 2 \times 2$ converges the lattice parameter to 0.01 Å. From the series of tests, a Monkhorst-Pack k point sampling of $2 \times 2 \times 2$ and cutoff energy of 300 eV is decided.

Finally, we use these parameters to determine the lattice constant. Fig. 5.7d shows the pressure as a function of lattice constant, with 6.64 Å corresponding to zero pressure.

In the literature, experimentally the lattice constant at room temperature is found to be 6.60 ± 0.28 Å [164]. Table 5.1 contains the comparison of results obtained from different levels of theoretical calculations, Hartree-Fock (HF) and DFT, using different exchange-correlation functionals and different basis sets expansion methods, linear combination of atomic orbitals (LCAO), pseudopotential plane wave (PPW) and linearized augmented plane wave (LAPW) methods.

Our value 6.64 Å is with good agreement with both experimental result (6.6 Å [164]) and previous DFT results shown in Table 5.1.

Next we consider the band structure. Fig. 5.8a shows the calculated band structure of KBr and for comparison in Fig.5.8b the bands calculated by Ching *et al.* [171] as given. There is general agreement, although some difference exist at higher energies and particularly be-

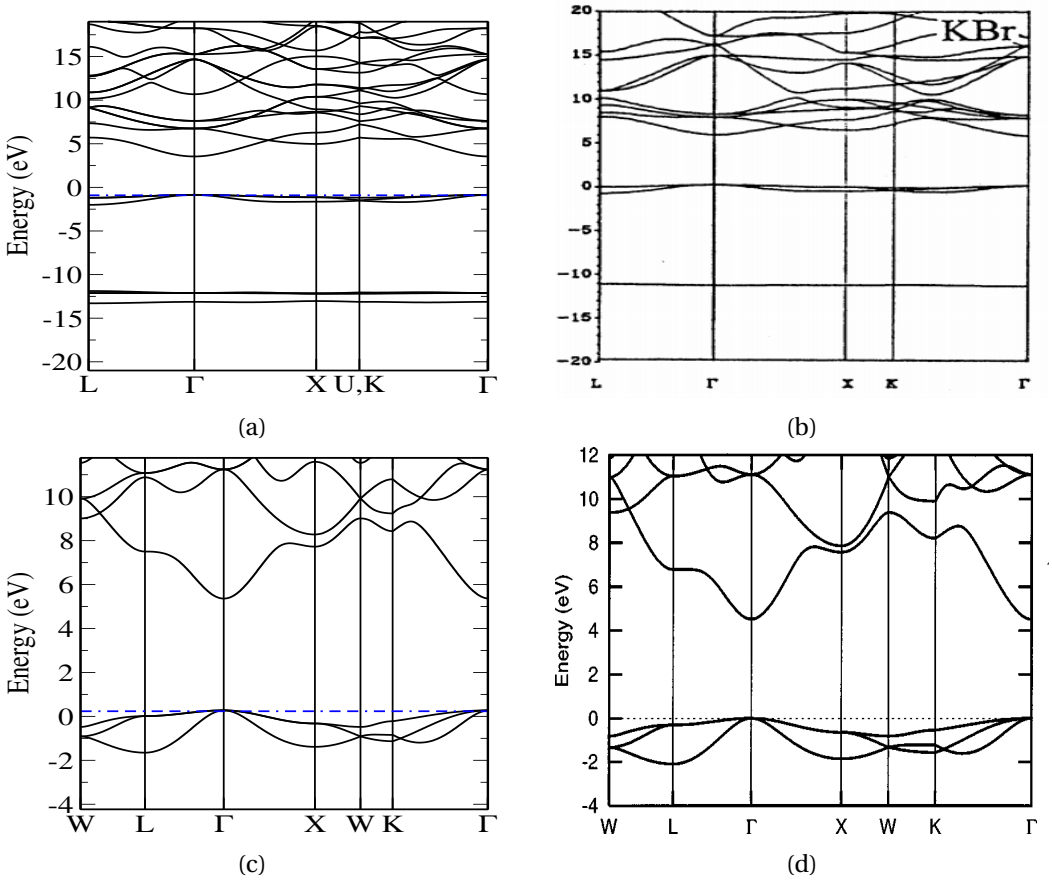

Figure 5.8: Band structure of KBr a) this work; b) LCAO calculation [171]; and NaCl c) this work; d) Pseudopotential plane wave calculation [172]. Blue dash line indicates the Fermi energy.

tween K and Γ, which is assumed to be the restricted basis used in [171]. There are also differences at lower energies because Ching *et al.* [171] treated the Br 4*s* and K 3*p* as core states. The NaCl band structure has been more widely studied, and for this system result calculated (Fig. 5.8c) shows good agreement with other pseudopotential calculations, Fig. 5.8d [172] . This is taken as evidence that the electronic structure calculation is performed correctly.

5.2.2 KBr surface

Now we are in a position to study the properties of the clean KBr surface. The most energetically favourable surfaces are the {001} surfaces [173]. Using the method of the previous section, the pseudopotential used here is GGA-PBE, a cutoff energy of 350 eV and k point

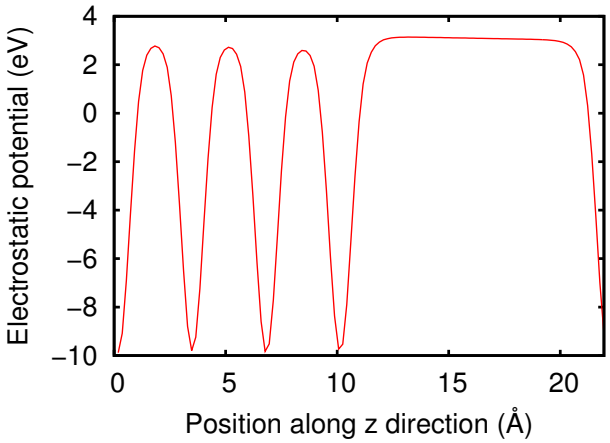

Figure 5.9: Electrostatic potential of 4 layers KBr slab with vacuum gap of 12 Å.

grid of $4 \times 4 \times 1$ has been used to converge the surface atom displacement to 0.01 Å. Since for plane wave pseudopotential calculations, the unit cell must be repeated periodically in three directions, for surface calculations, a thin film is modelled, periodically repeated in the direction normal to the film with a vacuum gap employed to isolate the interaction between the outer layers of adjacent cells. On the other hand, it is impractical to include too large a number of layers in the thin film when modelling a surface, since the calculation time increases rapidly ($\sim N^3$) with the number. Therefore, it is necessary to determine how many layers are required to provide an adequate description of a semi-infinite system. A 20 Å vacuum gap was used which is twice that employed by Li *et al.* [161] in their NaCl surface calculations. Structural relaxations in thin films of 2, 4, 6 and 8 layers of KBr were then calculated, and it was found that beyond 4 layers these were unchanged in the other layers to within 2×10^{-3} Å.

Having established the required thickness of KBr, we return to the the choice of vacuum gap to a value which is both accurate and efficient. Fig. 5.9 shows that for a gap of 12 Å, the electrostatic potential in the vacuum area is constant, indicating a good isolation of the interaction between two vertically neighboured unit cells. By monitoring the surface relaxations, it was identified that these remained unchanged to within 2×10^{-3} Å for gaps down to 12 Å. Therefore a vacuum gap of 12 Å was decided as sufficient for subsequent structures.

There are ways other than employing a large vacuum to eliminate the dipolar interactions between adjacent cells normal to the surface when using periodic boundary conditions, such as adding a sheet of "hydrogen" atoms with a nuclear charge of $Z = 1/2\,|e|$ and an electron charge of $1/2\ e$ to saturate the surface, suggested by Li *et al.* [174]. We have not used

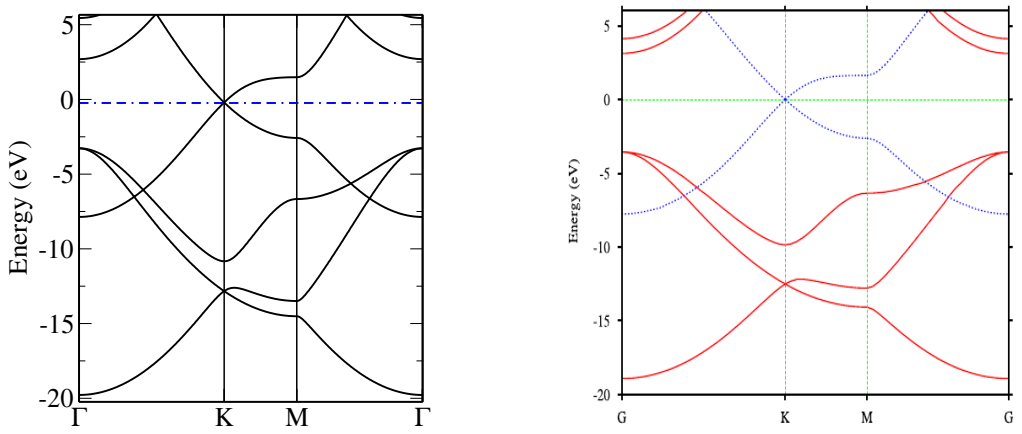

Figure 5.10: Graphene band structure along high symmetry directions. a) This work, blue dashed line indicates the Fermi energy; b) LCAO calculation [178].

this approach in this work.

It is worth noting that the ability to describe the displacements of atoms at the surface is important because they are not negligible. Using x-rays, Kashihara *et al.* [175] reported a 0.4 Å contraction of the outer layer separation at KBr(001). For the top layer, Losch and Niehus [173] reported that K ions moved inward by 0.5 Å and Br moved inward by 0.3 Å using impact collision atom scattering spectroscopy with detection of neutrals (NICASS). However, Vogt and Weiss [176] using low energy electron diffraction (LEED) found that K moved in about 0.05 Å and Br moved outward by the same amount. Although these studies identified the opposite displacements of K and Br, the rumpling they found are similar (0.1 ~ 0.2 Å). Our calculations indicate that K moves inward by 0.05 Å and Br moves outward by 0.05 Å in the top layer, corresponding to a rumpling of 0.1 Å. It is found that in good agreement with the mentioned experiments, and in very good agreement with Vogt and Weiss [176]. And for the upper layer, K moved outward less than 0.02 Å and Br moved inward about 0.02 Å.

Finally, the work function is another key surface property. The work function of KBr slab can be determined from Fig. 5.9, with $W_F = V_{pot} - E_F$, where E_F is the Fermi energy and V_{pot} is the vacuum potential far from the surface. This gives a calculated work function for KBr of 4.19 eV, in good agreement with previous DFT results 4.47 eV [169] and experiment 4.2 ±0.2 eV [177] obtained from Knudsen effusion mass spectrometry.

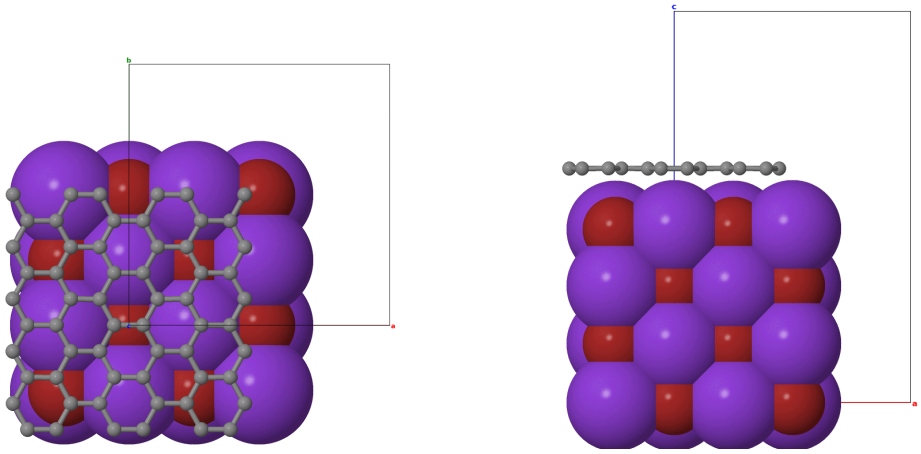

(a) (b)

Figure 5.11: Geometry of distorted graphene on KBr (001) surface (left: top view; right: side view). Grey atoms are graphene atoms and blue (red) atoms are the K (Br) atoms. Black box is the unit cell.

5.2.3 Graphene

We now consider the lattice parameter and electronic properties of monolayer graphene. Using the method presented in previous sections, a lattice constant of 2.46 Å is found using a cutoff energy of 280 eV, $4 \times 4 \times 1$ k point sampling and a vacuum of 12 Å. This convergences to < 0.01 Å. This result is in good agreement with the experimental value 2.46 Å [124]. The work function is found to be 4.31 eV, which is in agreement with the value 4.57 ± 0.05 eV obtained experimentally from Kelvin probe microscopy [179] and a DFT calculation result $4.55 \sim 4.60$ eV using GGA-PW91 functionals [180]. Fig. 5.10 shows the comparison of band structure from our result (Fig. 5.10a) and that found by Boukhvalov *et al.* [178] who used GGA-PBE in DFT calculations (Fig. 5.10b). The linear dispersion around the K point are shown clearly. The dotted lines in Fig 5.10b are the π bands and the solid lines are the σ bands.

These results indicate CASTEP with the stated parameters gives a good account of the electronic and structural properties of graphene.

5.2.4 Graphene on clean KBr surface

Now we consider the interaction between graphene and the KBr (001) surface. Graphene has a hexagonal lattice and KBr(001) has a square one, so it is necessary to distort one of them in order to use the periodic plane wave codes. In this section we choose to distort

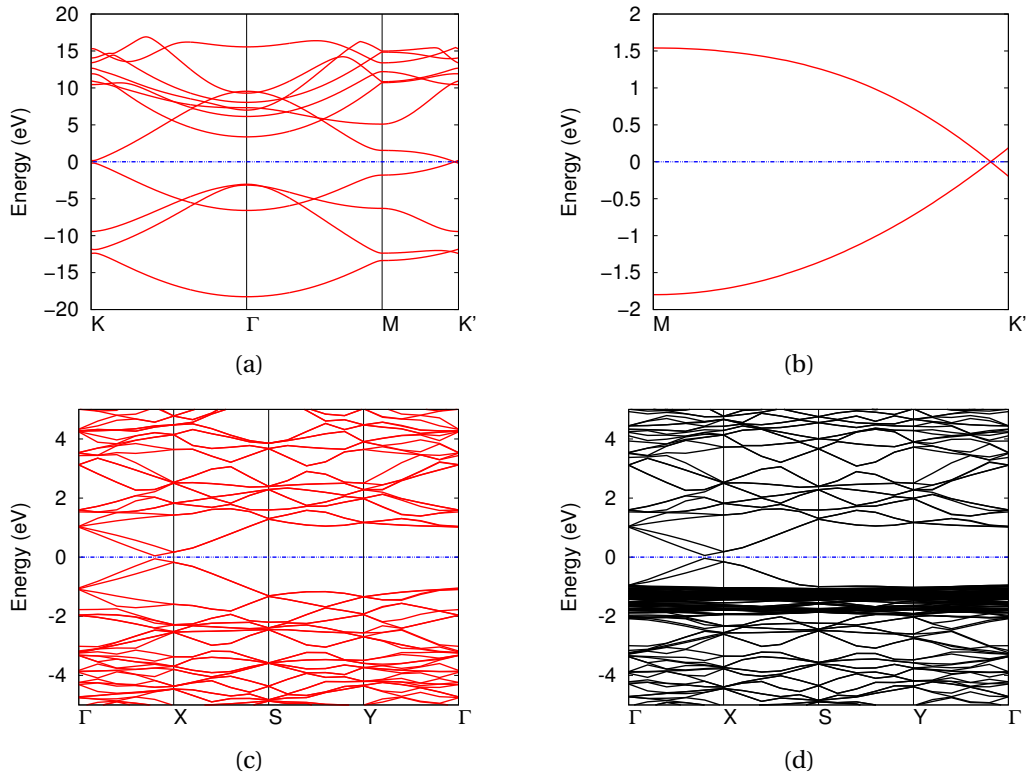

Figure 5.12: Band structure of distorted graphene a) along high symmetry direction of graphene; c) along high symmetry directions of KBr (001) and d) distorted graphene on KBr (001) surface, blue dashed line indicates the Fermi energy. b) is the zoom in of a).

graphene because it costs less energy to distort monolayer graphene than a semi-infinite KBr crystal. Fig. 5.11 shows the geometry of the distorted graphene on the KBr (001) surface, where the KBr (001) surface is in a (2× 2) supercell. Graphene has been distorted by 4% (8%) in the x (y) direction. The total area is enlarged by 12%. Distorted graphene may exhibit different electronic structure, although Choi *et al.* [181] have observed previously that no energy gap occurs with strains of up to 30%. To verify this, a band structure calculation of distorted monolayer graphene has been performed. Fig. 5.12a and Fig. 5.12b shows that the linear dispersion around K points has been preserved, the Dirac point is shifted towards M. This is consistent with Pereira *et al.* [16] and Gui *et al.* [182], who they report that the Dirac point and Fermi energy can shift with asymmetric stretching of graphene.

After a full geometry relaxation of the whole system, the graphene is found to sit at 3.40 Å above the KBr surface. Note that, 3.40 Å is in the van der Waals interaction range, so that extra validation is needed because the GGA lacks a mechanism to properly describe the van der Waals interactions. To investigate this, the position of the graphene plane has been

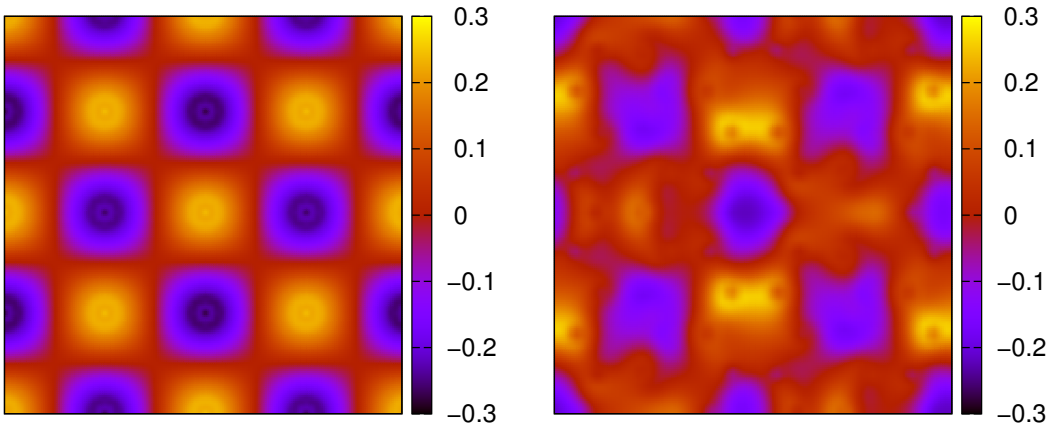

(a) (b)

Figure 5.13: Variation in the electrostatic potential calculated 3.40 Å above the KBr (001) surface of a) clean surface; b) difference between the whole system and the sum of graphene-only and slab-only.

manually shifted by ± 0.05 Å, and the energy bands calculated accordingly. It is found that the band structure near the Fermi level remain similar, so it is concluded that the distance between graphene and KBr in this range doesn't change the electronic properties near the Fermi level significantly.

Fig. 5.12d shows the band structure of distorted graphene on KBr (001) with a separation of 3.40 Å. The band structure of isolated distorted graphene has been also calculated along the high symmetry directions of the whole system, in order to have a direct comparison. Fig. 5.12c is the band structure of the same system as that in Fig. 5.12a, but along the high symmetry directions of KBr (001) surface. Note that these directions are not the high symmetry directions of graphene, therefore the Dirac points are not included and the linear dispersion around the Dirac points will not be shown in Fig. 5.12c. Comparing Fig. 5.12c and Fig. 5.12d, we can see that the bands near the Fermi energy remain unchanged and there are no KBr bands near the Fermi level, which indicates that around the Fermi level, putting the monolayer graphene on KBr (001) surface will not change its electronic structures.

Because the electrostatic potential is of our interest, we also examine this aspect of the system. In order to understand the effect of the electrostatic potential of KBr (001) surface in the graphene sheet, we calculate and compare the electrostatic potential of isolated graphene (will be referred as "graphene-only"), the clean KBr (001) surface (will be referred as "slab-only") and the graphene on KBr (001) system (will be referred as "whole"). The variation in the electrostatic potential found at 3.40 Å above the KBr (001) surface is shown

in Fig. 5.13a. Average value has been set to zero. This potential is the external potential graphene will feel if we introduce graphene into the system at this height. The potential alternates due to the alternating arrangement of the charged ions in KBr, with an amplitude of ±0.3 eV. With the graphene overlying on the KBr (001) at the height of 3.40 Å, this potential will cause the in plane redistribution of the electrons in the graphene layer and form an induced potential. In order to understand this effect, induced potential in graphene sheet is calculated as the potential difference of the whole system and the sum of graphene-only and slab-only: $V_{\text{whole}} - (V_{\text{graphene-only}} + V_{\text{slab-only}})$, shown in Fig. 5.13b. We can see that the signature of KBr lattice remains. At the same locations, slab-only potential and the induced potential has the opposite sign, which indicates that the redistribution of the electrons in graphene screen out the external potential. The amplitude of the induced potential is found to be ±0.25 eV. Now we introduce the screening factor F_{screen} as the ratio of the induced potential V_{ind} and the external potentialV_{ext} ,

$$F_{\text{screen}} = \frac{|V_{\text{ind}}|}{|V_{\text{ext}}|}. \tag{5.1}$$

Therefore, in this case, the screening factor is 0.83, meaning 83% of the external potential has been screened out.

5.2.5 KBr steps

We now consider steps on the KBr (001) surface. As mentioned in the Section 5.1, there are two kinds of steps on ionic crystal surfaces observed in experiment, non-polar steps which lie along <100>, and polar steps which are along other directions. In the absence of other defects, Li *et al.* [161] have shown that the non-polar steps are energetically favoured. We therefore begin by considering the non-polar steps.

Non-polar steps

The configuration of non-polar steps along <100> is shown in Fig. 5.14a (top view) and Fig. 5.14b (front view). A $4 \times 4 \times 1$ supercell is shown here for better visualization. Unless otherwise stated, this will be used throughout this Chapter. In order to describe an isolated step, a terrace width no less than 4 K-Br spacing and a step-step separation no less than 8 K-Br spacing are needed, so that the electrostatic potential of the center region of the upper and lower terrace mimic that of the clean KBr (001) surface better than 0.01 eV. We chose the smallest system that is able to describe an isolated step. Previously it was established that graphene sits 3.40 Å above the KBr (001) clean surface. Therefore, the electrostatic potential at this height above the upper terrace is calculated and shown in Fig. 5.14c. Except for di-

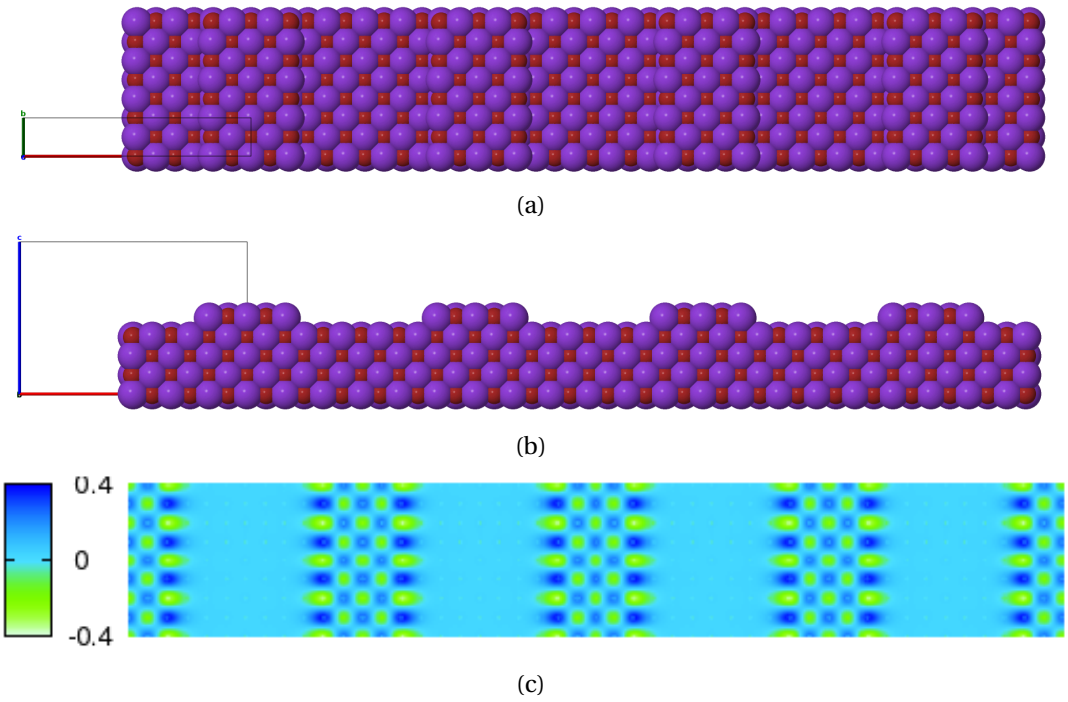

Figure 5.14: Configurations of non-polar steps on KBr (001). a) Top view; b) Front view; c) Electrostatic potential map (eV) at 3.40 Å above the step of non-polar steps. Blue (red) atoms are K (Br) atoms, black box showed the unit cell.

rectly at the step edges, the electrostatic potential on the terraces is similar to that above the clean surface, whilst it is significantly lower in regions above the lower terrace. At the step edge, comparison with Fig. 5.13a shows that the electrostatic potential at non-polar steps exhibits an enhancement of $\pm 0.1eV$. Even if the screen factor is 0, this value is still smaller than the 0.25 eV potential variation observed in the experiment [77]. This indicates that non-polar steps are unlikely to be the source of the significantly brighter contrast observed in the experimental results described in Chapter 1 [77] and Section 5.1 [150, 156].

Polar steps

Although the KBr surface has been widely studied experimentally, little is known about the actual configuration of the polar steps on the surface. As previously illustrated in Fig. 5.5a, Such *et al.* [159] have observed and the polar steps which they identified as being along the [620] direction. A 4-layer KBr surface with [620] steps separated by 12 K-Br spacing is a huge system containing several hundred atoms. We therefore perform a model calculation to gain some understanding of the electrostatic potential first. In this model, we treat the K and Br

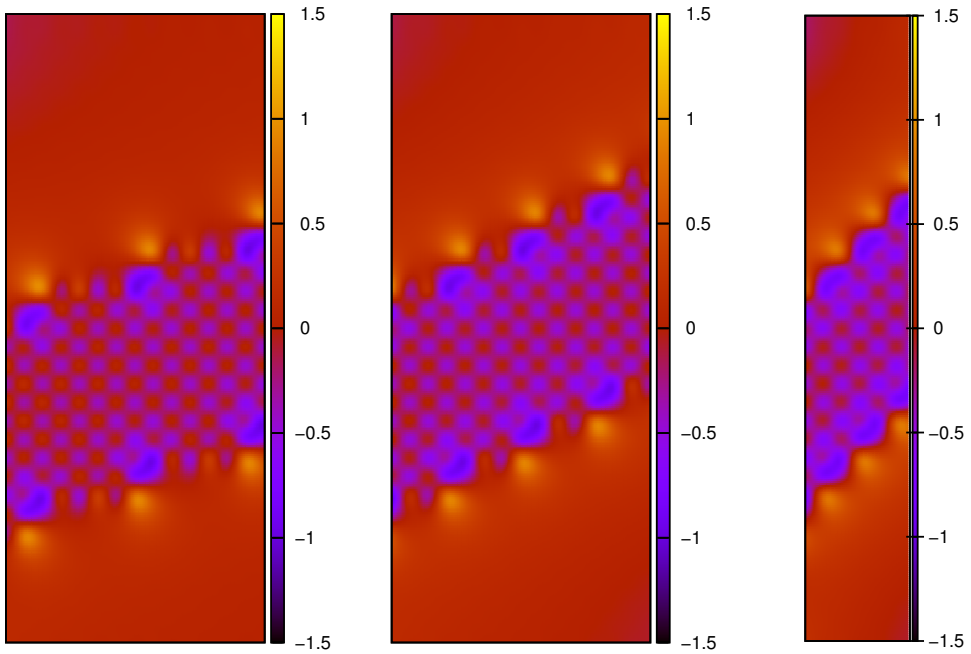

Figure 5.15: Electrostatic potential (eV) in a plane 3.40 Å above the point charge surface modelling the KBr (001) with a) [620] steps; b) [420] steps; c) [220] steps. The vertical range displaced is in 80 Å.

atoms as point charges with $\pm e$, located at the atomic sites of the crystal. The electrostatic potential at $\mathbf{r}$ is given by

$$V(\mathbf{r}) = \sum_i \frac{q_i}{4\pi\epsilon|\mathbf{r}-\mathbf{r}_i|} \tag{5.2}$$

where $\mathbf{r}_i$ is the position of charge q_i. Systems with [620] steps, [440] steps, and [220] steps have been considered. Fig 5.15 shows the electrostatic potential evaluated in a plane 3.40 Å above the point charge surface obtained using Eq. 5.2 for each of these systems. The potential variation with vicinity of the steps is as large as ±1.5 eV in [620], [420] and [220] cases. At the step edge, [220] steps showing a similar electrostatic potential as at [620] steps, but having 1/3 the number of atoms as that of [620] system, is adopted for further study. These calculations were also repeated using just 2 layers of KBr, the electrostatic potential differed from that found with 4 layers by less than 3×10^{-3} eV.

As was done for the non-polar steps, the effect of varying separation of the terrace width has been studied. Fig 5.16 shows the electrostatic potential found for above systems of varying the upper terrace width of 6, 12, 18 and 24 K-Br spacing calculated along the line of greatest

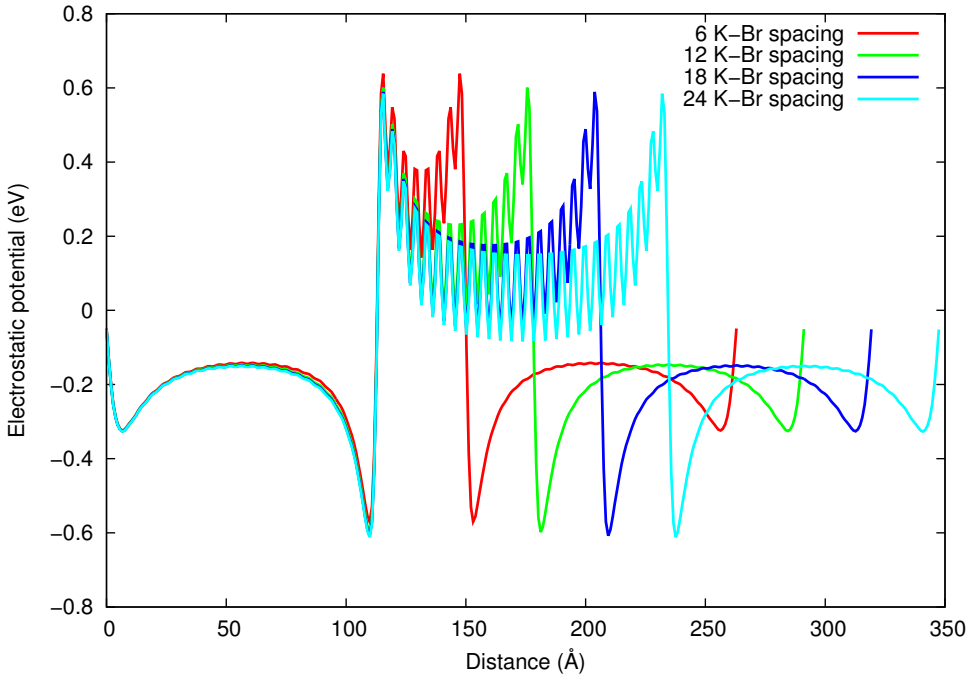

Figure 5.16: Electrostatic potential 3.40 Å above [220] polar steps for various upper terrace widths.

potential variation. The general native of the electrostatic potential variation is established when the upper terrace width is 12 K-Br spacing or above, so this value (~ 40 Å) was chosen for subsequent calculations. A similar analysis of the effect of varying the lower terrace width showed 6 K-Br spacing (~ 20 Å) was sufficient.

5.2.6 Graphene on stepped KBr

After gained an understanding of the stepped KBr (001) surface, we now put a monolayer of graphene on it. To make this calculation manageable, we model the KBr surface using point charges, calculated from the 2 layers model. The configuration of the point charges modelling KBr surface was not relaxed in this calculation. These calculations have been performed using the DFT package CRYSTAL [142], due to its ability to include point charges. Unlike in the previous section, here, we distort the KBr instead of graphene. Since distorted graphene shows slightly different electronic structures (as shown in Fig. 5.12d) and graphene is our primary interest.

The geometry of the system studied is illustrated in Fig. 5.17a (top view) and Fig. 5.17b (front view), and the upper layer of the stepped surface is shown in Fig. 5.17c. The substrate has been distorted by 8% in the direction perpendicular to the step edge and 5% in the di-

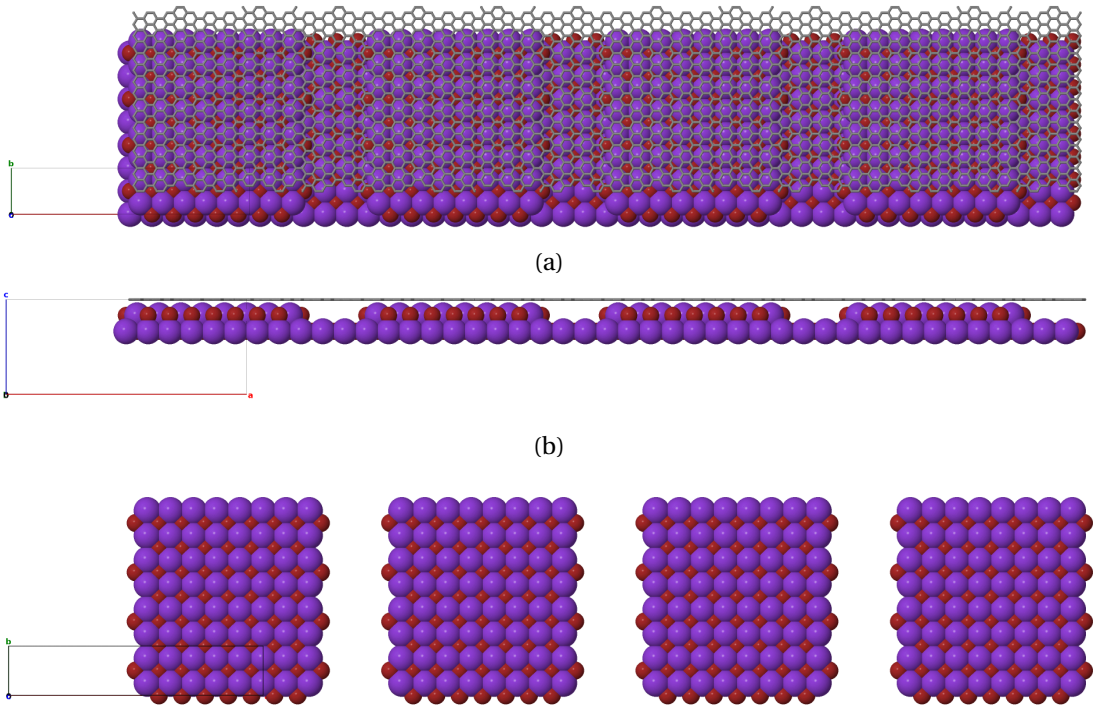

(a)

(b)

(c)

Figure 5.17: Configuration of monolayer graphene above a KBr (001) surface with [220] steps. a) Top view; b) Front view; c) Upper layer of the stepped surface. Blue (red) atoms are K (Br) atoms, and black box shows the unit cell.

rection parallel to the step edge. The width of the lower terrace is 18.8 Å and the width of the upper terrace is 37.6 Å.

The electrostatic potential difference calculated between graphene on stepped KBr (001) and isolated graphene in the graphene plane is shown in Fig 5.18. Fig. 5.18a shows the potential map of the system illustrated in Fig. 5.17 and Fig. 5.18b is that of a system with larger lower terrace width (28.2 Å) and upper terrace width (75.1 Å). They both show an amplitude of ±0.2 eV of the variation in electrostatic potential, and the potential with largest amplitude are confined around the step edges. The systems with the size in between this two also show similar properties of electrostatic potential. Fig. 5.18c shows the line plot across the steps of Fig. 5.18b, black line is the average, and the red (blue) line is the potential taken across the steps on top of Br (K) atoms (which is negative or positive charges here). The potential variation is 0.30 eV on the step edge, and 0.11 eV on the upper terrace. On the upper terrace, the value 0.11 eV agrees with the the result ±0.05 eV of clean slab calculation.

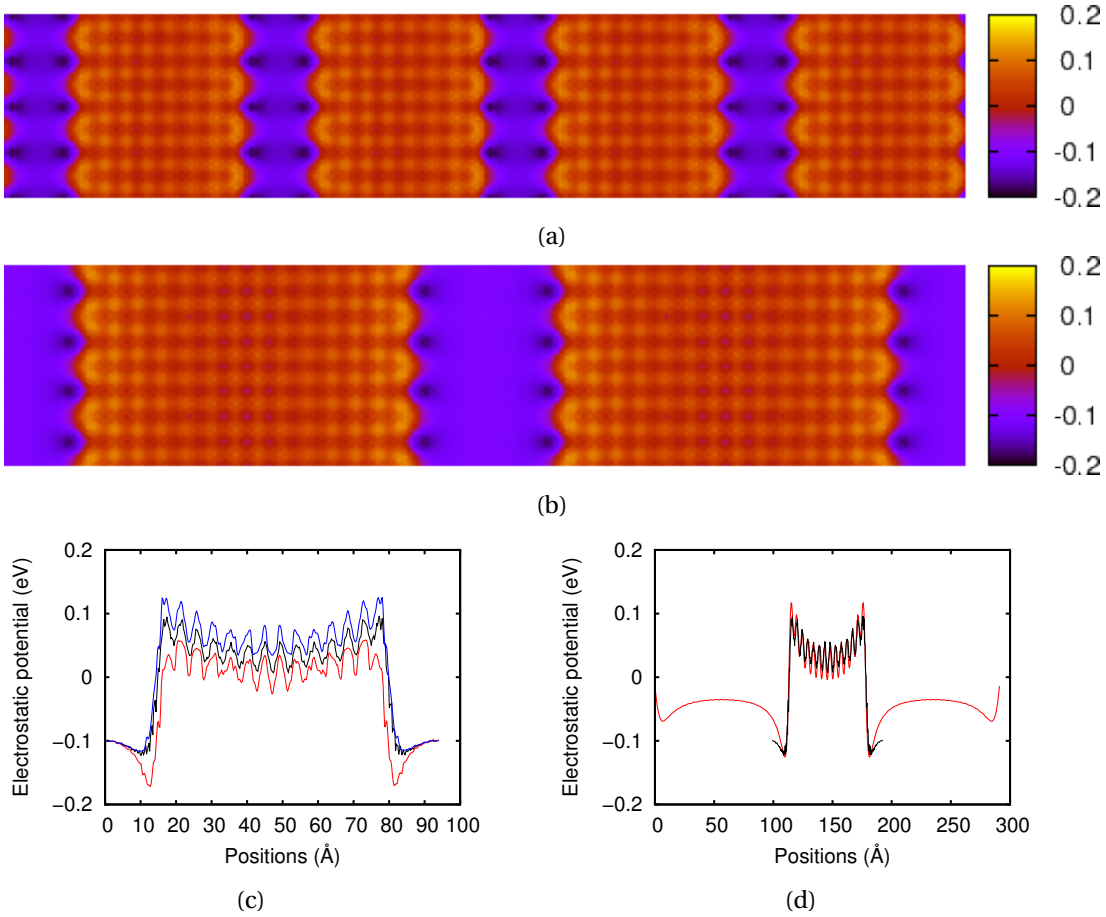

Figure 5.18: Electrostatic potential (eV) calculated in graphene plane of monolayer graphene on KBr (001) surface with [220] steps of a system with a) upper terrace width of 37.6 Å; b) upper terrace width of 75.1 Å. c) Electrostatic potential calculated along lines of b), black indicate the average, red is the line on top of Br atoms, blue is on top of K atoms. d) Comparison of the fractioned external potential (red) and the average potential in c) (black).

Now we consider the screening factor of this system. As shown in Fig. 5.18d, the red line is the electrostatic potential due to the point charges at the heightof 3.40 Å with a fraction of 1/5, and the black line is the average potential of Fig. 5.18c. We can see that the shape fit very well, so that the external potential has been screened out 4/5 due to the present of monolayer graphene. Therefore, the screening factor of this system is $F_{\text{screen}} = 0.8$, which is also agree with the screening factor of the clean KBr (001) surface.

5.2.7 Conclusions from DFT results

From the DFT result, we have obtained several benchmarks. Firstly, we obtained the KBr lattice constant 6.64 Å and the graphene lattice constant 1.42 Å; secondly, we learned that monolayer graphene sits 3.4 Å above the KBr (001) surface; thirdly, we acquired that 4 layer is enough to properly describe structural properties of a semi-infinite slab and 2 layer is enough to describe the electrostatic potential; fourthly, a lower terrace width no less than 20 Å and a upper terrace width no less than 40 Å is needed to describe the electrostatic potential of an isolated step; fifthly, the screening factor obtained using DFT is around 0.8 of both the clean KBr (001) surface and that surface with [220] steps; finally, KBr (001) surface with [220] steps can result in 0.3 eV electrostatic potential variation in the vicinity of the step edge on the monolayer graphene sheet.

However, we also realise that because of the cost to perform DFT calculations, there are further possibilities that are too expensive to calculate using DFT, such as registry of graphene and the substrate, the system with bilayer graphene, the other nanostructures with less periodicity, such as pits and the divalent impurities and cation vacancy pair. Therefore, we will employ semi-empirical methods to explore these possibilities.

5.3 DFTB calculations

Because the computational expensive of DFT calculations for very large systems, in this section we use the semi-empirical SCC-DFTB and SCCD-DFTB methods to investigate the electrostatic potential variation and electronic structures of monolayer and bilayer graphene on KBr (001) with various nanostructures. The nanostructures include [220] polar steps, [220] polar steps with divalent impurity and cation vacancy pair, pits with no kinks, pits with two kinks and pits with one kink which includes the divalent impurity and cation vacancy pair. We will also explore the registry of the graphene and the substrate, and investigate the effect of the displacement of the step edge atoms.

As with the DFT calculations described in Section 5.2.6, we continue to use 2 layers of point charges to model the KBr (001) surface with nanostructures, and the monolayer (or lower layer of the bilayer) graphene is placed at 3.40 Å above the surface. In order to perform calculations which require periodicity, we distort the substrate to construct the supercells. For the case of the steps, we distort the substrate -5% (-8%) in the direction perpendicular (parallel) to the step edges; for the case of pits, we distort the substrate -4% (-1%) in the direction align with armchair (zigzag) direction of graphene. The vacuum normal to the surface is fixed at 500 Å. All SCC-/SCCD-DFTB calculations are performed with the position of

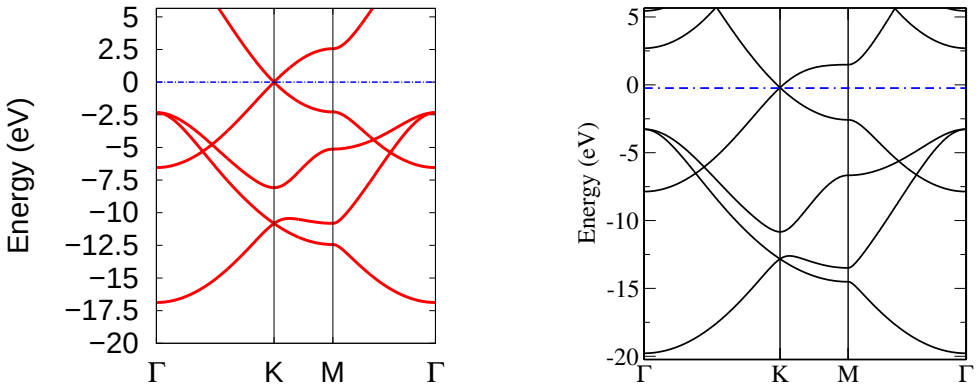

Figure 5.19: Comparison of calculated band structures of monolayer graphene. Left: this work, SCC-/SCCD-DFTB. Right: this work, DFT. The blue dashed lines indicate the Fermi level.

the atoms and point charges fixed. The Slater-Koster parametrisation used for the Carbon-Carbon atom pair are those referred to as 'pbc-0-1' [113] in the DFTB community. For all systems, the k point samplings are chosen to be equivalent to a $72 \times 72 \times 1$ ($576 \times 576 \times 1$) sampling of the Brillouin zone of ideal graphene when calculating the total energy (local density of states). For example, if the lattice vectors for a system is $\{\mathbf{a}_1, \mathbf{a}_2, \mathbf{a}_3\}$, the k point sampling for a total energy calculation is $\lceil \frac{|\mathbf{a}_1| \times 72}{2.46} \rceil \times \lceil \frac{|\mathbf{a}_2| \times 72}{2.46} \rceil \times 1$ [1].

5.3.1 Monolayer graphene on KBr(001) surface with nanostructures

We begin with the structural and electronic properties of monolayer graphene obtained by DFTB. As mentioned in Chapter 4, the lattice constant of monolayer graphene predicted by SCC-DFTB is 2.46 Å, in very good agreement with experimental results [124] and the DFT-CASTEP result reported in the previous section. Fig. 5.19 shows a comparison of the calculated band structures of monolayer graphene using SCC-/SCCD-DFTB (left) and DFT-CASTEP (right). The bands around the Fermi level in the vicinity of the K point are in good agreement, while the bands in the high energy range can be seen to differ. This can be attributed to the fact that the DFTB methods use minimal basis set, while DFT-CASTEP uses a more complicated basis set. For the π bands, in the ± 3 eV range which is the range of our main interest, the DFTB results are in satisfactory agreement with the more sophisticated DFT results.

Next we consider monolayer graphene on the KBr(001) surface with steps.

Firstly, we consider monolayer graphene on the KBr(001) surface with [220] steps using the

[1] $\lceil x \rceil$ means the integer no less than x

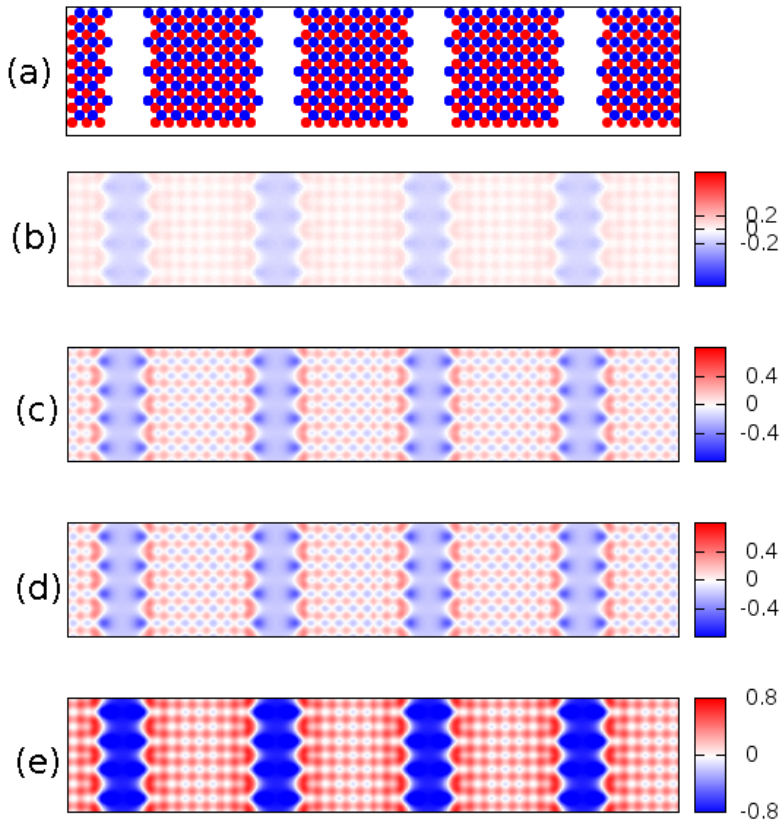

Figure 5.20: Configuration and electrostatic potential (eV) of monolayer graphene on KBr (001) with [220] steps. a) Configuration of the upper terrace of the steps. Calculated electrostatic potential from b) DFT-LCAO; c) SCC-DFTB; d) SCCD-DFTB. e) External potential at the height of graphene plane. The red (blue) discs indicate K (Br) atoms.

same system as that in Section 5.2.6, in order to gain directly comparison of the calculated electrostatic potential between DFTB methods and DFT-LCAO method. Fig. 5.20 shows the electrostatic potential in the graphene plane obtained from DFT-LCAO (Fig. 5.20b), SCC-DFTB (Fig. 5.20c) and SCCD-DFTB (Fig. 5.20d) calculations. It can be seen that the difference between SCC-DFTB and SCCD-DFTB are negligible, both predicting a potential variation of 0.8 eV, suggesting a screening factor of 0.5. The DFT-LCAO result shows a variation of just 0.3 eV, a screening factor 0.8. Fig. 5.21 shows the average induced electrostatic potential along y direction of the system discussed in Fig. 5.20. In order to compare with the results from SCC (red line) and SCCD-DFTB (green line), results from DFT (blue line) has been multiplied by a factor of 0.6. Although the error is not strictly multiplicative, it can

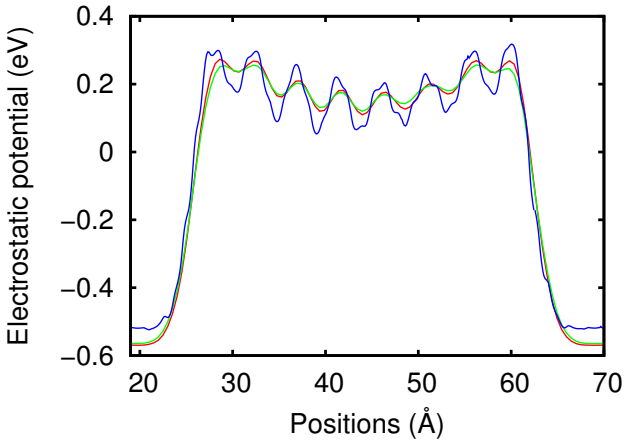

Figure 5.21: Comparison of the induced electrostatic potential (eV) of monolayer graphene on KBr (001) with [220] steps obtained from DFT and DFTB methods, averaged along y direction. Blue line is the result from DFT multiplied by a factor of 0.6, red (green) line is the result from SCC-DFTB (SCCD-DFTB).

still be found that SCC and SCCD-DFTB methods systematically underestimate the screening effect, indicating that less sophisticated DFTB methods can be used to gain a qualitative understandings.

In order to understand the effect of the electrostatic potential variations on the electronic structure of the graphene, we consider the local density of states (LDOS) of selected graphene atoms, shown in the left panel of Fig. 5.23. The chosen atoms are those located in the regions with the largest potential variations. Slight electron/hole symmetry breaking is shown, and shallow peaks at $\pm$ 0.2 eV can be seen. However, the peaks are not as pronounced as the peaks which are observed in experiments (see Section 1.3, Fig. 1.7).

As mentioned in Section 5.1, Barth and Henry [155] suggested that divalent impurity and cation vacancy pair on the edge of nanostructures can be important for the origin of sizeable electrostatic potential variations and the change of the electronic structures. Since the [220] steps have not given as pronounced peaks in the LDOS as observed in the experiments, next we consider [220] steps with divalent impurity and cation vacancy pair. From now on, [220] steps with divalent impurity and cation vacancy pair will be referred as [220] : 2^+ for short. The calculations are performed using SCC-DFTB.

For easy visualization and comparison with the [220] steps case, the configuration of the upper terrace of both [220] steps (first row) and [220]:2^+ steps (second row) are shown in

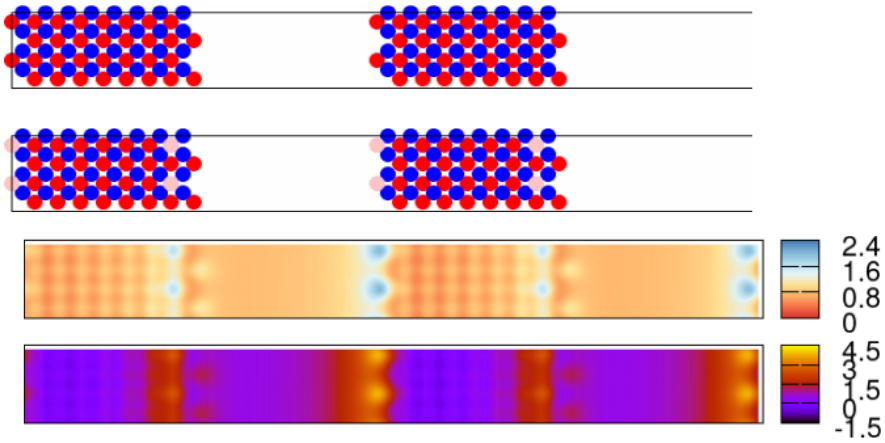

Figure 5.22: Configuration and electrostatic potential (eV) of monolayer graphene on KBr (001) with [220] or [220]:2^+ steps. First (second) row shows the configuration of the upper terrace of the [220] ([220]:2^+) steps. The red, blue and pink discs indicate K, Br and divalent atoms, respectively. The third row is the calculated electrostatic potential in the graphene plane for the [220]:2^+ case. The fourth row is the external potential at the height of graphene plane.

Fig. 5.22. The red, blue and pink discs indicate the K, Br and divalent impurities, respectively. The cation vacancy is construct by removing the nearest K atom on the lower layer. The upper terrace width is 42.3 Å and the lower terrace width is 36.6 Å. The panel on the third row is the calculated electrostatic potential in the graphene plane of the [220]:2^+ case, while the fourth row is the external potential at the height of graphene plane. It can be seen that the largest potential variation of 1.8 eV, is confined to the vicinity of the divalent impurities on the step edges, the divalent impurities surrounded by K and Br atoms having lower potential variations of 1.4 eV. 60 % of the external potential has been screened out, which is consistent with the screening seen in the case of the [220] step. The [220]:2^+ system creates a potential variation in the graphene plane 2.25 times that of the [220] step system, indicating [220]:2^+ system is more likely to be the configuration to introduce sizeable surface electrostatic potential variations.

For the electronic structures, the right panel of Fig. 5.23 shows the LDOS of selected graphene atoms of the [220]:2^+ steps system. The chosen atoms are those located in the regions with the largest potential variations. The electron/hole symmetry breaking is larger than the [220] steps system, and the peaks at ± 0.4 eV are also more visible than the [220] steps system. Accompanying larger electrostatic potential variation, [220]:2^+ steps system showed more pronounced peaks in the LDOS, indicating [220]:2^+ system is more likely to be the configuration to introduce pronounced changes in the electronic structures which is ob-

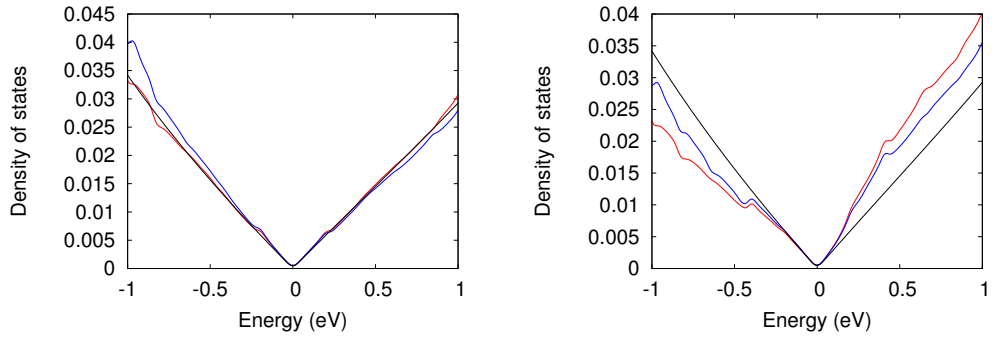

Figure 5.23: Calculated LDOS of the selected graphene atoms, of the monolayer graphene on KBr(001) surface with [220] steps (left) or [220] : 2^+ (right). The blue and red lines indicate different graphene atoms; the black lines are the LDOS of pure monolayer graphene.

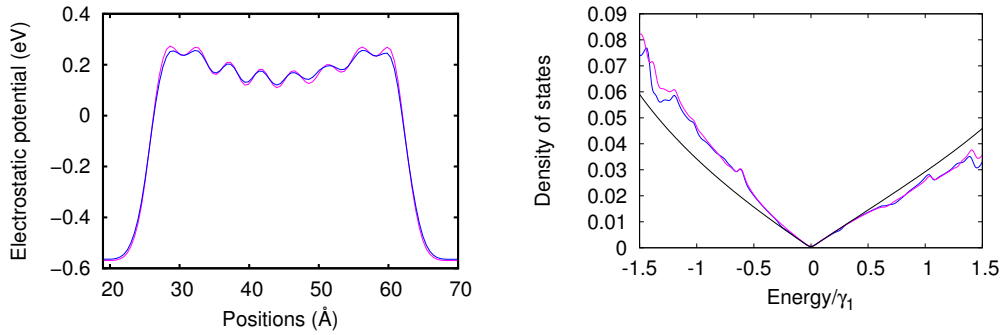

Figure 5.24: Comparison of results from SCC (purple line) and SCCD-DFTB (blue line). a) Average induced electrostatic potential along y direction of monolayer graphene on KBr(001) surface with [220] steps; b) LDOS of graphene on KBr (001) surface with pits with no kinks. Black line is the LDOS for pure monolayer graphene.

served in the experiments. However, no peaks are seen within ±0.1 eV window where they are observed in experiments. The system used in experiments shown in Section 1.3 was believed to be dominated by bilayer graphene, and ±0.1 eV energy window is essential for bilayer graphene because the dispersion is different within the hopping energy range. To gain the understanding of the experimental results, in the next section we will consider the bilayer graphene.

Calculations from SCC and SCCD-DFTB method on these systems show no significant difference in the predicted electrostatic potential or resulting electronic structure of graphene on the nanostructured substrates, as shown in Fig. 5.24. Fig. 5.24a) shows that the difference of induced electrostatic potential is smaller than 0.02 eV; Fig. 5.24b) shows the difference of the dispersion within [-γ_1,+γ_1] is negligible. However, the SCCD-DFTB calculations prove

to be slower to perform (this is believed to be due to the technical issues with the Broyden accelerator). Since bilayer graphene has twice as many atoms as does monolayer graphene, it was decided to use SCC-DFTB to perform calculations on the bilayer systems.

5.3.2 Bilayer graphene on nanostructured KBr(001)

Now we consider the effect on bilayer graphene of positioning it above a KBr(001) surface with various nanostructures. First we discuss the bilayer structural and electronic properties obtained using SCC-DFTB. The in-plane lattice constant found by SCC-DFTB is 2.46 Å, which is the same as that of monolayer graphene, and is similarly in good agreement with experiment [124]. The interlayer separation is 3.55 Å, which is 6.0 % higher than observed experimentally [124]. The parameters (Slater-Koster integrals and repulsive potentials) used in this work are fitted to DFT-PBE calculations [113]. Therefore, we performed a DFT-PBE calculation using CASTEP, and found the same interlayer spacing, and indeed it is known in literature that GGA functionals overestimate the interlayer spacing of bilayer graphene [183], whilst the LDA gives a result in better agreement. Using DFT-LDA and DFT-PBE with van der Waals corrections [112] to calculate the structures of the bilayer graphene gives values of 3.35 Å and 3.54 Å for the interlayer spacing, respectively. In the following calculations, the positions of the atoms in the bilayer graphene above the various nanostructures surface are fixed and it has been chosen to enforce a interlayer spacing of 3.35 Å. When comparing to ab-initio DFT calculations, we choose to compare to the DFT-LDA results.

Fig. 5.25a shows the comparison of band structure obtained from SCC-DFTB (red and blue) and DFT-LDA (black) calculations, and highlight another issue associated with the use of the DFTB methods for studying bilayer graphene systems. The red lines are results found using the default parametrisation for the Carbon-Carbon pair, and it can be seen (more clearly in Fig. 5.25b) highlighting near the Dirac points) that this parametrisation corresponds to an interlayer hopping parameter $\gamma_1 \approx 0.13$ eV, which is significantly less than the value of 0.38 eV which DFT-LDA predicts. Note that γ_1 can be identical as the minimum energy of the offset conduction band at K. The ability of the electrons to hop between layers is closely related to the confining potential that is used to construct the basis set in the DFTB scheme. Recall Eq. 3.16, which defines the modified effective potential used to generate the DFTB basis functions (reproduced here)

$$V_i^{\text{eff}}[n](\mathbf{r}) = V_{ext,i}(\mathbf{r}) + V_H[n](\mathbf{r}) + V_{xc}^{LDA}[n](\mathbf{r}) + \left(\frac{r_i}{r_0}\right)^N, \tag{5.3}$$

where $r_i = |\mathbf{r}_i| = |\mathbf{r} - \mathbf{R}_i|$ and $V_{ext,i}(\mathbf{r})$ is the electrostatic potential of ion i. The final term

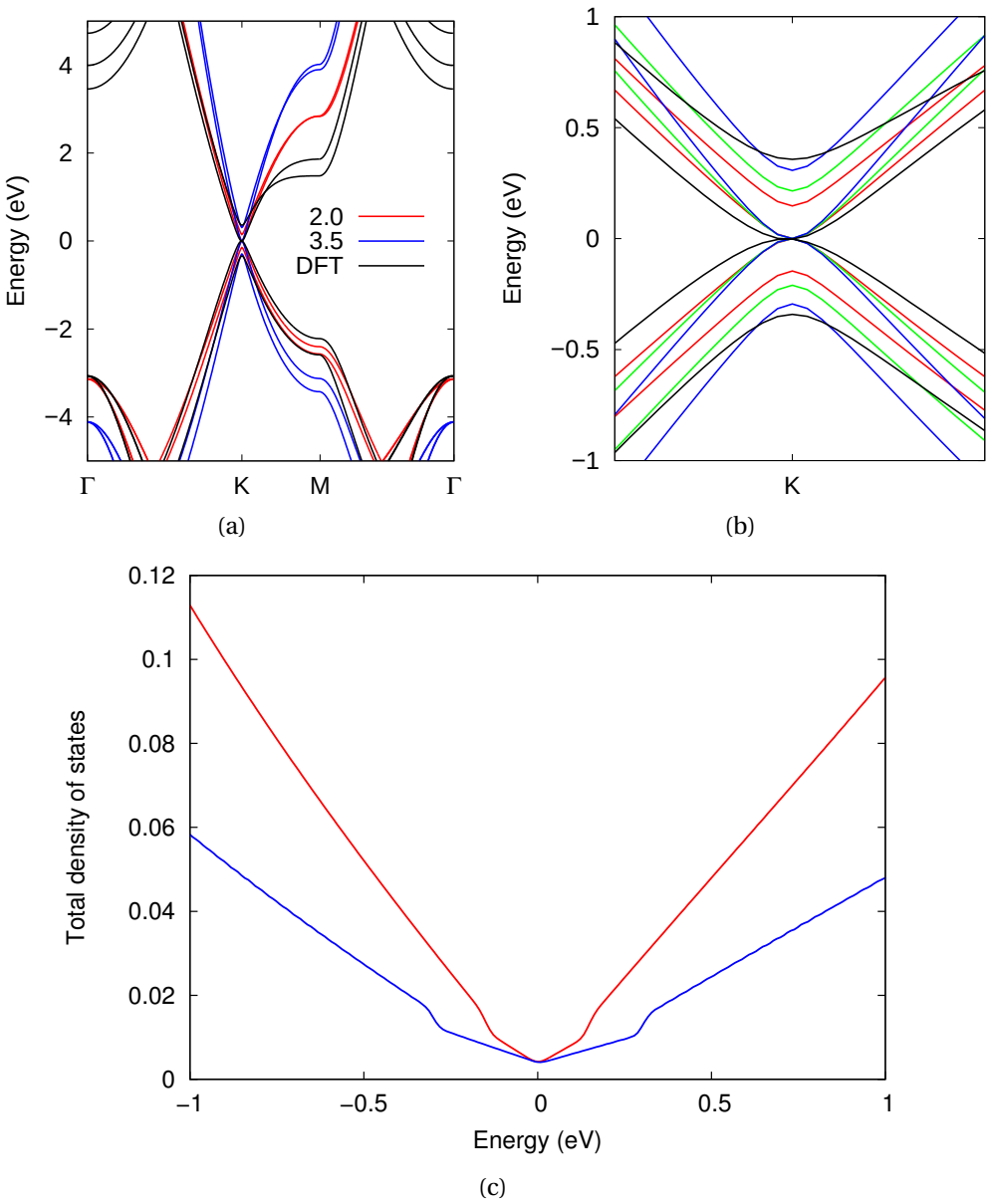

Figure 5.25: Calculated electronic structure of bilayer graphene. a) Comparison of band structure obtained from SCC-DFTB using different r_0 and DFT-LDA calculations. b) Comparison of the band structure in the vicinity of K point using SCC-DFTB with different confining radii r_0 = and the DFT-LDA result. c) Comparison of the total density of states using SCC-DFTB with the different r_0, red: $r_0 = 2.0 r_{cov}$, blue: $r_0 = 3.5 r_{cov}$. The red, green, blue lines are SCC-DFTB results using $r_0 = 2.0 r_{cov}$,$r_0 = 2.5 r_{cov}$ and $r_0 = 3.5 r_{cov}$ respectively, the black lines are the DFT-LDA results.

is the confining potential, and as suggested by Eschrig and Bergert [116] and Elstner *et al.* [113], $N = 2$ is always a good choice. To understand the importance of this term, we con-

sider variations in r_0. The default parametrisation uses $r_0 = 2r_{cov}$, where r_{cov} is the covalent radius for the atom (0.77 Å for Carbon). Increasing r_0 will result in less tightly confined orbitals which we might expect to increase interlayer hopping. Fig. 5.25b shows that indeed γ_1 increases with r_0, but is accompanies by a worsening in the agreement with DFT-LDA in the curvature of the bands. For $r_0 = 3.5r_{cov}$ (2.695 Å), the obtained γ_1 is 0.26 eV. Fig. 5.25c compares the total density of states of bilayer graphene found with $r_0 = 2r_{cov}$ (red) and $r_0 = 3.5r_{cov}$ (blue). Using $r_0 = 3.5r_{cov}$ gives significantly fewer electron states around the Fermi level. This result shows that a larger confining potential yields better in-plane dispersion, for the reason that larger confining potential resembles the tighter in-plane lattice potential; a smaller confining potential yields better out of plane hopping energy, for the reason that smaller confining potential allows the electrons to hop to a larger distance on the out of plane directions. To improve the situation increasing the basis set is needed, however, the basis set used in the DFTB scheme is minimal. Therefore no choice of r_0 gives the results that agree with both the interlayer hopping energy and the dispersion around Fermi level, we perform bilayer calculations using DFTB parameterisation found both with $r_0 = 2r_{cov}$ and $r_0 = 3.5r_{cov}$ for general insight.

Bilayer graphene on KBr(001) with steps

As discussed in the previous section, KBr (001) surface with [220]:2^+ steps introduces larger electrostatic potential variation and more pronounced change to the electronic structures of monolayer graphene overlayer. Although [220]:2^+ steps system is more promising to give explanation for the experimental observations, both KBr (001) surface with [220] and [220]:2^+ steps cases will be considered for the bilayer graphene cases in this section, the [220] step system will serve as comparison.

The steps geometries are the same as those in the monolayer study, as shown in Fig. 5.26a) and f). For the system containing the [220] steps, Figs. 5.26b) and d) show the calculated electrostatic potential in the lower and upper layer of the bilayer graphene, respectively. Figs. 5.26c) and e) display the external potential at the height of first and second graphene layer, respectively. The potential variation in the lower layer is found to be 0.9 eV, which is similar to that identified in the monolayer graphene above the same structure (0.8 eV). In the upper layer of graphene, it is found that 98% of the external potential has been screened out, leaving a potential variation of only 0.02 eV. In the [220]:2^+ steps systems, Figs. 5.26g) and i) show the calculated electrostatic potential in the lower and upper layer of bilayer graphene, respectively and Figs. 5.26h) and j) the external potential at the height of these layers. Again the electrostatic potential found in the lower layer of the bilayer graphene is

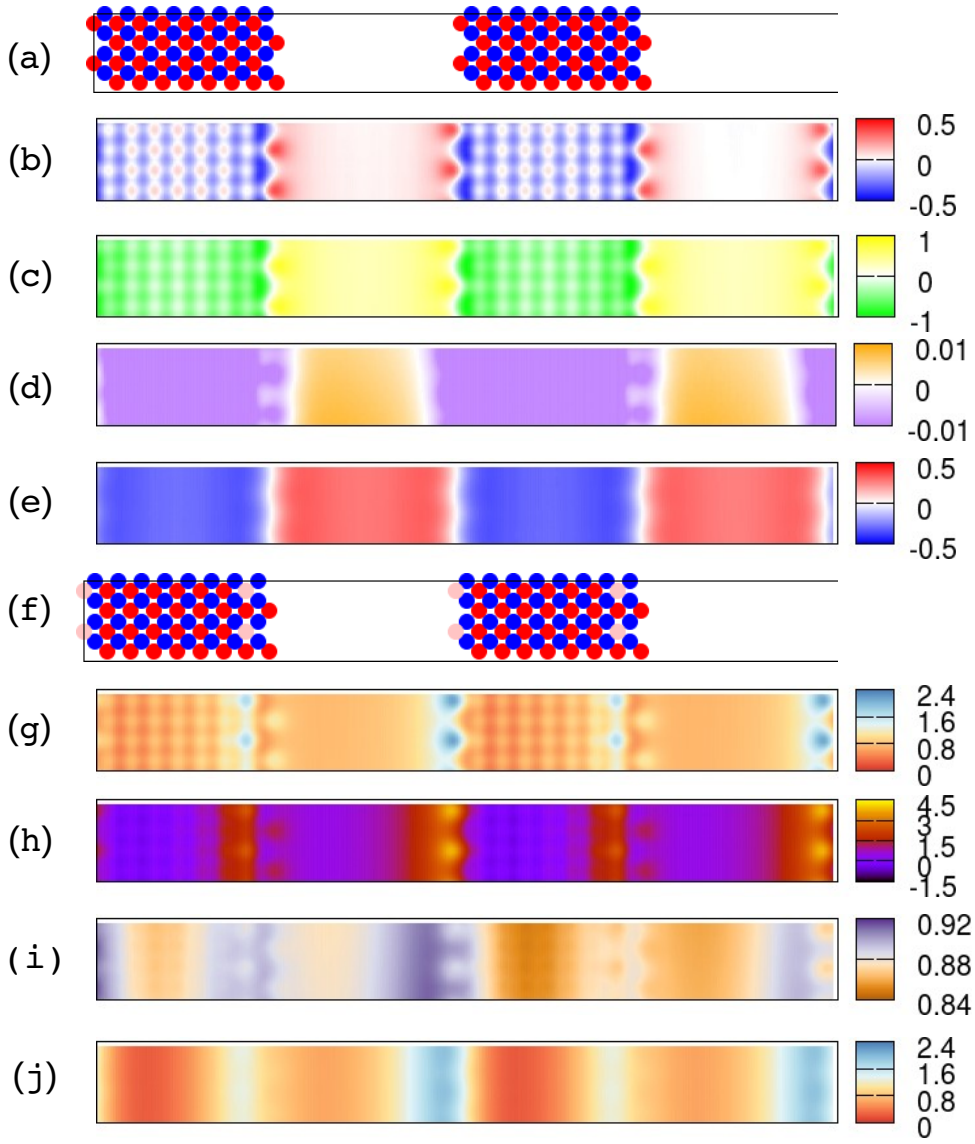

Figure 5.26: Configurations of the [220] or [220]:2^+ steps and the calculated electrostatic potential maps of the bilayer graphene on KBr(001) with [220] or [220]:2^+ steps. Configurations of uppermost layer of the a) [220] steps; f) [220]:2^+ steps . The red, blue and pink discs are K, Br and divalent atoms, respectively. Calculated electrostatic potential maps on the b) lower layer graphene on [220] steps; d) upper layer graphene on [220] steps; g) lower layer graphene on [220]:2^+ steps; i) upper layer graphene on [220]:2^+ steps. External potential maps (eV) at the heightof c) lower layer graphene of [220] case; e) upper layer graphene of [220] case; h) lower layer graphene of [220]:2^+ case; j) upper layer graphene of [220]:2^+ case.

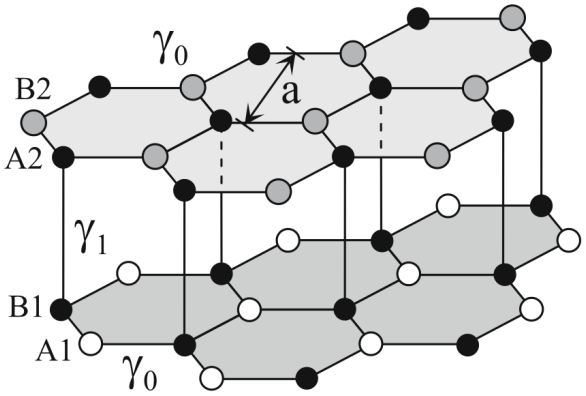

Figure 5.27: Configuration of bilayer graphene. Adapted from McCann [48].

very similar to that found for monolayer graphene above the same nanostructured surface, with the large variation of 1.8 eV found above the step edge containing divalent impurities, and a smaller variation of 1.4 eV found above the divalent impurities embedded in the upper terrace. For the upper layer, 97% of the external potential has been screened out, leaving a potential variation of just 0.08 eV.

The results correspond to screening factors in the lower layer of 0.55 for the surface with [220] steps, and 0.70 for the surface with [220]:2^+ steps, while the screening factors for the upper layer are 0.97 ~ 0.98 in both cases.

Next, we consider the electronic structures of these systems. Fig. 5.28 presents a comparison of the LDOS of selected atoms from both layers (red lines indicate the LDOS found on the at atom in the layer closer to the ionic surface, and blue lines the LDOS on the atom in the layer further from the ionic surface) compared with that found in pure bilayer graphene (indicated by black lines). The selected atoms are those in the region exhibiting the largest potential variation. The left or right panels present results from bilayer graphene aove KBr(001) with [220] steps or [220]:2^+ steps, respectively. Solid and dashed lines are used to distinguish between results found on atoms in site B or site A of the unit cell (see Fig. 5.27). This representation is used throughout unless otherwise stated.

Finally, the upper and lower panels show the LDOS over a larger of smaller energy range, respectively. Comparing the upper panels, both cases show electron/hole symmetry breaking, which is consistent with the behavior observed in the monolayer graphene cases. The LDOS of upper layer atoms changes relatively less than to that of the lower layer atom. A pronounced peak at 1.6 eV is found in bilayer graphene above the [220]:2^+ step system. In-

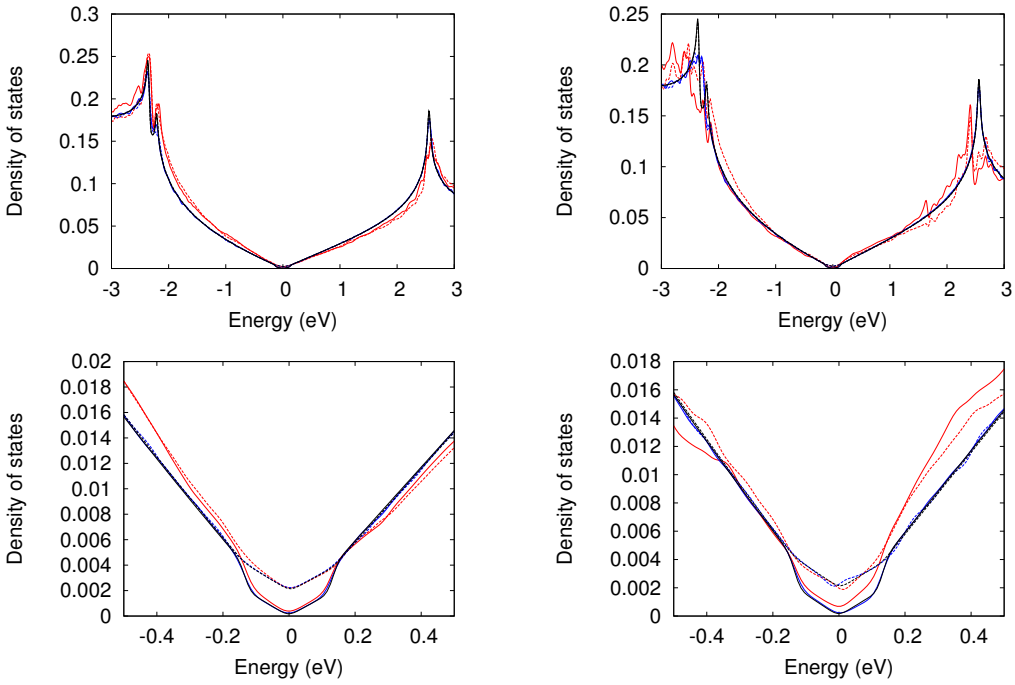

Figure 5.28: LDOS of selected Carbon atoms in both layers (red: lower layer, blue: upper layer) of bilayer graphene above KBr (001) with [220] (left panels) or [220]:2^+ steps (right panels). The upper (lower) panels show the calculated LDOS over a large (small) energy range. Black lines are used to display the LDOS of pure bilayer graphene. Solid or dashed lines distinguish site B and site A.

specting the lower panels, the LDOS on atoms in graphene above the [220]:2^+ step system exhibits features inside the $[-\gamma_1, \gamma_1]$ region. Note that both peaks and troughs will be called "peak" in this work.

Given that the peaks are observed inside the $[-\gamma_1, \gamma_1]$ region in the [220]:2^+ step system, and that it has previously been identified that the properties in this energy window are sensitive to the choice of confining potential radius r_0, we also calculate the LDOS on the same atoms above the same surface, but using DFTB parameterisation derived from orbitals found using $r_0 = 3.5 r_{cov}$. Fig. 5.29 shows the results. Comparing the upper panels, which present the LDOS over the larger energy range, a peak at 2.8 eV is found when $r_0 = 3.5 r_{cov}$, which its shape is very similar to the peak found at 1.6 eV when $r_0 = 2.0 r_{cov}$. Note that 2.8 eV is around 11 γ_1 for $r_0 = 3.5 r_{cov}$ and 1.6 eV is around 12 γ_1 for $r_0 = 2.0 r_{cov}$, so that these features are at similar positions relative to the γ_1 value obtained using each parameter. Comparing the lower panels, which present the LDOS over the smaller energy range, the LDOS of site A atoms obtained using both r_0 parameters have peaks around $\pm$ 30 meV, and with

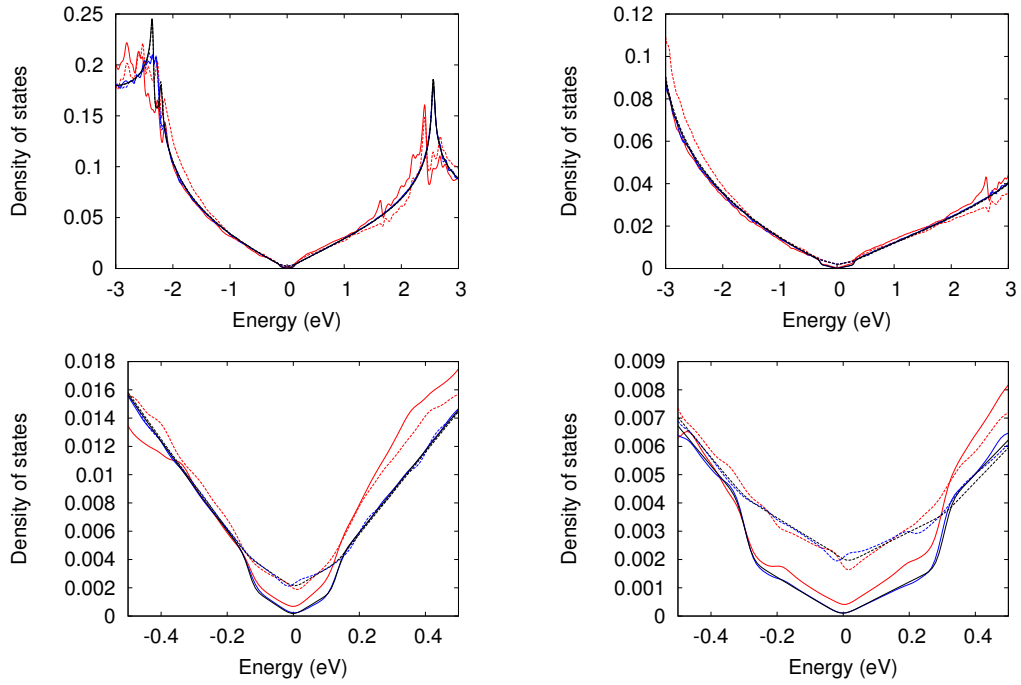

Figure 5.29: LDOS of selected Carbon atoms on both layers (red: lower layer, blue: upper layer) of bilayer graphene on KBr (001) with [220]:2^+ steps using different r_0. Left (right) panels are the results from $r_0 = 2.0r_{cov}$ ($r_0 = 3.5r_{cov}$). The upper (lower) panels are the calculated LDOS in large (small) range. The black lines are the LDOS of pure bilayer graphene. The solid (dashed) lines indicate site B (site A).

the peaks on the LDOS of the lower layer atoms located at negative energy while the peaks in the LDOS of the upper layer graphene occurs at the positive energy. The LDOS found using $r_0 = 3.5r_{cov}$ at site B atoms in both layers show another peak located at 0.19 eV, while for $r_0 = 2.0r_{cov}$, 0.19 eV is outside $[-\gamma_1, \gamma_1]$ region. Although there is some sensitivity to the parameter r_0, both choices used give peaks at $\pm$ 30 meV with similar shape and height. In subsequent calculations, we fix the parameter r_0 at $2.0r_{cov}$.

Fig. 5.30 magnifies and splits the calculated LDOS of lower and upper layer atoms presented in the lower left panel in Fig. 5.29. The red (blue) lines are the LDOS of the first (second) layer atom. Peaks within $\pm$ 30 meV on the opposite side of Fermi level can be seen for the lower layer and the upper layer atoms. In order to further understand the nature of this electronic features, LDOS maps at different energies (-30, -20, -10, +10, +20, +30 meV) for site A atoms are presented in Fig. 5.31 (lower layer) and Fig. 5.32 (upper layer). Zero has been set as the LDOS value of site A atom of pure bilayer graphene at the Dirac point.

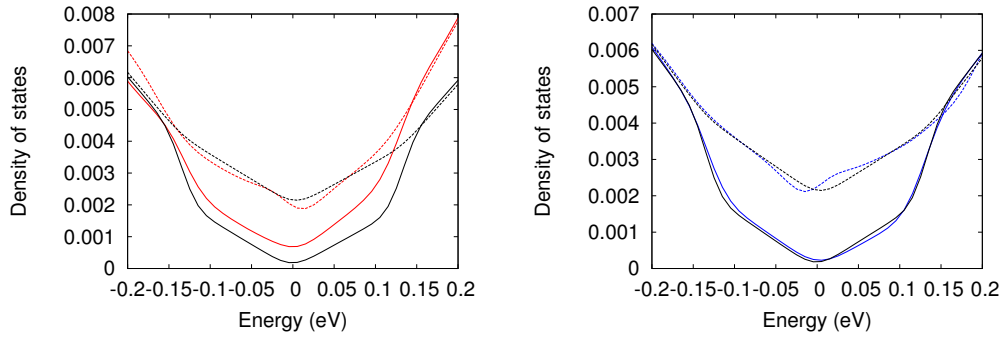

Figure 5.30: LDOS of selected Carbon atoms on both layers (left: lower layer, right: upper layer) of bilayer graphene on KBr (001) [220]:2^+ steps. The black lines are the LDOS of pure bilayer graphene. The solid (dashed) lines indicate site B (site A).

The panel in the first row of Fig. 5.31 is the atomic configuration of the upper terrace, and the panel in the second row shares the electrostatic potential within the lower graphene layer. The panel in the third row is a charge density difference map showing the difference between the charge density when the graphene is positioned above the nanostructured KBr (001) surface, and when it is in isolation. Positive numbers indicate a gain of electrons, and the charge density difference is seen to be consistent with the electrostatic potential, there being a gain of electrons where the potential is attractive. The panels in the fourth to the ninth row are maps of the LDOS at energy indicated at the left, and show that the peaks are most pronounced at the energy -30 meV and +10 meV, and coincide spatially with potential variation. The region with highest attractive potential has the lowest peak height at an energy of -30 meV, and the largest peak height at the energy +10 meV.

Turning now to Fig. 5.32, the panel in the first row again shows the atomic configuration of upper terrace of the nanostructured ionic surface. The panel in the second row now shows the electrostatic potential on the upper layer of the bilayer graphene, the layer further from the KBr. The panels in the third to the eighth row present LDOS maps calculated at the same set of energies. The peak is most pronounced at +10 meV, but the variations are much smaller overall in this layer.

To briefly summarize, from the calculations performed on bilayer graphene above KBr (001) nanostructured with [220] and [220]:2^+ step, we extract a potential variation of 0.9 eV and 1.8 eV for the lower layer, respectively, and 0.02 eV and 0.08 eV for the second. In the case of the [220]:2^+ step system, we also observe peaks in the LDOS within $\pm$ 30 meV of the Dirac point for the site A atoms in both layers. These peaks are not sensitive to the choice of the parameter r_0, and have opposite sign for lower and upper layer atoms. Although shallower

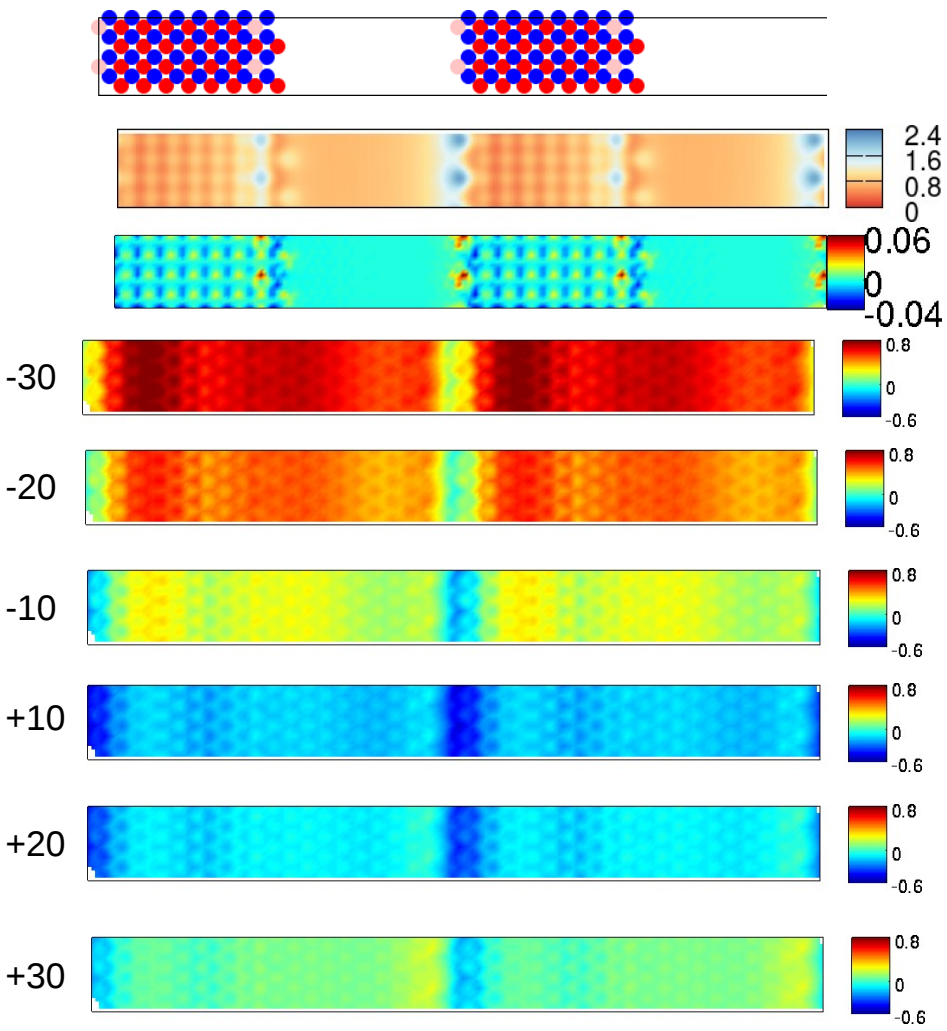

Figure 5.31: Configurations and LDOS maps for the lower layer site A atoms of the bilayer graphene on KBr (001) [220]:2^+ steps. Panels on the first and second row are the configuration of the steps and the electrostatic potential (in eV) on the lower layer graphene, the same as Fig. 5.26f) and Fig. 5.26g). Panel on the third row is the charge density difference map, positive means gaining electrons. Panels from the fourth to the ninth rows are the LDOS ($\times 10^{-3}$) of the lower layer graphene site A atoms taken at -30, -20, -10, 10, 20, 30 meV, respectively. Zero is chosen as the LDOS value of a site A atom of pure bilayer graphene at the Dirac point.

than the peaks observed in the experiments, the introduced divalent impurity and cation vacancy pair on the edges of the nanostructures could potentially explain the origin of the peaks seen in the experiments.

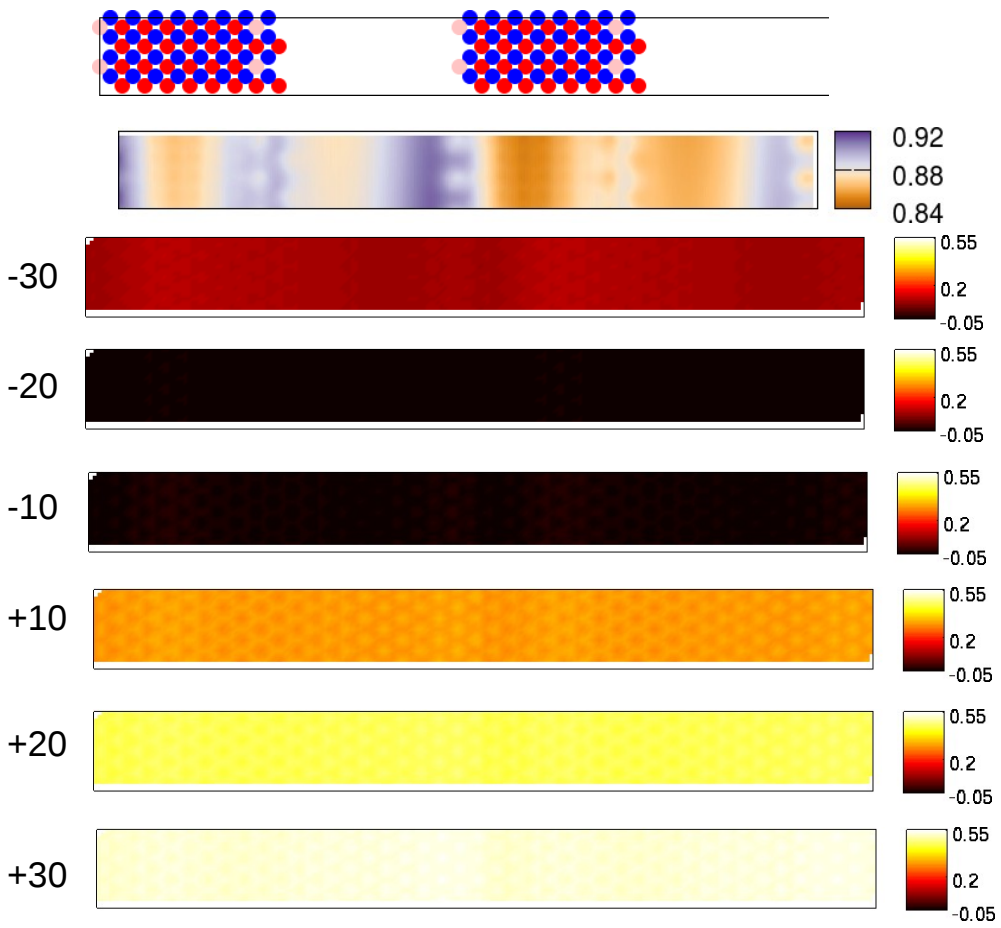

Figure 5.32: Configurations and LDOS maps for the upper layer site A atoms of the bilayer graphene on KBr (001) [220]:2^+ steps. Panels on the first and second row are the configuration of the steps and the electrostatic potential (in eV) on the upper layer graphene, the same as Fig. 5.26f) and Fig. 5.26i). Panels from the third to the eighth rows are the LDOS ($\times 10^{-3}$) of the upper layer graphene site A atoms taken at -30, -20, -10, 10, 20, 30 meV, respectively. Zero is chosen as the LDOS value of a site A atom of pure bilayer graphene at the Dirac point.

Bilayer graphene on KBr(001) with pits

We now consider electrostatic potential variation and electronic structure of bilayer graphene above KBr(001) nanostructured with pits. Since our experimental results showed larger contrast around one corner of the pits, and from the results of the steps cases, system containing

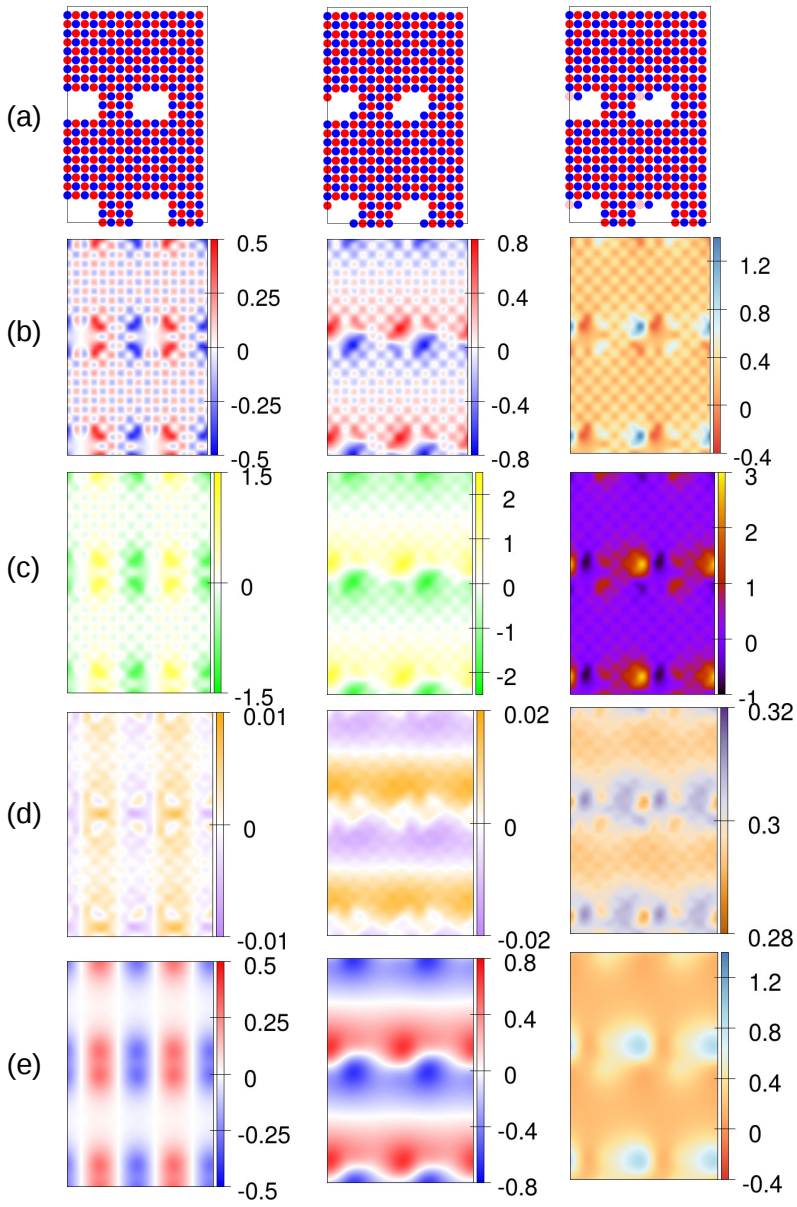

Figure 5.33: Configurations and calculated electrostatic potential map (eV) of the bilayer graphene on KBr (001) with pits. Panels on the first, second and third column are the results from pits with no kinks, two kinks and one kink, respectively. a) Configurations of uppermost layer of the pits, red, blue and pink discs are K, Br and divalent atoms, respectively . Calculated electrostatic potential maps on the b) lower layer graphene; d) upper layer graphene. External potential maps at the heightof c) lower layer graphene; e) upper layer graphene. Note that the colour range are different for panels on the different columns.

divalent impurity and cation vacancy pair seems to be more promising to serve as explanation for the experiments, pits with one kink consisting of a divalent impurity and cation

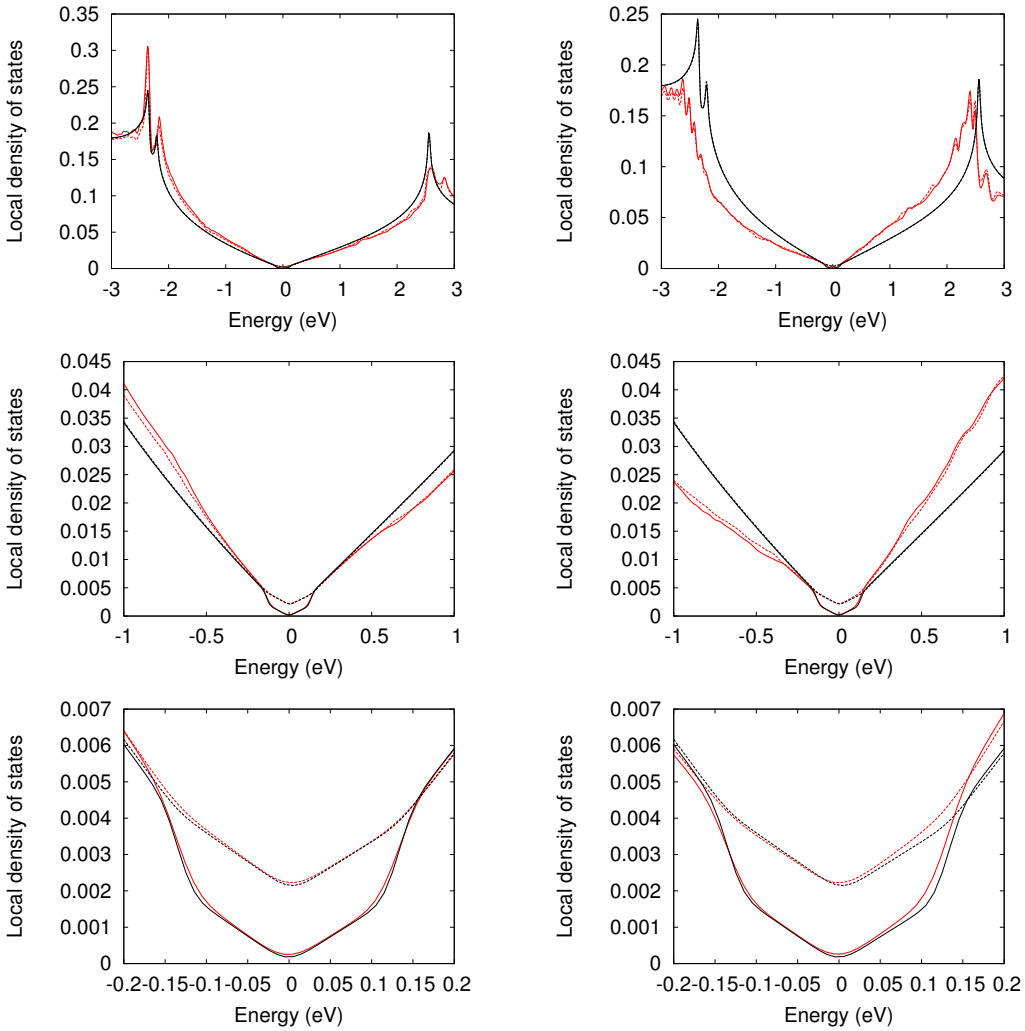

Figure 5.34: LDOS of selected lower layer Carbon atoms of bilayer graphene on KBr (001) with pits. Panels on the left (right) are the results from pits with no kinks (two kinks). The black lines are the LDOS of pure bilayer graphene. The solid (dashed) line indicates site B (site A). The panels on each row are the LDOS in different energy range.

vacancy pair will be the focus in this section, pits with no kinks and two kinks will serve as comparisons. As illustrated in Fig. 5.33a), three types of pits are studied : pits with no kinks (left), pits with two kinks (middle) and pits with one kink consisting of a divalent impurity and cation vacancy pair (right). The total area of the systems is 25.6 Å × 39.9 Å, with the pits themselves 13.3 Å × 9.9 Å. The cation vacancy is constructed by removing the nearest K atom underneath the divalent impurity, as was done for the [220]:2^+ step system. From now on, pits with one kink consisting of a divalent impurity and cation vacancy pair will be referred as pits with one kink for short. Then the columns in Fig. 5.33 show results from

the different systems : the left column are the results for the pits with no kinks, the middle column the pits with two kinks and the right column the pits with one kink. Fig. 5.33b) shows the electrostatic potential calculated within the lower layer of bilayer graphene, and d) shows calculated within the upper layer. Attention is drawn here and in the other panels of this figure to the scale bars accompanying each color map, which differ from on another in order for the spatial variation in the plots to be most clear represented. Fig. 5.33c) and e) show the external potential present at the height of lower layer and the upper graphene layer. Comparing Fig. 5.33b) and Fig. 5.33d) with Fig. 5.33c) and Fig. 5.33e), is clear that the variation in the electrostatic potential is concentrate at the corners or the kink sites. The potential variation (screening factor) for the lower graphene layer is 1.0 eV (0.67), 1.6 eV (0.6) and 1.7 eV (0.58) for pits with no kinks, two kinks and one kink cases, respectively, while for the upper graphene layer, the screening factor for all systems is $\sim$ 0.98. The variations induced by the surface containing pits with no kinks case is similar in magnitude to those induced by the presence of [220] steps.

Now we consider the effect on the electronic structure of the bilayer graphene. Since over the larger energy range the variation in the LDOS of atoms in the upper layer is less than 10% of that on atoms in the lower layer, only the LDOS of lower layer atoms are shown. Fig. 5.34 and Fig. 5.35 present the comparison of the LDOS of selected atoms in pits with no kink (left panels in Fig. 5.34), two kinks (right panels in Fig. 5.34 and left panels in Fig. 5.35) and one kink system (right panels in Fig. 5.35). Comparing the panels in the first and second rows of Fig. 5.34 and Fig. 5.35, pits with two and one kinks create stronger electron/hole asymmetry, and more pronounced peaks. Comparing the panels in the third rows which have the narrower energy range, the pits with no kink case indicate no narrow electronic features, while the pits with two kinks indicate very broad changes and pits with one kink indicate broad change, but narrower than those due to the pits with two kinks.

Fig. 5.36 magnifies and splits the LDOS of lower and upper layer atoms of the third row of the right hand panel in Fig. 5.35. The red (blue) lines are the LDOS of the lower (upper) layer atom. Compared to the results found for bilayer graphene above the KBr(001) surface nanostructured with [220]:2^+ steps, shown in Fig. 5.30, the induced change are smaller in this case. However, variations are again located at the energies around $\pm$ 30 meV. Fig. 5.37 maps the LDOS of site A atoms in the lower and upper layer at $\pm$30 meV, with the panels in the first row showing the electrostatic potential in the lower and upper layer of the bilayer graphene. It can be seen that, the amplitude of the variation in the LDOS varies with the change in the potential within the lower layer, while in the upper layer the variation changes are much smaller in size. The greatest changes in the LDOS coincide with the areas

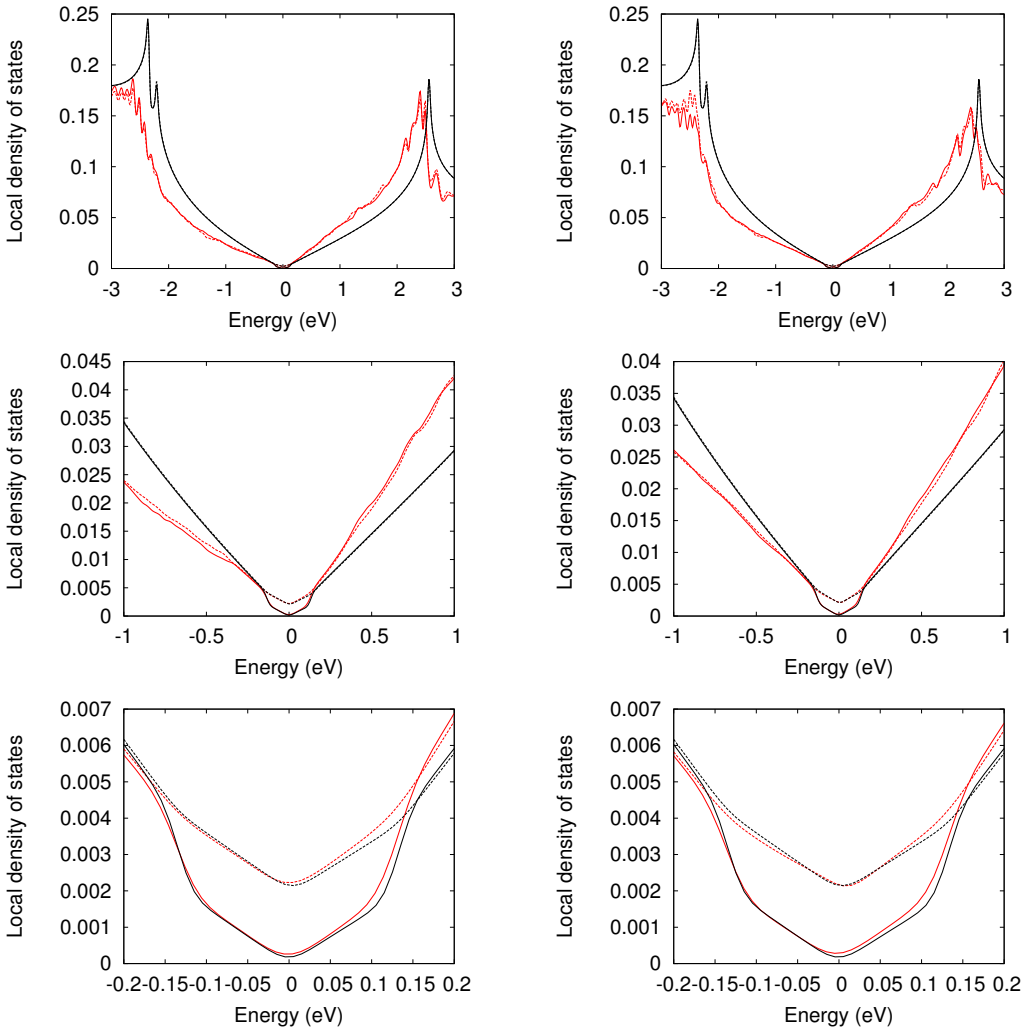

Figure 5.35: LDOS of selected lower layer Carbon atoms of bilayer graphene on KBr (001) with pits. Panels on the left (right) are the results from pits with two kinks (one kinks) . The black lines are the LDOS of pure bilayer graphene. The solid (dashed) line indicates site B (site A). The panels on each row are the LDOS in different energy range.

where there is greatest potential variation.

To briefly summarize, from the calculations of bilayer graphene on KBr (001) nanostructured with pits including no kink, two kinks and one kink, we identified potential variations of 1.0 eV, 1.6 eV and 1.7 eV within the lower layer closer to the KBr and 0.02 eV, 0.04eV and 0.04 eV within the upper layer. For the pits containing one kink, we observe change within ± 30 meV in the LDOS of site A atoms on both layers. Similar to bilayer graphene on KBr(001) nanostructured with [220]:2^+ step, these are of opposite sign for lower and upper

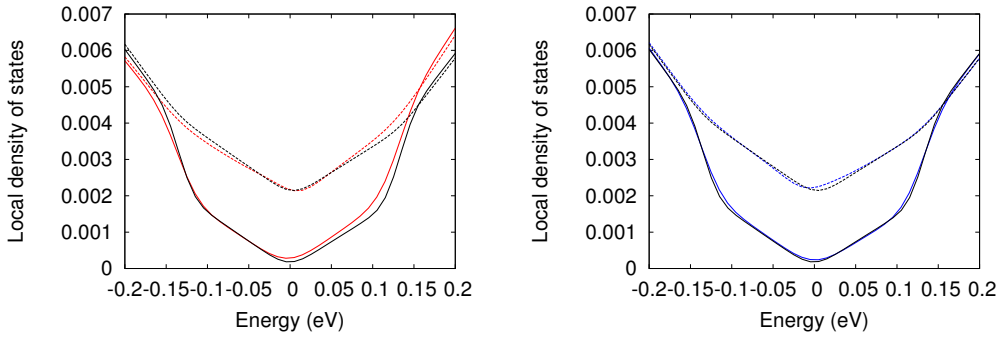

Figure 5.36: LDOS of selected Carbon atoms on both layers (left: lower layer, right: upper layer) of bilayer graphene on KBr (001) with pits with one kink. The black lines are the LDOS of pure bilayer graphene. The solid (dashed) lines indicate site B (site A).

layer atoms, but of much lower height. Note that a set of studies has also been performed on pits with half the size as described here, These given consistent results and are presented in Appendix C.

5.3.3 Registry and displacement

So far, the calculations reported have assumed a specific registry of the graphene on the nanostructured KBr (001) surfaces. Ideally, an investigation considering how sensitive the findings are to the angle and horizontal displacement on the graphene would be performed. However,an unfeasibly large supercell is needed to perform periodic calculations a small angle rotation of the graphene sheet is to be considered. Therefore, in this section, we restrict our attention to the effect of the horizontal displacement of the graphene.

Figs. 5.38a) and c) show the example of two registries and careful inspect especially in the vicinity of the pit areas makes clear the difference in the position of the bilayer graphene. Fig. 5.38b) shows the electrostatic potential calculated within the lower graphene layer of the system shown in Fig. 5.38a), and Fig. 5.38d) shows a *difference* plot of the electrostatic potential in the two systems in Figs. 5.38c) and a). It can be seen that the differences vary within ±0.02 eV, indicating changes at the 5% level. Other registries corresponding to different horizontal displacements have also been studied, and the resulting differences of the electrostatic potential in the lower graphene layer have similarly been found to be within ± 0.02 eV.

From the earlier studies of systems containing KBr(001) surfaces nanostructured with pits with two kinks and one kink, it was learned that a 0.2 eV potential difference in the lower

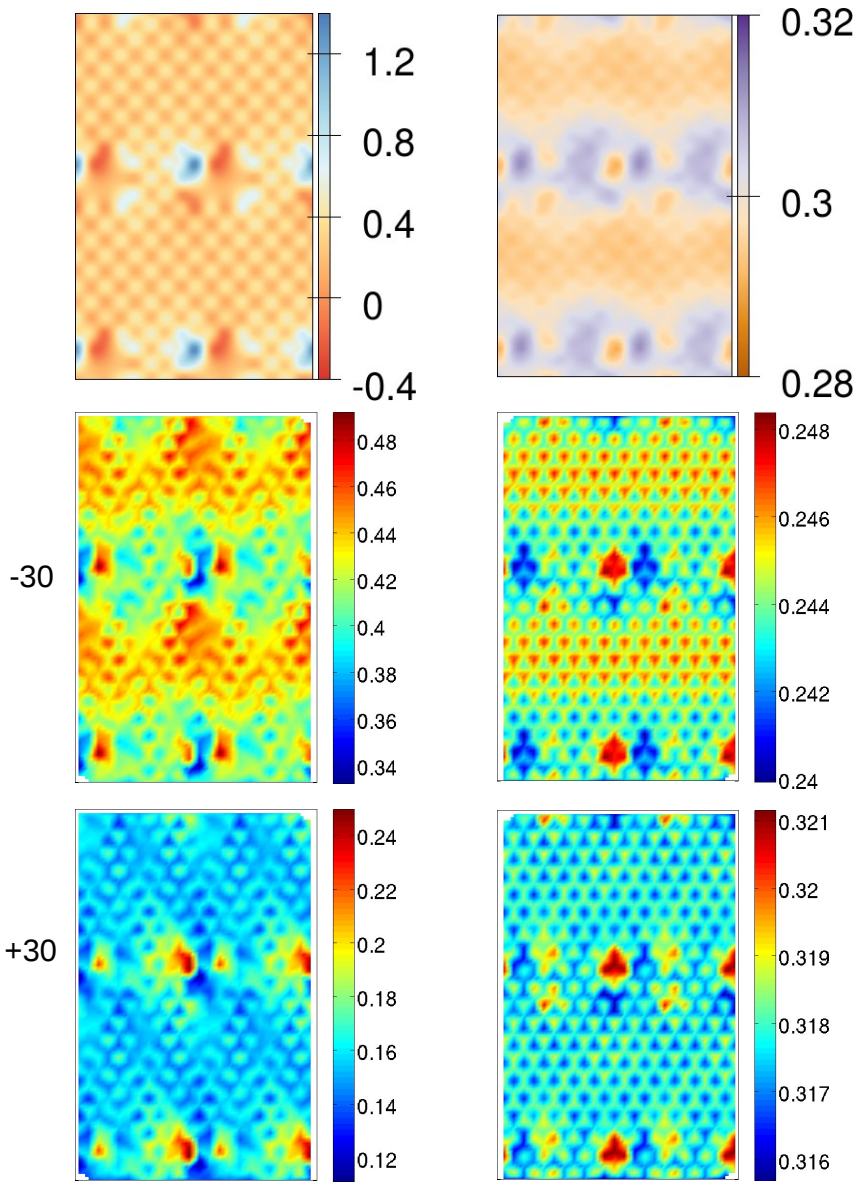

Figure 5.37: Electrostatic potential (eV) and LDOS map for the lower (left) and upper (right) layer site A atoms of the bilayer graphene on KBr (001) with pits with one kink. Panels on the first row is the electrostatic potential on the lower (left) and upper (right) layer graphene. Panels on the second and third rows are the LDOS ($\times 10^{-3}$) of the lower (left) and upper (right) layer graphene site A atoms taken at -30 and 30 meV, respectively. Zero is chosen as the LDOS value of site A atom of pure bilayer graphene at the Dirac point. Note that a difference colour range is used in each panel.

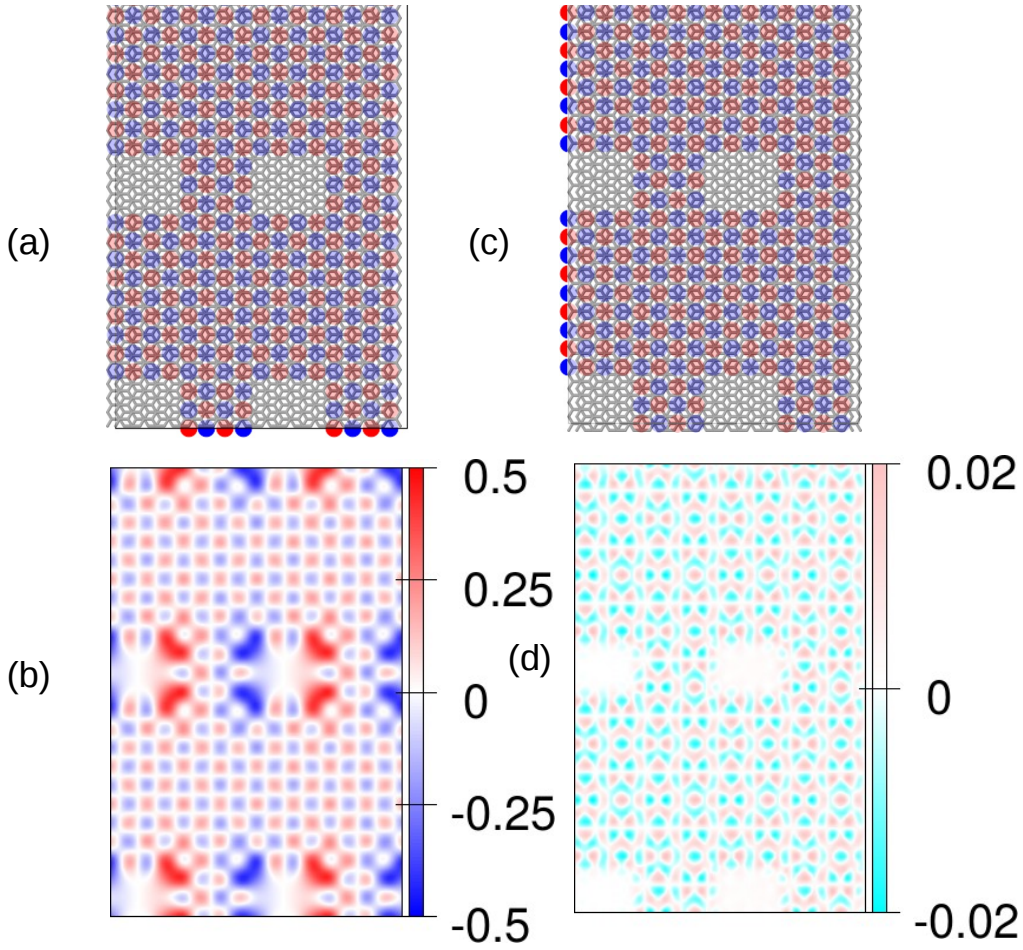

Figure 5.38: Atomic configurations and calculated electrostatic potentials (eV) of bilayer graphene on KBr (001) with pits. a) and c) Configurations of bilayer graphene on KBr(001) with pits of no kinks with different registry. Grey lines indicate the position of graphene, the red (blue) discs indicate the K and (Br) atoms. b) Calculated electrostatic potential within the lower graphene layer for a). d) The difference in the electrostatic potential within the lower graphene layer in the system of a) and c).

layer graphene does not cause significant changes in the electronic structure; hence ±0.02 eV scales changes accompanying the different horizontal displacements of the graphene will have no impact on the electronic structure, and our choice of a specific registry in the earlier studies is not a limiting factor.

Another factor is potentially more significant. As mentioned in Section 5.1, the divalent impurity and cation vacancy pair are likely to induce sizable atomic relaxation at the surface, especially in the position of the divalent impurity atoms. The average vertical displacement

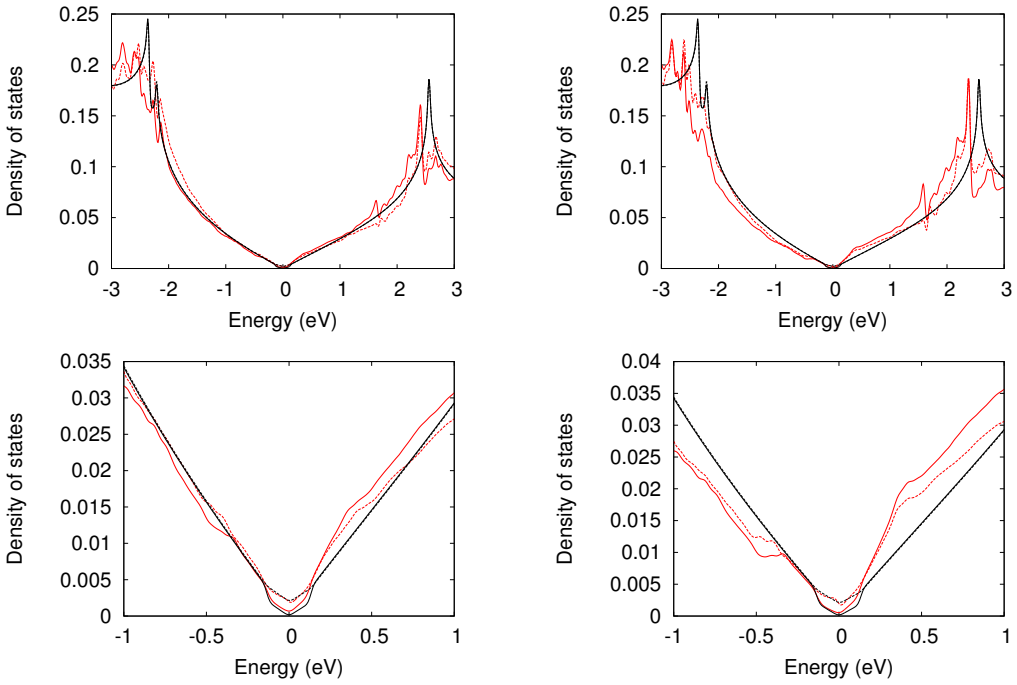

Figure 5.39: LDOS of selected Carbon atoms on lower layer of bilayer graphene on KBr (001) with [220]:2^+ steps (left panels) or [220]:2^+ steps with displaced 2^+ (right panels). The upper (lower) panels are the calculated LDOS in large (small) range. The black lines are the LDOS of pure bilayer graphene. The solid (dashed) lines indicate site B (site A).

of the divalent atoms in the Suzuki structure is reported to be 0.2 Å (outward) [155]. To quantify the importance of this we undertake a calculation in which the the divalent impurities are manually displaced by 0.2 Å (outward) in the [220]:2^+ system.

The displacement of the divalent impurity closer to the graphene layer, is expected to increase the electrostatic potential, and the calculated electrostatic potential within the graphene layers shows this, with the potential variation in the vicinity of the step edges increased from 1.8 eV to 2.0 eV for the lower layer, and remaining 0.08 eV for the upper layer. Fig. 5.39 shows the comparison of the LDOS found in the lower graphene layer of bilayer graphene on KBr(001) nanostructured with [220]:2^+ steps without (left) and with (right) outward atomic displacement of the divalent impurity. The peaks at 1.6 eV are enhanced in the displaced case, and the electron/hole asymmetry also stronger. Fig. 5.40 shows the LDOS from both cases presented over a smaller energy range. The red (blue) lines on the left (right) are the LDOS from the upper (lower) layer graphene atoms. The system with divalent atoms outwardly displaced has features at the same energies as in the unchanged case, but they are all stronger.

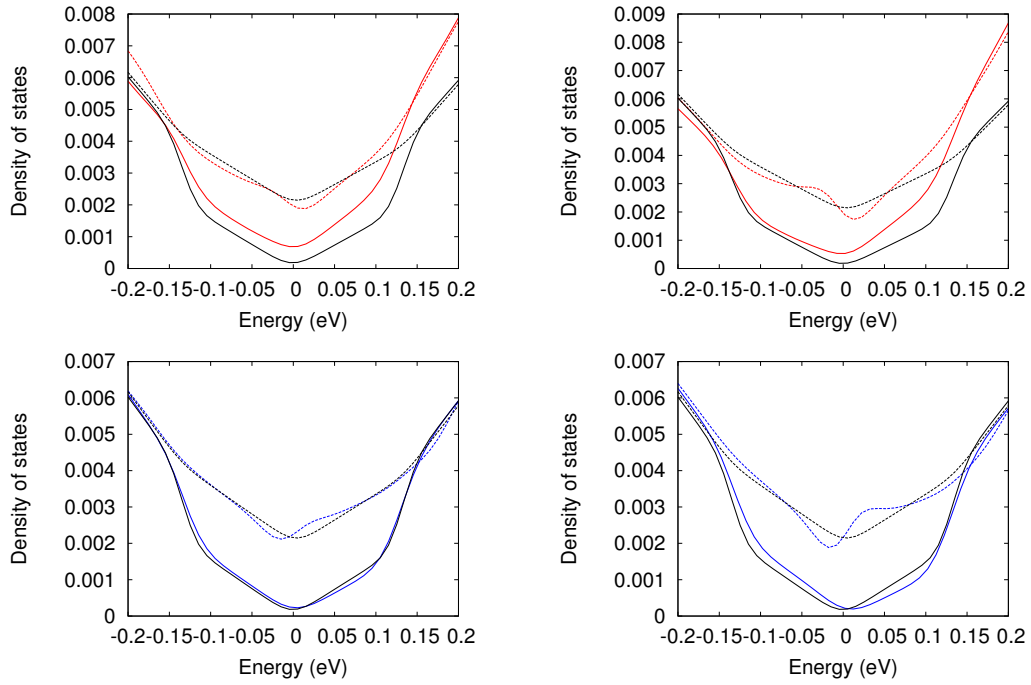

Figure 5.40: LDOS of selected Carbon atoms on both layers (red: lower layer, blue: upper layer) of bilayer graphene on KBr (001) with [220]:2^+ steps (left panels) or [220]:2^+ steps with displaced 2^+ (right panels). The black lines are the LDOS of pure bilayer graphene. The solid (dashed) lines indicate site B (site A).

In summary, the registry of the graphene sheet is not a significant factor determining the on-sheet potential. On the other hand, displacing the divalent impurity outward by 0.2 Å increases the electrostatic potential variation by 0.2 eV within the lower graphene layer, and results in enhanced features in the LDOS. Since the displacement of the divalent impurity is observed in the experimental studies of Suzuki structures [155], in the experiments, it is more realistic than unrelaxed surface. And the enhancement of the peaks seen in LDOS (shown in Fig. 5.40) is noticeable and agrees with the characteristics of the features seen in the experiments better, indicating the displacement of the impurity atoms is also essential.

5.3.4 Conclusions from graphene on nanostructured ionic system using DFTB

Studies of the monolayer graphene on KBr (001) with [220] steps and [220]:2^+ steps, indicate larger (1.8 eV) variations in the electrostatic potential within the graphene sheet in the latter than the former (0.8 eV), with stronger peaks and stronger electron/hole asymmetry induced in the LDOS. In the system containing [220] steps, SCC- and SCCD-DFTB predict a potential variation of 0.8 eV, while calculations using DFT-LCAO predict 0.3 eV.

Next considered was bilayer graphene on KBr (001) nanostructured with steps and pits. The same [220] steps and [220]:2^+ steps used in the monolayer cases are used have been considered, with the [220] steps introducing a potential variation of 0.9 eV (0.02 eV) on the lower (upper) graphene layer, with the corresponding value for the system with [220]:2^+ steps being 1.8 eV (0.08 eV). The [220]:2^+ system not only shows the stronger features and electron/hole asymmetry induced in the LDOS, but within the $[-\gamma_1, \gamma_1]$ energy region in the LDOS, peaks can be seen on both sides of the Fermi level from graphene atoms in bother layers of the bilayer. The strongest peaks are around -30 meV and +10 meV. In systems containing pits, pits with no kink, two kinks and one kink which includes a divalent impurity and cation vacancy pair have been considered. These induce 1.0 eV (0.02 eV), 1.6 eV (0.04 eV) and 1.7 eV (0.04 eV) electrostatic potential variations on the lower (upper) graphene layer, respectively. Pits with two kinks and one kink show some evidence of the electronic features in the [-30 meV, 30 meV] region, but they are weaker than those observed in the graphene above the surface with [220]:2^+ step.

We have considered the importance of the relative position of the graphene atoms and the substrate. By horizontally displacing the graphene layers, electrostatic potential variations of less than ± 0.02 eV are found to result for different relative positions. This is not sufficient to cause significant change in the graphene electronic structure.

Vertically displacing the divalent impurities outward, which is understood to occur in systems containing them, has also been considered. Displacement outward by 0.2 Å results in the electrostatic potential being enhanced by 0.2 eV on the lower graphene layer, and the induced features in the LDOS in the [-30 meV, 30 meV] range are also enhanced, occur at the same energies.

5.4 Overall summary and discussion

Both DFT and DFTB methods have been used to gain insight into the electrostatic potential and electronic structures of monolayer and bilayer graphene on nanostructured KBr (001) surfaces.

These studies confirm that the clean KBr(001) surface does not affect the monolayer graphene electronic structure in the vicinity of the Dirac points within ±1 eV of the Fermi level. It has also been established that the non-polar steps generate too small an electrostatic potential

at the height of a graphene overlayer (± 0.1 eV) to be responsible for the sizable electrostatic potential variations identified in experiments [77]. However, the KBr (001) surface with polar [220] steps can result in 0.3 eV electrostatic potential variations above the step edge within the monolayer graphene overlayer.

DFTB methods yield the electrostatic potential variations approximately twice as high as those from DFT. Whether this is an inherent limitation of the accuracy of DFTB, or a reflection of poor convergence in the DFT-LCAO calculations due to their inherent sign is not fully clear, but it may indicate that the absolute values obtained using DFTB are less meaningful than the trends they show. What is also in doubt is that far smaller potential variation induced in the upper layer of bilayer overlayers, and the very large screening factor (0.98).

Comparing systems containing steps and pits, [220] steps and pits with no kinks give the lowest electrostatic potential variations in graphene overlayers, pits with two kinks give larger potential variations, while [220]:2^+ steps and pits with one kink give even larger variations. With the increasing electrostatic potential, the electron/hole asymmetry and features induced in the LDOS become stronger. When the potential variation on the lower layer graphene is larger than 1.6 eV, peaks within $[-\gamma_1, \gamma_1]$ energy region, specifically at [-30 meV, 30 meV]. The height of the peaks varies with the electrostatic potential, but their location remains unchanged.

Both nanostructured surface with [220]:2^+ steps and pits with one kink contain a divalent impurity and cation vacancy pair. The former exhibits pronounced peaks within $[-\gamma_1, \gamma_1]$ energy region of the graphene LDOS. It has been found that possible outward relaxation of the divalent impurities at the step edges further enhances the electrostatic potential within the graphene layers, and results in an enhancement of the features within $[-\gamma_1, \gamma_1]$ energy region of the LDOS.

On the basis of these results, it is the divalent impurity and cation vacancy pair with possible relaxations that is considered to be key to the creation of large electrostatic potential variations in graphene overlayers, and responsible for peaks inside $[-\gamma_1, \gamma_1]$ energy region of the LDOS, with the peaks located at [-30 meV, 30 meV] identified as analogous to the peaks seen in experiments (Fig. 1.7). The peaks observed in experiments are found at -58 meV, and the system is bilayer graphene on NaCl (001) with pits. All of the peaks on the negative side of the Fermi level observed from DFTB calculations occur at -30 meV, independent of the strength of the electrostatic potential. The difference of the peak location may due to the different lattice constant of NaCl and KBr, but further investigations is needed to state

with complete confidence the origin of the peaks and their location and height, which will be discussed in detail in the next Chapter.

Chapter 6

Conclusions and future work

6.1 Summary

In this thesis, studies of graphene on nanostructured ionic substrate using DFT and DFTB methods have been presented.

Since self-consistently determining dipole are expected to be important in systems with asymmetric charge distributions, such as those of interest here, the standard SCC-DFTB scheme has been extended to a SCCD-DFTB scheme which includes dipole fluctuations. This involves modifying the total energy, evaluating the atomic dipole moments, constructing dipole matrix elements and updating the Hamiltonian. This enhanced formulation has been implemented and its parameterisation considered for Carbon-based systems. Calculations of the the polarizabilities and band structures of various Carbon-based systems share an improved description is achieved.

Using ab-initio DFT methods, firstly it has been confirmed that flat ionic substrates do not significantly influence the electronic structure of graphene in the vicinity of the Dirac points within the energy range of interest (within 1 eV of E_F). It has been found that the non-polar steps generate a relatively small electrostatic potential variation at the height of supported graphene layers ($\pm$ 0.1 eV), while polar [220] steps result in 0.3 eV potential variation at the step edge in a monolayer graphene sheet. This indicates that the non-polar steps are not the nanostructures responsible for generating sizeable electrostatic potential variations that have been reported in experiments [77], whilst polar steps are likely candidates that warrant further investigation.

Using the less computationally demanding DFTB approach has enable the study of large-

scale systems containing more complex nanostructures. From the result of these calculations, we identify that the electrostatic potential variation on graphene overlayers increases in the following order: polar steps and pits with no kinks; pits with two kinks; pits with one kink which includes the divalent impurity and cation vacancy pair; and polar steps with divalent impurity and cation vacancy pair. Accompanying the increasing potential variation in the graphene layers, stronger peaks and electron/hole asymmetry are observed in the local density of states, while peaks in the low energy range ($|E - E_F| < \gamma_1$) begin to appear in the systems possessing with largest potential variations.

Our result identified that the presence of divalent impurities and cation vacancy pairs with relaxation of the impurity atoms is the key to introducing sizeable electrostatic potential variation in graphene overlayers, and as well as the pronounced peaks in the LDOS within $|\gamma_1|$ of the Fermi energy. It is suggested that this is the explanation for the origin of the contrast in the electrostatic potential map and the electronic features in the lower energy range seen in the experiments (Fig. 1.7).

6.2 Future work

Further work is needed in order to state the conclusion with confidence.

Our current results reveals that the possible relaxation of the atoms on the edge plays important role in terms of both the electrostatic potential and the electronic structures, therefore a thorough understanding of the surface relaxation is needed. The distance between the graphene layer and the nanostructures and the in plane relaxation of graphene are the two key elements in this study. Fully relaxing the system can be one way. SCC-DFTB method can be used to relax the geometry, it requires proper parametrization of repulsive potentials of selected atom pairs. If SCCD-DFTB method will be used, force and geometry optimization needs to be extended and implemented in the scheme. On the other hand, DFT calculations of the electronic structures of free standing graphene with different curvatures can also gain some insight of the electronic effect when in plane relaxation of graphene is introduced.

To more accurately estimate the electrostatic potential of the mono/bilayer graphene on nanostructured ionic substrates and gain better understanding of the screening effect due to the polar nanostructures with divalent impurity and cation pair, calculations using different types of DFT methods on various systems will be performed. First of all, a suitable basis set (enough to converge the physical properties of interest) for our systems using DFT-LCAO

method will be determined by systematic increasing the basis sets. Secondly, the charge density and electrostatic potential on both layers of bilayer graphene on KBr (001) surface with [220]:2^+ steps and pits with one kink will be calculated, then the understanding of the charge redistribution causing by the screening effect due to the underneath nanostructures will be understood. Thirdly, in order to validate or modify the model that treating the ionic substrates as point charges, planewave type of DFT calculation using K and Br atoms rather than point charges will also be performed on the same system. The value for the point charges used in this work is $\pm\ e$, this value can be modified according to the results from planewave type of DFT calculation using K and Br atoms. Fourthly, because the experimental results are obtained from both KBr and NaCl samples, steps and pits on NaCl(001) with bilayer graphene on top will also be considered. Finally, calculations of systems with steps and pits of different size are also needed, in order to understand the long range perturbation and the scattering/reflection due to the nanostructures on the edges of the steps and pits.

To understand the features observed in the electronic structures, DFT calculations and analytical models will be needed. Since the experimental quantity that reveals the electronic perturbations is the differential conductivity, firstly, proper STM interpretation method that are available in DFT calculations will be studied. Secondly, using that method, both KBr and NaCl systems with divalent nanostructures of different size will be considered to gain some insight of the location and strength of the peaks and their dependency on the substrate/nanostructures characteristics. Finally, on the basis of the gained understanding, suitable analytical models will be introduced to further explain the origin of the electronic features, and potentially provide predictions of the electron behaviour of graphene on nanostructures with different geometries and/or on different substrates.

The transport properties of graphene on nanostructured ionic substrates are the final interest of this study, proper methods and models will be chosen according to the results of this work and the further work discussed above.

Appendix A

Charge-charge, charge-dipole and dipole-dipole interaction matrices.

The derivations of charge-charge $\hat{\Gamma}^{00}_{ij}$, charge-dipole $\hat{\Gamma}^{10}_{ij}$ and dipole-dipole interaction matrix $\hat{\Gamma}^{11}_{ij}$ are given here.

A.1 $\hat{\Gamma}^{00}_{ij}$

We first consider the evaluation of $\hat{\Gamma}^{00}_{ij}$ for the case of the Gaussian-type distribution. $\rho^{\text{iso}}_{i,\text{GTO}}(r_i)$ defined in Eq. 3.26:

$$\rho^{\text{iso}}_{i,\text{GTO}}(r_i) = \left(\frac{\sigma_i}{\pi}\right)^{\frac{3}{2}} e^{-\sigma_i|\mathbf{r}-\mathbf{R}_i|^2}. \tag{A.1}$$

$\hat{\Gamma}^{00}_{ij}$ is defined in Eq. 3.25

$$\hat{\Gamma}^{00}_{ij} = \int\int \frac{\rho^{\text{iso}}_i(r_i)\rho^{\text{iso}}_j(r_j)}{|\mathbf{r}-\mathbf{r}'|} d\mathbf{r}d\mathbf{r}'. \tag{A.2}$$

Inserting Eq. 3.26 into Eq. 3.25 gives

$$\begin{aligned}
\hat{\Gamma}^{00}_{ij,\text{GTO}} &= \int\int \frac{\left(\frac{\sigma_i}{\pi}\right)^{\frac{3}{2}} e^{-\sigma_i|\mathbf{r}-\mathbf{R}_i|^2} \left(\frac{\sigma_j}{\pi}\right)^{\frac{3}{2}} e^{-\sigma_j|\mathbf{r}'-\mathbf{R}_j|^2}}{|\mathbf{r}-\mathbf{r}'|} d\mathbf{r}d\mathbf{r}' \\
&= \left(\frac{\sigma_i\sigma_j}{\pi^2}\right)^{\frac{3}{2}} \int\int \frac{e^{-\sigma_i r_i^2} e^{-\sigma_j r_j^2}}{|\mathbf{r}-\mathbf{r}'|} d\mathbf{r}d\mathbf{r}' \\
&= \left(\frac{\sigma_i\sigma_j}{\pi^2}\right)^{\frac{3}{2}} \int \exp(-\sigma_j r_j^2) \left[\int \frac{\exp(-\sigma_i r_i^2)}{|\mathbf{r}-\mathbf{r}'|} d\mathbf{r}\right] d\mathbf{r}' \\
&= \left(\frac{\sigma_i\sigma_j}{\pi^2}\right)^{\frac{3}{2}} \int \exp(-\sigma_j r_j^2)\Phi(\mathbf{r}')d\mathbf{r}',
\end{aligned} \tag{A.3}$$

where $r_i = |\mathbf{r} - \mathbf{R}_i|$ and $r_j = |\mathbf{r}' - \mathbf{R}_j|$, and

$$\Phi(\mathbf{r}') = \int \frac{\exp(-\sigma_i r_i^2)}{|\mathbf{r} - \mathbf{r}'|} d\mathbf{r} \tag{A.4}$$

Noting

$$\frac{1}{x} = \frac{1}{\sqrt{\pi}} \int_{-\infty}^{+\infty} \exp(-t^2 x^2) dt, \tag{A.5}$$

if we denote $\mathbf{r}_p = \mathbf{r} - \mathbf{r}'$

$$|\mathbf{r} - \mathbf{r}'|^{-1} = \frac{1}{\sqrt{\pi}} \int_{-\infty}^{+\infty} \exp(-t^2 r_p^2) dt. \tag{A.6}$$

Then

$$\begin{aligned} \Phi(\mathbf{r}') &= \frac{1}{\sqrt{\pi}} \int \exp(-\sigma_i r_i^2) \int_{-\infty}^{+\infty} \exp(-t^2 r_p^2) dt d\mathbf{r} \\ &= \frac{1}{\sqrt{\pi}} \int_{-\infty}^{+\infty} \int \exp(-\sigma_i r_i^2) \exp(-t^2 r_p^2) d\mathbf{r} dt \\ &= \frac{1}{\sqrt{\pi}} \int_{-\infty}^{+\infty} \left\{ \int \exp\left[-(\sigma_i + t^2) r_s^2\right] d\mathbf{r} \right\} \exp\left(-\frac{t^2 \sigma_i}{t^2 + \sigma_i} R_{PI}^2 \right) dt, \end{aligned} \tag{A.7}$$

where

$$\mathbf{r}_s = \frac{t^2 \mathbf{r}_p + \sigma_i \mathbf{r}_i}{t^2 + \sigma_i}, r_s = |\mathbf{r}_s|, R_{pi} = |\mathbf{r}' - \mathbf{R}_i|. \tag{A.8}$$

Because

$$\int \exp\left[-(\sigma_i + t^2) r_s^2\right] d\mathbf{r} = \pi^{\frac{3}{2}} \left(\sigma_i + t^2\right)^{-\frac{3}{2}}, \tag{A.9}$$

Eq. A.7 becomes

$$\Phi(\mathbf{r}') = 2\pi \int_0^{+\infty} \left(\sigma_i + t^2\right)^{-\frac{3}{2}} \exp\left(-\frac{t^2 \sigma_i}{t^2 + \sigma_i} R_{pi}^2 \right) dt. \tag{A.10}$$

Introducing

$$u^2 = \frac{t^2}{\sigma_i + t^2} \tag{A.11}$$

then

$$\Phi(\mathbf{r}') = 2\pi \int_0^1 \frac{1}{\sigma_i} \exp\left(-\sigma_i u^2 R_{pi}^2\right) du = \left(\frac{\pi}{\sigma_i}\right)^{\frac{3}{2}} \frac{\operatorname{erf} \sqrt{\sigma_i} R_{pi}}{R_{pi}} \tag{A.12}$$

Inserting Eq. A.12 into Eq. A.3

$$\begin{aligned}\hat{\Gamma}^{00}_{ij,\mathrm{GTO}} &= 2\left(\frac{\sigma_i}{\pi}\right)^{\frac{1}{2}}\left(\frac{\sigma_j}{\pi}\right)^{\frac{3}{2}}\int \exp\left(-\sigma_j r_j^2\right)\int_0^1 \exp\left(-\sigma_i u^2 R_{pi}^2\right) du\, d\mathbf{r}' \\ &= 2\left(\frac{\sigma_i}{\pi}\right)^{\frac{1}{2}}\left(\frac{\sigma_j}{\pi}\right)^{\frac{3}{2}}\int_0^1 \left\{\int \exp\left[-(\sigma_j+\sigma_i t^2) r_m^2\right] d\mathbf{r}'\right\} \exp\left(-\frac{\sigma_i\sigma_j t^2}{\sigma_j+\sigma_i t^2} R_{ij}^2\right) du\end{aligned} \tag{A.13}$$

where

$$\mathbf{r}_m = \frac{\sigma_i t^2 \mathbf{R}_{pi} + \sigma_j \mathbf{r}_j}{t^2\sigma_i + \sigma_j} \qquad R_{ij} = |\mathbf{R}_i - \mathbf{R}_j|. \tag{A.14}$$

Similar as Eq. A.9, we have

$$\hat{\Gamma}^{00}_{ij,\mathrm{GTO}} = 2\sigma_i^{\frac{1}{2}}\sigma_j^{\frac{3}{2}}\pi^{-\frac{1}{2}}\int_0^1 \left(\sigma_j+\sigma_i t^2\right)^{-\frac{3}{2}} \exp\left(-\frac{\sigma_i\sigma_j t^2}{\sigma_j+\sigma_i t^2} R_{ij}^2\right) du. \tag{A.15}$$

Introducing

$$v^2 = \frac{u^2}{\frac{\sigma_j}{\sigma_i}+u^2}, \tag{A.16}$$

we have

$$\begin{aligned}\hat{\Gamma}^{00}_{ij,\mathrm{GTO}} &= 2\sigma_j^{\frac{1}{2}}\pi^{-\frac{1}{2}}\int_0^{\sqrt{\frac{\sigma_i}{\sigma_i+\sigma_j}}} \exp\left(-\sigma_j v^2 R_{ij}^2\right) dv \\ &= 2\sigma_j^{\frac{1}{2}}\pi^{-\frac{1}{2}}\int_0^1 \exp\left(-\frac{\sigma_i\sigma_j}{\sigma_i+\sigma_j}x^2 R_{ij}^2\right)\sqrt{\frac{\sigma_i}{\sigma_i+\sigma_j}}\, dx \\ &= \frac{\mathrm{erf}\left(\sqrt{\frac{\sigma_i\sigma_j}{\sigma_i+\sigma_j}} R_{ij}\right)}{R_{ij}}.\end{aligned} \tag{A.17}$$

When $i=j$, $R_{ij}=0$ and

$$\hat{\Gamma}^{00}_{ii,\mathrm{GTO}} = \lim_{R_{ij}\to 0}\frac{\mathrm{erf}\left(\sqrt{\frac{\sigma_i\sigma_j}{\sigma_i+\sigma_j}} R_{ij}\right)}{R_{ij}} = \sqrt{\frac{2\sigma_i}{\pi}} \tag{A.18}$$

This result is in agreement with Mayer [138] and Koskinen and Mäkinen [115].

We now consider the case when a Slater-type distribution is used. $\rho^{\mathrm{iso}}_{i,\mathrm{STO}}(r_i)$ is defined in Eq. 3.27

$$\rho^{\mathrm{iso}}_{i,\mathrm{STO}}(r_i) = \frac{\tau_i^3}{8\pi} e^{-\tau_i|\mathbf{r}-\mathbf{R}_i|}. \tag{A.19}$$

Inserting Eq. 3.27 into Eq. 3.25

$$
\begin{aligned}
\hat{\Gamma}^{00}_{ij,\mathrm{STO}} &= \int\int \frac{\frac{\tau_i^3}{8\pi} e^{-\tau_i|\mathbf{r}-\mathbf{R}_i|} \frac{\tau_j^3}{8\pi} e^{-\tau_j|\mathbf{r}'-\mathbf{R}_j|}}{|\mathbf{r}-\mathbf{r}'|} d\mathbf{r} d\mathbf{r}' \\
&= \frac{\tau_i^3}{8\pi}\frac{\tau_j^3}{8\pi} \int \exp(-\tau_j r_j) \left[\int \frac{\exp(-\tau_i r_i)}{|\mathbf{r}-\mathbf{r}'|} d\mathbf{r} \right] d\mathbf{r}' \\
&= \frac{\tau_i^3}{8\pi}\frac{\tau_j^3}{8\pi} \int \exp(-\tau_j r_j) \Phi(\mathbf{r}') d\mathbf{r}',
\end{aligned}
\tag{A.20}
$$

where r_i and r_j are as before, and

$$
\Phi(\mathbf{r}') = \int \frac{\exp(-\tau_i r_i)}{|\mathbf{r}-\mathbf{r}'|} d\mathbf{r}. \tag{A.21}
$$

Introducing the prolate spheroidal coordinates [184]

$$
\sigma = \frac{1}{R_{pi}} \left(|\mathbf{r}-\mathbf{r}'| + |\mathbf{r}-\mathbf{R}_i| \right), \quad \lambda = \frac{1}{R_{pi}} \left(|\mathbf{r}-\mathbf{r}'| - |\mathbf{r}-\mathbf{R}_i| \right), \quad R_{pi} = |\mathbf{r}'-\mathbf{R}_i|, \tag{A.22}
$$

where $\sigma \in [1, +\infty]$, $\lambda \in [-1, +1]$, $\phi \in [0, 2\pi]$ and $dV = \left(\frac{R_{pi}}{2}\right)^3 (\sigma^2 - \lambda^2) d\sigma d\lambda d\phi$. Therefore

$$
\begin{aligned}
\Phi(\mathbf{r}') &= \int \frac{\exp\left(\frac{-\tau_i(\sigma-\lambda)R_{pi}}{2}\right)}{\frac{(\sigma+\lambda)R_{pi}}{2}} dV \\
&= \int_0^{2\pi} d\phi \int_1^{+\infty} d\sigma \int_{-1}^{1} d\lambda \left(\frac{R_{pi}}{2}\right)^3 (\sigma^2-\lambda^2) \frac{\exp\left(\frac{-\tau_i(\sigma-\lambda)R_{pi}}{2}\right)}{\frac{(\sigma+\lambda)R_{pi}}{2}} \\
&= \frac{\pi R_{pi}^2}{2} \int_1^{+\infty} d\sigma \int_{-1}^{1} d\lambda (\sigma-\lambda) \exp\left[-\frac{\tau_i R_{pi}}{2} (\sigma-\lambda) \right].
\end{aligned}
\tag{A.23}
$$

We now let

$$
\omega = \frac{\tau_i R_{pi}}{2}, \tag{A.24}
$$

so that

$$
\begin{aligned}
\Phi(\mathbf{r}') &= \frac{\pi R_{pi}^2}{2} \frac{-\partial}{\partial\omega} \int_1^{+\infty} d\sigma \int_{-1}^{1} d\lambda \exp\left[-\omega(\sigma-\lambda)\right] \\
&= \frac{-\pi R_{pi}^2}{2} \left[\frac{2e^{-2\omega}}{\omega^2} - \frac{2}{\omega^3}\left(1-e^{-2\omega}\right) \right] \\
&= \frac{8\pi}{\tau_i^3} \frac{1}{R_{pi}} \left[1 - \left(1 + \frac{\tau_i R_{pi}}{2} \right) \exp(-\tau_i R_{pi}) \right].
\end{aligned}
\tag{A.25}
$$

Inserting Eq. A.25 into Eq. A.20 gives

$$\hat{\Gamma}^{00}_{ij,\mathrm{STO}} = \frac{\tau_j^3}{8\pi}\int \frac{1}{R_{pi}}\exp\left(-\tau_j r_j\right)\left[1-\left(1+\frac{\tau_i R_{pi}}{2}\right)\exp\left(-\tau_i R_{pi}\right)\right]d\mathbf{r}'. \tag{A.26}$$

Introducing the prolate spheroidal coordinates again

$$\sigma = \frac{1}{R_{ij}}\left(|\mathbf{r}'-\mathbf{R}_i|+|\mathbf{r}'-\mathbf{R}_j|\right), \quad \lambda = \frac{1}{R_{ij}}\left(|\mathbf{r}'-\mathbf{R}_i|-|\mathbf{r}'-\mathbf{R}_j|\right), \quad R_{ij} = |\mathbf{R}_i-\mathbf{R}_j|, \tag{A.27}$$

this becomes

$$\begin{aligned}\hat{\Gamma}^{00}_{ij,\mathrm{STO}} = \frac{\tau_j^3}{8\pi}\int_0^{2\pi} d\phi \int_1^{+\infty} d\sigma \int_{-1}^{1} d\lambda \left(\frac{R_{ij}}{2}\right)^3 (\sigma^2-\lambda^2) \\ \frac{2}{(\sigma+\lambda)R_{ij}}\exp\left[-\frac{\tau_j R_{ij}}{2}(\sigma-\lambda)\right]\left[1-\left(1+\frac{\tau_i(\sigma+\lambda)R_{ij}}{4}\right)\exp\left[-\frac{\tau_i R_{ij}}{2}(\sigma+\lambda)\right]\right].\end{aligned} \tag{A.28}$$

Repeating the integration performed in evaluating $\Phi(\mathbf{r}')$ yields

$$\begin{aligned}\hat{\Gamma}^{00}_{ij,\mathrm{STO}} = \frac{1}{R_{ij}} - e^{-\tau_i R_{ij}}\left(\frac{\tau_j^4\tau_i}{2(\tau_i^2-\tau_j^2)^2} - \frac{\tau_j^6-3\tau_j^4\tau_i^2}{(\tau_i^2-\tau_j^2)^3 R_{ij}}\right) \\ - e^{-\tau_j R_{ij}}\left(\frac{\tau_i^4\tau_j}{2(\tau_j^2-\tau_i^2)^2} - \frac{\tau_i^6-3\tau_i^4\tau_j^2}{(\tau_j^2-\tau_i^2)^3 R_{ij}}\right).\end{aligned} \tag{A.29}$$

When $\tau_i = \tau_j$ and $i \neq j$

$$\begin{aligned}\hat{\Gamma}^{00}_{ij,\mathrm{STO}} = \lim_{(\tau_i-\tau_j)\to 0}\{\frac{1}{R_{ij}} - e^{-\tau_i R_{ij}}\left(\frac{\tau_j^4\tau_i}{2(\tau_i^2-\tau_j^2)^2} - \frac{\tau_j^6-3\tau_j^4\tau_i^2}{(\tau_i^2-\tau_j^2)^3 R_{ij}}\right) \\ - e^{-\tau_j R_{ij}}\left(\frac{\tau_i^4\tau_j}{2(\tau_j^2-\tau_i^2)^2} - \frac{\tau_i^6-3\tau_i^4\tau_j^2}{(\tau_j^2-\tau_i^2)^3 R_{ij}}\right)\} \\ = \frac{1}{R_{ij}} - e^{-\tau_i R_{ij}}\left(\frac{1}{R_{ij}} + \frac{11}{16}\tau_i + \frac{3}{16}\tau_i^2 R_{ij} + \frac{1}{48}\tau_i^3 R_{ij}^2\right).\end{aligned} \tag{A.30}$$

When $i = j$, $R_{ij} = 0$, this becomes

$$\begin{aligned}\hat{\Gamma}^{00}_{ii,\mathrm{STO}} = \lim_{R_{ij}\to 0}\{\frac{1}{R_{ij}} - e^{-\tau_i R_{ij}}\left(\frac{1}{R_{ij}} + \frac{11}{16}\tau_i + \frac{3}{16}\tau_i^2 R_{ij} + \frac{1}{48}\tau_i^3 R_{ij}^2\right)\} \\ = \frac{5}{16}\tau_i.\end{aligned} \tag{A.31}$$

This is in agreement with that given by Elsner [117].

A.2 $\hat{\Gamma}^{10}_{ij}$

As defined in Eq. 3.72

$$\hat{\Gamma}^{10}_{ij} = \nabla_{\mathbf{R}_i} \int\int \frac{\rho_i^{\mathrm{iso}}(r_i)\rho_j^{\mathrm{iso}}(r_j)}{|\mathbf{r}-\mathbf{r}'|} d\mathbf{r} d\mathbf{r}' = \nabla_{\mathbf{R}_i} \hat{\Gamma}^{00}_{ij}. \tag{A.32}$$

For the Gaussian-type distribution, this gives immediately

$$\hat{\Gamma}^{10}_{ij,\mathrm{GTO}} = \frac{\mathbf{R}_{ij}}{R^3_{ij}} \left[-\mathrm{erf}\left(\sqrt{\frac{\sigma_i\sigma_j}{\sigma_i+\sigma_j}} R_{ij} \right) + \sqrt{\frac{4\sigma_i\sigma_j}{\pi(\sigma_i+\sigma_j)}} R_{ij} e^{-\frac{\sigma_i\sigma_j}{\sigma_i+\sigma_j} R^2_{ij}} \right], \tag{A.33}$$

while for the Slater-type distribution, the result is

$$\hat{\Gamma}^{10}_{ij,\mathrm{STO}} = -\frac{\mathbf{R}_{ij}}{R^3_{ij}} - \mathbf{R}_{ij} \begin{cases} e^{-\tau_i R_{ij}} \left(-\frac{\tau_j^4 \tau_i}{2(\tau_i^2-\tau_j^2)^2} \frac{\tau_i}{R_{ij}} + \frac{\tau_j^6 - 3\tau_j^4\tau_i^2}{(\tau_i^2-\tau_j^2)^3} \frac{\tau_i}{R^2_{ij}} + \frac{\tau_j^6-3\tau_j^4\tau_i^2}{(\tau_i^2-\tau_j^2)^3} \frac{1}{R^3_{ij}} \right) & \\ + e^{-\tau_j R_{ij}} \left(-\frac{\tau_i^4 \tau_j}{2(\tau_j^2-\tau_i^2)^2} \frac{\tau_j}{R_{ij}} + \frac{\tau_i^6 - 3\tau_i^4\tau_j^2}{(\tau_j^2-\tau_i^2)^3} \frac{\tau_j}{R^2_{ij}} + \frac{\tau_i^6-3\tau_i^4\tau_j^2}{(\tau_j^2-\tau_i^2)^3} \frac{1}{R^3_{ij}} \right) & i \neq j, \tau_i \neq \tau_j \\ -e^{-\tau_i R_{ij}} \left(\frac{1}{R^3_{ij}} + \frac{\tau_i}{R^2_{ij}} + \frac{\tau_i^2}{2R_{ij}} + \frac{7\tau_i^3}{48} + \frac{\tau_i^4 R_{ij}}{48} \right) & i \neq j, \tau_i = \tau_j \end{cases} \tag{A.34}$$

Because of symmetry, the on-site values for $\hat{\Gamma}^{10}_{ii,\mathrm{GTO}}$ and $\hat{\Gamma}^{10}_{ii,\mathrm{STO}}$ are both $\mathbf{0}$.

A.3 $\hat{\Gamma}^{11}_{ij}$

As defined in Eq. 3.73

$$\begin{aligned} \hat{\Gamma}^{11}_{ij} &= \nabla_{\mathbf{R}_j} \otimes \nabla_{\mathbf{R}_i} \int\int \frac{\rho_i^{\mathrm{iso}}(r_i)\rho_j^{\mathrm{iso}}(r_j)}{|\mathbf{r}-\mathbf{r}'|} d\mathbf{r} d\mathbf{r}' \\ &= \nabla_{\mathbf{R}_j} \otimes \nabla_{\mathbf{R}_i} \hat{\Gamma}^{00}_{ij} \\ &= \nabla_{\mathbf{R}_j} \otimes \hat{\Gamma}^{10}_{ij} = -\nabla_{\mathbf{R}_i} \otimes \hat{\Gamma}^{10}_{ij}. \end{aligned} \tag{A.35}$$

In this case, $\nabla_{\mathbf{R}_i}$ is differentiation with respect to the same vector as in $\hat{\Gamma}^{10}_{ij}$.

For arbitrary vector $\mathbf{a} = (a_x, a_y, a_z)$

$$\nabla \otimes \mathbf{a} = \begin{bmatrix} \frac{\partial a_x}{\partial x} & \frac{\partial a_y}{\partial x} & \frac{\partial a_z}{\partial x} \\ \frac{\partial a_x}{\partial y} & \frac{\partial a_y}{\partial y} & \frac{\partial a_z}{\partial y} \\ \frac{\partial a_x}{\partial z} & \frac{\partial a_y}{\partial z} & \frac{\partial a_z}{\partial z} \end{bmatrix}. \tag{A.36}$$

For both Gaussian-type distribution and Slater-type distribution cases, $\hat{\Gamma}^{10}_{ij}$ has the form

$$\hat{\Gamma}^{10}_{ij} = \mathbf{R}_{ij} F(\mathbf{R}_{ij}), \tag{A.37}$$

if we let

$$\mathbf{a} = \mathbf{r} F(r), \tag{A.38}$$

so that

$$a_x = xF(r), \quad a_y = yF(r), \quad a_z = zF(r), \tag{A.39}$$

the Eq. A.36 becomes

$$\begin{aligned} \nabla \otimes \mathbf{a} &= \begin{bmatrix} F + \frac{x^2}{r}\frac{\partial F}{\partial r} & \frac{xy}{r}\frac{\partial F}{\partial r} & \frac{xz}{r}\frac{\partial F}{\partial r} \\ \frac{xy}{r}\frac{\partial F}{\partial r} & F + \frac{y^2}{r}\frac{\partial F}{\partial r} & \frac{yz}{r}\frac{\partial F}{\partial r} \\ \frac{xz}{r}\frac{\partial F}{\partial r} & \frac{yz}{r}\frac{\partial F}{\partial r} & F + \frac{z^2}{r}\frac{\partial F}{\partial r}, \end{bmatrix} \\ &= F\mathbf{I} + \frac{1}{r}\frac{\partial F}{\partial r}\mathbf{r} \otimes \mathbf{r}, \end{aligned} \tag{A.40}$$

where $\mathbf{I}$ is the 3×3 identity matrix.

Therefore, for the Gaussian-type distribution

$$\begin{aligned} \hat{\Gamma}^{11}_{ij,\mathrm{GTO}} = {} & \frac{3\mathbf{R}_{ij} \otimes \mathbf{R}_{ij} - R^2_{ij}\mathbf{I}}{R^5_{ij}} \left[-\operatorname{erf}\left(\sqrt{\frac{\sigma_i \sigma_j}{\sigma_i + \sigma_j}} R_{ij} \right) + \sqrt{\frac{4\sigma_i \sigma_j}{\pi(\sigma_i + \sigma_j)}} R_{ij} e^{-\frac{\sigma_i \sigma_j}{\sigma_i + \sigma_j} R^2_{ij}} \right] \\ & + \frac{1}{R^2_{ij}} \sqrt{\frac{16\sigma^3_i \sigma^3_j}{\pi(\sigma_i + \sigma_j)^3}} e^{-\frac{\sigma_i \sigma_j}{\sigma_i + \sigma_j} R^2_{ij}} \mathbf{R}_{ij} \otimes \mathbf{R}_{ij}. \end{aligned} \tag{A.41}$$

The on-site $\hat{\Gamma}^{11}_{ii,\mathrm{GTO}}$ is the limit of Eq. A.41 as $\mathbf{R}_{ij}$ approaches $\mathbf{0}$, which is

$$\hat{\Gamma}^{11}_{ii,\mathrm{GTO}} = \lim_{\mathbf{R}_{ij} \to \mathbf{0}} \hat{\Gamma}^{11}_{ij,\mathrm{GTO}} = \frac{1}{3}\sqrt{\frac{2}{\pi}} \sigma^{3/2}_i. \tag{A.42}$$

For the case of the Slater-type distribution, the result is

$$\hat{\Gamma}^{11}_{ij,\mathrm{STO}} = \frac{-3\mathbf{R}_{ij} \otimes \mathbf{R}_{ij} + R^2_{ij}\mathbf{I}}{R^5_{ij}} + M_{ij}\mathbf{I} + N_{ij}\mathbf{R}_{ij} \otimes \mathbf{R}_{ij}, \tag{A.43}$$

where

$$M_{ij} = \begin{cases} e^{-\tau_i R_{ij}} \left(-\frac{\tau_j^4 \tau_i}{2(\tau_i^2-\tau_j^2)^2} \frac{\tau_i}{R_{ij}} + \frac{\tau_j^6 - 3\tau_j^4\tau_i^2}{(\tau_i^2-\tau_j^2)^3} \frac{\tau_i}{R_{ij}^2} + \frac{\tau_j^6-3\tau_j^4\tau_i^2}{(\tau_i^2-\tau_j^2)^3} \frac{1}{R_{ij}^3} \right) \\ + e^{-\tau_j R_{ij}} \left(-\frac{\tau_i^4 \tau_j}{2(\tau_j^2-\tau_i^2)^2} \frac{\tau_j}{R_{ij}} + \frac{\tau_i^6 - 3\tau_i^4\tau_j^2}{(\tau_j^2-\tau_i^2)^3} \frac{\tau_j}{R_{ij}^2} + \frac{\tau_i^6-3\tau_i^4\tau_j^2}{(\tau_j^2-\tau_i^2)^3} \frac{1}{R_{ij}^3} \right) & i \neq j, \tau_i \neq \tau_j \\ \\ -e^{-\tau_i R_{ij}} \left(\frac{1}{R_{ij}^3} + \frac{\tau_i}{R_{ij}^2} + \frac{\tau_i^2}{2R_{ij}} + \frac{7\tau_i^3}{48} + \frac{\tau_i^4 R_{ij}}{48} \right) & i \neq j, \tau_i = \tau_j \end{cases} \tag{A.44}$$

$$N_{ij} = \begin{cases} e^{-\tau_i R_{ij}} \left[\frac{\tau_j^4 \tau_i}{2(\tau_i^2-\tau_j^2)^2} \frac{\tau_i^2}{R_{ij}^2} + \left(\frac{\tau_j^4\tau_i}{2(\tau_i^2-\tau_j^2)^2} \tau_i - \frac{\tau_j^6-3\tau_j^4\tau_i^2}{(\tau_i^2-\tau_j^2)^3} \tau_i^2 \right) \frac{1}{R_{ij}^3} - 3\frac{\tau_j^6-3\tau_j^4\tau_i^2}{(\tau_i^2-\tau_j^2)^3} \frac{\tau_i}{R_{ij}^4} - 3\frac{\tau_j^6-3\tau_j^4\tau_i^2}{(\tau_i^2-\tau_j^2)^3} \frac{1}{R_{ij}^5} \right] \\ + e^{-\tau_j R_{ij}} \left[\frac{\tau_i^4 \tau_j}{2(\tau_j^2-\tau_i^2)^2} \frac{\tau_j^2}{R_{ij}^2} + \left(\frac{\tau_i^4\tau_j}{2(\tau_j^2-\tau_i^2)^2} \tau_j - \frac{\tau_i^6-3\tau_i^4\tau_j^2}{(\tau_j^2-\tau_i^2)^3} \tau_j^2 \right) \frac{1}{R_{ij}^3} - 3\frac{\tau_i^6-3\tau_i^4\tau_j^2}{(\tau_j^2-\tau_i^2)^3} \frac{\tau_j}{R_{ij}^4} - 3\frac{\tau_i^6-3\tau_i^4\tau_j^2}{(\tau_j^2-\tau_i^2)^3} \frac{1}{R_{ij}^5} \right] \\ \qquad\qquad i \neq j, \tau_i \neq \tau_j \\ \\ e^{-\tau_i R_{ij}} \left(\frac{3}{R_{ij}^5} + \frac{3\tau_i}{R_{ij}^4} + \frac{3\tau_i^2}{2R_{ij}^3} + \frac{\tau_i^3}{2R_{ij}^2} + \frac{\tau_i^4}{8R_{ij}} + \frac{\tau_i^5}{48} \right) \\ \qquad\qquad i \neq j, \tau_i = \tau_j. \end{cases} \tag{A.45}$$

In this case,

$$\hat{\Gamma}^{11}_{ii,\mathrm{STO}} = \lim_{\mathbf{R}_{ij} \to \mathbf{0}} \hat{\Gamma}^{11}_{ij,\mathrm{STO}} = \frac{1}{48}\tau_i^3. \tag{A.46}$$

Appendix B

Slater-Koster integrals

The Slater-Koster integrals $S^{\tau}_{\mu\nu}$ (see Section 3.1) are calculated numerically, using a homogeneous double grid of radial and angular points which specifying $\Delta r = r_{\text{cutoff}}/n_{max}$ and $\Delta\theta = \pi/m_{max}$ respectively:

$$\begin{aligned} r_n &= n\Delta r, \quad n = 1,2,...,n_{max} \\ \theta_{1,m} &= m\Delta\theta, \quad m = 1,2,...,m_{max}. \end{aligned} \tag{B.1}$$

The wave functions are generated with the additional confining potential (see Eq. 3.16), and so the cutoff radius r_{cutoff} is chosen to be slightly larger than the confining radius. For distance R_{ij}, $\tilde{r}$ and θ_2 are calculated accordingly

$$\begin{aligned} \tilde{r}_{n,m} &= \sqrt{r_n^2 + R_{ij}^2 - 2R_{ij}r_n\cos\theta_{1,m}} \\ \theta_{2,n,m} &= \pi - \arccos\frac{r_n\cos\theta_{1,m} - R_{ij}}{\tilde{r}_{n,m}}. \end{aligned} \tag{B.2}$$

Then

$$S^{\tau}_{\mu\nu} = \sum_n \sum_m R_{\mu}(r_n)R_{\nu}(\tilde{r}_{n,m})\Theta_{\tau}(\theta_{1,m},\theta_{2,n,m})r_n^2\sin\theta_{1,m}\Delta r\Delta\theta. \tag{B.3}$$

This method has been used to calculate $S^{\tau}_{\mu\nu}$ for the Carbon-Carbon pair, and the results compared with the existing Slater-Koster tabulated data published on the DFTB community [113]. The wave function R_{μ} used here is that referred as 'pbc-0-1' which is extracted using the "DFTB+" utilities "Waveplot", where it is defined as a linear combination of Slater-type functions. As shown in Fig. B.1, using the same radial function, $S^{\tau}_{\mu\nu}$ calculated using the above numerical scheme agrees very well, with the standard tabulation.

Given this success, a similar approach is used to calculate the Slater-Koster integrals needed

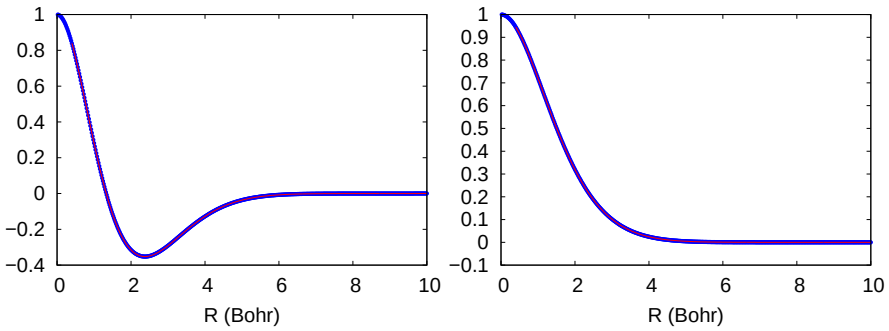

(a) $ss\sigma$ (b) $sp\sigma$

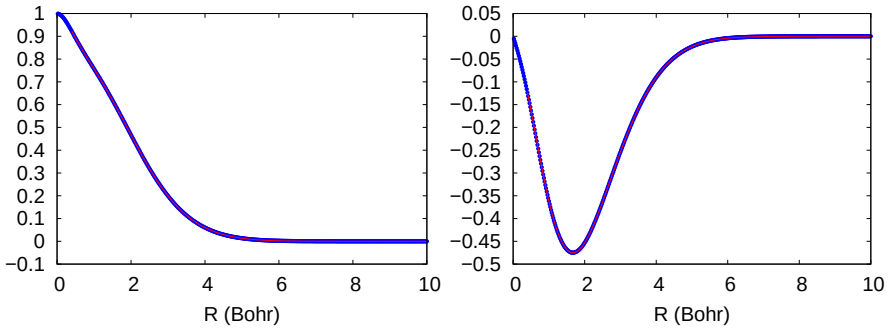

(c) $pp\sigma$ (d) $pp\pi$

Figure B.1: A comparison of Slater-Koster integrals for the Carbon-Carbon pair as a function of the bond length R calculated using the scheme described above (blue dots) or as in the standard tabulation [113] (red lines). The definition of τ for Carbon-Carbon are listed in Table. 3.2.

for the dipole matrix, namely $P^{\tau}_{\mu\nu}$ introduced in Section 3.2. They are found numerically as

$$P^{\tau}_{\mu\nu} = \sum_n \sum_m r_n^3 R_\mu(r_n) R_\nu(\tilde{r}_{n,m}) \Theta_\tau(\theta_{1,m}, \theta_{2,n,m}) \sin\theta_{1,m} \Delta r \Delta\theta. \tag{B.4}$$

and the $P^{\tau}_{\mu\nu}$ for Carbon-Carbon is shown in Fig B.2. Note the notation τ here is different than that of $S^{\tau}_{\mu\nu}$, the first two letters denote the radial part, and the remaining three letters has the same definition as $S^{\tau}_{\mu\nu}$, see Section 3.2.3 for details.

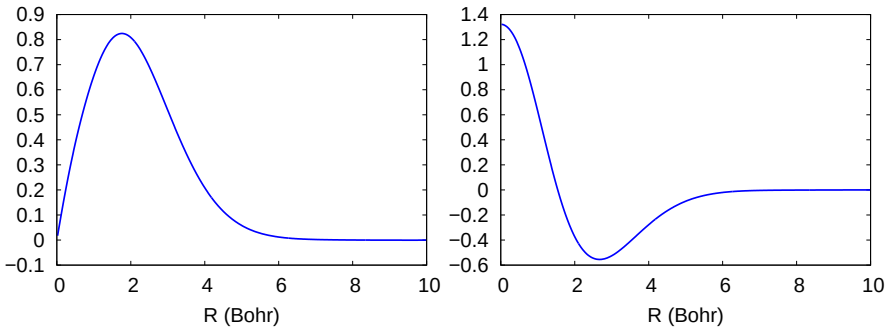

(a) $ss\,ps\sigma$ (b) $sp\,pp\sigma$

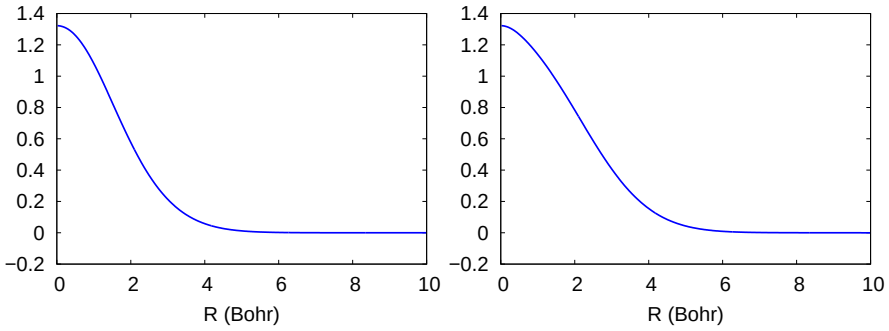

(c) $sp\,pp\pi$ (d) $ps\,ss\sigma$

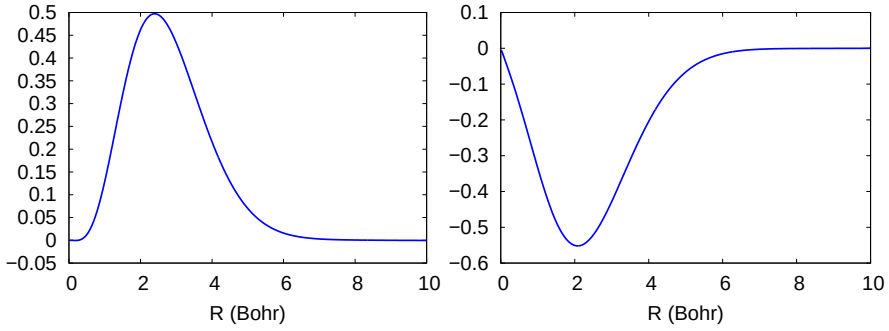

(e) $ps\,ds\sigma$ (f) $pp\,sp\sigma$

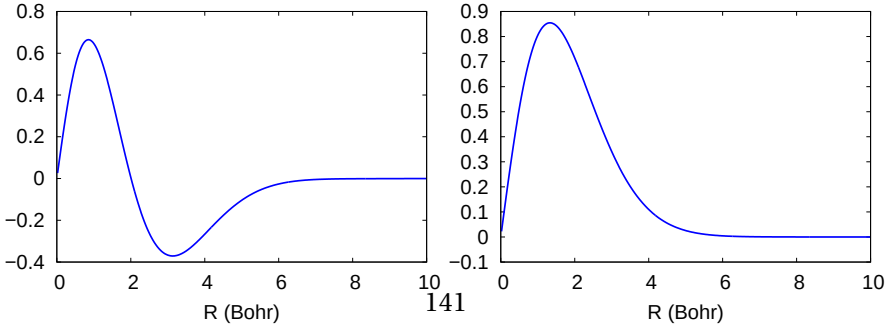

(g) $pp\,dp\sigma$ (h) $pp\,dp\pi$

Figure B.2: Calculated Slater-Koster integrals needed for dipole matrix of Carbon-Carbon pair, as a function of the bond length R using the scheme described above.

Appendix C

Additional results from DFTB

Here are some additional results from DFTB calculations. Details are in the captions.

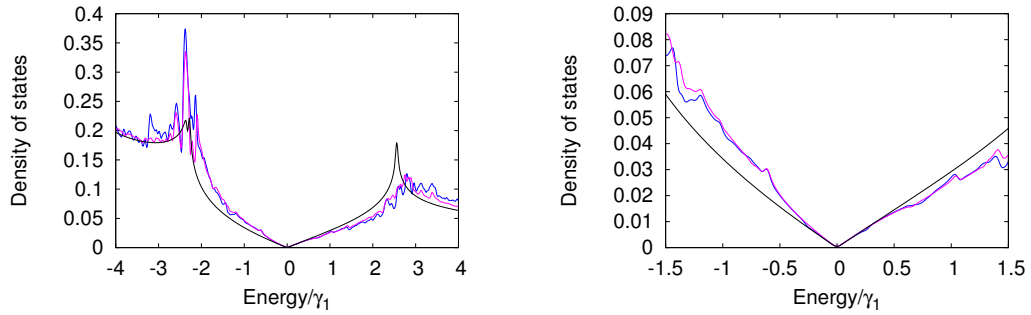

Figure C.1: LDOS of monolayer graphene on pits with two kinks. Blue (purple) line is the results from SCCD-DFTB (SCC-DFTB) of graphene with pits, and the black line is the LDOS for pure monolayer graphene.

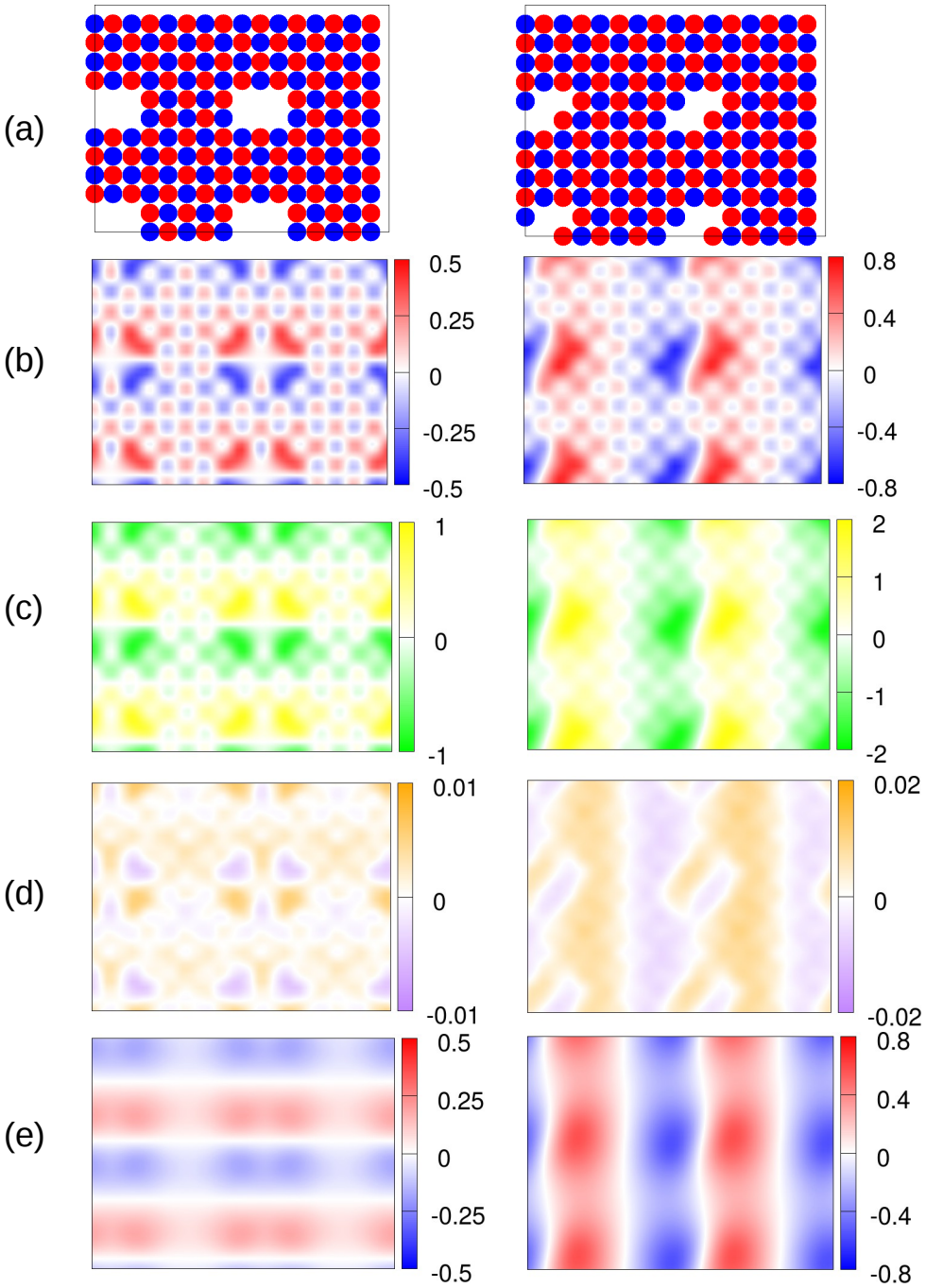

Figure C.2: Configurations and calculated electrostatic potential map (eV) of the bilayer graphene on KBr (001) with pits. Panels on the left (right) are the results from pits with no (two) kinks. a) Configurations of uppermost layer of the pits, red (blue) discs are K (Br) atoms. Calculated electrostatic potential maps on the b) lower layer graphene; d) upper layer graphene. External potential maps at the height of c) lower layer graphene; e) upper layer graphene. Note that the color ranges are different for left and right panels.

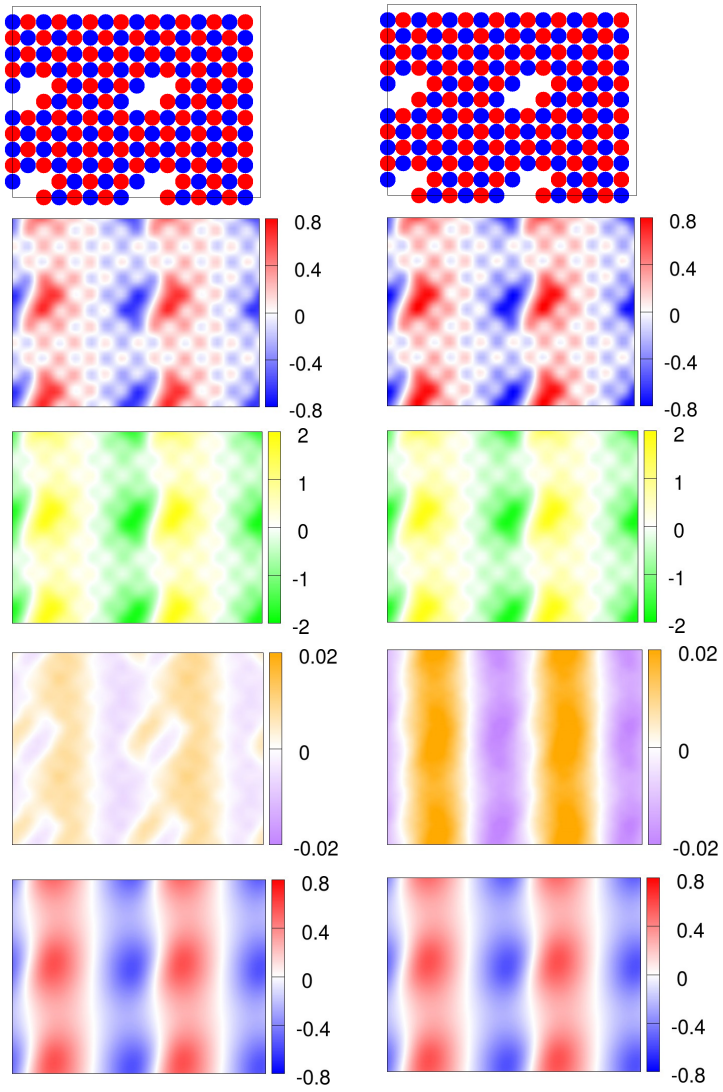

Figure C.3: Configurations and electrostatic potential obtained using different parameters of the bilayer graphene on pits with two kinks. Panels on the first row are the configurations of uppermost layer of the pits, red discs are K atoms and blue ones are Br; panels on the second (fourth) row are the electrostatic potential maps on the lower (upper) layer graphene; panels on the second (fourth) row are the external potential maps at the height of lower (upper) layer graphene. Left (right) panels are results with the parameter $r_0 = 2.0 r_{cov}$ ($r_0 = 3.5 r_{cov}$).

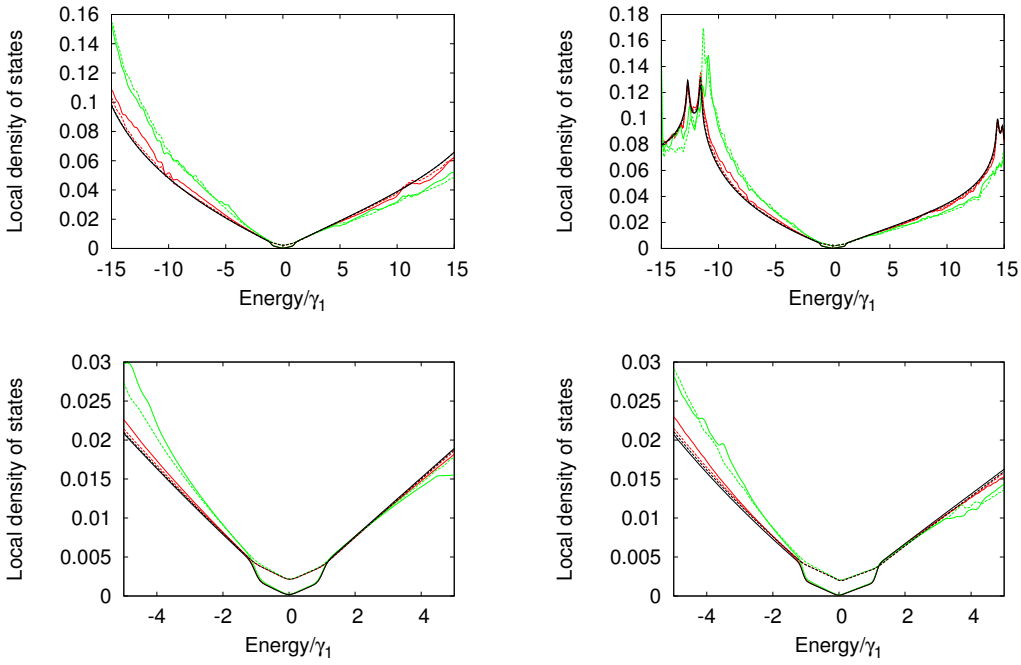

Figure C.4: LDOS of selected lower layer Carbon atoms of bilayer graphene on pits. Red, green and black lines is the result from the pits with no kink, two kinks and pure bilayer graphene. And the solid (dash) line indicates site B (site A). The upper (lower) panels are the calculated LDOS in large (small) range, and the left (right) panels are the LDOS calculated using the parameter $r_0 = 2.0 r_{cov}$ ($r_0 = 3.5 r_{cov}$).

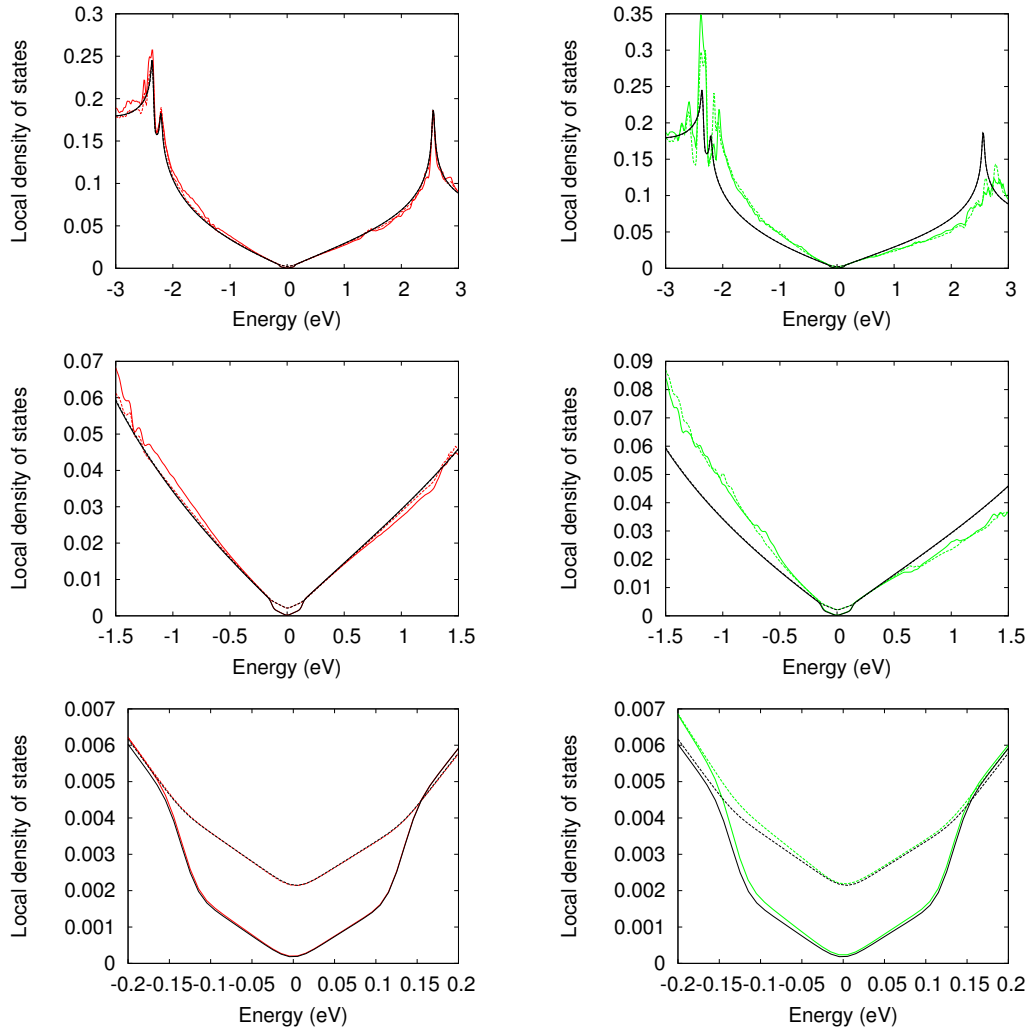

Figure C.5: LDOS of selected lower layer Carbon atoms of bilayer graphene on KBr (001) with pits. Panels on the left (right) are the results from pits with no (two) kinks. The black lines are the LDOS of pure bilayer graphene. The solid (dashed) line indicates site B (site A). The panels on each row are the LDOS in different energy range.

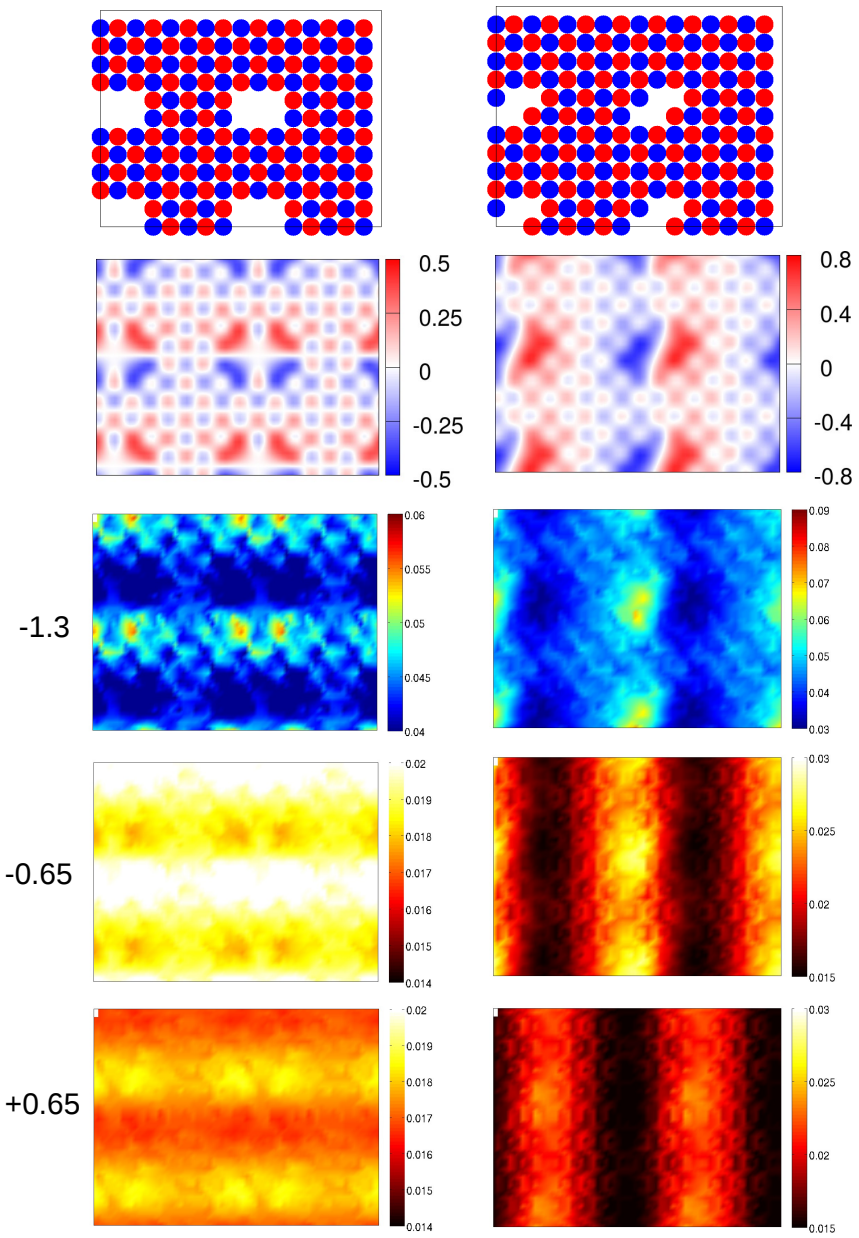

Figure C.6: Configurations, electrostatic potential (eV) and LDOS maps of the bilayer graphene on KBr (001) with pits. Panels on the left (right) are the results from pits with no (two) kinks. Panels on the first and second row are the configuration of the steps and the electrostatic potential on the upper layer graphene, the same as Fig. C.2a) and Fig. C.2b) . Panels from the third to fifth row are the LDOS of the lower layer graphene with the energy of $-10\gamma_1$ (-1.3 eV), $-5\gamma_1$ (-0.65 eV) and $5\gamma_1$ (0.65 eV), respectively.

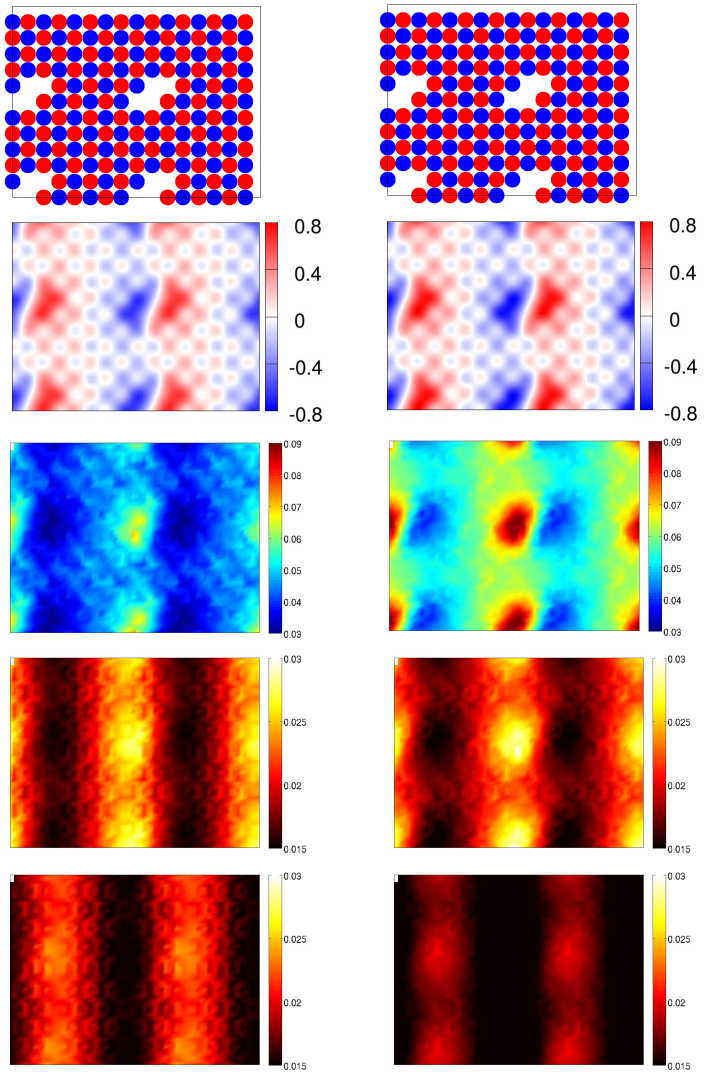

Figure C.7: Configurations, electrostatic potential (eV) and LDOS maps obtained using different parameters of the bilayer graphene on pits with two kinks. Panels on the first row and the second row are the same as Fig. C.3. Panels on the third, fourth and fifth row are the LDOS of the lower layer graphene with the energy of $-10\gamma_1$, $-5\gamma_1$ and $5\gamma_1$, respectively. Left (right) panels are results with the parameter $r_0 = 2.0r_{cov}$ ($r_0 = 3.5r_{cov}$).

Bibliography

[1] A. K. Geim and K. S. Novoselov, *Nature Materials*, 2007, **6**, 183–191.

[2] K. S. Novoselov, A. K. Geim, S. V. Morozov, D. Jiang, Y. Zhang, S. V. Dubonos, I. V. Grigorieva and A. A. Firsov, *Science*, 2004, **306**, 666–669.

[3] Nobelprize.org, *The Nobel Prize in Physics 2010*, 2010.

[4] C. Jacoboni, C. Canali, G. Ottaviani and A. Alberigi Quaranta, *Solid-State Electronics*, 1977, **20**, 77–89.

[5] P. R. Wallace, *Phys. Rev.*, 1947, **71**, 622–634.

[6] G. W. Semenoff, *Phys. Rev. Lett.*, 1984, **53**, 2449–2452.

[7] H. Boehm, R. Setton and E. Stumpp, *Carbon*, 1986, **24**, 241–245.

[8] R. E. Peierls, *Ann. I. H. Poincare*, 1935, **5**, 177–222.

[9] L. D. Landau, *Phys. Z. Sowjetunion*, 1937, **11**, 26–35.

[10] N. D. Mermin, *Phys. Rev.*, 1968, **176**, 250–254.

[11] J. C. Meyer, A. K. Geim, M. I. Katsnelson, K. S. Novoselov, T. J. Booth and S. Roth, *Nature*, 2007, **446**, 60–63.

[12] N. Savage, *Nature*, 2012, **483**, S38–S39.

[13] Y. Lin, A. Valdes-Garcia, S. Han, D. B. Farmer, I. Meric, Y. Sun, Y. Wu, C. Dimitrakopoulos, A. Grill, P. Avouris and K. A. Jenkins, *Science*, 2011, **332**, 1294–1297.

[14] M. Voutilainen, M. Rouvala and P. Pasanen, *Sensing of photons*, 2012, p. US 20120205518.

[15] C. Lee, X. Wei, J. W. Kysar and J. Hone, *Science*, 2008, **321**, 385–388.

[16] V. M. Pereira, A. H. Castro Neto and N. M. R. Peres, *Phys. Rev. B*, 2009, **80**, 045401.

[17] J. S. Bunch, S. S. Verbridge, J. S. Alden, A. M. van der Zande, J. M. Parpia, H. G. Craighead and P. L. McEuen, *Nano Letters*, 2008, **8**, 2458–2462.

[18] M. D. Stoller, S. Park, Y. Zhu, J. An and R. S. Ruoff, *Nano Letters*, 2008, **8**, 3498–3502.

[19] J. T. Robinson, M. Zalalutdinov, J. W. Baldwin, E. S. Snow, Z. Wei, P. Sheehan and B. H. Houston, *Nano Letters*, 2008, **8**, 3441–3445.

[20] J. S. Bunch, A. M. v. d. Zande, S. S. Verbridge, I. W. Frank, D. M. Tanenbaum, J. M. Parpia, H. G. Craighead and P. L. McEuen, *Science*, 2007, **315**, 490–493.

[21] F. Schedin, A. K. Geim, S. V. Morozov, E. W. Hill, P. Blake, M. I. Katsnelson and K. S. Novoselov, *Nature Materials*, 2007, **6**, 652–655.

[22] B. Huang, Z. Li, Z. Liu, G. Zhou, S. Hao, J. Wu, B.-L. Gu and W. Duan, *J. Phys. Chem. C*, 2008, **112**, 13442–13446.

[23] H. Chen, M. B. Müller, K. J. Gilmore, G. G. Wallace and D. Li, *Advanced Materials*, 2008, **20**, 3557–3561.

[24] A. A. Balandin, S. Ghosh, W. Bao, I. Calizo, D. Teweldebrhan, F. Miao and C. N. Lau, *Nano Letters*, 2008, **8**, 902–907.

[25] E. Pop, D. Mann, Q. Wang, K. Goodson and H. Dai, *Nano Letters*, 2006, **6**, 96–100.

[26] K. Saito, J. Nakamura and A. Natori, *Phys. Rev. B*, 2007, **76**, 115409.

[27] Z. Wang, R. Xie, C. T. Bui, D. Liu, X. Ni, B. Li and J. T. L. Thong, *Nano Letters*, 2011, **11**, 113–118.

[28] N. Li, J. Ren, L. Wang, G. Zhang, P. Hänggi and B. Li, *Rev. Mod. Phys.*, 2012, **84**, 1045–1066.

[29] L. Wang and B. Li, *Phys. Rev. Lett.*, 2007, **99**, 177208.

[30] L. Wang and B. Li, *Phys. Rev. Lett.*, 2008, **101**, 267203.

[31] K. F. Mak, M. Y. Sfeir, Y. Wu, C. H. Lui, J. A. Misewich and T. F. Heinz, *Phys. Rev. Lett.*, 2008, **101**, 196405.

[32] S. Thongrattanasiri, F. H. L. Koppens and F. J. Garcia de Abajo, *Phys. Rev. Lett.*, 2012, **108**, 047401.

[33] J. Liu, A. R. Wright, C. Zhang and Z. Ma, *Appl. Phys. Lett.*, 2008, **93**, 041106–041106–3.

[34] F. Bonaccorso, Z. Sun, T. Hasan and A. C. Ferrari, *Nature Photonics*, 2010, **4**, 611–622.

[35] Z. Sun, T. Hasan, F. Torrisi, D. Popa, G. Privitera, F. Wang, F. Bonaccorso, D. M. Basko and A. C. Ferrari, *ACS Nano*, 2010, **4**, 803–810.

[36] D. Cohen-Tanugi and J. C. Grossman, *Nano Letters*, 2012, **12**, 3602–3608.

[37] N. Mohanty and V. Berry, *Nano Letters*, 2008, **8**, 4469–4476.

[38] W. Hu, C. Peng, W. Luo, M. Lv, X. Li, D. Li, Q. Huang and C. Fan, *ACS Nano*, 2010, **4**, 4317–4323.

[39] M. Lemme, T. Echtermeyer, M. Baus and H. Kurz, *IEEE Electr. Device. L*, 2007, **28**, 282 –284.

[40] T. Echtermeyer, M. Lemme, M. Baus, B. Szafranek, A. Geim and H. Kurz, *IEEE Electr. Device. L*, 2008, **29**, 952 –954.

[41] R. Sordan, F. Traversi and V. Russo, *Appl. Phys. Lett.*, 2009, **94**, 073305.

[42] H. Wang, D. Nezich, J. Kong and T. Palacios, *IEEE Electr. Device. L*, 2009, **30**, 547 –549.

[43] F. Torrisi, T. Hasan, W. Wu, Z. Sun, A. Lombardo, T. S. Kulmala, G.-W. Hsieh, S. Jung, F. Bonaccorso, P. J. Paul, D. Chu and A. C. Ferrari, *ACS Nano*, 2012, **6**, 2992–3006.

[44] A. H. Castro Neto, F. Guinea, N. M. R. Peres, K. S. Novoselov and A. K. Geim, *Rev. Mod. Phys.*, 2009, **81**, 109–162.

[45] G. S. Painter and D. E. Ellis, *Phys. Rev. B*, 1970, **1**, 4747–4752.

[46] H. Ibach and H. Lüth, *Solid-State Physics: An Introduction to Principles of Materials Science*, Springer Science & Business Media, 2013.

[47] F. Bloch, *Z. Phys. A-Hadron. Nucl.*, 1929, **52**, 555–600.

[48] E. McCann, in *Graphene Nanoelectronics*, ed. H. Raza, Springer Berlin Heidelberg, 2011, pp. 237–275.

[49] S. Reich, J. Maultzsch, C. Thomsen and P. Ordejón, *Phys. Rev. B*, 2002, **66**, 035412.

[50] C. W. J. Beenakker, *Rev. Mod. Phys.*, 2008, **80**, 1337–1354.

[51] K. S. Novoselov, D. Jiang, F. Schedin, T. J. Booth, V. V. Khotkevich, S. V. Morozov and A. K. Geim, *P. Natl. Acad. Sci. USA*, 2005, **102**, 10451–10453.

[52] A. Gupta, G. Chen, P. Joshi, S. Tadigadapa and Eklund, *Nano Letters*, 2006, **6**, 2667–2673.

[53] A. C. Ferrari, J. C. Meyer, V. Scardaci, C. Casiraghi, M. Lazzeri, F. Mauri, S. Piscanec, D. Jiang, K. S. Novoselov, S. Roth and A. K. Geim, *Phys. Rev. Lett.*, 2006, **97**, 187401.

[54] J.-H. Chen, C. Jang, S. Xiao, M. Ishigami and M. S. Fuhrer, *Nature Nanotechnology*, 2008, **3**, 206–209.

[55] C. Berger, Z. Song, X. Li, X. Wu, N. Brown, C. Naud, D. Mayou, T. Li, J. Hass, A. N. Marchenkov, E. H. Conrad, P. N. First and W. A. d. Heer, *Science*, 2006, **312**, 1191–1196.

[56] K. V. Emtsev, A. Bostwick, K. Horn, J. Jobst, G. L. Kellogg, L. Ley, J. L. McChesney, T. Ohta, S. A. Reshanov, J. Röhrl, E. Rotenberg, A. K. Schmid, D. Waldmann, H. B. Weber and T. Seyller, *Nature Materials*, 2009, **8**, 203–207.

[57] T. Shen, J. J. Gu, M. Xu, Y. Q. Wu, M. L. Bolen, M. A. Capano, L. W. Engel and P. D. Ye, *Appl. Phys. Lett.*, 2009, **95**, 172105–172105–3.

[58] V. Geringer, M. Liebmann, T. Echtermeyer, S. Runte, M. Schmidt, R. Rückamp, M. C. Lemme and M. Morgenstern, *Phys. Rev. Lett.*, 2009, **102**, 076102.

[59] J. Kedzierski, P.-L. Hsu, P. Healey, P. Wyatt, C. Keast, M. Sprinkle, C. Berger and W. de Heer, *IEEE T. Electron. Dev.*, 2008, **55**, 2078 –2085.

[60] A. Mattausch and O. Pankratov, *Phys. Rev. Lett.*, 2007, **99**, 076802.

[61] P. A. Khomyakov, G. Giovannetti, P. C. Rusu, G. Brocks, J. van den Brink and P. J. Kelly, *Phys. Rev. B*, 2009, **79**, 195425.

[62] A. Reina, X. Jia, J. Ho, D. Nezich, H. Son, V. Bulovic, M. S. Dresselhaus and J. Kong, *Nano Letters*, 2009, **9**, 30–35.

[63] K. S. Kim, Y. Zhao, H. Jang, S. Y. Lee, J. M. Kim, K. S. Kim, J.-H. Ahn, P. Kim, J.-Y. Choi and B. H. Hong, *Nature*, 2009, **457**, 706–710.

[64] J. Vaari, J. Lahtinen and P. Hautojärvi, *Catalysis Letters*, 1997, **44**, 43–49.

[65] H. Ueta, M. Saida, C. Nakai, Y. Yamada, M. Sasaki and S. Yamamoto, *Surface Science*, 2004, **560**, 183–190.

[66] D. Starr, E. Pazhetnov, A. Stadnichenko, A. Boronin and S. Shaikhutdinov, *Surface Science*, 2006, **600**, 2688–2695.

[67] J. Coraux, A. T. N'Diaye, C. Busse and T. Michely, *Nano Letters*, 2008, **8**, 565–570.

[68] S. Marchini, S. Günther and J. Wintterlin, *Phys. Rev. B*, 2007, **76**, 075429.

[69] Y. Souzu and M. Tsukada, *Surface Science*, 1995, **326**, 42–52.

[70] A. Grüneis and D. V. Vyalikh, *Phys. Rev. B*, 2008, **77**, 193401.

[71] M. Amft, S. Lebegue, O. Eriksson and N. V. Skorodumova, *J. Phys. Cond. Matter*, 2011, **23**, 395001.

[72] C. R. Dean, A. F. Young, I. Meric, C. Lee, L. Wang, S. Sorgenfrei, K. Watanabe, T. Taniguchi, P. Kim, K. L. Shepard and J. Hone, *Nature Nanotechnology*, 2010, **5**, 722–726.

[73] G. Giovannetti, P. A. Khomyakov, G. Brocks, P. J. Kelly and J. van den Brink, *Phys. Rev. B*, 2007, **76**, 073103.

[74] C. Yelgel and G. Srivastava, *Appl. Surf. Sci.*, 2012, **258**, 8338–8342.

[75] C. H. Lui, L. Liu, K. F. Mak, G. W. Flynn and T. F. Heinz, *Nature*, 2009, **462**, 339–341.

[76] S. Akcöltekin, M. El Kharrazi, B. Köhler, A. Lorke and M. Schleberger, *Nanotechnology*, 2009, **20**, 155601.

[77] G. J. Jones, A. Kazemi, S. Crampin, M. Phillips and A. Ilie, *Appl. Phys. Express*, 2012, **5**, 045103.

[78] A. Kazemi Sheikh Shabani, *Engineering the wave function in graphene systems(PhD thesis)*, University of Bath, 2015.

[79] J. R. Williams, T. Low, M. S. Lundstrom and C. M. Marcus, *Nature Nanotechnology*, 2011, **6**, 222–225.

[80] R. Martin, *Electronic Structure: Basic Theory and Practical Methods*, Cambridge University Press, 2004.

[81] M. Born and R. Oppenheimer, *Ann. Phys. (Leipzig)*, 1927, **84**, 457–484.

[82] R. Shankar, *Principles of Quantum Mechanics*, Springer US, 2012.

[83] P. Hohenberg and W. Kohn, *Phys. Rev.*, 1964, **136**, B864–B871.

[84] W. Kohn and L. J. Sham, *Phys. Rev.*, 1965, **140**, A1133–A1138.

[85] L. H. Thomas, *Math. Proc. Cambridge.*, 1927, **23**, 542–548.

[86] E. Fermi, *Zeitschrift für Physik A Hadrons and Nuclei*, 1928, **48**, 73–79.

[87] E. H. Lieb, *Rev. Mod. Phys.*, 1981, **53**, 603–641.

[88] J. W. Sheldon, *Phys. Rev.*, 1955, **99**, 1291–1301.

[89] E. Teller, *Rev. Mod. Phys.*, 1962, **34**, 627–631.

[90] P. a. M. Dirac, *Math. Proc. Cambridge.*, 1930, **26**, 376–385.

[91] D. M. Ceperley and B. J. Alder, *Phys. Rev. Lett.*, 1980, **45**, 566–569.

[92] L. A. Cole and J. P. Perdew, *Phys. Rev. A*, 1982, **25**, 1265–1271.

[93] J. P. Perdew and A. Zunger, *Phys. Rev. B*, 1981, **23**, 5048–5079.

[94] S. H. Vosko, L. Wilk and M. Nusair, *Can. J. Phys.*, 1980, **58**, 1200–1211.

[95] M. D. Towler, A. Zupan and M. Causá, *Comput. Phys. Commun.*, 1996, **98**, 181–205.

[96] D. C. Langreth and J. P. Perdew, *Solid State Commun.*, 1975, **17**, 1425–1429.

[97] J. P. Perdew, K. Burke and M. Ernzerhof, *Phys. Rev. Lett.*, 1996, **77**, 3865–3868.

[98] J. P. Perdew and Y. Wang, *Phys. Rev. B*, 1992, **45**, 13244–13249.

[99] A. Ruzsinszky, G. I. Csonka and G. E. Scuseria, *J. Chem. Theory Comput.*, 2009, **5**, 763–769.

[100] S. Ross, *Measuring the Performance of Recent Generalized Gradient Approximations to Density Functional Theory in Molecules and Solids (PhD thesis)*, Ball State University, Muncie, Indiana, 2010.

[101] D. R. Hamann, M. Schlüter and C. Chiang, *Phys. Rev. Lett.*, 1979, **43**, 1494–1497.

[102] D. Vanderbilt, *Phys. Rev. B*, 1990, **41**, 7892–7895.

[103] W. J. Hehre, R. F. Stewart and J. A. Pople, *J. Chem. Phys.*, 1969, **51**, 2657–2664.

[104] A. D. McLean and G. S. Chandler, *J. Chem. Phys.*, 1980, **72**, 5639–5648.

[105] R. A. Kendall, T. H. D. Jr and R. J. Harrison, *J. Chem. Phys.*, 1992, **96**, 6796–6806.

[106] C. G. Broyden, *Math. Comp.*, 1965, **19**, 577–593.

[107] D. D. Johnson, *Phys. Rev. B*, 1988, **38**, 12807–12813.

[108] E. Runge and E. K. U. Gross, *Phys. Rev. Lett.*, 1984, **52**, 997–1000.

[109] F. Ortmann, F. Bechstedt and W. G. Schmidt, *Phys. Rev. B*, 2006, **73**, 205101.

[110] S. Grimme, *J. Comput. Chem.*, 2006, **27**, 1787–1799.

[111] P. Jurečka, J. Černý, P. Hobza and D. R. Salahub, *J. Comput. Chem.*, 2007, **28**, 555–569.

[112] A. Tkatchenko and M. Scheffler, *Phys. Rev. Lett.*, 2009, **102**, 073005.

[113] M. Elstner, D. Porezag, G. Jungnickel, J. Elsner, M. Haugk, T. Frauenheim, S. Suhai and G. Seifert, *Phys. Rev. B*, 1998, **58**, 7260.

[114] D. Porezag, T. Frauenheim, T. Köhler, G. Seifert and R. Kaschner, *Phys. Rev. B*, 1995, **51**, 12947.

[115] P. Koskinen and V. Mäkinen, *Comp. Mater. Sci.*, 2009, **47**, 237.

[116] H. Eschrig and I. Bergert, *Phys. Stat. Sol. (b)*, 1978, **90**, 621.

[117] J. Elsner, *Surfaces and Extended Defects in Wurtzite GaN (PhD thesis)*, Universität-Gesamthochschule Paderborn, Paderborn, 1998.

[118] R. S. Mulliken, *J. Chem. Phys.*, 1955, **23**, 1833.

[119] J. C. Slater and G. F. Koster, *Phys. Rev.*, 1954, **94**, 1498.

[120] W. Harrison, *Electronic Structure and the Properties of Solids: The Physics of the Chemical Bond*, Freeman, 1980.

[121] E. Wigner and J. Griffin, *Group Theory and Its Application to the Quantum Mechanics of Atomic Spectra*, Academic Press, 1959.

[122] B. Aradi, B. Hourahine and T. Frauenheim, *J. Phys. Chem. A*, 2007, **111**, 5678–5684.

[123] K. Hedberg, L. Hedberg, D. S. Bethune, C. A. Brown, H. C. Dorn, R. D. Johnson and M. D. Vries, *Science*, 1991, **254**, 410–412.

[124] R. Saito, G. Dresselhaus and M. Dresselhaus, *Physical Properties of Carbon Nanotubes*, Imperial College Press, 1998.

[125] E. K. Yu, D. A. Stewart and S. Tiwari, *Phys. Rev. B*, 2008, **77**, 195406.

[126] E. McCann and V. I. Fal'ko, *Phys. Rev. Lett.*, 2006, **96**, 086805.

[127] L. A. Falkovsky, *Phys. Rev. B*, 2009, **80**, 113413.

[128] F. Guinea, A. H. Castro Neto and N. M. R. Peres, *Phys. Rev. B*, 2006, **73**, 245426.

[129] P. Gava, M. Lazzeri, A. M. Saitta and F. Mauri, *Phys. Rev. B*, 2009, **79**, 165431.

[130] L. M. Zhang, Z. Q. Li, D. N. Basov, M. M. Fogler, Z. Hao and M. C. Martin, *Phys. Rev. B*, 2008, **78**, 235408.

[131] E. V. Castro, K. S. Novoselov, S. V. Morozov, N. M. R. Peres, J. M. B. L. dos Santos, J. Nilsson, F. Guinea, A. K. Geim and A. H. C. Neto, *Phys. Rev. Lett.*, 2007, **99**, 216802.

[132] H. Min, B. Sahu, S. K. Banerjee and A. H. MacDonald, *Phys. Rev. B*, 2007, **75**, 155115.

[133] S. Latil and L. Henrard, *Phys. Rev. Lett.*, 2006, **97**, 036803.

[134] E. Sohmen, J. Fink and W. Krätschmer, *Z. Physik B - Condensed Matter*, 1992, **86**, 87–92.

[135] R. Antoine, P. Dugourd, D. Rayane, E. Benichou, M. Broyer, F. Chandezon and C. Guet, *J. Chem. Phys.*, 1999, **110**, 9771–9772.

[136] I. Compagnon, R. Antoine, M. Broyer, P. Dugourd, J. Lermé and D. Rayane, *Phys. Rev. A*, 2001, **64**, 025201.

[137] D. Jonsson, P. Norman, K. Ruud, H. Ågren and T. Helgaker, *J. Chem. Phys.*, 1998, **109**, 572–577.

[138] A. Mayer, *Phys. Rev. B*, 2007, **75**, 045407.

[139] M. van Faassen, L. Jensen, J. A. Berger and P. L. de Boeij, *Chem. Phys. Lett.*, 2004, **395**, 274–278.

[140] R. R. Zope, *J. Phys. B: At. Mol. Opt. Phys.*, 2007, **40**, 3491.

[141] A. F. Hebard, R. C. Haddon, R. M. Fleming and A. R. Kortan, *Appl. Phys. Lett.*, 1991, **59**, 2109–2111.

[142] R. Dovesi, R. Orlando, B. Civalleri, C. Roetti, V. R. Saunders and C. M. Zicovich-Wilson, *Zeitschrift für Kristallographie*, 2005, **220**, 571–573.

[143] R. Dovesi, M. Causa, R. Orlando, C. Roetti and V. R. Saunders, *J. Chem. Phys.*, 1990, **92**, 7402–7411.

[144] M. A. Spackman and A. S. Mitchell, *Phys. Chem. Chem. Phys.*, 2001, **3**, 1518–1523.

[145] M. F. Peintinger, D. V. Oliveira and T. Bredow, *J. Comput. Chem.*, 2013, **34**, 451–459.

[146] J. P. Perdew, *Phys. Rev. B*, 1986, **33**, 8822–8824.

[147] M. Bammerlin, R. Lüthi, E. Meyer, A. Baratoff, J. Lü, M. Guggisberg, C. Loppacher, C. Gerber and H.-J. Güntherodt, *Appl. Phys. A*, 1998, **66**, S293–S294.

[148] R. Bennewitz, A. S. Foster, L. N. Kantorovich, M. Bammerlin, C. Loppacher, S. Schär, M. Guggisberg, E. Meyer and A. L. Shluger, *Phys. Rev. B*, 2000, **62**, 2074–2084.

[149] R. Bennewitz, S. Schär, V. Barwich, O. Pfeiffer, E. Meyer, F. Krok, B. Such, J. Kolodzej and M. Szymonski, *Surface science*, 2001, **474**, L197–L202.

[150] C. Barth and C. R. Henry, *Phys. Rev. Lett.*, 2007, **98**, 136804.

[151] F. J. Giessibl, *Rev. Mod. Phys.*, 2003, **75**, 949–983.

[152] R. Bennewitz, M. Bammerlin, M. Guggisberg, C. Loppacher, A. Baratoff, E. Meyer and H.-J. Güntherodt, *Surf. Interface Anal.*, 1999, **27**, 462–466.

[153] B. Such, P. Czuba, P. Piatkowski and M. Szymonski, *Surface Science*, 2000, **451**, 203–207.

[154] C. Barth and C. R. Henry, *Nanotechnology*, 2006, **17**, S155.

[155] C. Barth and C. R. Henry, *New J. Phys.*, 2009, **11**, 043003.

[156] C. Barth and C. R. Henry, *Phys. Rev. Lett.*, 2008, **100**, 096101.

[157] A. S. Foster, C. Barth and C. R. Henry, *Phys. Rev. Lett.*, 2009, **102**, 256103.

[158] K. Suzuki, *J. Phys. Soc. Jpn.*, 1961, **16**, 67–78.

[159] B. Such, T. Trevethan, T. Glatzel, S. Kawai, L. Zimmerli, E. Meyer, A. L. Shluger, C. H. M. Amijs, P. de Mendoza and A. M. Echavarren, *ACS Nano*, 2010, **4**, 3429–3439.

[160] T. Trevethan, B. Such, T. Glatzel, S. Kawai, A. L. Shluger, E. Meyer, P. de Mendoza and A. M. Echavarren, *Small*, 2011, **7**, 1264–1270.

[161] B. Li, A. Michaelides and M. Scheffler, *Phys. Rev. B*, 2007, **76**, 075401.

[162] S. J. Clark, M. D. Segall, C. J. Pickard, P. J. Hasnip, M. I. J. Probert, K. Refson and M. C. Payne, *Zeitschrift für Kristallographie*, 2005, **220**, 567–570.

[163] H. J. Monkhorst and J. D. Pack, *Phys. Rev. B*, 1976, **13**, 5188–5192.

[164] V. Meisalo and O. Inkinen, *Acta Crystallographica*, 1967, **22**, 58–65.

[165] K. Doll and H. Stoll, *Phys. Rev. B*, 1998, **57**, 4327–4331.

[166] P. Cortona, *Phys. Rev. B*, 1992, **46**, 2008–2014.

[167] W. Zhang, Y. Zhou, L. Zhong, X. Nie and D. Wang, *Opt. Commun.*, 1996, **126**, 61–65.

[168] J. Li, C.-g. Duan, Z.-q. Gu and D.-s. Wang, *Phys. Rev. B*, 1998, **57**, 2222–2228.

[169] M. H. Hakala, O. H. Pakarinen and A. S. Foster, *Phys. Rev. B*, 2008, **78**, 045418.

[170] C. Wieferink, P. Krüger and J. Pollmann, *Phys. Rev. B*, 2011, **83**, 235328.

[171] W. Y. Ching, F. Gan and M.-Z. Huang, *Phys. Rev. B*, 1995, **52**, 1596–1611.

[172] P. K. de Boer, *Am. J. Phys.*, 1999, **67**, 443.

[173] A. Losch and H. Niehus, *Surface Science*, 1999, **420**, 148–156.

[174] H. Li, L. K. Schirra, J. Shim, H. Cheun, B. Kippelen, O. L. A. Monti and J.-L. Bredas, *Chemistry of Materials*, 2012, **24**, 3044–3055.

[175] Y. Kashihara, S. Kimura and J. Harada, *Surface Science*, 1989, **214**, 477–492.

[176] J. Vogt and H. Weiss, *Surface Science*, 2002, **501**, 203–213.

[177] A. M. Dunaev, L. S. Kudin, M. F. Butman and V. B. Motalov, *ECS Trans.*, 2013, **46**, 251–258.

[178] D. W. Boukhvalov, M. I. Katsnelson and A. I. Lichtenstein, *Phys. Rev. B*, 2008, **77**, 035427.

[179] Y.-J. Yu, Y. Zhao, S. Ryu, L. E. Brus, K. S. Kim and P. Kim, *Nano Lett.*, 2009, **9**, 3430–3434.

[180] X. Sha and B. Jackson, *Surface Science*, 2002, **496**, 318–330.

[181] S.-M. Choi, S.-H. Jhi and Y.-W. Son, *Phys. Rev. B*, 2010, **81**, 081407.

[182] G. Gui, J. Li and J. Zhong, *Phys. Rev. B*, 2008, **78**, 075435.

[183] L. A. Girifalco and M. Hodak, *Phys. Rev. B*, 2002, **65**, 125404.

[184] G. Arfken, H. Weber and F. Harris, *Mathematical Methods for Physicists: A Comprehensive Guide*, Elsevier, 2012.